

**Tidal and Non-tidal Contributions to
Surface Loading Processes on Station Coordinates**

Paulo Jorge Mendes Cerveira

Veröffentlichung des
Instituts für Geodäsie und Geophysik

2007

Published by the Institute
of the Course on 'Geodesy and Geoinformation'
of the Vienna University of Technology
Gusshausstrasse 27-29
A-1040 Vienna

Responsible for this issue: Prof. Dr.-Ing. Harald Schuh
Printed by: Grafisches Zentrum HUT GmbH

Die Kosten für den Druck wurden vom '**Fonds National de la Recherche FNR,
Luxemburg**' getragen.



Diese Arbeit wurde an der Fakultät für Mathematik und Geoinformation der Technischen Universität Wien zur Erlangung des akademischen Grades eines Doktors der technischen Wissenschaften eingereicht.

Begutachter:

Prof. Dr. techn. Robert Weber
Institut für Geodäsie und Geophysik der Technischen Universität Wien
A-1040 Wien, Gusshausstraße 27-29, Österreich

Dr. Peter Varga
Geodetic and Geophysical Research Institute of
the Hungarian Academy of Sciences HAS, Seismological Observatory
Meredek 18, 1112 Budapest, Ungarn

Tag der mündlichen Prüfung: 27.06.2006

Auflage: 100 Stück

ISSN 1811-8380

Acknowledgements

First of all, I would like to gratefully acknowledge the support of the Government of the Grand Duchy of Luxembourg, who funded my research project, entitled "Tidal and non-tidal contributions to surface loading processes on station coordinates", by allocating me the Bourse Formation Recherche BFR 03/29. I would also like to express my thanks to the Centre de Documentation et d'Information sur l'Enseignement Supérieur (CEDIES) for its financial contribution to my work. This thesis would not have been possible without their support.

I wish to express my gratitude to my supervisors, Dr. Robert Weber and Prof. Harald Schuh, who have provided me with their guidance, support, insightful comments and helpful advice. Both introduced me to the field of GPS and VLBI, and gave me the means to develop my research with remarkable freedom of thought. They encouraged me to participate in many scientific meetings, so as to share my findings with the broader scientific community. I am especially proud to have come into their circular orbit, although the orbit was rather elliptical at times and even nearly hyperbolic. Special thanks to Prof. Schuh, who, after taking care of my mental capacities, tried (in vain) to exhaust my physical aptitude too.

My sincere thanks are extended to Dr. Tonie van Dam and Dr. Olivier Francis for inviting me to participate in the Journées Luxembourgeoises de Géodynamique in 2004, and for giving me the possibility to spend several weeks at the European Centre for Geodynamics and Seismology (ECGS). They contributed to the broadening of my knowledge in the field of geophysical geodesy and the enhancing of my critical acumen in relation to research that has already been carried out. My time at the ECGS also gave me the possibility to visit my family, who reside in Luxembourg, at regular intervals. In addition, I am highly indebted to Dr. Tonie van Dam, who gave me the permission to use some of her graphics in Chapter 4 of this thesis. A huge amount of Chapter 4 is a result of the joint efforts of many scientists, one of the leaders being Dr. Tonie van Dam, with hers many contributions.

I have the pleasant duty of recording my indebtedness to Dr. Peter Varga, who has read and corrected the whole manuscript with the greatest care and removed many blemishes, which might have escaped less vigilant eyes. I am also thankful to Dr. Peter Varga and Dr. Gyula for the invitation to Sopron and Budapest in December 2004. They broadened my knowledge beyond the boundaries of geodesy by teaching me a basic survival vocabulary kit for foreigners in Hungary... Unfortunately, significant tides in my glass of sör (sometimes full, rarely empty...) resulted in black holes in my head. I think I am definitely more gifted in geodesy than in Hungarian!

It is also with deep gratitude that I wish to thank Dr. Ladislav Brimich and Dr. Peter Vajda, with whom I shared some fresh air and wine in Bratislava, Vyhne and High Tatras. It was a real pleasure to spend some time there, especially at Smolenice Castle... I discovered, by the way, that I would have enjoyed living there in the Middle Ages as an alchemist!

I am deeply indebted to Dr. Bruno Meurers for imparting knowledge on the tides and free oscillations of planet Earth, and for his excellent introductory lecture notes.

Dr. Thomas Hobiger and Dr. Johannes Böhm are excellent motivators, when I was feeling uninspired. Additionally, both very kindly agreed to read the integral work and made helpful suggestions. Dr. Böhm deserves special thanks for pushing me to take part in the weekly IGG run.

To the rest of the academic staff of the Institute of Geodesy and Geophysics in Vienna, and to the staff of the European Centre for Geodynamics and Seismology in Luxembourg, a big "THANK YOU".

Special thanks go to the system administrator of the ECGS, Gilles Celli, who convinced me to buy a Macintosh, so as to complete my great collection of computers. Now, my room looks like the spacecraft operations centre at NASA!

To Mag. Florent Marciacq, whose eyes definitely lost $3/10^{\text{th}}$ of visual faculty by checking the final manuscript in English. I promise I will never again use the font Times New Roman in 6 pt!

I would also like to acknowledge the International VLBI Service for Geodesy and Astrometry (IVS), the International GNSS Service (IGS), and the Scripps and Orbit Permanent Array Centre (SOPAC), for

providing their data for free. These agencies/services spend many resources in distributing cutting-edge scientific products to the community. Sometimes, I was frustrated when I encountered inconsistencies in their data, but on the whole, I must admit that these services are the real driving forces of scientific breakthroughs.

I also want to take this opportunity to express thanks to various agencies for financial support during the last few years: the University of Luxembourg, who contributed financially to my research; the Bourse Fondation Mathieu (BFM) who supported me in 2004 and 2005, to whom I owe my participation in several meetings (IGS meeting 2004 in Berne, EGU meeting 2006 in Vienna, and WIGFR meeting 2006 in Smolenice); the Fonds National de la Recherche of Luxembourg for integrally financing the travel expenses to the American Geophysical Union (AGU) Meeting 2003 in San Francisco; the International Association of Geodesy (IAG) who financed my participation to the meeting of Lanzarote in 2005; the ECGS for financing the travel expenses to the International Symposium on Earth tides held in Ottawa in 2004; the BFR for financing the travel expenses to the Deuxième Journée des Boursiers in 2005 as part of the Science Festival; and finally, the Institut de Physique du Globe de Paris (IPGP) for funding the Congrès des Doctorants in March 2005.

To my roommates, Florent and Ivana, and Ivana's mother, Gordana, for all those nice evenings we spent enjoying good wine and Bosnian meals. Jacques and our neighbours deserve special thanks for their incredible resources! In this context, long life to the "Rakja"!

To my Landlord Wolfgang, Noriko and their son Takuya, thank you for your endless support in administrative tasks, for your countless invitations and ...

To Michi, Wurmi, Paul and Alexandar, wherever you have settled down. You showed me the best places in Vienna, even though I could not remember the way back – thanks to all taxi drivers, by the way!

To Suzanne Reuter and Kurt Bretterbauer, my warmest wishes for your enthusiasm and competence in teaching scholars and students.

Last but not least, I am forever grateful to my parents, Clement and Adelina, and my brothers Bruno and Eric, for their (non) understanding of what I was doing, for not asking questions about my work, but giving me unexpected and kind advice when it was most needed. To my uncles (Manuel and Agostinho), aunts (Maria Alice and Albertina), cousins (Jhemp, Anabella, Christina, Carlos), Steve, Theo, and Hanni for their countless dinner invitations, some of which I could accept, some of which have been postponed.

The text of Chapter 5 is partly a reformatted version of the material as it appears in:

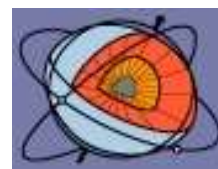
MENDES CERVEIRA, P.J., R. HEINKELMANN, J. BOEHM, R. WEBER AND H. SCHUH, **(2006a)**. “Contributions of GPS and VLBI in Understanding Station Motions”, *Journal of Geodynamics*, DOI:10.1016/j.jog.2005.08.024, pp. 87-93.

The dissertation author was the primary researcher and author, and the co-authors listed in this publication helped, directed and supervised the research which forms the basis for that chapter. Copyright © by Elsevier, Journal of Geodynamics

The text of Chapter 7 is partly a reformatted version of the material as it will appear in:

MENDES CERVEIRA, P.J., T. HOBIGER, R. WEBER AND H. SCHUH, **(2006b)**. “Spatial Spectral Inversion of SOPAC GPS Data”, *IAG Scientific Assembly 2005*, Springer Verlag, in print.

The dissertation author was the primary researcher and author, and the co-authors listed in this publication helped, directed and supervised the research which forms the basis for that chapter. Copyright © by Springer, International Association of Geodesy IAG



Abstract

Space geodesy allows to monitor large-scale mass transfers caused by hydrological variations, ocean currents, sea level rise, and ice mass changes. One method, known as “GPS (Global Positioning System) inversion”, directly relates surface mass redistribution to geometric deformation by using global space geodetic networks. This is currently the leading method due to its outstanding widespread spatial distribution. However, this method requires high precision 3D geometric deformations on a global scale. In addition, Earth models and their associated parameters, i.e. the degree-dependent Load Love Numbers (LLNs), play an integral role. These LLNs directly link the deformation, induced by a surface-normal load, to an equivalent load height column usually representing seawater. In the processing of global coordinate time series many influencing factors, e.g. episodic displacements due to earthquakes and antenna changes, all tidal contributions, and changes due to software strategy improvements and their corresponding reductions need to be accounted for. In this respect, intra- and inter-technique comparisons, i.e. between VLBI (Very Long Baseline Interferometry) and GPS, are instructive and useful for finding systematic biases. Topics such as the inverted barometer assumption, reference frames along with geocentre motion and Earth models are key issues in computing displacements caused by surface-normal loads.

The objective of this thesis was to find a method to test Earth’s mechanical properties, i.e. azimuth-dependent LLNs. In order to estimate these low-degree LLNs, the load and the geometric deformation have to be known accurately. In fact the load is unknown, since this is exactly what ongoing satellite gravity missions are trying to retrieve. However, a one-to-one correspondence exists between the radial and lateral spectral deformation and the ratios of the radial and lateral LLNs. The seasonal deformation provided by SOPAC (Scripps and Orbit Permanent Array Centre) was used to focus on the determination of Earth’s mechanical properties. The degree-2 ratios of radial and lateral poloidal coefficients, corresponding to the degree-2 ratios of the height and lateral Load Love Numbers were estimated. Presently, the estimated ratios of poloidal coefficients show a clear order-dependence and disagree with results derived from theoretical Earth models. This indicates that the spectral deformation coefficients still lack stability in terms of the estimation of the equivalent load height column coefficients.

This thesis embraces the state-of-the-art description of all known loading effects on station positions. It is inevitable that in the near future, a consistent strategy for an inter-technique joint inversion will significantly stabilize the spectral deformation coefficients. The latter are only one intermediate step in the determination of stable equivalent load height column coefficients.

Zusammenfassung

Geodätische Weltraumverfahren gestatten, großräumige Massentransporte an der Erdoberfläche zu beobachten. Solche Massenverlagerungen werden durch hydrologische Variationen, durch Merresströmungen, durch Schwankungen des Meeresspiegels oder der Eisbilanz verursacht. Eine heute eingesetzte Methode, auch als „GPS-Inversion“ bekannt, verknüpft oberflächennahe Massenverlagerungen mit geometrischen Deformationen. Als Datenquelle werden globale geodätische Netze verwendet und das Global Positioning System (GPS) steht dabei wegen seiner flächendeckenden Stationsverteilung an vorderster Front. Jedoch erfordert diese Methode eine außerordentlich hohe Genauigkeit der abgeleiteten geometrischen Deformationen. Eine zentrale Rolle bei der Untersuchung von Auflasteffekten spielen die Modelle des Erdkörpers, speziell die Elastizitätsparameter der Erdkruste und hier insbesondere die gradabhängigen Auflastzahlen (Load Love Numbers, LLNs). Diese LLNs erlauben es, die durch eine oberflächennormale Last hervorgerufenen Deformationen mit der gleichwertigen Höhe einer Meereswassersäule zu verknüpfen. In der Verarbeitung von Zeitserien globaler Stationskoordinaten müssen viele Faktoren berücksichtigt werden. Dazu gehören plötzlich auftretende Verschiebungen durch Erdbeben, oder Antennenwechsel, gezeitenbedingte Deformationen sowie scheinbare Verschiebungen, die durch die Verbesserungen der Modelle und der dazugehörigen Auswertungssoftware verursacht werden. Vergleiche der Ergebnisse aller geodätischer Raumverfahren ermöglichen das Erkennen systemimmanenter Unterschiede. Bei der Berechnung von geometrischen Deformationen kommen der invers-barometrischen Approximation, dem Bezugsrahmen einschließlich der Geozentrumsvariation sowie den Erdmodellen Schlüsselpositionen zu.

Die Zielsetzung dieser Arbeit war es eine Methode zu finden, um die mechanischen Eigenschaften der Erde und insbesondere die positionsabhängige LLNs unabhängig zu überprüfen. Um diese LLNs zu bestimmen, müssten die Auflasten sowie die geometrische Deformation genau bekannt sein. Dies ist zwar derzeit noch nicht der Fall, jedoch versuchen aktuelle Satelliten-Schwerefeldmissionen (CHAMP, GRACE) die Auflastvariationen abzuleiten. Es besteht aber eine Eins-zu-eins-Korrespondenz der Quotienten von radialer und lateraler spektraler Deformation zu den Verhältnissen der radialen und lateralen LLNs. Deshalb wurde die jährliche und halbjährliche geometrische Deformation verwendet, die von SOPAC (Scripps and Orbit Permanent Array Centre) bereitgestellt wird, um diese Quotienten zu schätzen. Theoretisch sind die Quotienten der radial- und lateral-poloidalen Koeffizienten zweiten Grades proportional zu denjenigen der radialen und lateralen LLNs zweiten Grades. Die geschätzten Quotienten weisen jedoch eine azimutale Abhängigkeit auf und stehen im klaren Widerspruch zu den theoretischen Werten. Das deutet darauf hin, dass die aus GPS-Messungen abgeleiteten spektralen Deformationskoeffizienten derzeit nicht zur Ableitung der gleichwertigen Höhe einer Meeressäule benutzt werden sollten.

Diese Arbeit beschreibt umfassend alle bekannten Auflasteffekte auf Stationskoordinaten. In Zukunft wird die Schaffung einer ausreichenden Redundanz und Komplementarität unter den Beobachtungsverfahren eine gegenseitige Überprüfung ermöglichen. Insbesondere wird durch eine kombinierte Inversion eine Erhöhung der Genauigkeit und Stabilität der abgeleiteten Meereswassersäule erwartet.

Table of Contents

Acknowledgements.....	iv
Abstract.....	vii
Zusammenfassung	viii
Table of Contents.....	ix
Chapter 1 Introduction	12
1.1 The role of GPS and VLBI in Earth surface deformation studies.....	12
1.2 Research objectives	12
1.3 Thesis outlines	13
Chapter 2 Earth surface displacements: observables and services	14
2.1 Ground Motion	14
2.2 Astronomical tides	15
2.3 Deformation due to surface loading	16
2.3.1 Equations of deformation	16
2.3.2 Variety of Love Numbers	17
2.3.3 Computation methods of surface loading effects.....	18
2.3.4 Ocean loading.....	18
2.3.5 Pole tide loading.....	19
2.3.6 Atmospheric loading.....	19
2.3.7 Other geophysical sources of station displacement	19
2.4 Global Positioning System (GPS)	20
2.5 Very Long Baseline Interferometry (VLBI)	23
2.6 Comparison of GPS and VLBI.....	24
2.7 Institutions and data centres of GPS and VLBI.....	25
2.7.1 International GNSS Service (IGS).....	25
2.7.2 International VLBI Service (IVS).....	28
Chapter 3 Tides and deformation due to surface loading	30
3.1 Description of tides	30
3.2 Tide generating potential	30
3.3 Body (solid Earth) tides	36
3.4 Permanent tides	40
3.5 Load tides.....	40
3.6 Pole tide: rotational deformation due to polar motion	44
3.7 Atmospheric tides.....	45
3.8 Radiational tides	46
3.9 Equation of motion of Earth tides	46
3.10 Calculation of Earth models	47

Chapter 4 Atmospheric loading models	49
4.1 History and services	49
4.2 Products	50
4.3 Meteorological models	50
4.3.1 ECMWF vs. NCEPR	51
4.3.2 Surface versus sea level pressure	51
4.3.3 Reference pressure	52
4.4 Interpolation	53
4.5 Atmospheric pressure tides	54
4.6 Land-ocean mask (coastline)	54
4.7 Green's functions	56
4.8 Spherical harmonics vs. global convolution	58
4.9 Lateral components	59
Chapter 5 Global coordinate time series analysis	60
5.1 Background	60
5.1.1 Global reference frames and geocentre motion	60
5.1.2 Coordinates vs. Baselines	62
5.1.3 SINEX	63
5.2 VLBI analysis	63
5.2.1 OCCAM VLBI software	63
5.2.2 IGG coordinate time series solutions	64
5.2.3 Baselines	64
5.2.4 Topocentric coordinate time series and trends	66
5.3 GPS analysis	68
5.3.1 Analysis Centres of the IGS	68
5.3.2 Constraints handling	70
5.3.3 Similarity transformation parameters	73
5.3.4 Data cleaning	77
5.3.5 Model parameters	80
5.3.6 Comparison between AC solutions	81
5.3.7 Seasonal variations	83
5.3.8 Unreported and unexplained offsets	86
5.3.9 Very short baselines	87
5.3.10 Comparison with atmospheric loading displacements	88
Chapter 6 Inversion for ratios of Load Love Numbers	94
6.1 Introduction	94
6.2 Theoretical aspects	94
6.3 Inversion related issues	98

Chapter 7 Spectral approximation	102
7.1 Background	102
7.2 Approach	102
7.3 Temporal aliasing effects	104
7.4 Degree-0 investigation	105
7.5 Degree-1 investigation	106
7.6 Degree-2 investigation	108
7.7 Ratios of degree-2 poloidal coefficients	109
Chapter 8 Conclusions	111
8.1 Summary of results and remarks	111
8.2 Directions for future research	112
Appendix A Acronyms	113
Appendix B Estimated vertical site rates [mm/y] and RMS of selected ACs.....	116
Appendix C Observed annual signals [mm] and RMS in vertical component for selected ACs	119
Bibliography	122
List of Figures	130
List of Tables	136
Curriculum vitae	137

Chapter 1

Introduction

1.1 The role of GPS and VLBI in Earth surface deformation studies

Modern space techniques such as the Very Long Baseline Interferometry (VLBI) and Global Positioning System (GPS) (AMBROSIOUS *et al.*, 1998) are key contributors to the establishment and densification of Celestial and Terrestrial Reference Frames as well as to the determination of Earth Rotation Parameters. Since the commencement of this thesis in 2002, both space geodetic techniques have undergone striking modelling improvements, e.g. tropospheric (BOEHM *et al.*, 2006a) or ionospheric (HAWAREY *et al.*, 2005; FRITSCH *et al.*, 2005) parameters, and now allow for an unprecedented accuracy in global point determination groping at the sub-cm level (BEUTLER *et al.*, 2005). Recently, the new precession-nutation International Astronomical Union (IAU) 2000 models (MATHEWS *et al.*, 2002; CAPITAINE, 2002) have been applied in most space geodetic software. However, the use of the non-rotating-origin (NRO) is still pending. One of the still limiting effects in data modelling, apart from atmospheric delays, are tidal and non-tidal loading processes, which have an impact on, first and foremost, the height component.

1.2 Research objectives

From the discussion of the very demanding applications of the VLBI and GPS space geodetic techniques, it is obvious that the high precision and quality of the observations, as well as the right modelling of observables, along with their reductions, are of utmost importance.

One goal of this thesis is to evaluate the existing atmospheric loading models in terms of their validity in representing the remaining cyclic coordinate variations observed during various time scales.

Another aim of this thesis is to focus on available coordinate series of the technique specific observing sites in order to separate tidal from non-tidal effects such as ocean and atmospheric loading. The objectives are:

- to compare technique specific coordinate solutions (BEUTLER *et al.*, 1999) provided by the International Global Navigation Satellite System (GNSS) Service (IGS). This comparison should be especially instructive and useful in finding systematic biases between the technique-specific coordinate time series. These biases might stem from inconsistent data modelling and are currently hidden by averaging processes along with empirical weighting of the individual Analysis Centres (ACs) solutions
- to assess and exclude all nuisance signals on coordinate time series, so that only the variations due to hydrological loading effects on continental areas might remain.

The ultimate objective is to derive position dependent corrections, i.e. azimuth-dependent Load Love Numbers (LLNs) purely from geometric deformation. At present, nominal LLNs are applied in data modelling to account for load-induced site displacements, although the International Earth Rotation and Reference Systems Service (IERS¹) Conventions 2003² (MCARTHY AND PETIT, 2003) propose azimuth-dependent LLNs, due to resonances in the diurnal band, for the corrections of nominal ocean tide loading (OTL) displacements.

¹ <http://www.iers.org/>

² <http://tai.bipm.org/iers/conv2003/conv2003.html>

Subsequently, the objective is to check the agreement between the GPS data, the VLBI data, and model predictions concerning surface deformation. The research project should reveal existing deficiencies and inconsistencies in data modelling in the IGS Analyses Centres, and should conclude on the ability to estimate degree- and order-dependent LLNs from space geodetic observations.

1.3 Thesis outlines

The objectives described above lead to some basic information on ground motion, surface deformation, astronomical tides, the GPS and VLBI techniques and their respective international services, which are described in Chapter 2. Each observable is intimately related to three major components: geometry, clock and atmosphere. The geometry component contains information on satellite (or sources) positions and station coordinates, which are represented with respect to an appropriate frame. These reference frames have to be properly related to each other in space and time.

Once we have suitable reference frames, all kind of tides and their indirect impact on station displacements are considered in Chapter 3. The equation of motion of tides, along with the knowledge on Earth models, enables one to obtain theoretical Load Love Numbers.

Chapter 4 gives an overview of present atmospheric loading models and focuses especially on the impact of different loading model parameters on station displacements.

Several investigations of global weekly station coordinate time series (and baselines) from eight IGS ACs, one daily Scripps Orbit and Permanent Array Centre (SOPAC) coordinate solution, as well as baseline solutions computed by the Institute of Geodesy and Geophysics (IGG) and Goddard Space Flight Centre (GSFC) are described in greater detail in Chapter 5.

The outcome of Chapter 5 is crucial, because it serves as input for the spatial spectral approximation of surface displacements. The theoretical basis is expanded in Chapter 6.

In Chapter 7, the spectral deformation coefficients are estimated from SOPAC data in order to calculate the ratio between azimuth-dependent Load Love Numbers. These ratios can be compared to theoretical values, based on a specific Earth model, in a specific centre of frame.

Finally, Chapter 8 summarizes my entire project, draws several concluding remarks and suggests new directions for future research.

Chapter 2

Earth surface displacements: observables and services

2.1 Ground Motion

Plate tectonics, as explained by WEGENER (1929/1966), describes the linear and abrupt motion of the rigid plates that make up the mechanically strong lithosphere over the relatively weak asthenosphere (see Figure 1). Plates meet at boundaries that are divergent, convergent or conservative, and their movement is driven by a number of different forces (e.g. STACEY, 1977). Forces acting as downgoing slabs, at convergent plate boundaries, are the strongest. At conservative boundaries, the plates move in relation to each other along lateral shear transform faults. A resistive frictional force counters shear sliding along transform faults (TURCOTTE AND SCHUBERT, 2002). Variations in frictional resistance lead to instabilities and sudden stress drops, followed by periods of non-motion while the stress recharges (NIKOLAIDIS, 2002). This stick-slip behaviour is the basic mechanism of earthquakes. Crustal deformation in plate boundary zones happens over a broad range of temporal scales. Geodesy is the science for monitoring the variations in the shape and gravity of the Earth, and includes the study of permanent crustal deformation that occurs either gradually with the steady motion of plates, or suddenly with earthquakes. An integral component for understanding surface strains accompanying tectonic plate motion and earthquake faulting is GPS, as well as VLBI. The International Terrestrial Reference Frame (e.g. ITRF2000; ITRF2005³ will probably be made available publicly in 2006) describes the long-term motion (decades) of individual stations. A possible cause for triggering eruptions of volcanoes may be related to astronomical tides.

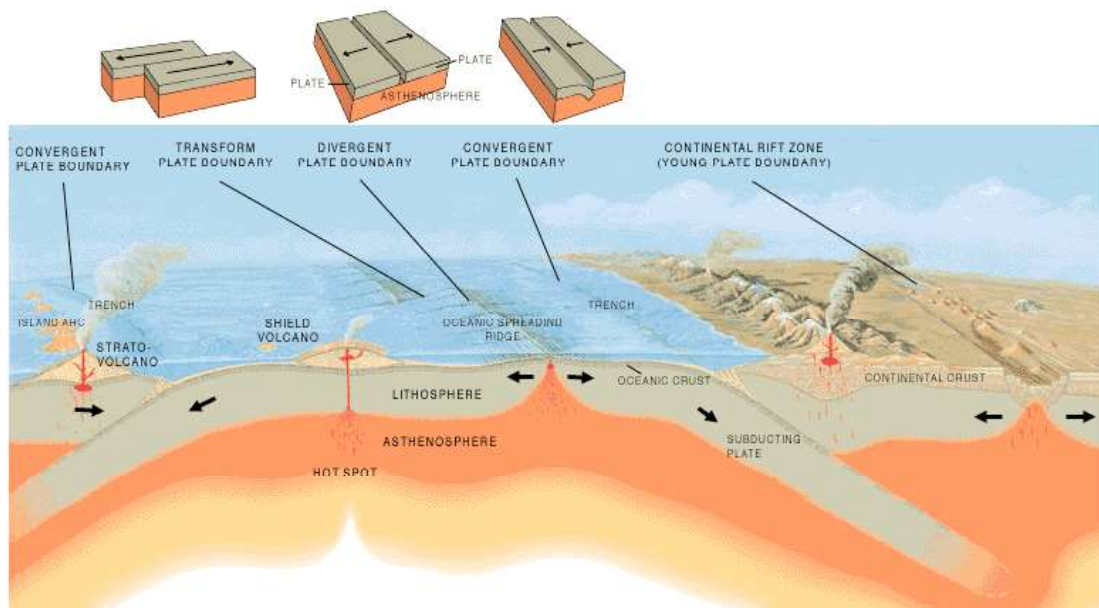


Figure 1: Cross-section illustrating the main types of plate boundaries (source from USGS⁴)

³ http://itrf.ensg.ign.fr/ITRF_solutions/2005/ITRF2005.php

⁴ <http://pubs.usgs.gov/publications/text/Vigil.html>

2.2 Astronomical tides

NEWTON (1687/1999) laid out in his monumental work the *Principia*, the principles of time, force and motion. The *Principia* also roughly explained the astronomical tides (e.g. GONDHALEKAR, 2001; CARTWRIGHT, 1999). Contrary to previous descriptions of linear or abrupt motion, e.g. the solid Earth body tide causes periodical displacements on the Earth's surface of a few decimetres. It arises from combined gravitational and centrifugal forces, predominately of the Earth-moon and the Earth-sun systems. These periodic forces are imposed on the solid Earth, oceans and atmosphere. We first distinguish between the Earth body tide, pure ocean tide and Ocean Tide Loading (OTL) (BAKER *et al.*, 1995; LAMBERT *et al.*, 1998). This distinction is useful in theory and practice, since the same lunisolar forces have different effects. In addition, the ways in which they are measured and modelled are different. Basically, tide gauges only measure the pure ocean tide, while altimeters measure the sum of ocean loading and Earth body tide.

To begin with, the pure ocean tide is what is observed while standing on the beach: the sea level rises and falls with respect to one's position on the solid Earth. It is also what tide gauges attached to coastlines a pressure gauge placed at the ocean floor measure (e.g. MELLOR, 1996). It is a hydrodynamic effect. The amplitude of water tides is largest in shallow waters and enclosed basins with resonant properties (e.g. KANTHA AND CLAYSON, 2000).

One consequence of the pure ocean tide is the OTL (e.g. URSCHL *et al.*, 2005; KING AND PADMAN, 2005), which is the deformation of the ocean floor and nearby land in response to the redistribution of water (HATANAKA *et al.*, 2001). A tide gauge cannot measure this component, because it is anchored to the same land that is rising and falling due to the OTL. An oceanless Earth would consequently have no ocean tide and no OTL.

The Earth body tide is caused by the direct effect of the lunisolar force on the whole Earth's crust including the ocean floor. It affects the same ocean floor as the loading tide. However, if there were no oceans, there would still be an Earth body tide (JEFFREYS, 1962).

The Earth tides (e.g. MELCHIOR, 1978) include body and loading tides. CARTWRIGHT (1999) has written an authoritative scientific history of tides. The Earth tides phenomenon can be measured on land, e.g. by gravimeters. All ocean tide models concentrate on estimating the very energetic semi-diurnal tidal components M_2 within a 12.42-hour period or S_1 within a 24-hour period. Components with the longest periods (larger than 7 days) are generally smaller than 2 cm (DARWIN, 1886), and their signal is difficult to receive from the first 2 or 3 years of an altimetric dataset (e.g. TOPEX/POSEIDON or JASON⁵).

The pole tide, which is a tide-like motion, has nothing to do with the lunisolar forcing. It is forced by small perturbations of the Earth's rotation (e.g. LAMBECK, 1980; MORITZ and MUELLER, 1987; ZHARKOV *et al.*, 1996; SCHUH *et al.*, 2003; SEITZ, 2004) with primarily an annual period and one around 432 days (e.g. SEITZ, 2004, who considered the nonlinear Liouville equation), a period inheriting the name of Chandler wobble (e.g. VICENTE AND WILSON, 1997; SCHUH *et al.*, 2001) with about 100 mas amplitude. To model the Chandler wobble, a time series perturbation to the Earth rotation⁶ routinely measured with space techniques is needed. Recently, VICENTE AND WILSON (2005) questioned if there is a need for a new definition of a conventional international origin, which is the reference origin for describing polar motion.

The atmospheric tides (CHAPMAN AND LINDZEN, 1970; VOLLAND, 1997), observed e.g. in pressure (e.g. MENTES, 2004) or temperature data, affect OTL models. Atmospheric pressure, with its own tidal variations, affects the sea level. Usually, one applies a model of sea level motion called Inverted Barometer (IB), whereby a 1 mbar increase in local atmospheric pressure locally depresses sea level by 1 cm (e.g. WUNSCH AND STAMMER, 1997; VAN DAM *et al.*, 2003). The non-inverted barometer (NIB) assumption transmits atmospheric pressure variations integrally to the ocean floor (e.g. SCHUH *et al.*, 2003; PETROV

⁵ <http://topex-www.jpl.nasa.gov/>

⁶ <http://hpiers.obspm.fr/eop-pc/>

AND BOY, 2004). The pressure data comes from atmospheric models, e.g. from the European Centre for Medium-Range Weather Forecasts (ECMWF) or the National Centres for Environmental Prediction (NCEP). The directions for handling the S_1 and S_2 atmospheric pressure tides are still under development in the IERS Conventions.

2.3 Deformation due to surface loading

Surface loads cause many deformations of the Earth's surface on a global and local scale, and were studied by, e.g., THOMSON and TAIT (1879), and DARWIN⁷ (1882). One task of geophysics is to formulate the Earth's response to these loads over time (e.g. FARRELL, 1972; VAN DAM *et al.*, 1994a, 2003; ENGELS, 2006; PETROV and BOY, 2004). In 1926, STONELEY computed, for the first time, the Earth's tidal deformations, PERKERIS and JAROSCH formulated the eigenvalue problem for an elastic gravitating sphere in 1958, and SLICHTER and CAPUTO were the first to solve the response of surface loading for simple Earth models in 1960 (FARRELL, 1972). Given the dimensions and mechanical properties of the Earth as a whole or of parts of it, and given the loads acting on the body, the deformation strain and stress of the body through time can be evaluated (LAMBECK, 1988).

2.3.1 Equations of deformation

OGDEN (1997) gives a meticulous and precise account of the theory of non-linear elastic deformations. For describing the response of a load on a body, four basic equations must be fulfilled:

- a kinematic equation relating displacements u_i to strain ε_{ij} (e.g. LANDAU AND LIFSCHITZ, 1991):

$$\varepsilon_{ij} = \frac{1}{2}(\partial_j u_i + \partial_i u_j + \partial_i u_l \partial_j u_l) \quad (2.3.1)$$

- an equation expressing the linear relation between stress σ_{ij} and strain (C_{ijkl} is a fourth-rank tensor possessing 21 independent coefficients), which is commonly known as Hooke's law :

$$\sigma_{ij} = C_{ijkl} \varepsilon_{kl} \quad (2.3.2)$$

- a relation equating the rate of change of linear momentum of an element of volume (of density ρ from the point of view of the observer frame) with the applied body forces k_i (per unit of volume) and surface forces $\partial_j \sigma_{ij}$:

$$\rho \frac{\partial^2 u_i}{\partial t^2} = \partial_j \sigma_{ij} + k_i \quad (2.3.3)$$

- and finally, the deformation satisfying the equation of continuity:

$$\frac{\partial \rho}{\partial t} + \partial_i \left(\rho \frac{\partial u_i}{\partial t} \right) = 0 \quad (2.3.4)$$

Equations (2.3.1)-(2.3.4) are valid in general, but may be simplified considerably under several assumptions concerning the elasticity, isotropy, homogeneity, small displacements and deformations of the Earth (leading to the well-known Lamé parameters λ^L and μ^L). The complete set of equations (2.3.1)-(2.3.4) is solved with a number of boundary conditions that include (e.g. LAMBECK, 1988):

- regularity at the origin

⁷ http://gemini.gsfc.nasa.gov/aplo/darwin_1882/

- continuity of deformation and stress across surfaces of discontinuity
- vanishing stresses at free surfaces
- continuity of potentials and their gradients across boundaries

The above-mentioned equations are a requirement for deriving the equation of motion of Earth tides and the associated indirect effects (see section 3.9).

2.3.2 Variety of Love Numbers

The *Love Numbers* notation (MATHEWS, 2001) is reserved for the deformation by a volume force or potential that does not load the surface such as a tidal potential or the harmonic part of the centrifugal force (LOVE, 1911/1967). However, if a potential does load the Earth, as occurs in the case of the gravitational potential of the ocean tide or of an ice load, the appropriate parameters are called *Load Love Numbers* (MUNK AND MACDONALD, 1960). This difference stems from the different boundary conditions in the two cases: In the latter, a normal stress acts on the free surface that is absent in the former (LAMBECK, 1988). The surface load can be an ocean tide, ice load, or a variation in atmospheric pressure. In order to describe horizontal deformations arising from surface wind or ocean currents, *Shear Love Numbers* are adopted (e.g. VARGA, 1983). Analytical solutions for the Love Numbers exist only for simple models e.g. for an incompressible homogeneous elastic sphere or for an incompressible homogeneous mantle surrounding a fluid core (LAMBECK, 1980). In a static solution, deformations are assumed to be independent of frequency, if the frequency of the forcing function does not lie close to free oscillation frequencies, e.g. the Nearly Diurnal Free Wobble (NDFW) or tilt-over mode (TOM), of the Earth (MORITZ AND MUELLER, 1987). In particular, the variation of the observed response as a function of the frequency in the tidal band tells us something about the interior of our planet that seismology cannot provide. This variation with frequency is caused by resonant behaviour of the Earth near 1 cycle per day, due to a normal mode of the rotating Earth. This mode is the NDFW with a period of about 1 day, if observed in the terrestrial reference frame. It is related to the liquid outer core and is caused due to the non-alignment of the rotation axis of the outer core and of the mantle of the Earth.

In order to obtain the high precision Love Numbers from space geodetic data analysis, sophisticated models, especially the ocean tide ones, are crucial. This is because the solid Earth, ocean and atmosphere affect the geopotential variations and site displacements at the same frequency associated with each tidal constituent. Ideally, if consistent models are applied within the data processing, the resulting station coordinate time series should contain almost no tidal contribution, which is presently not the case (e.g. TREGONING AND VAN DAM, 2005b). Remaining tidal signals are due to an unrealistic choice of model parameters for nominal Love Numbers or an improper force modelling, which affects the station coordinates. The chosen model for troposphere refraction at diurnal intervals frequently affects the station heights. This effect has to be separated from the tidal influence. Presently, both space-geodetic techniques GPS and VLBI are in principle sensitive to a variety of tidal effects (e.g., HAAS AND SCHUH, 1996).

First of all, local site displacements due to solid Earth tides have to be taken into account. The effect of solid Earth tides is discussed extensively in the IERS Conventions 2003 (MC CARTHY AND PETIT, 2003). Application of the available equations describes the vertical as well as horizontal displacement at the 1 mm level. To achieve this accuracy, MATHEWS *et al.* (1995) introduced a new notation to represent the latitude dependence of the effective Love and Shida Numbers: terms of multiple h and l parameters are used, causing some confusion for non-specialists. In this notation, the parameters $h^{(0)}$ and $l^{(0)}$ represent the common used degree-2 Love and Shida Numbers h_{2m} and l_{2m} , allowing for order dependency. Additionally, the latitude dependence of the Love and Shida Numbers is accounted for by five additional parameters $h^{(2)}$, h' , $l^{(1)}$, $l^{(2)}$ and l' . All these parameters are described in a complex notation, i.e. with a real and imaginary part (allowing the description of in-phase and out-of-phase displacements). For corrections of the solid Earth tides displacement, MATHEWS *et al.* (1997) recommend a two-step procedure, which will be explored in greater detail in subsection 3.3.

2.3.3 Computation methods of surface loading effects

For the actual computation of loading effects, surface load data are required for all relevant loads. The latter are then convolved with the Earth's response either in the space or the wave number domain. In this way, the loading effects, e.g. surface displacements, gravity variations and geocentric displacements, are determined (e.g. FARRELL, 1972). Loading responses to surface loads are normally computed in one of three ways:

- the surface load can be expanded into a series of spherical harmonics. Then, a summation in the wave domain is carried out such that each term of degree n , in the associated load potential, is multiplied by the appropriate Load Love Number of the same degree (see e.g. GEGOUT⁸).
- the Green's function approach is more convenient when the load covers only a fraction of the Earth's surface or it is only known in the vicinity of the point in question, because the spherical harmonics expansion would be required to a very high degree (see e.g. VAN DAM⁹ and PETROV¹⁰).
- the third method employed uses a local regression coefficient determined by fitting local changes in pressure to the vertical component of observed deformation, e.g. by VAN DAM *et al.* (1994a), MCCARTHY AND PETIT (2003), KANIUTH AND VETTER (2005), or as available at the Special Bureau for Loading SBL¹¹.

2.3.4 Ocean loading

Movements induced by ocean tide loading may reach the range of a few centimetres in the vertical (e.g. SCHUH AND MOEHLMANN, 1989; SCHERNECK, 1996; SCHUH AND HAAS, 1997; BOS AND BAKER, 2000). Available ocean tide models are tabulated in the IERS Conventions 2003: e.g. the Schwiderski hydrodynamic model, NAO.99b, FES99 (LEFEVRE *et al.*, 2002), CSR4.0 (EANES AND BETTADPUR, 1996, 1999), GOT00.2 and TPXO.5. In the meantime, much newer models have been made publicly available, the most recent being FES2004 (LETELLIER, 2004) and a pre-release of TPXO7.0. Until recently, the TPXO6.2 model was said to be one of the most accurate global tidal solutions, particularly for high latitudes since it utilizes recent Antarctic grounding line information and Antarctic and Arctic tide height data (EGBERT AND EROFEEVA, 2002; KING AND PADMAN, 2005).

However, the IERS recommendations for ocean loading are rather general and vague on crucial points (personal communication by RAY J., 2005). The IERS Conventions 2003 recommend that users adopt the site-specific amplitudes and phases for the 11 largest partial tides generated by BOS AND SCHERNECK¹² (SCHERNECK, 1991, 1996), preferably using the GOT00.2 tidal model of RAY (1999) for a TOPEX/POSEIDON⁵ derived solution, or FES99 for a hydrodynamic solution. A specific official implementation to compute site displacements is still lacking. No official routine is available as yet to compute the displacements.

In this context, AGNEW¹³ provided a program to compute OTL displacements for any given site using the usual amplitudes and phases, and adopting SCHWIDERSKI'S computations (1983), as generated by BOS AND SCHERNECK¹². AGNEW'S implementation considers a total of 141 tidal constituents whose amplitudes and phases are found by spline interpolation of the tidal admittance based on the 11 main tides. A precision of about 1% is guaranteed. Tests versus other implementations, usually regarded as highly

⁸ http://www.sbl.statkart.no/products/research/ITRF_sites/gegout_2004.php

⁹ http://www.sbl.statkart.no/products/research/ITRF_sites/vandam_2004.php

¹⁰ <http://gemini.gsfc.nasa.gov/aplo/>

¹¹ <http://www.sbl.statkart.no/products/research/regression/>

¹² <http://www.oso.chalmers.se/~loading/>

¹³ <http://sio.ucsd.edu/rab/>

accurate, are still underway. A copy of AGNEW'S source code, which is part of the ocean loading SPOTL¹⁴ software, can be obtained at the National Geodetic Survey (NGS¹⁵).

In test comparisons against a simple OTL routine with no minor tides and no nodal modulations, HUGENTOBLE found radial RMS differences over fourteen days of about 2 mm for a globally distributed network of ~250 stations using the GOT00.2 ocean model (personal communication RAY J., 2006). Differences tend to be greater at higher latitudes, with the largest RMS difference being 5.0 mm at the Antarctic station OHIG.

Users should also note that SCHERNECK has recently added the new TPXO.7.0 and FES2004 ocean models to his OTL website¹². Older models can be problematic in areas such as Antarctica (KING AND PADMAN, 2005).

2.3.5 Pole tide loading

As mentioned previously, the pole tide causes small variations in the station coordinates up to a few cm with periods primarily annual and around the Chandler wobble (SEITZ, 2004; SEITZ *et al.*, 2004). Movements are forced by a small part of the centrifugal potential which stems from the time dependent offset of the instantaneous rotation pole from the mean (see subsection 3.6). Its geometrical correction is imposed using the formulas adopted by the IERS Conventions 2003 (MCARTHUR AND PETIT, 2003). The modelling of displacements due to the pole tide arising from the oceanic mass redistribution is still under development.

2.3.6 Atmospheric loading

Since 1985, several studies on atmospheric loading have been carried out e.g. by RABEL AND ZSCHAU (1985), RABEL AND SCHUH (1986), VAN DAM AND WAHR (1987), MANABE *et al.* (1991), VAN DAM AND HERRING (1994), MACMILLAN AND GIPSON (1994), VAN DAM *et al.* (1994), SUN *et al.* (1995), HAAS *et al.* (1997), SCHERNECK (2000), and PETROV AND BOY (2004). Although atmosphere loading may cause vertical displacements of several mm, an adequate correction is not applied by the IGS Analysis Centres at the moment. This is relevant to the discussion on the reliability of the available models, and the question at which periods the inverted and non-inverted barometer assumption for the response of the oceans due to changes in air pressure is valid. Recommendations concerning the handling of the S_1 and the S_2 atmospheric tides are under development in the IERS Conventions. Recently, BOY AND CHAO (2005) evaluated the atmospheric loading effects on Earth's time-variable gravity field.

2.3.7 Other geophysical sources of station displacement

Other geophysical sources of station displacements are: hydrological loading, soil moisture and snow mass loading, and non-tidal ocean mass loading. At annual periods, variations in continental water storage are significant. The modelled vertical displacements range up to 30 mm with an RMS as large as 8 mm. Several new global models exist for soil moisture: HUANG *et al.* (1996), which provides monthly results for 1979-1993; Global Soil Wetness Project (GSWP), DOUVILLE *et al.* (1999); MILLY *et al.* (2002), which provides groundwater soil moisture and snow figures for the period 1978-1998. The following models of snow cover are available: International Satellite Land Surface Climatology Project (ISLSCP), MEESON *et al.* (1995); Global Soil Wetness Project (GSWP), DOUVILLE *et al.* (1999); MILLY *et al.* (2002). For non-tidal oceanic loading, data from TOPEX/POSEIDON and from the Parallel Ocean Climate Model (POCM) by JOHNSON *et al.* (1999) are available. The discrepancy between the two models is rather large but fortunately the effect itself is very small SCHUH *et al.* (2002, 2003), and will therefore not play a considerable part in this thesis.

¹⁴ <ftp://bilby.ucsd.edu/pub/spotl/>

¹⁵ <ftp://ftp.ngs.noaa.gov/dist/jimr/hardisp.f>

2.4 Global Positioning System (GPS)

High-precision geodetic measurements with GPS are performed using carrier beat phase pseudoranges in combination with code pseudoranges (BLEWITT, 1989, 1991, 1993, 1997, 1998a, 1998b, 2000). For the highest relative-positioning precisions, these observations are obtained simultaneously at each epoch from several stations, for several satellites, and at both the L1 (1575.42 MHz) and L2 (1227.6 MHz) GPS frequencies.

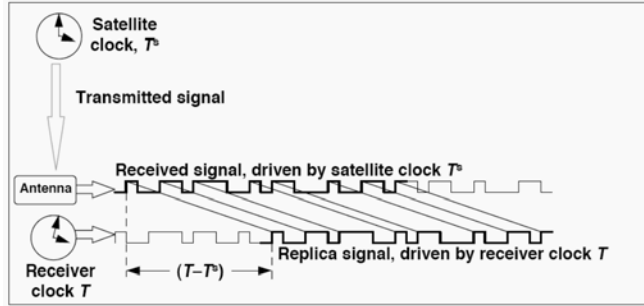


Figure 2: Schematic diagram showing how GPS pseudorange observations are related to the satellite and receiver clocks (here T stands for T_k ; source obtained from BLEWITT¹⁶).

The observable can be related to the clock time T , and is equal to the true reception time t plus a clock bias τ , for both receiver k and satellite clocks s :

$$\begin{aligned} T_k &= t_k + \tau_k \\ T^s &= t^s + \tau^s \end{aligned} \quad (2.4.1)$$

The basic code pseudorange observation P_k^s from station k to satellite s can be written as:

$$\begin{aligned} P_k^s &= c(T_k - T^s) \\ P_k^s &= c[t_k + \tau_k - (t^s + \tau^s)] \\ P_k^s &= \rho_k^s(t_k, t^s) + c\tau_k - c\tau^s \end{aligned} \quad (2.4.2)$$

For a more evolved model, taking into account e.g. the refractivity of the electromagnetic wave in the atmosphere or the theory of relativity etc., denoted by δc , the code pseudorange P_k^s between a station k and a satellite s is basically composed as follows:

$$\begin{aligned} P_k^s + v_k^s &= (c + \delta c)(t_k - t^s) + (c + \delta c)(\tau_k - \tau^s) \\ P_k^s + v_k^s &= \rho_k^s(t_k, t^s) + c(\tau_k - \tau^s) + \underbrace{\delta c(t_k - t^s + \tau_k - \tau^s)}_{atm, rel, multi} \end{aligned} \quad (2.4.3)$$

$$P_k^s + v_k^s = \rho_k^s(t_k, t^s) + c(\tau_k - \tau^s) + \underbrace{\Delta\rho_{k,ion}^s + \Delta\rho_{k,trop}^s + \Delta\rho_{k,multi}^s + \Delta\rho_{k,rel}^s}_{atm, rel, multi} \dots \quad (2.4.4)$$

while the phase pseudorange L_k^s reads:

$$L_k^s + v_k^s = \rho_k^s(t_k, t^s) + c(\tau_k - \tau^s) - \Delta\rho_{k,ion}^s + \Delta\rho_{k,trop}^s + \Delta\rho_{k,multi}^s + \Delta\rho_{k,rel}^s + \lambda \cdot N_k^s \dots \quad (2.4.5)$$

where the following formula convention is used:

¹⁶ <http://www.nbm.unr.edu/staff/pdfs/>

v_k^s	residual
ρ_k^s	geometric range satellite-receiver
$c\tau_k$	receiver clock correction
$c\tau^s$	satellite clock correction
$\Delta\rho_{k,ion}^s$	ionospheric correction
$\Delta\rho_{k,trop}^s$	tropospheric correction
$\Delta\rho_{k,multi}^s$	multipath correction
$\Delta\rho_{k,rel}^s$	relativistic corrections
λ, c	wavelength, speed of light in vacuum
N_k^s	ambiguity

Note that the pseudoranges refer to the reception time. In addition, station coordinates, in a terrestrial reference frame for a reference epoch (ITRF2000), need to be converted into an intermediate celestial reference frame using the matrix of diurnal rotation \mathbf{D} (polar motion and UT1). Besides, a first requirement of any GPS geodetic experiment is an accurate model of the motion of satellites \mathbf{s} , subject to gravitational and non-gravitational forces. The satellite positions, usually available in an inertial reference frame for a reference epoch (J2000), need be transformed into an intermediate celestial reference frame for the specific emission time t^s , by applying the precession-nutation matrix \mathbf{P} .

The geometric range $\rho_k^s(t_k, t^s)$ reads:

$$\left[\rho_k^s(t_k, t^s)\right]^2 = (\mathbf{P}\mathbf{s} - \mathbf{D}\mathbf{r}_k)^T \cdot (\mathbf{P}\mathbf{s} - \mathbf{D}\mathbf{r}_k) \quad (2.4.6)$$

The geometric range $\rho_k^s(t_k, t^s)$ still includes effects arising from solid Earth tides, alterations of the Earth's surface due to ocean tide loading, atmospheric pressure loading, hydrological loading, local geological processes, and long-term tectonic motion hidden in the station positions \mathbf{r}_k . For convenience's sake, the station positions are usually given in the terrestrial reference frame. In addition $\rho_k^s(t_k, t^s)$ contains all Earth rotation parameters, in the sense of CHAP (1985). One complication arises as ρ_k^s is calculated from the true signal travel time: the satellite position \mathbf{s} must be calculated at transmission time t^s , while the station position \mathbf{r}_k is given at reception time t_k . In other words, the range ρ_k^s is a function of two different time epochs (emission time t^s , and reception GPS time t_k). It may be expanded into a Taylor series (by neglecting higher order terms) w.r.t. the transmit GPS time t^s (e.g. HOFMANN-WELLENHOF *et al.*, 1997):

$$\rho_k^s = \rho_k^s(t_k, t^s) = \rho_k^s(t^s + \delta t, t^s) = \rho_k^s(t^s) + \underbrace{\frac{d\rho_k^s(t^s)}{dt^s}}_x \delta t + \dots \quad (2.4.7)$$

where $t_k = t^s + \delta t$ and

$$\left[\rho_k^s(t_k, t^s)\right]^2 = \left(X^s(t^s) - x_k(t_k)\right)^2 + \left(Y^s(t^s) - y_k(t_k)\right)^2 + \left(Z^s(t^s) - z_k(t_k)\right)^2 \quad (2.4.8)$$

The correction term x in equation (2.4.7) may amount to 60 m.

Other methods for handling ρ_k^s are achieved by, e.g., the light time equation¹⁷. Starting with the reception GPS time t_k , the transmission time t^s can be computed iteratively:

¹⁷ <http://www.nbmj.unr.edu/staff/pdfs/Blewitt%20Basics%20of%20gps.pdf>

$$\begin{aligned}
 t_0^s &= t_k \\
 t_1^s &= t_k - \frac{\rho_k^s(t_k, t_0^s)}{c} \\
 t_2^s &= t_k - \frac{\rho_k^s(t_k, t_1^s)}{c} \\
 &\vdots
 \end{aligned} \tag{2.4.9}$$

where the satellite position \mathbf{s} and hence $\rho_k^s(t_k, t^s)$ are computed at each step. The algorithm is stopped when the computed range converges to a negligible amount set by the analyst. Finally, the observation equation may be denoted by:

$$\begin{aligned}
 L_k^s - \underbrace{\left(\underbrace{\Delta\rho_{k,ion}^s + \Delta\rho_{k,trop}^s + \Delta\rho_{k,multi}^s + \Delta\rho_{k,rel}^s}_{atm,rel} \right)}_{L_{red}} - c\tau^s + v_k^s \\
 = \underbrace{\sqrt{(\mathbf{P}\mathbf{s} - \mathbf{D}\mathbf{r}_k)^T \cdot (\mathbf{P}\mathbf{s} - \mathbf{D}\mathbf{r}_k)}}_{\rho_k^s(t^s)} + c\tau_k + \lambda \cdot N_k^s \dots \\
 \underbrace{\hspace{10em}}_{F(\bar{\mathbf{u}})}
 \end{aligned} \tag{2.4.10}$$

It is worth mentioning that equation (2.4.10) still does not contain models of antenna, satellite phase centre offsets and variations, whose effects are not negligible, as reported by SCHMID AND ROTHACHER (2003). Nevertheless, equation (2.4.10) can already be brought to a more concise form:

$$\begin{aligned}
 L_{red} + v_k^s &= F(\bar{\mathbf{u}}) \\
 \Leftrightarrow L_{red} + \mathbf{v} &= F(\mathbf{u}_0 + \mathbf{x}) \\
 \Rightarrow L_{red} + \mathbf{v} &= F(\mathbf{u}_0) + \frac{\partial F_{u_0}}{\partial \bar{\mathbf{u}}} \mathbf{x} + \dots \\
 \Rightarrow \mathbf{v} &= \underbrace{\frac{\partial F_{u_0}}{\partial \bar{\mathbf{u}}}}_{\mathbf{A}} \mathbf{x} - \underbrace{[L_{red} - F(\mathbf{u}_0)]}_{\mathbf{l}} \\
 \Rightarrow \mathbf{v} &= \mathbf{A}\mathbf{x} - \mathbf{l}
 \end{aligned} \tag{2.4.11}$$

where \mathbf{x} are the corrections to the unknown (estimated) a priori parameters \mathbf{u}_0 , and \mathbf{A} is the partial derivative of the mathematical model w.r.t. the unknowns. Apart for the datum defect, usually, many constraints (or even conditions) are introduced as pseudo-observations to ensure non-singularity of the normal equation system $\mathbf{N} = \mathbf{A}^T \mathbf{A}$. Singularity occurs, e.g., if at a specific time some parameter cannot be resolved with the real observations at hand.

The usual approach is to reduce or modify the original observations to be compatible with the mathematical model. The more reductions applied, e.g. of ionospheric or atmospheric nature, the less general the mathematical model becomes. The final mathematical model highly depends on the purpose of the adjustment (LEICK, 2005). For example, various main focuses can be Earth rotation, satellite position, station position, ionospheric, tropospheric, geophysical, relativistic, or multipath parameters. It always depends on the assumptions of correctness or accuracy of the available a priori information. The right relation between observations (or reduced observations) and parameterization is of highest importance to the success of estimation and always requires much attention.

If receiver stations on the ground have hydrogen-maser oscillators, then a single differences can be as useful as this observation type is for the VLBI technique (KING AND BOCK, 2005), which is described in the next subsection.

Analysis of GPS observations is best described in the Bernese GPS Software Version 5.0 document¹⁸ by HUGENTOBLE et al. (2006) as well as in the GAMIT & GLOBK package documentation¹⁹ by KING AND BOCK (2005). SOVERS AND BORDER (1990) have also given an excellent overview of the observation model and parameter partials²⁰.

2.5 Very Long Baseline Interferometry (VLBI)

In VLBI, one derived observable is the duration of the group time delay τ_G between the arrival at two Earth-fixed antennas of a radio wavefront emitted by a distant quasar (see Figure 3). SOVERS AND FANSELOW (1998) have given an excellent review of theoretical models that flow into the VLBI observables. An approximate expression for $c \cdot \tau_G$ is given by:

$$c \cdot \tau_G = \mathbf{D}(\mathbf{r}_1 - \mathbf{r}_2) \mathbf{P} \mathbf{s} + \Delta \rho_{k,ion}^s + \Delta \rho_{k,trop}^s + \Delta \rho_{k,rel}^s \dots \quad (2.5.1)$$

where c denotes the speed of light in a vacuum, \mathbf{r}_k , the vectors of station coordinates in the terrestrial reference frame, \mathbf{s} , the vector of source position in the celestial reference frame, and \mathbf{D} and \mathbf{P} , the matrices of diurnal rotation and precession-nutation respectively. The time delay remains invariable to a common translation applied to station positions. A small rotation of site positions is equivalent to adding a constant to pole coordinates and universal time (PETROV AND MA, 2003).

A large number of time difference measurements from many quasars observed within a global network of antennas are used. One product of VLBI is the estimation of relative station positions to the cm level and the quasar positions to fractions of one milliarcsecond (mas). Temporal changes in the antenna locations indicate tectonic plate motion, regional deformation and local uplift or subsidence. The future of VLBI lies in the technology research of measurement systems, and in the integration with other space geodetic techniques. VLBI is the only technique to define a quasi-inertial reference frame with high precision, and to measure the Earth's orientation in this frame (with the exception of less accurate methods, i.e. optical astrometry, see Figure 4 for UT1).

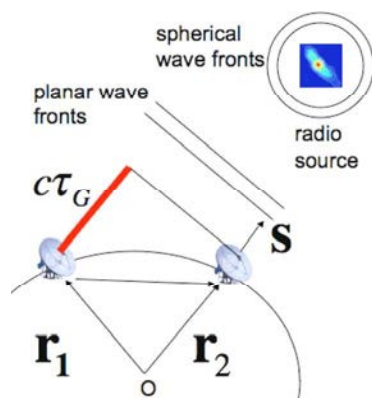


Figure 3: Basic principle of VLBI time delay.

The causes of Earth's orientation variations in inertial space are primarily due to:

- the gravitational forces of the sun and moon

¹⁸ <http://www.bernese.unibe.ch/docs/DOCU50draft.pdf>

¹⁹ <http://www-gpsg.mit.edu/~simon/gtgk/docs.htm>

²⁰ http://ntrs.nasa.gov/archive/nasa/casi.ntrs.nasa.gov/19900018458_1990018458.pdf

- the redistribution of total angular momentum among the solid Earth, ocean and atmosphere
- the Earth's fluid outer core.

VLBI measurements provide the basis for improving geophysical models of Earth's orientation in space, e.g. the new International Astronomical Union (IAU) IAU2000 precession-nutation model²¹ (e.g., HERRING *et al.*, 2002; MATHEWS *et al.*, 2002). Extragalactic objects form an inertial reference frame, because at great distances their proper motions across the sky are nearly undetectable. Positions of stars in our galaxy are tied to this frame of reference, and this is the same frame of reference used for measuring Earth orientation. The response of the Earth to external forces depends on the detailed structure of the Earth. Therefore, VLBI serves as the most accurate geodetic probe of the deep structure of the Earth. Discrepancies between predicted and observed values for nutation parameters have contributed to an update of the models of the Earth's core (MATHEWS *et al.*, 2002; BUFFET *et al.* 2002).

The best VLBI data thus far acquired was obtained during a two-week campaign CONT05 (in September 2005) of continuous VLBI sessions. These nearly continuous data are being closely analyzed by geodesists and compared to detailed tidal and atmospheric models.

In the context of realizing inertial reference frames, the European Space Agency (ESA) plans to launch GAIA²² in 2011. GAIA is an ambitious mission to chart a 3-D map of our galaxy and the Milky Way. The goals of GAIA are manifold:

- to provide unprecedented positional and radial velocity measurements of about one billion stars
- to quantify the early formation, and subsequent dynamical, chemical and star formation evolution of the Milky Way galaxy
- to detect and classify orbits of tens of thousands of extra-solar planetary systems
- to make a comprehensive survey of objects ranging from the plethora of minor bodies in our solar system to some 500000 distant quasars
- to provide a number of stringent tests of general relativity and cosmology.

A combination of GAIA with VLBI can only be a benefit for science.

2.6 Comparison of GPS and VLBI

The GPS technique is very efficient for the densification required for regional deformation studies and for the determination of polar motion (see Figure 4), due to its increasing number of globally distributed network stations. Both GPS and VLBI use radio frequencies, and therefore some of their error sources are very similar. A significant source of random and systematic error in both VLBI and GPS is the neutral atmosphere. The latter slows the incoming radio waves and causes an excess delay of the radio signal. This delay depends on the temperature pressure and humidity along the ray path and must be measured or estimated to obtain accurate geodetic parameters. VLBI and GPS estimates of the atmospheric parameters give similar, but independent, results (SCHMID *et al.*, 2005; VEY *et al.*, 2006). The temporal atmospheric delay variations are azimuth-dependent. The correct analysis of these fluctuations is one aspect of atmospheric modelling, which continues to be a strong interest of the VLBI community (BOEHM *et al.*, 2006a). More rapid VLBI measurements of higher quality (e.g. CONT05) will certainly improve the atmospheric modelling parameters, which will be relevant to other radio measurements, e.g. GPS (TREGONING AND VAN DAM, 2005b).

²¹ <http://hpiers.obspm.fr/eop-pc/>

²² <http://gaia.esa.int/science-e/www/area/index.cfm?fareaid=26>

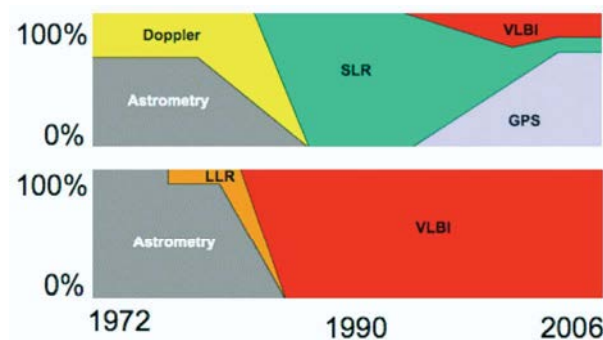


Figure 4: Contribution of techniques to combination in polar motion (top) and UT1 (bottom) (source from GAMBIS²³), over the last decades.

VLBI remains essential due to:

- its long history of measurements
- its ability to be connected to the celestial reference frame
- its long-term UT1 estimation (see Figure 4), which is fundamental to any satellite trackings (ROTHACHER *et al.*, 2001).

The strength of GPS is:

- its low operational cost of dense networks for deformation zone monitoring (enhancement in polar motion determination)
- its flexibility in terms of its ability to go anywhere and everywhere where measurements are needed (on land)
- its continuous temporal coverage
- its ability to observe more sources, i.e. satellites, simultaneously.

The analysis complexities and immense data handling requirements that are necessary to integrate space geodetic data on a regular basis within the Global Geodetic Observing System (GGOS) are future challenges for space geodetic techniques in general, especially for both VLBI and GPS. Finally, the VLBI and GPS data contain the totality of geophysical models and provide state-of-the-art measurements, which may lead to striking new discoveries in Earth science.

2.7 Institutions and data centres of GPS and VLBI

2.7.1 International GNSS Service (IGS²⁴)

The International Global Navigation Satellite System (GNSS) Service (IGS), formerly called the International GPS Service for Geodynamics, founded in 1991, is a voluntary federation of more than 200 worldwide agencies. Permanent GPS and Russian Global Navigation Satellite System (GLONASS) receiver stations (WEBER *et al.*, 2005) are set up to generate precise products. The IGS is committed to providing the highest quality data and products as the standard for Global Navigation Satellite Systems GNSS in support of Earth science research, multidisciplinary applications and education. In the future, it intends to incorporate new satellite navigation systems, i.e. GALILEO, whose first test satellite GIOVE-A was launched successfully on December 28th, 2005. All IGS products are based on tracking data from a permanent global station network (see Figure 5).

²³ www.iers.org/workshop_2005/presentations/Session-3_Gambis.pdf

²⁴ <http://igsceb.jpl.nasa.gov/>

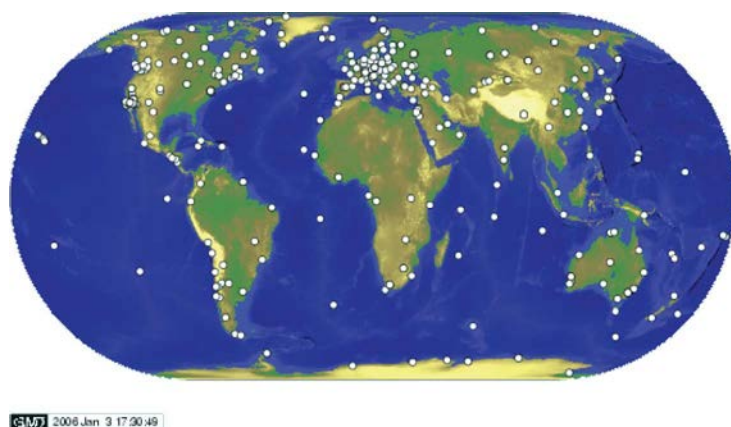


Figure 5: IGS 332 active stations as of January 4th, 2006 (source from IGS²⁵).

The ultimate accuracy in processing GPS data is achieved in post-processing mode. Here, it is imperative to use IGS precise orbits²⁶. Nowadays, these ephemerides obtained as a weighted combination of up to eight IGS Analysis Centre submissions are a quasi standard for a large number of applications. Various improvements in GPS orbit modelling over the last few years have led to a current orbit accuracy level of approximately 5 cm root mean square (RMS). To achieve that accuracy, a number of tidal effects both in the applied force field governing the satellite motion as well as in calculating station displacements have to be taken into account. The consistent handling of these effects by various Analysis Centres (ACs) is crucial in order to avoid systematic differences. Table 2 and Table 3 show how different ACs (see Table 1 for acronyms) handled (and still handle) the tide-related part in their analysis strategy. We recognize that, as of April 2006, no single AC applies atmospheric loading corrections to the observables for routine processing. The implementation of displacement corrections varies from one AC to another. However, the present information, concatenated in the processing strategy summary (in the so-called ACN²⁷ files), seems to be out-of-date.

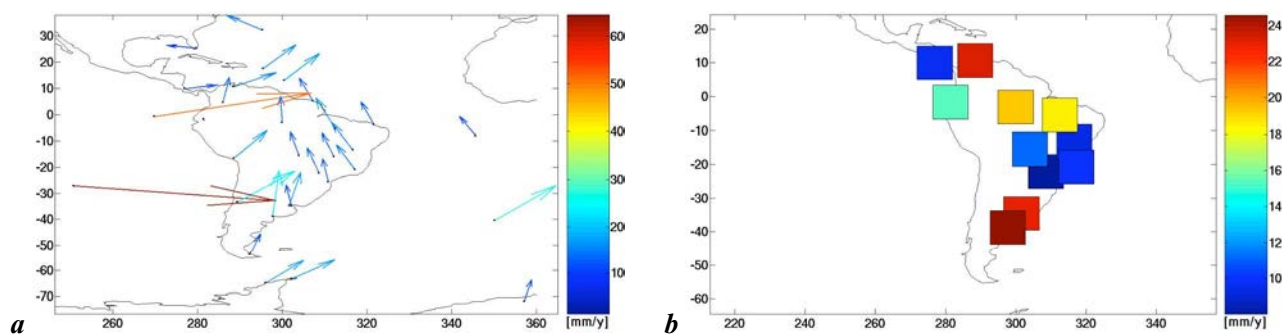


Figure 6: (a) Horizontal velocities of all 31 SIRGAS stations available in the ITRF2000 reference frame and (b) vertical velocities of 12 SIRGAS stations that have a standard deviation larger than 5 [mm/year].

Currently, IGS processes data from more than 200 globally distributed stations on a daily basis. Geocentric coordinate time series of these stations are available daily (e.g. at Scripps Orbit and Permanent Array Centre

²⁵ <http://igsceb.jpl.nasa.gov/network/netindex.html>

²⁶ <http://igsceb.jpl.nasa.gov/components/data.html>

²⁷ <http://igsceb.jpl.nasa.gov/igsceb/center/analysis/>

SOPAC²⁸) and weekly in standard Software Independent Exchange (SINEX²⁹) format. Recognizing the deficiencies in prior SINEX format versions (e.g. 2.00), the VLBI community (MA AND PETROV, 2003) proposed a new SINEX version, which unfortunately is presently only implemented in the CALC/SOLVE software. The SINEX issue will be explained in greater detail in subsection 5.1.3.

The available IGS coordinate time series cover periods from months up to a decade with steadily increasing precision and accuracy. Moreover, regional densifications such as the European Reference Frame (EUREF³⁰) or the Geodesic Reference System for the Americas (SIRGAS³¹ Sistema de Referencia Geocéntrico para las Américas) provide coordinate information for a huge number of additional stations but mainly over shorter periods of time (see Figure 6).

Table 1: Acronyms of ACs used in Table 2.

Code	Agency Name	City	Location
CODE	Centre for Orbit Determination in Europe, CODE	Berne	Switzerland
EMR	Natural Resources Canada, NRCan, former EMR	Ottawa, Ontario	Canada
ESOC	European Space Operations Centre, ESOC	Darmstadt	Germany
GFZ	GeoForschungsZentrum	Potsdam	Germany
JPL	Jet Propulsion Laboratory	Pasadena, California	USA
SIO	Scripps Institution of Oceanography	San Diego, California	USA
NOAA	National Oceanic and Atmospheric Administration	Silver Spring, Maryland	USA
USNO	U.S. Naval Observatory	Washington, DC	USA

²⁸ <http://sopac.ucsd.edu/processing/>

²⁹ <http://tau.fesg.tu-muenchen.de/~iers/web/sinex/format.php>

³⁰ <http://www.epncb.oma.be/>

³¹ <http://www.dgfi.badw.de/dgfi/SIRGAS/sirgas.html>

Table 2: Tides-related part of the Analysis Strategy Summaries of the IGS ACs (status of December 2001, source taken from GPS WG6 report³²).

	CODE	EMR	ESOC	GFZ	JPL	NOAA	SIO	USNO
Solid Earth Displacement	Model IERS96 nominal h_2/l_2 0.6078/0.0847 +corrections	Model IERS92 nominal h_2/l_2 0.609/0.085 $dh_2(K1):0.089$	Model IERS92 nominal h_2/l_2 0.609/0.085 $dh_2(K1):0.089$	Model IERS92 nominal h_2/l_2 0.609/0.085 $dh_2(K1):0.089$	Williams	nominal h_2/l_2 0.6067/0.0844 +corrections	Model IERS92 nominal h_2/l_2 0.609/0.085 $dh_2(K1):0.089$	Williams
Force	frequ. indep. Love's Nr: $k_2 = 0.300$	frequ. indep. Love's Nr: $k_2 = 0.300$	frequ. depend. Wahr; nominal $k_2 = 0.300$	frequ. depend. Wahr; nominal $k_2 = 0.300$	nominal $k_{2(0-2)}$ 0.299/0.3/0.302 $k_{3(0-3)} = 0.093$ +34 frequ.dep corrections	frequ. depend. Wahr; nominal $k_2 = 0.300$	frequ. indep. Love's Nr: $k_2 = 0.300$	nominal $k_{2(0-2)}$ 0.299/0.3/0.302 $k_{3(0-3)} = 0.093$ +34 frequ.dep corrections
Perm. Tide Displacement	not applied	not applied	no info	applied	no info	not applied	no info	no info
Force	applied	applied		applied		applied		
Pole Tide	appl. / IERS96 mean m1/m2 0.033/0.331	appl. / IERS92	not appl.	appl. / IERS92	appl. / IERS92	not appl.	not appl.	appl. / IERS92
Ocean Loading Displacement	Scherneck	Pagiatakis	Scherneck	Scherneck	Scherneck	not appl.	not appl.	Pagiatakis
Force	UT CSR 3.0	UT CSR 3.0	Schwiderski	Schwiderski	UT CSR 3.0 + TEG-2B data	not appl.	UT CSR 3.0	UT CSR 3.0 + TEG-2B data
Atmosphere Loading	not applied	not applied	not applied	not applied	not applied	not applied	not applied	not applied

Table 3: Tides-related part of the Analysis Strategy Summaries of the IGS ACs (status as of April 2006, source from IGS³³) for the displacement.

	CODE	EMR	ESOC	GFZ	JPL	NOAA	SIO	USNO
Solid Earth	IERS96	Williams	IERS96 h2=.609, l2=.0852	IERS92	IERS	IERS2003	applied	Williams
Perm. Tide	not applied	no info	not applied	applied	no info	not applied	no info	no info
Pole Tide	applied IERS96 mean m1/m2 0.033/0.331	applied	not applied	applied	applied	applied IERS2003	applied	applied
Ocean Load.	Scherneck	Scherneck model 1991	Scherneck	Pagiatakis	FES02	Schwiderski	Scherneck	Pagiatakis
Atmo. Load.	not applied	not applied	not applied	not applied	not applied	not applied	not applied	Not applied

2.7.2 International VLBI Service (IVS³⁴)

The International VLBI Service for Geodesy and Astrometry (IVS) was founded in 1999 (SCHLUETER *et al.*, 2002). The goals of IVS are:

- to provide a service to support geodetic geophysical and astrometric research and operational activities

³² http://www.gps.oma.be/publications/2002/GPS_WG6_subgroup_report.pdf

³³ <http://igscb.jpl.nasa.gov/igscb/center/analysis/>

³⁴ <http://ivscc.gsfc.nasa.gov/index.html>

- to interact with the community of users of VLBI products
- to integrate VLBI into a global Earth observing system, and
- to promote research and development activities in all aspects of the geodetic and astrometric VLBI technique.

Data is acquired by network stations and then processed by correlators that submit databases (DBs) to Data Centres (DCs). The processed DBs are analyzed by Analysis Centres (ACs) to generate products. Contents of the DCs are organized into two types³⁵:

- primary data such as database and NGS card files
- auxiliary data such as schedule and log files.

Some primary and unique products of the IVS are:

- the International Celestial Reference Frame (ICRF)
- Earth Rotation Parameters (ERPs) in the sense of IAU (1985).

Other products available from more than one space geodetic technique are: pole coordinates, terrestrial reference frame, as well as certain geodynamical and geophysical parameters. VLBI uniquely provides some products such as Universal Time 1 (UT1), quasar positions and celestial pole.

IVS Analysis Centres analyze geodetic and astrometric VLBI data to generate IVS products and to perform research in Earth science. The software packages, which are commonly used for analysis, are developed and maintained by various IVS components. The packages, which are available for free, are:

- CALC/SOLVE³⁶
- OCCAM³⁷
- SteelBreeze³⁸.

³⁵ <http://ivscc.gsfc.nasa.gov/products-data/data.html>

³⁶ <http://gemini.gsfc.nasa.gov/solve>

³⁷ <http://ivscc.gsfc.nasa.gov/analysis/occam.html>

³⁸ <http://steelbreeze.sourceforge.net/>

Chapter 3

Tides and deformation due to surface loading

The tides are primarily the result of the combined gravitational and centrifugal forces of the Earth-moon and Earth-sun systems. The net force on an oceanic particle is small but gives rise to surface elevations up to an order of ten meters depending on the geographical position. The aim in this chapter is to give a brief overview of the underlying physics and consequences of astronomical forcing. The solid Earth tides, described in section 3.3, are quite important for a variety of applications related to gravity, such as the analysis of modern gravimeters, precision tracking of satellites, GPS, VLBI and the calculation of oceanic tides. As far as their effect on oceanic tides is concerned, their principal influence is to reduce the amplitude of the equilibrium tides that the ocean feels, because the Earth deforms in the same direction as the oceans under the tidal forcing by celestial objects. To compute tides of the solid Earth, one usually considers an elastic, oceanless Earth and solves the linearized governing equations for the deformation (discussed in section 3.9), assuming a constitutive law relating stress to strain. The so-called load tides will be treated in section 3.5.

3.1 Description of tides

In order to understand tides, it is necessary to have a minimum knowledge of the orbital characteristics of the moon around the Earth and in those of the Earth around the sun. The Earth rotates around its spin axis once every sidereal day (86164 s). The Earth and the moon revolve around a slightly varying common centre (see Figure 8) once every sidereal month (27.3212 d). This common centre of mass is located inside the Earth. Due to eccentricity, the perigee of moon's orbit is 10% closer than the apogee. The inclination between the plane of the moon's orbit around the Earth and the equatorial plane of the Earth varies from 18.5° to 28.5°, modulated over a period of 18.613 years. The Earth itself makes a revolution around the sun once every tropical year (365.2422 d). The plane of the Earth's orbit (ecliptic plane) is inclined at 23.5° to the equatorial plane. The lunar orbit is inclined at 5°08' to the ecliptic plane. Its perigee varies with a period of 8,861 years (MELCHIOR, 1978). All these orbital variations have an impact on the resulting tides. The description above explains the basic mechanism of tides. Now, we will apply a mathematical approach of the lunisolar gravitational potential in order to infer quantitative deductions.

3.2 Tide generating potential

The tidal acceleration \mathbf{b} is the resultant of the gravitational acceleration \mathbf{b}_g due to celestial bodies and the centrifugal acceleration \mathbf{b}_z due to the motion around the common centre:

$$\mathbf{b} = \mathbf{b}_g + \mathbf{b}_z \quad (3.2.1)$$

Following the third Newtonian axiom, actio equals reactio in an equilibrium state:

$$\mathbf{b}_z = -\mathbf{b}_g \quad \text{at} \quad \mathbf{e}_j = \mathbf{R}_j \quad (3.2.2)$$

The absolute value of the gravitational b_g and centrifugal b_z acceleration due to the celestial body, in the centre of the Earth, is equal and reads:

$$b_g = |-\mathbf{b}_g| = \sum_j \frac{GM_j}{|\mathbf{e}_j|^2} \quad \text{and} \quad b_z = |-\mathbf{b}_z| = \sum_j \frac{GM_j}{|\mathbf{R}_j|^2} \quad (3.2.3)$$

where M_j is the mass of the celestial body (e.g., moon, sun, Venus, Jupiter), \mathbf{R}_j is the vector from the geocentre towards that body, \mathbf{r} the vector towards the station, and $\mathbf{e}_j = \mathbf{R}_j - \mathbf{r}$.

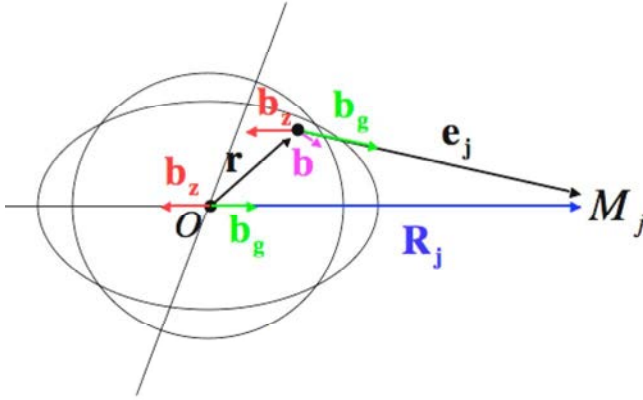


Figure 7: Vectors involved in tidal acceleration.

The gravitational acceleration b_g is balanced by the centrifugal acceleration b_z of the Earth and the celestial body rotating about a common axis (see Figure 8). The result is that b_z is constant for every particle of the Earth, and acts in a constant direction parallel to the line between both centres. The total centrifugal acceleration on the Earth is balanced by the total gravitational acceleration (and likewise for the celestial body), so that:

$$\frac{GM_E}{(r_1 + r_2)^2} = \omega_1^2 r_1 \quad \text{and} \quad \frac{GM_j}{(r_1 + r_2)^2} = \omega_2^2 r_2 \quad (3.2.4)$$

where M_E is Earth's mass, and $\omega_1 = \omega_2$ is the orbital angular speed about the common centre of mass (the subscript 1 or 2 denotes at which body, i.e. Earth or celestial body, the orbital angular speed is considered).

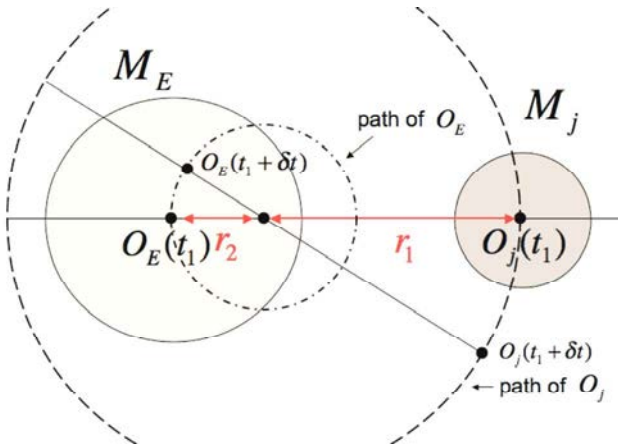


Figure 8: Two bodies revolving about a common axis placed at their barycentre.

As both angular velocities ω_1 and ω_2 are identical, it follows that the centrifugal acceleration $\mathbf{b}_{z,j}$ is a homogeneous vector field and thus may be represented as a gradient of a potential Z_j (see Figure 9):

$$\mathbf{b}_{z,j} = \left(\underbrace{-b_{z,j} \cos \Theta_j}_{\frac{\partial Z_j}{\partial r}}, \underbrace{b_{z,j} \sin \Theta_j}_{\frac{\partial Z_j}{r \partial \Theta_j}}, 0 \right) \quad (3.2.5)$$

$$Z_j = -b_{z,j} r \cos \Theta_j = -GM_j \frac{r}{R_j^2} \cos \Theta_j \quad (3.2.6)$$

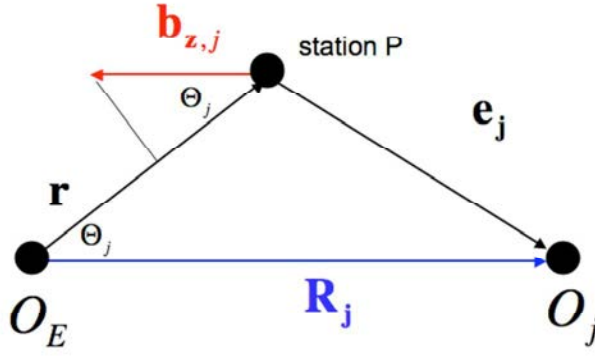


Figure 9: Centrifugal acceleration is a homogeneous vector field.

where Θ_j is the angle between the unit vectors (in the subsequent text denoted with a hat) from the geocentre towards the celestial body $\hat{\mathbf{R}}_j$ and towards the station $\hat{\mathbf{r}}$, R_j is the geocentric distance of that body, and r is the radius of the influenced body, i.e. the radius of the Earth.

The gravitational potential of the mass M_j acting at a distance e_j is simply (see Figure 9):

$$V_j = \frac{GM_j}{e_j} \quad (3.2.7)$$

Thus, the tidal potential W results as a superposition of the gravitational V_j and centrifugal Z_j potentials (for various celestial bodies j):

$$W = \sum_j W_j = \sum_j (V_j + Z_j) = \sum_j GM_j \left(\frac{1}{e_j} - \frac{r}{R_j^2} \cos \Theta_j - \frac{1}{R_j} \right) \quad (3.2.8)$$

The last term in brackets of equation (3.2.8) arises because, for $r = 0$, i.e. $e_j = R_j$, we make the tidal potential W_j vanish. If $r < R_j$, then $1/e_j$ can be expanded into Legendre functions (e.g. KELLOGG, 1929/1954):

$$\frac{1}{e_j} = \frac{1}{R_j} \sum_{n=0}^{\infty} \left(\frac{r}{R_j} \right)^n P_n(\cos \Theta_j) = \frac{1}{R_j} + \frac{r}{R_j^2} \cos \Theta_j + \frac{1}{R_j} \sum_{n=2}^{\infty} \left(\frac{r}{R_j} \right)^n P_n(\cos \Theta_j) \quad (3.2.9)$$

Replacing equation (3.2.9) with equation (3.2.8), the net tidal potential W takes the form:

$$W = \sum_j W_j = \sum_j \frac{GM_j}{R_j} \sum_{n=2}^{\infty} \left(\frac{r}{R_j} \right)^n P_n(\cos \Theta_j) = \sum_j \sum_{n=2}^{\infty} W_{n,j} \quad (3.2.10)$$

and the net tidal acceleration \mathbf{b} is simply the gradient of the tidal potential:

$$\mathbf{b} = b_i = \partial_i W \quad (3.2.11)$$

Making use of spherical geometry (see Figure 10) and expressing angle Θ_j in terms of the Greenwich longitude λ and latitude φ of the point on Earth under consideration P , as well as the corresponding values α_j (right ascension) and δ_j (declination) for the centre of mass of the celestial body Σ_j (see Figure 10), we can deduce that:

$$\cos \Theta_j = \sin \varphi \sin \delta_j + \cos \varphi \cos \delta_j \cos \tau_j \quad (3.2.12)$$

where τ_j is the hour angle of the celestial body Σ_j .

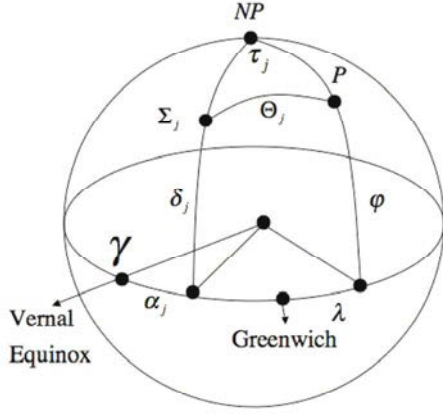


Figure 10: Graphic illustrating equation (3.2.12).

Decomposing Legendre functions in Θ_j into those in λ and φ (e.g. LAMBECK, 1988), we obtain:

$$W_j = \frac{GM_j}{R_j} \sum_{n=2}^{\infty} \sum_{m=0}^n \left(\frac{r}{R_j} \right)^n (2 - \delta_{0m}) \frac{(n-m)!}{(n+m)!} P_{nm}(\sin \varphi) P_{nm}(\sin \delta_j) \cos m\tau_j \quad (3.2.13)$$

where P_{nm} are associated Legendre polynomials of degree n and order m , and δ_{0m} is the Kronecker delta.

As the denominator $(n+m)!$ increases considerably for larger degrees and orders, it is more convenient to use normalized associated Legendre functions. DESAI (1996) proposes the following normalization:

$$\bar{P}_{nm} = a_{nm} P_{nm} = (-1)^m \sqrt{\frac{(2n+1)(n-m)!}{4\pi(n+m)!}} P_{nm} \quad (3.2.14)$$

so that:

$$\begin{aligned} W_j &= \frac{GM_j}{R_j} \sum_{n=2}^{\infty} \sum_{m=0}^n \left(\frac{r}{R_j} \right)^n \frac{a_{nm}^2}{2n+1} P_{nm}(\sin \varphi) P_{nm}(\sin \delta_j) \cos m\tau_j \\ &= \sum_{n=2}^{\infty} \sum_{m=0}^n \bar{P}_{nm}(\sin \varphi) [b_{nm,j}(t) \cos m\lambda + c_{nm,j}(t) \sin m\lambda] \end{aligned} \quad (3.2.15)$$

whereby

$$\begin{aligned} b_{nm,j}(t) &= \frac{4\pi GM_j}{R_j} \frac{(2 - \delta_{0m})}{2n+1} \left(\frac{r}{R_j} \right)^n \bar{P}_{nm}(\sin \delta_j) \cos m\alpha_j \\ c_{nm,j}(t) &= \frac{4\pi GM_j}{R_j} \frac{(2 - \delta_{0m})}{2n+1} \left(\frac{r}{R_j} \right)^n \bar{P}_{nm}(\sin \delta_j) \sin m\alpha_j \end{aligned} \quad (3.2.16)$$

As the monthly and yearly orbital motions of the moon and sun have low frequencies compared to the frequency of the rotation of the Earth, the above-mentioned coefficients have principal frequencies of around m cycles per day, being modulated with the orbital motions.

The infinite series in equation (3.2.15) may be truncated at some degree, as the factor $(r/R_j)^n$ decreases rapidly for higher degrees. In this respect, WENZEL AND ZUERN (1990) used the expansions of TAMURA

(1987) and showed that, for modern gravimeters, it is necessary to retain $n = 3$ solar and $n = 4$ lunar terms.

The tidal potential can thus be calculated for any point on the Earth's surface at any time t . The coefficients b_{nm} and c_{nm} depend only on the ephemeris of the celestial body (especially of the moon and sun) and time, and are predictable centuries in advance, since the motion of celestial bodies is well-known at a high degree of accuracy, e.g. the JPL DE405³⁹.

Recently, KUDRYAVTSEV (2004) developed the tide-generating potential (TGP) KSM03⁴⁰, based on the latest NASA Jet Propulsion Laboratory (JPL) ephemerides DE/LE-405(406) (STANDISH, 1998). The TGP catalogue KSM03 includes 26753 Poisson series. It claims to exceed the accuracy of any previously made harmonic development of the Earth TGP in the time domain by a factor of at least three.

The ephemerides of the moon and the sun, in geocentric coordinates, are usually defined by five astronomical arguments, and expressed as an infinite series of these angles. The tidal potential, composed by a harmonic series, uses functions of these five astronomical arguments and, in addition, a sixth one involving the hour angle of the moon. DARWIN (1886) and DOODSON (1921) were pioneers in expanding the tidal potential into a harmonic series. CARTWRIGHT AND TAYLER (1971) and CARTWRIGHT AND EDDEN (1973) used spectral techniques to expand the lunar tidal potential to degree 3 and solar to degree 2. TAMURA (1987) did it for the next higher degree (for the lunar and solar tidal potential), adding additional significant digits and many more spectral components. The combined luni-solar tidal potential can be written as (e.g. KANTHA AND CLAYSON, 2000):

$$W = \sum_{j=M,S} W_j = g \sum_{n=2}^{\infty} \sum_{m=0}^n \sum_{j=M,S} H_{nm,j} \bar{P}_{nm}(\sin \varphi) \cos(m\lambda + \omega_{nm,j}t + \alpha_{nm,j}) \quad (3.2.17)$$

$$\omega_{nm,j}t + \alpha_{nm,j} = d_1\tau_M + (d_2 - 5)s_0 + (d_3 - 5)h_0 + (d_4 - 5)p_0 + (d_5 - 5)n_s + (d_6 - 5)p_s - \chi_{nm} \frac{\pi}{2}$$

$$\chi_{nm} = 1 \text{ (for odd } n+m)$$

$$\chi_{nm} = 0 \text{ (for even } n+m)$$

where d_i are integers that constitute Doodson's argument number $d_1d_2d_3d_4d_5d_6$. The meaning of the six astronomical arguments is explained in Table 4. The time dependence of the coefficients $H_{nm,j}$ is very small and usually ignored (e.g. CARTWRIGHT AND TAYLER, 1971; LAMBECK, 1988).

The origin of each tidal component can be deduced from this Doodson number. The value d_1 defines the tidal species (0, 1 and 2 cycles per day), d_1d_2 define the group number (each separated by about 1 cycle per month) and $d_1d_2d_3$ define the constituent number (each separated by about 1 cycle per year). The harmonic development calculated by different authors is resumed in Table 5.

³⁹ <http://www.willbell.com/software/jpl.htm>

⁴⁰ <http://lnfm1.sai.msu.ru/neb/ksm/tgp/ksm03.dat>

Table 4: Six astronomical arguments. The meaning of msd is mean solar days.

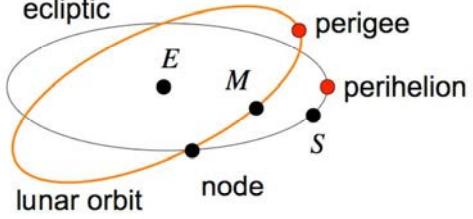
τ_M	mean lunar time	1.0351	msd	
s_0	mean longitude of the moon (M)	27.3217	msd	
h_0	mean longitude of the sun (S)	365.2422	msd	
p_0	mean longitude of lunar perigee	8.8500	tropic years	
n_s	negative mean longitude of the ascending lunar node	18.6100	tropic years	
p_s	mean longitude of solar perigee (perihelion)	20942	tropic years	

Table 5: Harmonic development of the luni-solar tidal potential.

	Author	LP	D	SD	TD	FD	SUM	n (M)	n (S)	σ_1 [ngal]	σ_2 [ngal]
1921	Doodson	99	158	115	14		370	3	2	102	0.34
1971,1973	Cartwright, Edden, Tayler	128	205	155	17		505	3	2	38	0.13
1985	Buellesfeld	169	246	195	42	4	656	4	2	24	0.08
1987	Tamura	281	450	377	82	10	1200	4	3	7	0.023
*		2	2	4							
1989	Xi 🍏						2934	4	3	8	0.028
1993	Tamura ⁴¹ 🍏						2114	4	3	3.2	0.011
1995	Hartmann, Wenzel 🍏						12935 1483	6	3	1.2	0.004
	**										
2004	Kudryavtsev 🍏						26753				

LP=long periodic, D=diurnal, SD=semidiurnal, TD=terdiurnal, FD=fourthdiurnal, SUM=sum of terms, σ_1 =standard deviation in time domain, σ_2 =standard deviation in frequency domain, *= Venus and Jupiter included, **= Mercure, Venus, Mars, Jupiter and Saturn included, n= degree (M=moon, S=sun), 🍏 only the sum of waves.

However, not only the ocean responds to tidal forcing. The solid Earth (see section 3.3) and the atmosphere (see section 3.5) do too. However, for the atmosphere, the gravitational tides are very small, and there the tides are principally driven by solar diurnal heating (see section 3.7).

⁴¹ <http://www.geo.uni-jena.de/geophysik/etc/etcdat/tamura93/tamura93.for>

3.3 Body (solid Earth) tides

The Earth does not behave like a rigid body, but responds to tidal forcing quasi elastically. Thus, these body tides have a rich spectrum of components. The deformations caused are very small so that the displacements and the potential of deformation may be linearized (LOVE, 1911/1967).

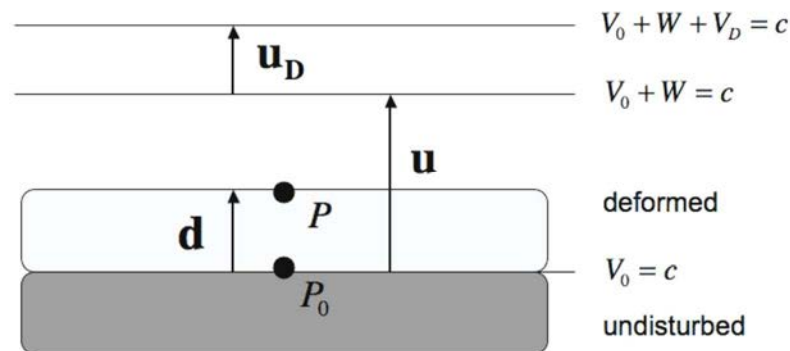


Figure 11: Graphic illustrating the theory of LOVE, where c is a constant.

We must distinguish between three effects (see Figure 11):

- First, there is a superposition of the Earth's own gravitational potential V_0 by the tidal potential W . The radial component u_r of the displacement \mathbf{u} (the lateral component is denoted by u_β) corresponding to the equipotential surface $V_0 + W = \text{constant}$, with respect to an undisturbed surface $V_0 = \text{const}$, is given by BRUNS' theorem (1878) ($g_{0,r}$ is the gravity of the spherical Earth on the Earth's surface, and the subscripts r and β denote the radial and lateral components respectively):

$$\mathbf{u} = (u_r, u_\beta) = \left(\sum_{n=2}^{\infty} \underbrace{\frac{W_n}{g_{0,r}}}_{u_{r,n}}, \sum_{n=2}^{\infty} \underbrace{\frac{1}{g_{0,r}} \frac{\partial W_n}{\partial \beta}}_{u_{\beta,n}} \right) \quad \text{with} \quad |g_{0,r}| = \frac{GM}{r^2} \quad (3.3.1)$$

- Thereupon, a displacement \mathbf{d} of a point on Earth's surface P_0 towards P follows (due to the deformation \mathbf{u}). In a first approximation \mathbf{d} is proportional to \mathbf{u} . The factors of proportion are called the Love Numbers $H_n(r)$ and Shida Numbers $L_n(r)$, which, under assumption of a spherical non-rotating elastic and isotropic Earth (SNREI), only depend on the radius r and the degree n of the expansion of the tidal potential:

$$\mathbf{d} = (d_r, d_\beta) \quad d_r = \sum_{n=2}^{\infty} u_{r,n} H_n(r) \quad d_\beta = \sum_{n=2}^{\infty} u_{\beta,n} L_n(r) \quad (3.3.2)$$

- Finally, the displacement \mathbf{d} , inducing a redistribution of mass, increases the tidal potential by an amount V_D , with the associated deformation potential V_D . The latter is proportional to the tide-generating forces and its factors are the Love Numbers $K_n(r)$:

$$V_D = \sum_{n=2}^{\infty} W_n K_n(r) \quad (3.3.3)$$

The Love and Shida Numbers depend on the density distribution and elastic parameters of the Earth's interior (e.g. FARRELL, 1972). On the Earth's surface, the amplitude factor (being the quotient of the observed to the theoretical tidal acceleration) for the radial and horizontal components is given, e.g. by MELCHIOR (1978):

$$\begin{aligned}\delta_n &= 1 + \frac{2}{n}h_n - \frac{n+1}{n}k_n \\ \gamma_n &= 1 - h_n + k_n\end{aligned}\tag{3.3.4}$$

where $h_n = H_n(a)$, $k_n = K_n(a)$, and $l_n = L_n(a)$, with a being Earth's mean radius. The Love Numbers h_n and k_n were introduced by LOVE in 1909, whereas SHIDA introduced l_n in 1912 (MELCHIOR, 1978).

It is therefore possible to invert equations (3.3.4) for the degree- n Love Numbers h_n and k_n from observations, i.e. from gravimeters and tiltmeters:

$$\begin{aligned}h_n &= \frac{1}{n-1}[(2n+1) - n\delta_n - (n+1)\gamma_n] \\ k_n &= \frac{1}{n-1}[(n+2) - n\delta_n - 2\gamma_n]\end{aligned}\tag{3.3.5}$$

This inversion is formally correct, but in practice it is not possible to obtain h_n and k_n precisely enough due to disturbances of the amplitude factor γ_n (personal communication VARGA, 2006). In fact, the amplitude factors need to be observed to an order of magnitude more precisely than the aimed precision of Love Numbers (e.g. MEURERS, 2002).

The displacement d_r is known as a body tide. It increases the potential by an amount $k_n W_n$ at the Earth's surface. However, as a particle on the surface is displaced by d_r , there is a local decrease in the potential by $h_n W_n$. This results in an effective tide potential of $(1 - h_n + k_n)W_n = \gamma_n W_n$. It is surprising that the horizontal amplitude factor γ_n defines the effective tidal potential.

Each spherical component of the tidal potential of degree- n and order- m has a corresponding set of Love Numbers h_{nm} , l_{nm} and k_{nm} . The dependence on order- m is so small that it has usually been ignored. However, MATHEWS *et al.* (1995) demonstrated the necessity of refining the definition of these numbers. In fact, JEFFREYS AND VICENTE (1966) were the first to suggest the frequency dependence of these numbers. Now, if station positions with accuracy of better than 1 mm are needed, additional effects are considered for the characterization of the Love and Shida Numbers. These numbers depend on the station latitude and the tidal frequency. MATHEWS *et al.* (1995) conclude that the most reasonable definition of the tidal potential is the one that uses an ellipsoid for reference, implying that Love Numbers are latitude-dependent. MATHEWS *et al.* (1995, 1997, 2002) gave a complete treatment of the frequency dependence of the tidal response. Due to the Earth's rotation, the Earth ellipticity and the Coriolis force (DE CORIOLIS, 1835) cause latitude dependence and small frequency-dependent variations. The resonance due to ocean loading also influences the values of the Love and Shida Numbers. Within the diurnal band, the Nearly Diurnal Free Wobble (NDFW) resonance (SLICHTER, 1961; DE VRIES AND WAHR, 1991; HERRING *et al.*, 2002) produces strong frequency dependence. In the long-period tidal band, mantle anelasticity also leads to corrections of the elastic Love and Shida Numbers.

Table 6: Effects influencing the effective values of Love and Shida Numbers.

Ellipticity of the Earth
Coriolis force
Nearly Diurnal Free Wobble (NDFW)
Resonance due to ocean tidal loading
Mantle anelasticity

The frequency-dependent contributions, resumed in Table 6, cause the tidal displacements to lag slightly behind the tide generating potential W_n , and are the reason for introducing real and imaginary Love and Shida Numbers.

In order to account for all these effects due to solid Earth tides, the IERS Conventions 2003 propose to calculate the variations of station coordinates by using a two-step procedure. A FORTRAN code for computing all these corrections is available on one server of the Royal Observatory of Belgium (ROB⁴²).

MATHEWS *et al.* (1995) employ hitherto a new definition of Love Numbers, and accommodate the definition of the tidal potential for a frequency-dependency of the form $\mathbf{W}(\mathbf{r})e^{i\omega t}$, creating the possibility to contain a specific spatial spectral type of degree- n and order- m denoted by:

$$\mathbf{W}(\mathbf{r}) = -W_{nm} r^n Y_{nm}(\theta, \lambda) \quad (3.3.6)$$

where r , θ and λ denote the geocentric distance, the colatitude and the longitude of \mathbf{r} , and $Y_{nm}(\theta, \lambda)$ is the spherical harmonic 4π -normalized over the unit sphere. For a degree-2 excitation, the displacement of the Earth $\mathbf{d}(\mathbf{r})$ may be described, to the first order in Earth's flattening $f \approx 1/300$, as:

$$\mathbf{d}(\mathbf{r}) = \sum_{i=0,2,4} U_{im} \mathbf{R}_{im} + \sum_{i=2,4} V_{im} \mathbf{S}_{im} + \sum_{i=1,3} W_{im} \mathbf{T}_{im} \quad (3.3.7)$$

where \mathbf{R}_{im} , \mathbf{S}_{im} and \mathbf{T}_{im} denote, respectively, the spheroidal and toroidal vector spherical harmonic field. The new definition of degree-2 Love Numbers (MATHEWS *et al.* 1995) (slightly modified) reads:

$$\mathbf{d} = d_i(\mathbf{r}) = \frac{W_{2m} r^2}{|g_{0,r}|} = \frac{(h_2(\theta)Y_{2nm} + h')}{r} r_i + l_2(\theta) r \partial_i Y_{2m} + (\mathbf{i} \cdot l^T(\theta) \epsilon_{ijk} r_j \partial_k Y_{2m} + l' t_{1m,i}) \quad (3.3.8)$$

where \mathbf{i} is the imaginary unit, h' and l' are independent of latitude (and have nothing to do with the Load Love Numbers, and will be ignored in the subsequent treatment), ϵ_{ijk} is the epsilon tensor, $h_2(\theta) = h^{(0)} + h^{(2)} P_2(\cos \theta)$, $l_2(\theta) = l^{(0)} + l^{(2)} P_2(\cos \theta)$, $l^T(\theta) = l^{(1)} + l^{(2)} P_1(\cos \theta)$ and $t_{1m,i}$ are degree-1 toroidal fields, defined below in the equation (3.3.9), while l' ensures that the degree-1 toroidal parts, which represent wobble motions and rotation rate variations, do not contaminate the deformation field $d_i(\mathbf{r})$.

$$t_{1m} = \mathbf{i} \begin{pmatrix} -\sin \theta \sin \lambda & -\mathbf{i} \cos \theta \\ \sin \theta \cos \lambda & \cos \theta \\ 0 & \mathbf{i} \sin \theta e^{i\lambda} \end{pmatrix} \quad (3.3.9)$$

A two-step procedure, for the displacement due to solid Earth tides, is recommended in the IERS Conventions 2003:

- in step one, several corrections are computed in the **time domain**:
 - in-phase contribution by means of *real latitude-dependent Love Numbers* $h_2(\varphi)$ and $l_2(\varphi)$ at all degree-2 tides:

$$h_2 = h_2(\varphi) = h^{(0)} + \frac{h^{(2)}}{2} (3 \sin^2 \varphi - 1) \text{ and } l_2 = l_2(\varphi) = l^{(0)} + \frac{l^{(2)}}{2} (3 \sin^2 \varphi - 1)$$

$$\text{where} \quad \begin{aligned} h^{(0)} &= 0.6078 & h^{(2)} &= -0.0006 \\ l^{(0)} &= 0.0847 & l^{(2)} &= +0.0002 \end{aligned}$$

⁴² <ftp://omaftp.oma.be/dist/astro/dehant/IERS/>

- in-phase contribution by means of *real Love Numbers* h_3 and l_3 at all *degree-3 tides*, (only the contribution of the moon is relevant, causing maximum radial displacements in the order of 1.7 mm):
 $h_3 = 0.292$ and $l_3 = 0.015$
- out-of-phase correction for *imaginary degree-2 Love Numbers* $\Im(h_{2m}^{(0)}) = h^I$ and $\Im(l_{2m}^{(0)}) = l^I$, only for the *diurnal (D) and semi-diurnal (SD) tidal band*:
 D : $h^I = -$ $= -0.0007$
 SD: $h^I = -$ $= -0.0007$
- in-phase correction (only for horizontal components) accounting for latitude dependence by means of the *real part of the* $l^{(1)}$ term, solely for the *diurnal (D) and semi-diurnal (SD) tidal band*:
 D : $l^{(1)} = -0.0012$
 SD: $l^{(1)} = -0.0024$
- in step two, corrections are computed in the **frequency domain** and must be added to the displacements obtained in step one:
 - in-phase correction for degree-2 accounting for frequency dependence, solely for the *diurnal (D) tidal band*.
 - in-phase and out-of-phase correction for degree-2 accounting for frequency dependence, solely for the *long-period tidal band*.

The sum (in step one of the two first corrections) of degree-2 and degree-3 displacement, can be denoted concisely as:

$$\mathbf{d}_{sol,2+3} = \begin{pmatrix} d_r \\ d_\beta \end{pmatrix} = \sum_{j=M,S} F_j \begin{pmatrix} h_2 P_2(\cos \Theta_j) + Q_j h_3 P_3(\cos \Theta_j) \\ 3 \sin \Theta_j \left[l_2 \cos \Theta_j - \frac{Q_j l_3}{2} (5 \cos^2 \Theta_j - 1) \right] \end{pmatrix} \quad (3.3.10)$$

with $Q_j = R_E / R_j$ and $F_j = Q_j^3 M_j R_E / M_E$, where M_j is the mass for the moon (M) or the sun (S), M_E is Earth's mass, R_E is its equatorial radius, Θ_j is the angle between the unit vectors from the geocentre towards the moon/sun $\hat{\mathbf{R}}_j$ and towards the station $\hat{\mathbf{r}}$, and R_j is the geocentric distance of that body. The direction of the lateral component d_β is:

$$\hat{\mathbf{d}}_\beta = \sum_{j=M,S} \frac{\hat{\mathbf{R}}_j - (\hat{\mathbf{R}}_j \cdot \hat{\mathbf{r}}) \hat{\mathbf{r}}}{\sin \Theta_j} \quad (3.3.11)$$

For the Chandler period (ca. 432 days), ΞETZ (2004) finds a Love Number $k_2 = 0.352 + i \cdot 0.0042$ that has the highest correlation with the C04⁴³ polar motion time series, and shows that the real part $\Re(k_2)$ and imaginary part $\Im(k_2)$ are independent up to a very high degree. The estimated imaginary part $\Im(k_2)$ differs

⁴³ <http://hpiers.obspm.fr/eop-pc/>

significantly from the one derived from theoretical models, where $k_2 = 0.35 + i \cdot 0.0036$ (MATHEWS *et al.*, 2002).

3.4 Permanent tides

The degree-2 tidal potential includes a permanent time-independent part. In order to compute ‘mean tide’ coordinates from ‘conventional tide free’ coordinates (which contain a time independent term), the IERS Conventions 2003 recommend the following corrections for radial δr_{pd} and lateral δl_{pd} displacement components, in units of mm (where the subscript pd denotes permanent deformation):

$$\begin{aligned}\delta r_{pd} &= [-120.6 + 0.1 P_2(\cos \theta)] P_2(\cos \theta) \\ \delta l_{pd} &= [-25.2 + 0.1 P_2(\cos \theta)] \cos 2\theta\end{aligned}\tag{3.4.1}$$

The radial correction amounts to -12.05 cm at the poles and +6.03 cm at the equator, while the lateral correction reaches +2.51 cm at -45° latitude and -2.51 cm at 45° latitude, as shown in Figure 12.

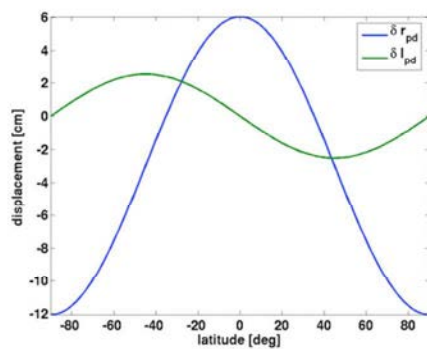


Figure 12: Permanent deformation correction from “conventional tide free” to “mean tide” coordinates.

3.5 Load tides

Several sets of Love Numbers are in practical use: the first, described in section 3.3, corresponds to the response of the Earth to an applied potential without loading the surface. The second is used to describe the deformation of the Earth under a variable surface load, and is denoted as Load Love Numbers h_n' , k_n' and l_n' . The latter were first introduced by MUNK AND MACDONALD (1960), and are shown on Figure 13, using different scales for the left and right panels, for a centre of mass frame (containing the solid Earth and atmosphere system).

A third set of Love Numbers, due to the response of horizontal frictional forces, e.g. ocean currents, are called Shear Love Numbers h_n'' , k_n'' and l_n'' (e.g. VARGA, 1983). However, out of these nine Love Numbers, Load Love Numbers and Shear Love Numbers, only six are independent (LAMBECK, 1988). In this thesis, we will focus on the second set, the so-called Load Love Numbers (LLNs).

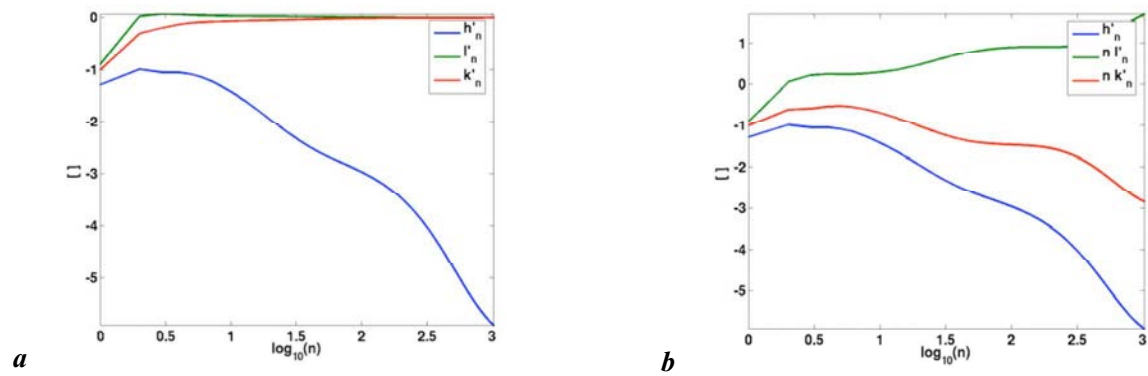


Figure 13: Load Love Numbers (from Gegout⁸) up to degree 1024, expressed in the reference frame of the total Earth system's centre of mass CM (solid Earth + atmosphere).

In numerous instances, the load tides are a consequence of mass redistribution over the Earth's surface, e.g. an exchange of mass between polar ice caps, oceans, a redistribution of water between oceans, atmosphere and groundwater, or a redistribution of mass within the atmosphere (LAMBECK, 1980). The load tides affect the rigid Earth, which is deformed elastically. In most applications (e.g. gravimetry, GPS, VLBI and geophysics), load tides are just a nuisance and need to be removed as accurately as possible in order to properly interpret residual signals. Body and load tides must also be taken out when deducing oceanic tides from altimetric measurements, since an altimeter measures geocentric tides (KANTHA AND CLAYSON, 2000). An accurate method for calculating the loading effects is to use equivalent LLNs, a Green's function approach and an Earth model. The loads must be known accurately to compute the load tides, which, in turn, affect the tides through modification of the effective tidal potential.

The spatial distribution of ocean depth, which is composed of a depth H from an undisturbed state and sea tidal height \mathbf{u}_0 , is very complicated due to the ocean currents arising from the Coriolis force and friction terms. Additionally, the time and space-varying load deforms the solid Earth, causing a displacement \mathbf{d}' . This displacement is opposite to the displacement \mathbf{d} generated by the solid Earth tides (see Figure 14).

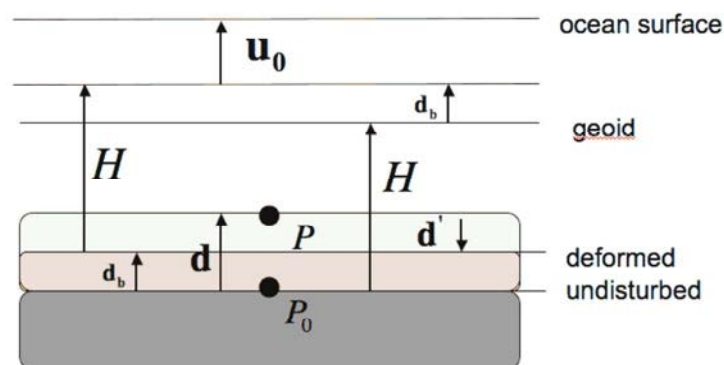


Figure 14: Graphic illustrating the deformation due to indirect effects (e.g. due to ocean tides).

The so-called indirect effects fall into three categories:

- the load distribution is responsible for an additional gravitational potential V'
- the solid Earth, e.g. the ocean bottom, is deformed, and the load effect overlays in opposite direction due to the gravitational displacement, resulting in a displacement of the solid Earth denoted by \mathbf{d}'

- the deformation \mathbf{d}' induces the additional deformation potential V'_D , due to density redistribution.

The net displacement, due to the solid Earth tides and the indirect effects, is $\mathbf{d}_b = \mathbf{d} + \mathbf{d}'$ (see Figure 14).

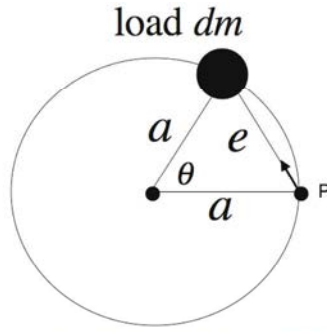


Figure 15: Sketch illustrating the gravitational attraction of a mass element at a point P.

The gravitational potential V' of a load particle dm (see Figure 15) is given by:

$$V' = G \frac{dm}{e} = G \frac{dm}{2a \sin(\theta/2)} = \sum_{n=0}^{\infty} G \underbrace{\frac{dm}{a}}_{V'_n} P_n = \sum_{n=0}^{\infty} V'_n \quad \text{with} \quad \sum_{n=0}^{\infty} P_n = \frac{1}{2 \sin(\theta/2)} \quad (3.5.1)$$

where θ is the angular distance between the load particle and the point P, with radius a , on the Earth's surface. Following the theorem of BRUNS (1878), the displacement of the original potential surface due to the additional potential V' reads:

$$\mathbf{u}' = (u'_r, u'_\theta) = \left(\sum_{n=0}^{\infty} \underbrace{\frac{V'_n}{|g_{0,r}|}}_{u'_{r,n}}, \sum_{n=0}^{\infty} \underbrace{\frac{1}{|g_{0,r}|} \frac{\partial V'_n}{\partial \theta}}_{u'_{\theta,n}} \right) \quad (3.5.2)$$

resulting in a displacement vector \mathbf{d}' due to the combined gravitation and load of mass redistributions (the subscript θ denoting the lateral component):

$$\mathbf{d}' = (d'_r, d'_\theta) \quad d'_r = \sum_{n=0}^{\infty} h'_n u'_{r,n} \quad d'_\theta = \sum_{n=0}^{\infty} l'_n u'_{\theta,n} \quad (3.5.3)$$

This displacement \mathbf{d}' engenders an additional deformation potential V'_D :

$$V'_D = \sum_{n=0}^{\infty} k'_n V'_n \quad (3.5.4)$$

The LLNs h'_n and k'_n are negative, as the load effect is larger than the gravitational effect (FARRELL, 1972).

If the LLNs are known (e.g. derived from Earth models, as described in subsection 3.10), the displacement vector on the Earth's surface can be calculated as a function of the geocentric angle of the load particle:

$$d'_r(\theta) = \sum_{n=0}^{\infty} h'_n \frac{V'_n}{|g_{0,r}|} = \frac{1}{|g_{0,r}|} G \frac{dm}{a} \sum_{n=0}^{\infty} h'_n P_n = dm \underbrace{\frac{a}{M_E} \sum_{n=0}^{\infty} h'_n P_n}_{G'_{d_r}} \quad \text{with} \quad |g_{0,r}| = G \frac{M_E}{a^2}$$

$$d'_\theta(\theta) = \sum_{n=0}^{\infty} l'_n \frac{1}{|g_{0,r}|} \frac{\partial V'_n}{\partial \theta} = dm \underbrace{\frac{a}{M_E} \sum_{n=0}^{\infty} l'_n \frac{\partial P_n}{\partial \theta}}_{G'_{d\theta}} \quad (3.5.5)$$

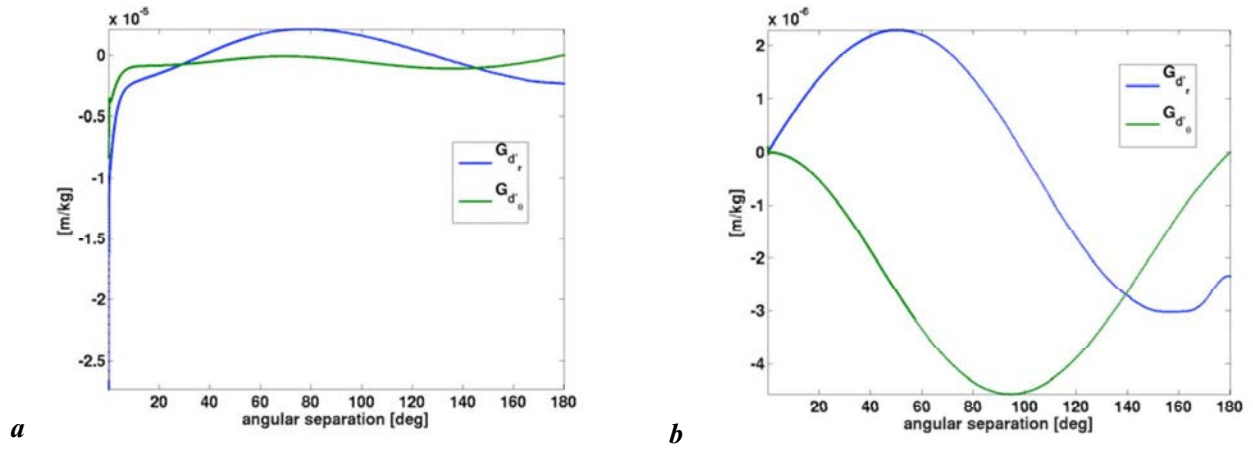


Figure 16: Green's functions (for radial and horizontal displacements) in the centre of solid Earth frame (CE) (a) and their difference compared to the centre of mass frame of solid Earth and the mass which causes the loading (CM) (b).

The disturbed acceleration in radial and lateral components (FARRELL, 1972) reads:

$$\begin{aligned} \delta g'_r(\theta) &= dm \underbrace{\frac{|g_{0,r}|}{M_E} \sum_{n=0}^{\infty} [n - (n+1)k'_n + 2h'_n] P_n}_{G'_{\delta g_r}} \\ \delta g'_\theta(\theta) &= dm \underbrace{\frac{|g_{0,r}|}{M_E} \sum_{n=0}^{\infty} [1 + k'_n - h'_n] \frac{\partial P_n}{\partial \theta}}_{G'_{\delta g_\theta}} \end{aligned} \quad (3.5.6)$$

Equations (3.5.5) and (3.5.6) contain the so-called Green's functions (see Figure 16 and its caption), which are the kernel for computing the total effect over the Earth's surface. In fact, they represent a convolution of the Green's functions (weighted Load Love Numbers) with a specific filter function (e.g. ocean loading or atmospheric pressure variations including respectively their inherent tides).

We recognize from equation (3.5.6) that gravity perturbations, due to surface loads, are sensitive to the LLNs h'_n and k'_n . On the other hand, equation (3.5.5) shows that space geodetic techniques (e.g. GPS and VLBI) are sensitive to h'_n and l'_n .

FARRELL (1972) and DAHLEN (1976) were the first to derive LLNs. More recent LLNs have been developed by LAMBECK (1988), PAGIATAKIS (1990) and CARTWRIGHT (1993).

The calculation of load tides can be tedious, as a very high degree must be included for global integration. Moreover, an iterative scheme is used to calculate load tides from ocean tides, because of the induced tidal potential V'_D . However, load tides may also be computed using spherical harmonic decomposition of, e.g. oceanic tides and LLNs (MUNK AND MACDONALD, 1960, FARRELL, 1972; FRANCIS AND MAZZEGA, 1990). This approach requires that the surface load be given as a spherical harmonic expansion.

3.6 Pole tide: rotational deformation due to polar motion

Apparent inertial accelerations appear in a rotating reference system (using the subscript R), to which the measurement systems (GPS antenna, VLBI telescope etc.) are attached, for e.g.:

$$\ddot{\mathbf{r}} = \frac{d^2 \mathbf{r}}{dt^2} = \frac{d_R^2 \mathbf{r}}{dt^2} + \underbrace{\boldsymbol{\Omega} \times (\boldsymbol{\Omega} \times \mathbf{r})}_{\text{centrifugal term}} + \underbrace{2\boldsymbol{\Omega} \times \frac{d_R \mathbf{r}}{dt}}_{\text{Coriolis term}} + \underbrace{\frac{d_R \boldsymbol{\Omega}}{dt} \times \mathbf{r}}_{\text{Euler term}} \quad (3.6.1)$$

where $\boldsymbol{\Omega}$ is the instantaneous Earth rotation vector. The centrifugal acceleration $\ddot{\mathbf{r}}_c$ may be transformed to (e.g. LOVELOCK AND RUND, 1989):

$$\ddot{\mathbf{r}}_c = \underbrace{\boldsymbol{\Omega} \times (\boldsymbol{\Omega} \times \mathbf{r})}_{\text{centrifugal term}} = \varepsilon_{ijk} \Omega_j \varepsilon_{kls} \Omega_l r_s = (\delta_{il} \delta_{js} - \delta_{is} \delta_{jl}) \Omega_j \Omega_l r_s \quad (3.6.2)$$

$$\Rightarrow \ddot{\mathbf{r}}_c = \Omega_s \Omega_l r_s - \Omega_l \Omega_i r_i = \boldsymbol{\Omega} \cdot (\boldsymbol{\Omega} \cdot \mathbf{r} - \quad (3.6.3)$$

This means that the centrifugal acceleration may also be described as a second-order tensor T_{il} multiplied by the instantaneous Earth rotation vector Ω_l :

$$\ddot{\mathbf{r}}_c = (\Omega_l r_l - \Omega_l r_i) \Omega_l = T_{il} \Omega_l \quad (3.6.4)$$

where $\boldsymbol{\Omega} = \Omega \cdot [m_1 \ m_2 \ (m_3 + 1)]^T$, Ω is the mean angular speed of Earth rotation vector, and m_i are the time dependent offsets of the instantaneous rotation pole.

The potential of the centrifugal term at a point P , at a distance l from the instantaneous rotation axis, is given by e.g. LAMBECK (1980):

$$V_c = \frac{1}{2} |\boldsymbol{\Omega}|^2 l^2 = \frac{1}{2} |\boldsymbol{\Omega}|^2 \left[r^2 - \frac{1}{|\boldsymbol{\Omega}|^2} (\boldsymbol{\Omega} \cdot \mathbf{r})^2 \right] = \frac{1}{2} \left[r^2 |\boldsymbol{\Omega}|^2 - (\mathbf{r} \cdot \boldsymbol{\Omega})^2 \right] \quad (3.6.5)$$

The use of the potential V_c for the centrifugal acceleration means that polar motion must always be accounted for.

A first order perturbation of the potential V_c (neglecting variations in m_3 , which induce displacements below 1 mm) has been arrived at by, e.g., SCHWEYDAR (1916), WAHR (1985) or by PETROV (1998), who gives an even clearer derivation:

$$V_{c1}(r, \theta, \lambda) = -\frac{\Omega^2 r^2}{2} (m_1 \cos \lambda + m_2 \sin \lambda) \sin 2\theta \quad (3.6.6)$$

The displacements, in units of mm, due to the potential V_{c1} are obtained using the Love-number formalism (MCCARTHY AND PETIT, 2003):

$$\mathbf{S} = \begin{pmatrix} S_r \\ S_\theta \\ S_\lambda \end{pmatrix} = \frac{1}{|g_{0,r}|} \begin{pmatrix} h_2 V_{c1} \\ l_2 \partial_\theta V_{c1} \\ \frac{l_2}{\sin \theta} \partial_\lambda V_{c1} \end{pmatrix} = \begin{pmatrix} -32(m_1 \cos \lambda + m_2 \sin \lambda) \sin 2\theta \\ -9(m_1 \cos \lambda + m_2 \sin \lambda) \cos 2\theta \\ 9(m_1 \cos \lambda - m_2 \sin \lambda) \cos \theta \end{pmatrix} \quad (3.6.7)$$

In equation (3.6.7), the time dependent offsets m_1 and m_2 of the instantaneous rotation pole from the mean pole have been reduced to:

$$m_1 = x_p - \bar{x}_p \quad m_2 = -(y_p - \bar{y}_p) \quad (3.6.8)$$

where x_p and y_p are the polar motion variables, as defined in Chapter 5 of the IERS Conventions 2003, and where \bar{x}_p and \bar{y}_p represent their secular variation, as shown in Figure 17a. The nominal values $h_2=0.6067$ and $l_2=0.0836$, as well as $r=6378$ km, have been substituted in equation (3.6.7). The maximum radial displacement is approximately 25 mm, whereas the lateral displacement is 7 mm.

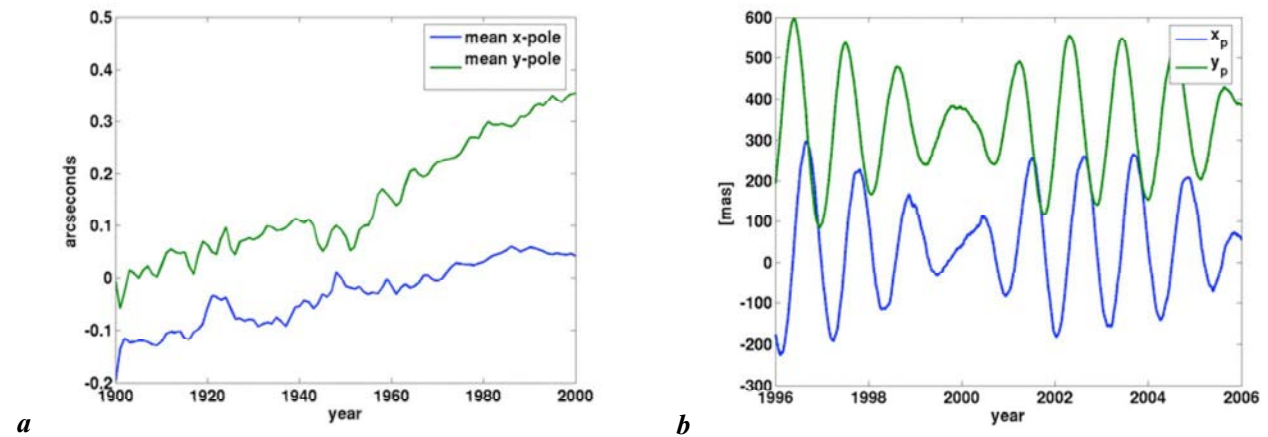


Figure 17: Mean pole coordinates (a) for the 20th century available at BIPM⁴⁴, and C04 long-term pole coordinates⁴⁵ (b) for the period 1996-2006.

3.7 Atmospheric tides

As previously mentioned, tides also occur in the atmosphere, however, the dominant part arises from solar thermal forcing, and not from the gravitational one. The atmospheric tides can be observed from surface pressure and temperature records (e.g. MENTES, 2004). Excellent reviews of atmospheric tides can be found in CHAPMAN AND LINDZEN (1970), VOLLAND (1988) and VOLLAND (1997). The pressure wave is most pronounced at the 12-hour period (semi-diurnal), leading the temperature wave by about 10 hours. The temperature wave is largest at a 24-hour period (diurnal). In mid-latitudes, the surface pressure signals are swamped with large meteorological disturbances. In the tropics, the tidal surface pressure signals are about 1200 Pa, corresponding to 1 cm amplitude of equivalent water level fluctuations, and can thus be filtered easily. Towards the poles, the surface pressure variation is less than 200 Pa, and the atmospheric tides are therefore not easily discernible (KANTHA AND CLAYSON, 2000).

The ocean, of course, responds to pressure changes produced by atmospheric tides, and tends to adjust like an inverted barometer. A rise of 1 mb surface pressure drops sea level approximately by 1 cm. The ocean tide constituent most affected is S_2 . At this frequency, the radiational tidal forcing is predominant with a contribution from 84% to 94% over the Earth's surface (KANTHA AND CLAYSON, 2000). In some coastal regions, the diurnal S_1 tide appears with amplitudes of a few cm. Strong diurnal breezes, generated by solar land and sea heat, are one probable cause.

Firstly in the 1960s, it became clear that absorption of solar radiation by water vapour in the troposphere and ozone in the stratosphere accounts for most of the semi-diurnal surface pressure fluctuations (CHAPMAN AND LINDZEN, 1970).

⁴⁴ <ftp://tai.bipm.org/iers/conv2003/chapter7/annual.pole>

⁴⁵ <http://hpiers.obspm.fr/eop-pc/products/longterm/longterm.html>

3.8 Radiational tides

So far, only gravitational ocean tides have been considered. However, observations divulge that the solar semi-diurnal, diurnal and annual tides have amplitudes and phases differing from those expected from their neighbour constituents (KANTHA AND CLAYSON, 2000). One principal cause is the diurnal and annual solar heating of the atmosphere and the ocean. The most affected constituent is S_2 . The upper layers of the ocean are heated and cooled diurnally by the sun. A consequence is the expansion and contraction in sea level on the order of 1 cm. This phenomenon is called the radiational tide with exactly the same frequency as S_2 . Seasonal heating and cooling of the oceans, Earth's surface and atmosphere also affect the diurnal S_2 and the annual S_a tides. Radiational tides may be defined using a pseudo-potential W_R (MUNK AND CARTWRIGHT, 1966; KANTHA AND CLAYSON, 2000):

$$W_R = S \frac{R_s}{4\bar{R}_s} \left[1 + 2P_1 \cos(\Theta_s) + \frac{5}{4}P_2 \cos(\Theta_s) + \dots \right] \quad (3.8.1)$$

where S is the solar constant (1380 W/m²), R_s is the distance to the sun and \bar{R}_s , its mean value. The angle Θ_s subtends the direction between the sun and the station on the Earth's surface.

3.9 Equation of motion of Earth tides

Earth models are needed to derive theoretical parameters such as LLNs, which can be compared with estimated ones, in order to be accepted, refined or even refuted. A first step, for deriving Love Numbers or LLNs, consists in setting up the equation of motion for Earth tides.

A simplified equation of motion for Earth tides uses the following assumptions:

- validity of Hooke's law
- radial dependence of the Earth's density and Lamé parameters
- hydrostatic equilibrium
- perturbing accelerations are small compared to the gravitational accelerations.

The equation of motion for a spherical non-rotating perfectly elastic isotropic (SNREI) model is given by (e.g. MEURERS, 2002):

$$\begin{aligned} \ddot{u}_i \rho_0 = & \rho_0 \partial_i (W + V_D) - \partial_i V_0 \partial_j (\rho_0 u_i) + \partial_i (u_j \partial_j p_0) + \partial_i \lambda^L \partial_j u_j + 2\varepsilon_{ij} \partial_j \mu^L \\ & + (\lambda^L + 2\mu^L) \partial_i \partial_j u_j - \varepsilon_{ijk} \partial_j \varepsilon_{krs} \partial_r u_s \end{aligned} \quad (3.9.1)$$

where ρ_0 is the undisturbed initial density, and p_0 is the hydrostatic pressure. The unknowns in this partial differential equation (PDE) are the displacement vector u_i and the deformation potential V_D , which is connected to u_i by the Poisson PDE (ρ is the disturbed final density):

$$\partial_i \partial_i V_D = -4\pi G(\rho - \rho_0) = 4\pi G \partial_i (\rho_0 u_i) \quad (3.9.2)$$

The next step consists of transforming the PDE-system into polar coordinates:

$$\begin{pmatrix} u_r \\ u_\vartheta \\ u_\lambda \end{pmatrix} = \begin{pmatrix} \sin \vartheta \cos \lambda & \sin \vartheta \sin \lambda & \cos \vartheta \\ \cos \vartheta \cos \lambda & \cos \vartheta \sin \lambda & -\sin \vartheta \\ -\sin \lambda & \cos \lambda & 0 \end{pmatrix} u_i \quad (3.9.3)$$

The perturbing acceleration can be brought to a sum of harmonic waves:

$$\ddot{u}_i = -\omega^2 u_i \quad (3.9.4)$$

Assuming the above-mentioned presuppositions, the Lamé parameters, λ^L and μ^L in equation (3.9.1) as well as the density ρ , only take radial-dependent values. Therefore, the displacement vector and the deformation potential may be expressed as a linear combination of the tidal potential and the Love Numbers. These three radial-dependent Love Number functions are the new unknowns. The equations of motion of second order can, e.g., be transformed into six PDEs of first order. The six integration constants are taken from various boundary conditions, e.g. no displacement occurs at the geocentre. The PDE-system may be solved numerically, if the radial dependence of the Earth's density and Lamé parameters are known. The assumptions made on the derivation of the equation of motion determine the type of Earth model in question (see section 3.10).

Theoretical Load Love Numbers are estimated in the same way as the Love Numbers if the following substitutions are made in the equation of motion (3.9.1):

$$W = V' \quad V_D = V'_D \quad \mathbf{u} = \mathbf{d}' \quad (3.9.5)$$

In addition, different boundary conditions are necessary for the Earth's surface, as the load is responsible for a stress.

More complex Earth models (e.g. MATHEWS *et al.*, 1995, 1997, 2002; BUFFET *et al.*, 2002) consider the rotation of an elliptic Earth with a fluid outer core. Centrifugal, Coriolis and Euler accelerations have to be taken into account. In 1961, Molodensky calculated two dynamic Earth models MO1 and MO2 (MELCHIOR, 1978; ZHARKOV *et al.*, 1996). The latter includes a rigid inner core. WAHR (1981) calculated another solution, on the basis of the Earth model of GILBERT AND DZIEWONSKI (1975) and DZIEWONSKI AND ANDERSON (1981) including the ellipticity of the core-mantle and mantle-crust boundaries. As a consequence, the amplitude factors of equation (3.3.4) show up a small latitude dependence. The most recent Earth models are from DEHANT (1987), WANG (1994), MATHEWS *et al.* (1995, 1997, 2002) and BUFFET *et al.* (2002). All models show the frequency dependence of the amplitude factors near the resonance frequency (and consequently also the frequency dependence for the Love Numbers). Frequency dependent Love Numbers were quantitatively estimated and validated for the VLBI technique (e.g. HAAS AND SCHUH, 1996).

3.10 Calculation of Earth models

Earth models are characterized by their geometry, their mechanical properties and their rheology. The most widely used models are hydrostatically pre-stressed spherical non-rotating elastic isotropic (SNREI) ones. Most of the information used to produce Earth models like the Preliminary Reference Earth Model (PREM) (DZIEWONSKI AND ANDERSON, 1981) comes from seismology. However, for the computation of LLNs, PREM poses at least some problems. For e.g., it has a global ocean of 3 km in depth, which must be replaced by a solid layer, and it is a visco-elastic model, based on a rheology which cannot provide elastic values for the shear and bulk modulus (VAN DAM *et al.*, 2004). For isotropic models, the velocity of the primary v_p and secondary v_s waves is connected to the Earth's density ρ and Lamé parameters, λ^L and μ^L , by:

$$v_p = \sqrt{\frac{\lambda^L + 2\mu^L}{\rho}} \quad v_s = \sqrt{\frac{\mu^L}{\rho}} \quad (3.10.1)$$

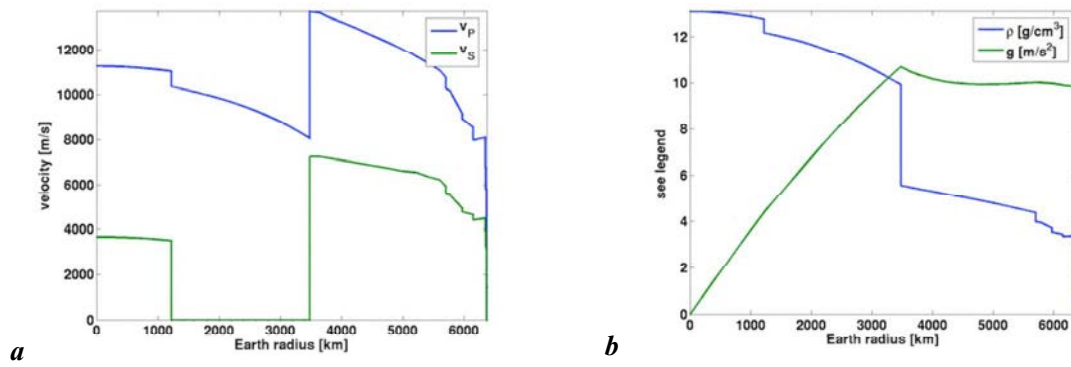


Figure 18: Primary and secondary waves' velocity (a) and density/gravity (b) for PREM⁴⁶.

The Adams-Williamson equation of second order establishes the density distribution (e.g. GUTENBERG, 1951):

$$\frac{d}{dr} \left(k(r) \frac{r^2}{\rho^2(r)} \frac{d\rho}{dr} \right) = 4\pi G r^2 \rho(r) \quad (3.10.2)$$

where $k(r)$ is the bulk modulus. The integration constants are chosen so as to reflect results known from satellite geodesy, e.g., the Earth's mass, its moments of inertia or its mean radius.

The Gutenberg-Bullen A Earth model (GUTENBERG, 1951) and PREM have benefited from great popularity, because the Green's functions for such models are rather simple, depending only on the angular distance between the load and the observer (VAN DAM *et al.*, 2003). For laterally heterogeneous models, the Green's functions depend on the position of the load and the observer. This is a major computational burden of the response to loads. More recent information on Earth models can be found at the Reference Earth Model (REM) homepage⁴⁷.

⁴⁶ http://solid_Earth.ou.edu/prem.html

⁴⁷ <http://mahi.ucsd.edu/Gabi/rem.html>

Chapter 4

Atmospheric loading models

The purpose of this chapter is to present comparisons between available atmospheric pressure loading (APL) predictions, which could become a standard correction to observables of space geodetic techniques in future IERS Conventions, in terms of reducing raw observables. In this context, a paper entitled “Statistical Comparison of Publicly Available Atmospheric Loading Corrections” by VAN DAM, T.M., J.-P. BOY, P. GEGOUT, H. KIERULF, P.J. MENDES GERVEIRA, L. PETROV, H.-P. PLAG, AND H.-G. SCHERNECK is in preparation.

4.1 History and services

D’ABBADIE in France (MELCHIOR, 1978) and DARWIN (1882) in England were the first to point out and evaluate the possible influence of loading (e.g. oceanic tides) on the surface of the Earth. For a decade, such loading deformations have been detected in GPS station coordinate time series or baselines (VAN DAM *et al.*, 1994; DONG *et al.* 2002) and VLBI coordinates (VAN DAM AND HERRING, 1994; MACMILLAN AND GIPSON, 1994; SCHUH *et al.*, 2002; PETROV AND BOY, 2004). Thereupon, the IERS decided in 2002 to establish the Special Bureau for Loading (SBL⁴⁸) whose initial job was to generate, in near real time, global grids of atmospheric pressure loading effects. The SBL initially provided time series of 3-D displacements of geodetic sites from 1990 to the present, and became operational in 2004, supplying 3-D global grids of atmospheric loading in near real time. As VLBI is a prototyping tool par excellence, the Goddard VLBI group (PETROV AND BOY, 2004) decided to start operating an Atmospheric Pressure Loading Service (APLO⁴⁹) themselves, which became active in December 2002. In addition to these services, three individual scientists, namely VAN DAM (TVD), GEGOUT (PG) and SCHERNECK (HGS), make available their own displacement predictions through the SBL or via their own webpages⁵⁰. These different services use different computational methodologies and atmospheric data sets. As a consequence, different displacements appear, in the order of 1 to 2 mm. Horizontal displacement predictions are typically smaller by a factor of 6. Sometimes, the periodic differences are also due to the handling or non-handling of atmospheric tides. This chapter reveals in detail the causes of the differences between the atmospheric-induced displacement predictions. Investigating the different characteristics between the subsets of products highlights most of the issues introducing the differences. Recently, TVD generated gridded deformations for implementation into the GAMIT (KING AND BOCK, 2005) GPS processing software (TREGONING AND VAN DAM, 2005b). The conclusions of the latter paper are:

- *the power spectral density of the APL predicted vertical deformation, aside from the diurnal and semi-diurnal periods, contains very little power in the sub-daily frequencies*
- *the present tidal APL models improve the analysis at sites near the equator but seem to degrade the height estimates at other latitudes*
- *the majority of the non-tidal deformation can be modelled by applying a daily-averaged correction to daily estimates of coordinates, but a greater improvement in height RMS is obtained if non-tidal APL is applied at the observation level*

⁴⁸ <http://www.sbl.statkart.no/>

⁴⁹ <http://gemini.gsfc.nasa.gov/aplo/>

⁵⁰ <http://www.oso.chalmers.se/~hgs/apload.html>

4.2 Products

Table 7 outlines the fundamental characteristics of the different atmospheric loading products:

- the source of the input data set (atmospheric pressure), namely
 - the European Centre for Medium-Range Weather Forecasts (ECMWF) or
 - the National Centre for Environmental Prediction Reanalysis (NCEPR⁵¹)
- the surface from which the input pressure is derived
- whether time series (TS) or grids (GG) are produced
- the Earth model used, i.e. PREM or Gutenberg-Bullen (G-B)
- whether atmospheric tide corrections are applied or not
- the actual computational approach, i.e. convolution (GC) or spherical harmonics (SH)

Furthermore, the land-ocean mask (available at APLO⁵² in NETCDF⁵³ format) is a major issue and plays a major role in discrepancies.

In fact, this study allowed finding errors in the Green's functions at APLO, errors in the land-ocean mask at TVD, and errors in the conversion of surface pressure (SFCP) derived from sea-level pressure (SLP) at the SBL.

Service	Time Series versus Grids	Pressure Data Set Resolution(deg)	Surface	Earth Model	Tides	Method
SBL-OP	GG and TS	ECMWF	SLP	G-B	N	GC
SBL-Res	TS	ECMWF	SLP	G-B	N	GC
APLO	TS	NCEPR(2.5°)	SFCP	PREM	Y	GC
TVD	GG and TS	NCEPR (2.5°)	SFCP	G-B	Y/N	GC
PG	GG and TS	NCEPR/ ECMWF (l=512)	SFCP	PREM	N	SH
HGS	TS	ECMWF(1.0°)	SFCP	G-B	N	GC

Table 7: Characteristics of publicly available atmospheric loading products (source⁵⁴ taken from a presentation given by VAN DAM at the IERS Workshop Combination 2005).

4.3 Meteorological models

Firstly, pressure data sets used as input into the calculations need to be considered, including:

- the difference between ECMWF Operational and NCEP Reanalysis surface pressure versus sea-level pressure
- the reference pressure used
- the spatial resolution of the data set

⁵¹ <http://www.cdc.noaa.gov/cdc/data.ncep.reanalysis.html>

⁵² http://gemini.gsfc.nasa.gov/aplo/land_sea_0.25deg.nc

⁵³ <http://www.unidata.ucar.edu/software/netcdf/>

⁵⁴ http://www.iers.org/workshop_2005/presentations/Session-4_van_Dam.pdf

4.3.1 ECMWF vs. NCEPR

In this section, the differences introduced into the predictions of radial surface displacement by using either the ECMWF Operational or NCEP reanalysis surface pressure will be evaluated. The average RMS (for about 400 global geodetic stations over the period 1992–2004) of the difference in the radial displacement is 0.15 mm, with a maximum RMS of 0.74 mm (see Figure 19a). Thus, when using ECMWF instead of NCEPR, the average RMS of the difference in the predicted heights will be sub-mm. The maximum difference, when analyzing each individual time series for the maximum difference in height from the two product sets, is, on average, 0.5 mm. However, maximum differences between 1 and 2 mm in predicted height changes occur at about 10 percent of the stations, e.g. Wuhan (see Figure 19b).

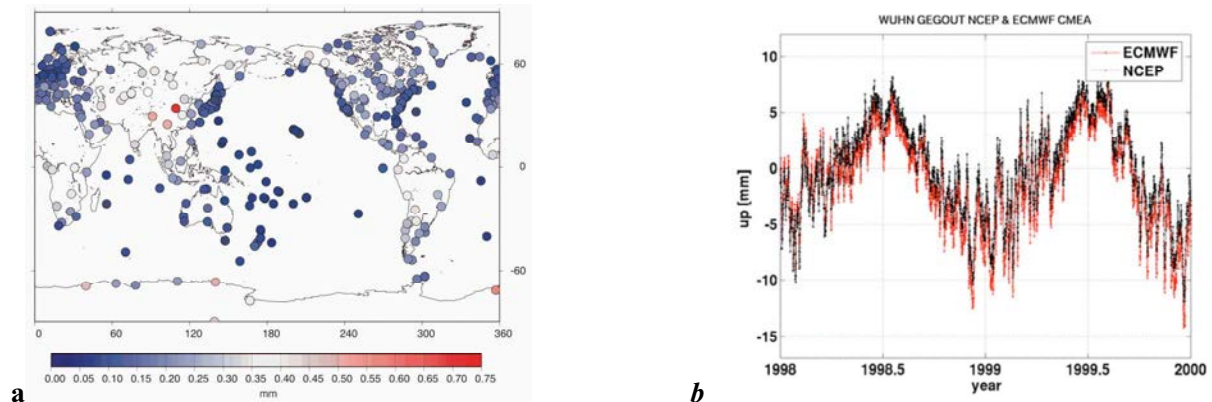


Figure 19: Radial displacement: (a) RMS distribution of difference NCEPR vs. ECMWF in the CM frame (source: VAN DAM⁵⁴), and (b) NCEPR vs. ECMWF for station Wuhan (WUHN), China.

4.3.2 Surface versus sea level pressure

The RMS of vertical surface displacements, due to the use of either the surface pressure (TVD) or the modelled sea level pressure (SBL) to surface pressure, are highest on the Antarctic continent (see Figure 20a & b), but also exist for stations in mountainous regions, e.g. Himalayan or Andes. Figure 20b shows the RMS of the difference between National Meteorological Centre (NMC/NCEP) derived surface displacements and the ones of the SBL using ECMWF data, being nearly identical to Figure 20a. Both figures underpin the difficulty of modelling a given sea-level pressure for any height, leading to RMS differences larger than 1 mm in mountainous regions.

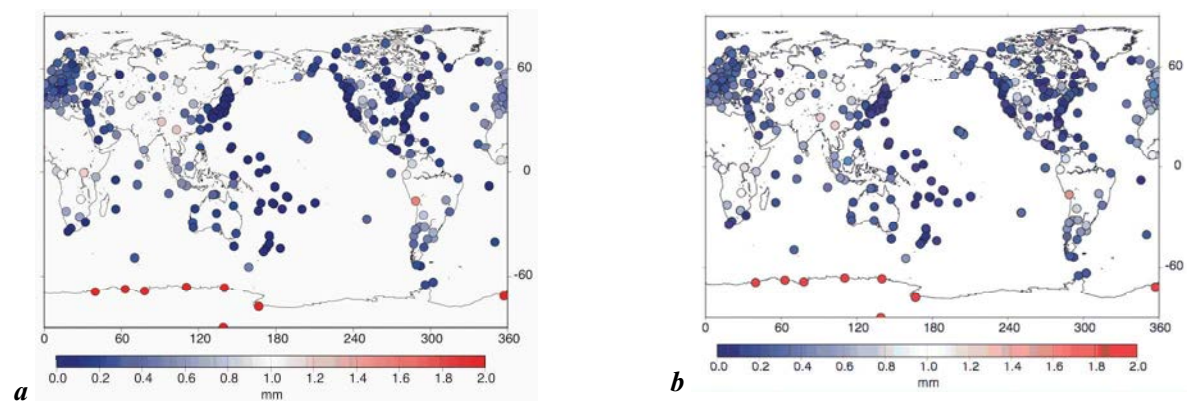


Figure 20: Surface versus sea level pressure: RMS of radial surface displacement between ECMWF (TVD) – ECMWF (SBL) (a), and NMC/NCEP (TVD) – ECMWF (SBL) (b). Source: VAN DAM⁵⁴.

Recently, within the SBL, an error in the conversion of the ECMWF sea pressure fields to pressure at topographic heights, which are used to compute the surface pressure anomalies in near-real time, has been discovered. This error affects the pressure anomalies particularly in areas of high elevation. The SBL is currently working on the recomputation of all operational products. Until further notice, users of the operational products should be aware of the fact that the predictions are erroneous on a level of several mm, with the error depending on the topographic height. Users who envisage problems due to this error should contact the SBL⁵⁵ for more information.

Figure 21 illustrates the effect of the error in computation of the surface pressure field from pressure at sea level and temperature at the 1000 hPa level. This error affected all operational products of the SBL and the SBL time series for research. These products are currently recomputed and will be replaced with the correct products as soon as possible. The recomputation is very demanding in terms of computer resources and it is expected that the corrected products will be available by the end of April 2006. Figure 21a shows the correct surface pressure field for an arbitrary day (January 1, 2000), which was computed from sea level pressure and temperature at the 1000 hPa level, and then validated against the geopotential and the surface pressure field provided by ECMWF. In areas with elevations close to sea level, the two fields were identical or nearly identical. However, in areas with high elevations, differences were clearly visible. The error in surface pressure was quite large and differences reached values of more than 60 hPa (see Figure 21b). However, since the reference pressure surface was also computed with this error, the effect on the pressure anomalies was minor, except for a few areas with large seasonal temperature variations. In these areas, the error mainly introduces a seasonal signal in the predictions of displacements in these regions.

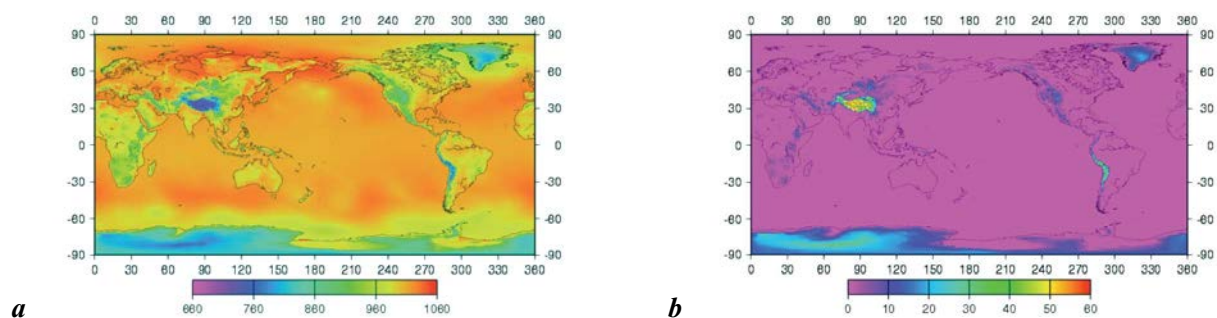


Figure 21: Surface pressure field (a) for January 1, 2000, at 00 hours UTC, computed from sea level pressure and temperature at the 1000 hPa level. The scale is in units of hPa. Difference between correct and erroneous surface pressure fields (b). For topographic heights above zero, the erroneous pressure field is lower than the correct surface pressure. The difference depends both on the topographic height and the temperature at the 1000 hPa level. The scale is in units of hPa. Source: KIERULF⁵⁶.

4.3.3 Reference pressure

All atmospheric loading displacements are reduced with respect to a reference pressure field. For instance, APLO uses a 23-year average of surface pressure derived from the NCEP reanalysis as their reference pressure, while TVD uses a 15-year average of the same data set. Figure 22 shows the offsets to radial displacement from using either APLO or TVD. The different reference pressure mainly adds a sub-mm

⁵⁵ <http://www.sbl.statkart.no/products/operational/>

⁵⁶ http://www.sbl.statkart.no/products/research/ITRF_sites/

offset to the time series. Errors in the land-ocean mask over Antarctica, at TVD, are the cause for the difference in the negative offset as shown in Figure 22.

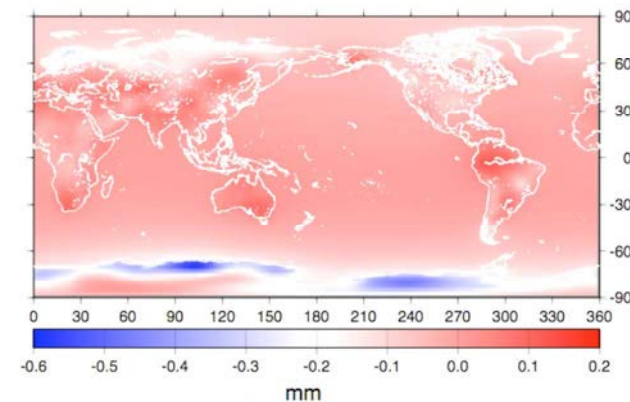


Figure 22: Offset (APLO-TVD) introduced into the predicted radial displacements by using either APLO or the TVD reference pressure. Source: VAN DAM⁵⁴.

4.4 Interpolation

As shown in Table 7, it is possible to acquire global grids as well as displacement time series of the atmospheric loading effects for any particular geodetic station. Regarding the precision of current space geodetic techniques, it is more and more viable to reduce the effects of atmospheric pressure loading displacements from the raw observables (e.g. PETROV AND BOY, 2004; TREGONING AND VAN DAM, 2005b).

On the one hand, global grids are especially useful for studying large-scale global effects. From an operational point of view, it is also easier to generate global grids of the predicted deformation. However, using global grids is not suitable if geodynamic information is to be extricated from time series in a local region. One problem with interpolation is its loss of accuracy in terms of the precision of time series produced for the position-specific coordinates. The reason emerges from the angular dependence of the Green's functions, leading to a deformation at a given station being more sensitive to the load in the very near field. RMS differences of not larger than 0.5 mm can be expected at most sites when using a simple bilinear interpolation (personal communication VAN DAM, 2005). However, for bilinear or bicubic interpolations, maximum differences of 2.25 mm may occur (see Figure 23b for the bicubic interpolation). One consequence is sporadic outliers in coordinate or baseline time series.

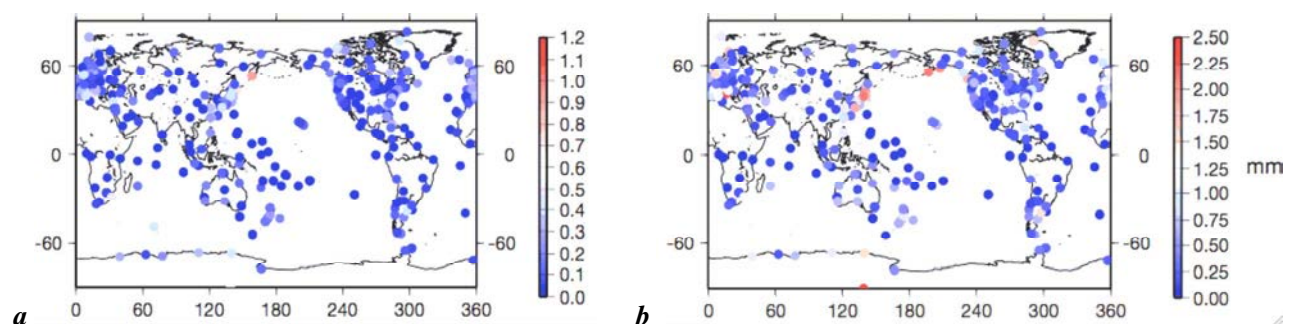


Figure 23: RMS (a) and maximum (b) of the difference between the 'exact' time series (see text) and time series estimated by extracting data using the bicubic interpolation method for the radial component. Source: VAN DAM⁵⁴.

4.5 Atmospheric pressure tides

Atmospheric pressure tides are an issue because some analysis groups disregard them (e.g. SBL), while others do not (e.g. APLO). A comparison of the S_2 atmospheric pressure tide, at a number of barometric sites, with estimates of the tides derived from the ECMWF and NCEPR global analyses, revealed significant inadequacies in the representation of the S_2 tide in both global pressure analyses, when compared to meteorological station data. Similar detailed comparisons for the S_1 tide are missing, but significant discrepancies between theoretical and observed estimates have been noted (e.g. BRASWELL AND LINDZEN, 1998; RAY, 1998). For this reason, PONTE AND RAY (2002) developed a superior model for the S_1 and S_2 atmospheric pressure tides. Maximum amplitudes of the difference between the radial surface displacement, predicted from the NCEP reanalysis and PONTE AND RAY (2002) S_1 tides, are less than 1 mm over the entire Earth. On the other hand, the differences for the S_2 tide can be as large as 2 mm between 30°N and 30°S latitude. However, if a user is only interested in 24-hour averages, the atmospheric pressure tide correction does not need to be concerned: averaging the 1 cycle per day and 2 cycles per day effect over 24 hours removed the signal almost entirely. Presently, R. RAY and T. VAN DAM are preparing IERS recommendations for the handling of atmospheric pressure tides.

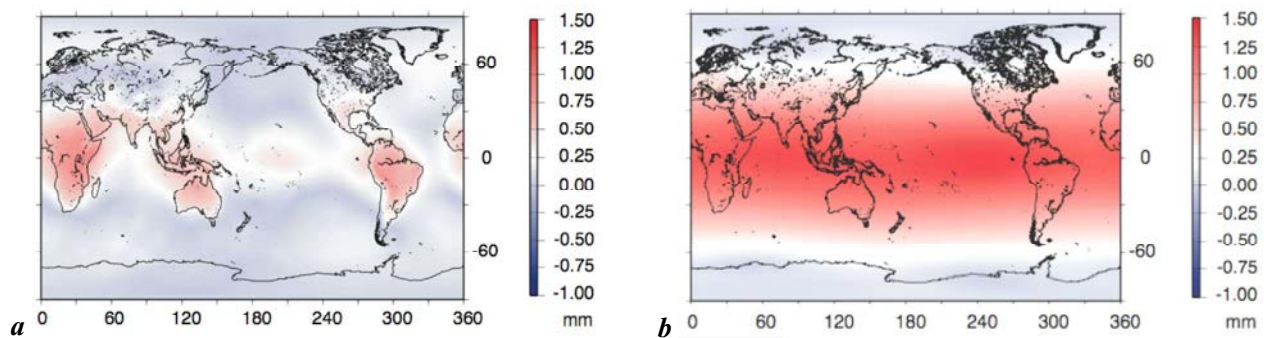


Figure 24: Radial displacements caused by the loading of the diurnal S_1 (a) and semi-diurnal S_2 (b) variations in the atmospheric pressure (non-inverted barometer NIB assumption over the oceans). N.B.: Even if (a) looks like an IB assumption, it is not. Applying IB to the oceans at these frequencies is physically wrong. Source: VAN DAM.

4.6 Land-ocean mask (coastline)

In this section, the application of different land-ocean masks on load-induced station displacements will be investigated. The RMS of the radial difference between APLO and TVD, for a spatial grid of 2.5° by 2.5° during the year 2004, is, on average, 0.39 mm. An acceptable relative difference between APLO and TVD would be around 5% (personal communication PETROV, 2005). However, its computation for the year 2004 reached 17%, using equation (4.6.1):

$$\sqrt{\frac{\sum_{i=1}^n (\text{APLO}_i - \text{TVD}_i)^2}{\sum_{i=1}^n (\text{APLO}_i)^2}} = 0.17 \quad (4.6.1)$$

High RMS values and maximum differences (for the period 1992-2004) were observed for stations around the Baltic Sea (see Figure 26 for station VIS0), the Black, the Caspian and Kara Seas, the Persian Gulf, and for stations near the coast (e.g. station LPGS in La Plata, Argentina, see Figure 27b). The differences between APLO and TVD at these sites can be explained by the differences in the land-ocean mask used in the calculation of the deformations. TVD, the SBL and APLO use a 15' land-ocean mask. We note from Table 7 that the mask used by TVD and the SBL is generated from ETOPO5, which is a 5' topographic grid, while the APLO mask is derived from FES99 (LEFEVRE *et al.*, 2002). Both TVD/SBL and APLO apply a

modified inverted barometer correction to adjust for the pressure load over the oceans. However, APLO does not apply the IB correction to enclosed or semi-enclosed seas such as the Black Sea and the Baltic Sea (PETROV AND BOY, 2004). The differences between the land-ocean mask used by TVD and APLO respectively is shown in Figure 25. The positive values, red points, are locations where the TVD mask indicates that there is land while the APLO mask indicates there is water; the negative indicate the opposite. There are some discrepancies along the coasts, but the most striking differences are the blue patches in the Baltic, the Black, the Red, the Kara and the Caspian Seas, and the Persian Gulf. For enclosed or nearly enclosed bays, PETROV AND BOY (2004) assume a non-inverted barometer response to the pressure loading. The actual response of semi-enclosed bays to pressure loading is probably dependent on the frequency of the pressure forcing and has not been verified yet (MATHERS AND WOODWORTH, 2001). Geodetic sites near enclosed bays are subjected to this major difference between the APLO and TVD land-ocean masks.

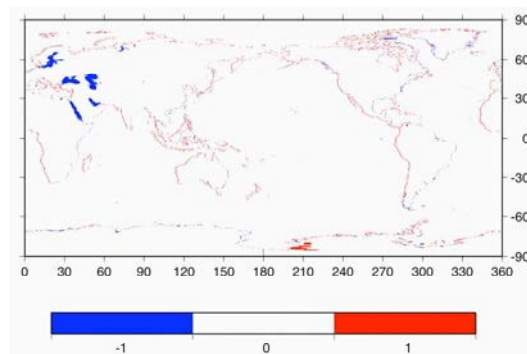


Figure 25: Differences between the land-ocean mask used by TVD and APLO. Red patches are locations where the TVD mask indicates that there is land and the APLO mask indicates there is water. Blue patches indicate the opposite. Source: VAN DAM.

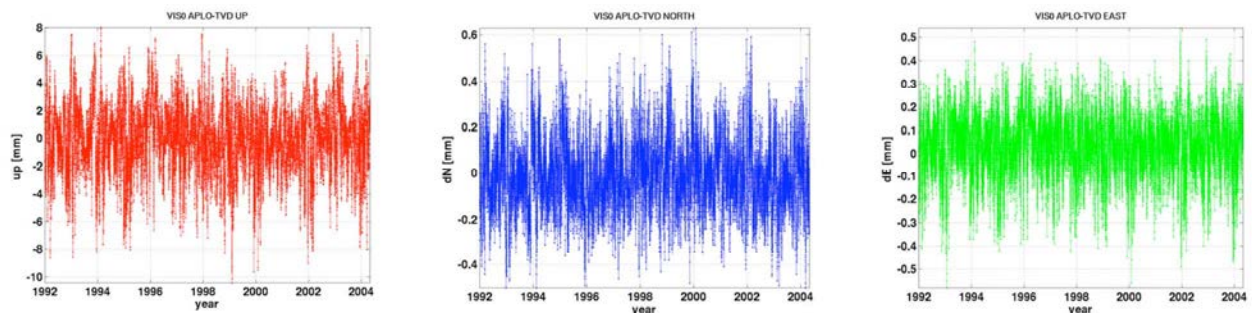


Figure 26: Differences (APLO-TVD) in radial (left), latitudinal (middle) and longitudinal displacement (right) at station VIS0 situated in the Baltic Sea.

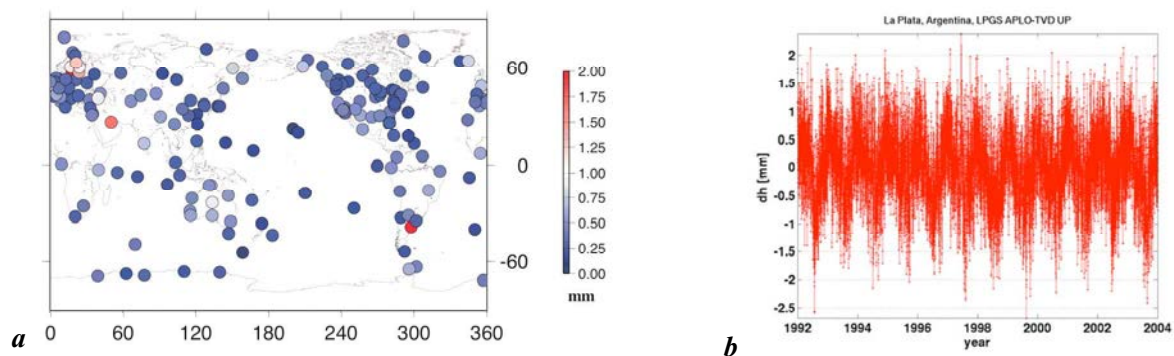


Figure 27: Observed regional variability of RMS (APLO-TVD) for the radial component (year 2004, source: VAN DAM⁵⁴) (a), and difference of APLO-TVD over the years 1992-2004 for the station LPGS, La Plata, Argentina (b).

The differences over Antarctica have been proven to originate from an error in the land-ocean mask of TVD, which is derived assuming that negative topography represents ocean.

4.7 Green's functions

Another difference between the APLO computations and those of TVD and SBL are the Green's functions used in the calculations of the deformations. From Table 7, we see that TVD uses Green's functions for a Gutenberg-Bullen (GB) Earth model while APLO uses Green's functions determined from the PREM. Figure 28a plots the actual horizontal and radial Green's functions for GB and PREM. However, when using the different Green's functions and keeping the same input data, the same approximation algorithm etc., the difference in the displacements due to the choice of a specific Earth model is at the sub-mm RMS level (see Figure 28b, c, d).

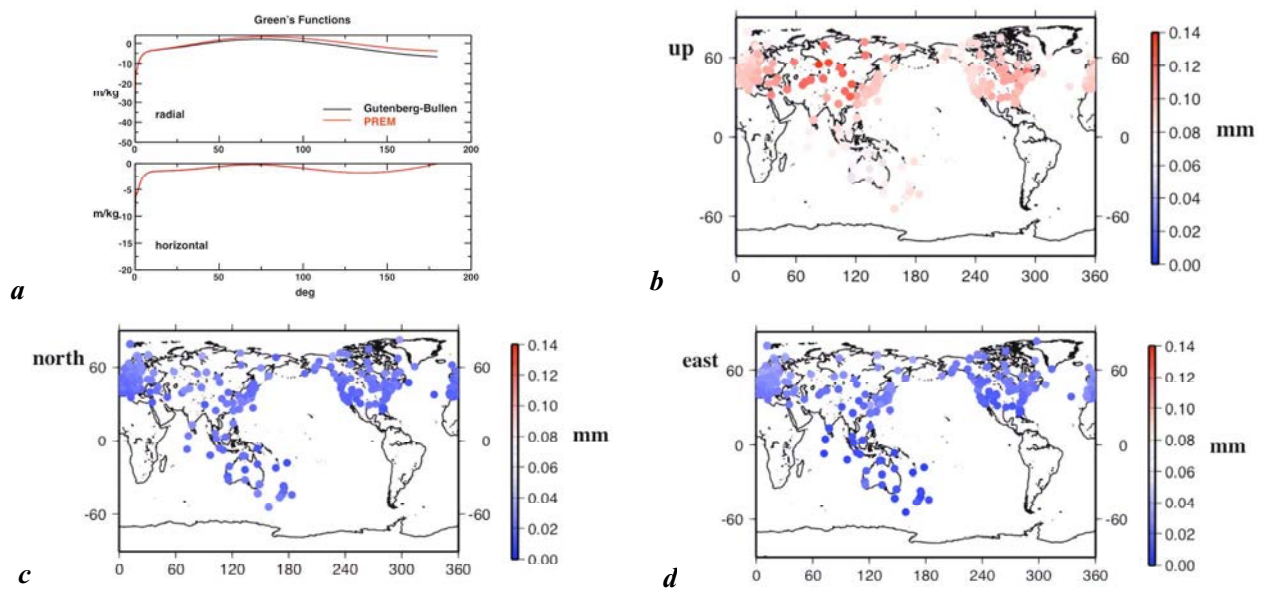


Figure 28: Influence (RMS) of the Earth model (GB-A or PREM) on the Green's functions and on the induced displacements. Source: VAN DAM⁵⁴.

In May 2005, TVD's and APLO's Green's functions were compared in two different reference frames, namely in the centre mass of the solid Earth frame (CE) and in the centre of mass of the solid Earth plus atmosphere frame (CM). Whereupon, TVD discovered a bug in APLO's Green's functions when given in the CM frame. The logic for identifying the bug will be explored in greater detail. First of all, the only noticeable difference between the Green's functions calculated in the CE and CM frame resides in the degree-1 Load Love Numbers (e.g. BLEWITT, 2003). Following FARRELL (1972), the displacement u in function of the angular separation distance θ , for a unity mass element, reads:

$$u[\theta]_{CE} = \frac{a}{M_E} \sum_{n=0}^{\infty} P_n h_n'^{CE} \quad (4.7.1)$$

$$u[\theta]_{CM} = \frac{a}{M_E} \sum_{n=0}^{\infty} P_n h_n'^{CM}$$

where $h_n'^{CM}$ and $h_n'^{CE}$ indicate the Load Love Numbers in the CM and CE frame, respectively, and where a is Earth's mean radius and M_E is Earth's mass. Rearranging equations (4.7.1), it follows that:

$$u[\theta]_{CM} = \frac{a}{M_E} \left[P_0 h_0' + P_1 h_1'^{CM} + \sum_{n=2}^{\infty} P_n h_n' \right]$$

$$= \frac{a}{M_E} \left[P_0 h_0' + P_1 h_1'^{CM} + \sum_{n=2}^{\infty} P_n h_n' + (P_1 h_1'^{CE} - P_1 h_1'^{CE}) \right] \quad (4.7.2)$$

Thus, we obtain:

$$u[\theta]_{CM} = \frac{a}{M_E} \left[P_0 h_0' + P_1 h_1'^{CE} + \sum_{n=2}^{\infty} P_n h_n' \right] + \frac{a}{M_E} P_1 (h_1'^{CM} - h_1'^{CE})$$

where the term in bracket equals $u[\theta]_{CE}$, which is given in the first equation of (4.7.1), so that:

$$u[\theta]_{CM} = u[\theta]_{CE} + \frac{a}{M_E} P_1 (h_1'^{CM} - h_1'^{CE}) \quad (4.7.3)$$

For PREM, $h_1'^{CM} = -1.29$ and for the Gutenberg-Bullen A Earth model $h_1'^{CM} = -1.288$ (e.g. BLEWITT, 2003), i.e. the differences between Earth models for the degree-1 Load Love Numbers are really small (0.16%). We should regard the transformation of CE to CM frame as nothing but a shift of centre of mass of the solid Earth to the centre of mass of the solid Earth plus load. As a result, $h_1'^{CE} - h_1'^{CM} = 1$ is exact. In other words, it does not depend at all on the chosen elastic model of the Earth (personal communication BOS M., 2006). The numerical precision of the theoretical calculations of the degree-one LLNs $h_1'^{CM}$ and $h_1'^{CE}$ have been estimated to be approximately 0.002 (personal communication by VARGA, 2006). Substituting these values into equation (4.7.3), we obtain:

$$u[\theta]_{CM} = u[\theta]_{CE} - \frac{a}{M_E} \cos \theta \quad (4.7.4)$$

This means that, when using the Green's functions in the CE frame, one can easily generate the CM Green's functions without summing over the Load Love Numbers again. However, since the difference between $h_1'^{CM}$ and $h_1'^{CE}$ is exactly 1 by definition, and completely independent on any Earth model, BOS AND BAKER (2005) explain that this equation should not be used. BOS AND BAKER (2005) use a program called CARGA (meaning "load" in Portuguese), whose results, i.e. displacements due to loading, are in complete agreement (sub-mm) with APLO most of the time, especially when using the same coastline. The program CARGA is not particularly better than the other programs, only more flexible (personal communication by BOS, 2006).

Nevertheless, when using equation (4.7.4), taking the CE Green's functions from the APLO website, TVD obtained Green's functions that were similar to the ones computed without making use of the CE frame Load Love Numbers. However, these Green's functions in the CM frame are significantly different from those reported on APLO's webpage¹⁰.

The erroneous CM Green's functions of APLO introduced significant differences, in the order of 6 mm, for the loading. However, in the CE reference frame, both APLO and TVD results were extremely consistent. This bug was rectified at APLO on June 22nd 2005. The new displacement solution revealed significant differences from the old solution. Figure 29 shows a plot of the differences (new solution minus old solution) for radial displacements on January 9th 2004, in the CM frame, with atmospheric tides removed. Maximum deviations appear in the order of 6 mm. Reprocessing of more than 20 years of VLBI data could not uncover this error. The reason is that the differences are mainly translational, and VLBI is insensitive to translations. The two pressure loading series produced the same fit.

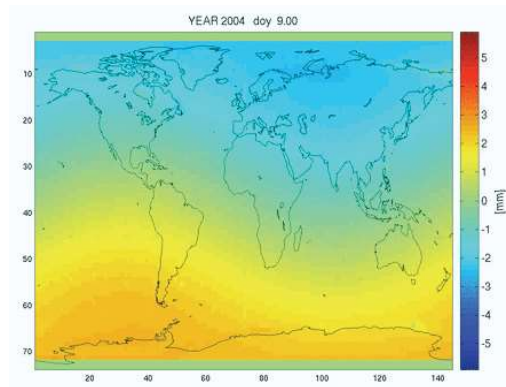


Figure 29: Difference of radial displacement between the erroneous and corrected CM Green's functions (after June 22nd 2005) at the APLO service on day of year (doy) 9.00 of the year 2004. N.B.: previous APLO versions did not include displacements for the polar regions!

4.8 Spherical harmonics vs. global convolution

As previously mentioned, there are two principal ways of computing the surface displacements from surface loading:

- the global convolution sum, using Green's functions (FARRELL, 1972)
- the spherical harmonics with their respective Load Love Numbers.

For long wavelengths, loading effects on a global Earth produce similar results for both approaches. However, the computation speed is largely directed to the convolution approach. There are time series of atmospheric pressure loading available at the SBL website, which are computed by PG. These time series have been computed using the spherical harmonic approach. PG makes products available through the SBL for both the NCEP reanalysis data set and the ECMWF operational data set. The products are both in the CE and CM reference frames. Thus, by comparing TVD's predictions with PG's NCEP results in the CE frame, the differences introduced into a time series by using either the convolution sum or the spherical harmonic method may be estimated. One negligible difference can be noted from Table 7: TVD and PG use different Earth models for the calculation of the load effects. However, as previously demonstrated, this is a very small effect. The radial pressure effects using the convolution sum approach versus the spherical harmonic approach are shown in Figure 30: The average RMS of the differences is about 0.4 mm with a maximum RMS reaching 1 mm. The RMS of the difference is, in general, larger for coastal and island stations. Discerning the coastline to the 0.25-degree spacing used in TVD would require degree 720 in the spherical harmonic expansion of the pressure field. The maximum single epoch difference can reach 4 mm, whereas the mode is about 1 mm.

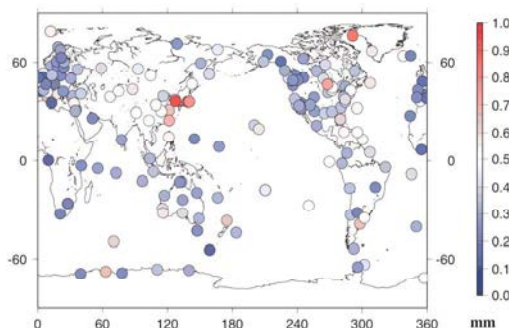


Figure 30: RMS of the differences of radial displacement due to pressure effects when using the convolution sum versus the spherical harmonic approach. Source: VAN DAM.

One more point to mention is the approximation of the computation of the convolution integral. APLO uses an integration technique (PETROV AND BOY, 2004), which, however, keeps the error of approximation below 1%.

4.9 Lateral components

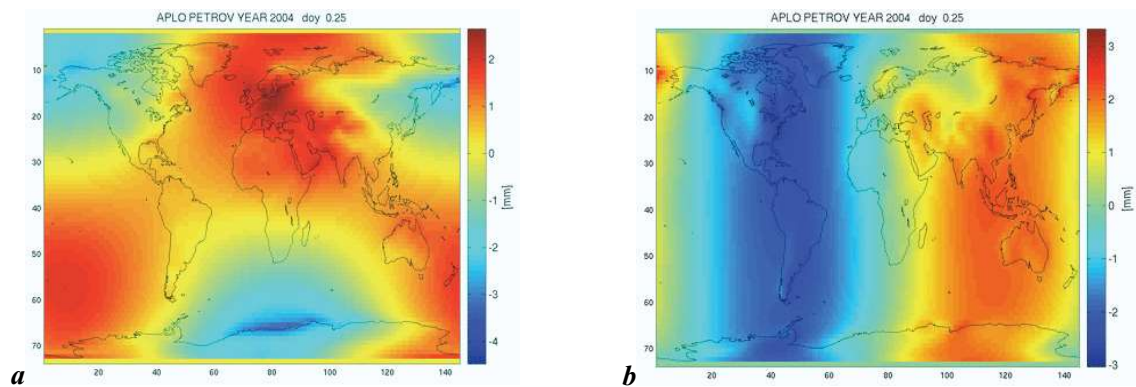


Figure 31: North (a) and east (b) deformation due to atmospheric pressure loading for January 1st, 6 UT of the year 2004 (APLO in CE frame, atmospheric tides removed).

Horizontal displacements due to tide loading (e.g. ocean tide loading in SCHERNECK AND HAAS, 1999) have an influence on polar motion and UT1, in a virtual case that a small number of sites have a common rigid mode (motion). In this context, the pattern of eastern component displacements due to atmospheric loading (tides excluded in APLO) (see Figure 31b) reveals striking longitudinal gradients. Two major factors may explain this feature:

- motion of air masses, which is more longitudinal than latitudinal
- stretching of continental lines in latitudinal direction (Atlantic and Pacific)

Nevertheless, the computed pattern of lateral displacements due to atmospheric pressure loading is quite intriguing. This should be a topic for future research.

Chapter 5

Global coordinate time series analysis

In this chapter, two Very Long Baseline Interferometry (VLBI) and ten weekly Global Positioning System (GPS) coordinate time series solutions will be investigated. Three GPS solutions are combined solutions, including the IGS final solution. Additionally, one GPS daily solution stems from the Scripps Orbit and Permanent Array Centre (SOPAC), as described by NIKOLAIDIS (2002). One major topic of this chapter is the handling of constraints imposed on the GPS solutions by several Analysis Centres (ACs), as well as coordinate transformations to a common frame for comparison purposes. For baselines longer than 5000 km, the precision of the GPS technique is superior to the VLBI technique from the point of view of baseline length repeatability. The improvement on VLBI baseline length repeatability, after applying the atmospheric pressure loading time series provided by the Goddard Space Flight Centre (GSFC) VLBI group, reaches 3.3% (median value). Furthermore, for the GPS technique, seasonal signals in the height component with amplitudes of up to 9 mm for a few sites on the Asian continent were recovered (see Appendix C).

5.1 Background

Space geodetic techniques observe electromagnetic waves propagating from quasars or from satellites. The observation equations are differential, defining a family of solutions. To obtain one solution, boundary conditions are applied. Different Analysis Centres (ACs) use different boundary conditions, which is one of the reasons why their solutions are not identical. Both techniques apply a multitude of corrections to the raw observables for effects such as tropospheric refraction, pole tide, solid Earth tides, or ocean tide loading. The effects of atmospheric pressure (VAN DAM *et al.*, 1994) and hydrological loading on station positions have been investigated for several years. DONG *et al.* (2002) discuss seasonal signals in GPS position time series, whereas PETROV AND MA (2003) analyze harmonic VLBI site variations. PENNA AND STEWART (2003) show that mismodelled diurnal or semi-diurnal tidally induced station height variations can map into annual or semi-annual terms. In the most recent study on atmospheric pressure loading, PETROV AND BOY (2004) propose a new model, already described in Chapter 4, for routine processing of space geodetic observations.

The motivation of this chapter is twofold, namely:

- to show the cutting-edge limits of space geodetic solutions, on which geophysical interpretations are based
- to derive 3D geometric deformations, i.e. annual and semi-annual variations of coordinate time series, which is a potential requirement for the next chapter, if of sufficiently high quality.

5.1.1 Global reference frames and geocentre motion

Transformations between reference frames are primordial in geodetic analysis. Accurate estimates of geophysical parameters (site velocities, seasonal signals or geocentre motion) highly depend upon which methodology (to derive these parameters) is used.

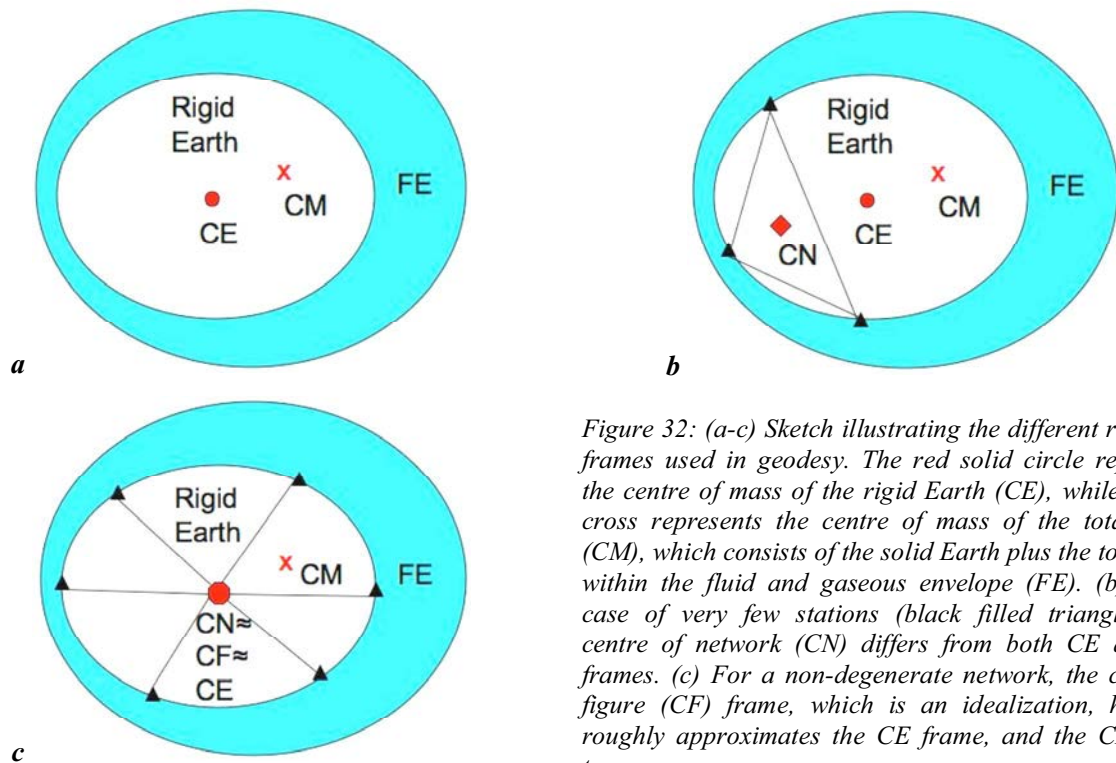


Figure 32: (a-c) Sketch illustrating the different reference frames used in geodesy. The red solid circle represents the centre of mass of the rigid Earth (CE), while the red cross represents the centre of mass of the total Earth (CM), which consists of the solid Earth plus the total mass within the fluid and gaseous envelope (FE). (b) In the case of very few stations (black filled triangles), the centre of network (CN) differs from both CE and CM frames. (c) For a non-degenerate network, the centre of figure (CF) frame, which is an idealization, however, roughly approximates the CE frame, and the CN frame too.

In general, the CE frame does not coincide with the CM frame (see Figure 32a) (VIGUE *et al.*, 1992). Both frames are related by a translation, usually called “geocentre motion”, arising due to a spatially and temporally varying fluid and gaseous envelope (FE) (TREGONING AND VAN DAM, 2005a). On the one hand, satellites revolve around the centre of mass of the total Earth (the Stokes coefficients of degree-1 are set to zero in the satellite orbits parameterization). On the other hand, the a priori coordinates of the tracking sites are defined in the International Terrestrial Reference Frame (ITRF). In the long-term, the ITRF can be considered as a CM frame, but in the short-term it is assumed to be close to an idealized CF frame (DONG *et al.*, 1997, 2003), when it is, in fact, always only a centre of network (CN) frame.

Presently, two methods are commonly used for estimating the geocentre motion:

- the network shift approach
- degree-1 deformation approach.

On the one hand, the “network shift approach” (BLEWITT *et al.*, 1992; DONG *et al.*, 2003) consists in estimating seven (or better, six, excluding the scale) Helmert transformation parameters (three translations, three rotations and additionally one scale), where the translations are direct estimates of the geocentre motion. The estimation of these parameters from a “fiducial-free” network towards an externally derived frame, e.g. the ITRF2000 or IGB00 (see the horizontal velocity field in Figure 33 for the GPS sites) is somehow questionable and contradictory. When using the ITRF2000 a priori coordinates and imposing a no-net-translation (NNT) condition on the station coordinates to the observation equations, a “fiducial-free” network is achieved. Thus, in this case, when using the network shift approach, the geocentre motion will be zero. However, the common approach of space-geodetic observations is to compute a fiducial-free network, using pseudo-observations, i.e. loosely constrained coordinates of the tracking stations. It is the use of loosely constrained pseudo-observations (coordinates), usually in the ITRF2000, that enables retrieval of the non-zero geocentre motion determined by the network shift approach, although the Stokes coefficients of the satellite orbits have been set to zero.

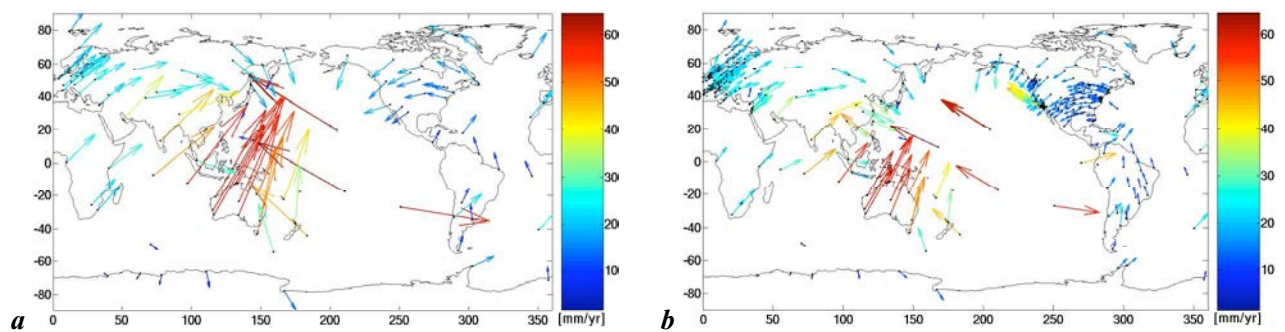


Figure 33: Horizontal station velocities of (a) the IGS specific reference frame Igb00 and (b) ITRF2000 for GPS only. N.B.: Note that colours represent the scale of the arrows in both figures!

On the other hand, the degree-1 deformation approach (BLEWITT *et al.*, 2001; DONG *et al.*, 2003) estimates the transformation parameters between reference frames and the so-called load moment simultaneously, rather than sequentially. In the case of a two-step procedure, any errors introduced by the transformation process into the terrestrial reference frame will affect the accuracy of the geocentre motion (TREGONING AND VAN DAM, 2005a). Moreover, differences in modelling a degree-1 load will directly propagate into the estimates of the geocentre. The degree-1 deformation can only be determined from satellite techniques, if and only if, one assumes that the position of the geocentre is fixed. On the mm level accuracy, one cannot assume the position of the geocentre to be known, and at the same time be willing to estimate it. This means that a degree-1 load cannot be observed like, e.g. a permanent tide. Its modelling is a question of agreement and convention.

5.1.2 Coordinates vs. Baselines

Coordinates themselves do not have a physical meaning, and such an interpretation is erroneous, as soon as we seek for the sub-cm accuracy. Physical meaningful problems are reference frame invariant. This is the reason why VLBI derived station coordinates should be carefully interpreted for comparison versus GPS due to the emphasized reference frame problematic. For small networks (only approximately five stations participate in each VLBI session), the VLBI derived station coordinates procedure is not adequate. These time series are biased to some degree. Nevertheless, the site repeatability gives a useful indication of the distribution and quality of the data. There is a coordinate scatter due to both errors in site position determination and non-uniformity of boundary conditions. The observed scatter of station A contributes to the scatter at this station, plus non-negligible contribution of errors at station B, C, D etc. Another consideration is that time series of site positions are not the goal in geodynamical studies, but only intermediate tools for further analysis. As demonstrated by PETROV AND BOY (2004), atmospheric loading effects on site positions cannot directly be seen in VLBI time series. The GPS space geodetic technique suffers from the same reference frame problem at a lower level, given the large number of contributing stations. However, it is faulty to think that atmospheric loading corrections can simply be applied to the GPS time series on the result level (TREGONING AND VAN DAM, 2005b) when aiming at the mm precision.

The fundamental geodetic measurements are time delays, which translate into baselines between sites forming an observing network relative to the frame of extragalactic sources or satellites. From these measurements, geophysical assumptions, and mathematical conditions, it is possible to obtain usable information about individual sites in a terrestrial reference frame (TRF). Derived quantities include positions at reference epoch, velocities, and time series of topocentric position. The latter is most useful for understanding the details of the measurements while the velocities are most useful for geophysical modelling.

Epoch positions are derived from the geodetic data in a least squares estimation process. Relative positions are converted to individual site positions by minimizing the differences in position (for a selected set of sites) with respect to ITRF2000 or some technique-related frame, e.g. Igb00. For each day, the relative

positions of the sites of that network are estimated. The a priori frame is the TRF positions projected to the date of interest by TRF velocities and oriented by the a priori Earth Orientation Parameters (EOPs) values. The relative positions are attached to the instantaneous a priori frame by minimizing the Cartesian differences between the estimated positions and the a priori positions for all the sites of the network on that day. This condition is described as no-net-translation (NNT). Usually, a no-net-rotation (NNR) condition is necessary too. The Cartesian coordinates are also converted to topocentric residuals with respect to the a priori positions of date with corresponding topocentric formal errors. In general, the vertical error is larger than the horizontal errors, especially due to the half space of visibility and state of the atmosphere. The results for a given station are accumulated as a time series. These time series are displayed as site repeatability plots. The scatter as indicated by the standard deviation of unity weight, however, is usually statistically too large and indicates that the error budget is incomplete. The actual level of scatter is a function of both the quality of data from a site and the overall quality of the networks in which the site participated. The number of sites in a single VLBI session is small, on average less than five for the entire data set. An underlying assumption of this type of analysis is that the sites are moving uniformly and that wild outliers are inexistent. If a station does not move uniformly, then the NNT condition causes the positions of the other sites to be displaced. The time series of these sites will show false systematic effects caused by the wandering site. Such a wandering site should be excluded from the NNT condition, a feature that is not routinely yet implemented. Likewise, if a site's position is exceptionally discrepant on a particular day, then the time series of the other sites in that network will also show an outlier. Anomalously noisy sites should also be excluded from the NNT condition, e.g. station TIGO in Concepción, Chile, for the VLBI technique.

5.1.3 SINEX

SINEX⁵⁷ stands for Solution INdependent EXchange format. BLEWITT *et al.* (1994) developed this format⁵⁸ to facilitate the task of combining several GPS solutions. However, subsequently, this format evolved towards a common solution for other space geodesy techniques, VLBI and Satellite Laser Ranging (SLR). Later, attempts were made to overcome the flaws of the original design. This process of evolution is not yet completed. Therefore, different software systems implement slightly different variants of the SINEX format.

Each SINEX file should have the matrix of constraints and their reciprocal weights instead of vague flags "strong" or "weak" constraints. The block SOLUTION/MATRIX_A PRIORI is an inverse of the weight matrix. But the weight matrix can be singular, and therefore, the inverse does not exist. There cannot be an a priori covariance matrix if one applies singular constraints, e.g. no-net-rotation (NNR). The solution to this problem is to put the weight matrix and the column vectors of a priori coordinates and of constraints in the SINEX file. The purpose of SINEX should provide sufficient information on how the solution has been calculated.

5.2 VLBI analysis

5.2.1 OCCAM VLBI software

Presently, the latest release of the VLBI data analysis software OCCAM version 6.0 relies on a broad international cooperation. The new version of OCCAM provides all the features that are necessary to analyze VLBI data with the highest level of accuracy. Within the International VLBI Service (IVS) this software is used by several Analysis Centres and applied by three operational Analysis Centres.

⁵⁷ http://alpha.fesg.tu-muenchen.de/iers/sinex/sinex_v2_appendix1.pdf

⁵⁸ <http://www.dgfi.badw-muenchen.de/gps/sinex.html>

The author of OCCAM (initially called BVSS) is JAMES CAMPBELL (Geodetic Institute of the University of Bonn, Germany), who designed the software for analyzing geodetic VLBI data. Initially, the accuracy of the geodetic results reached several decimetres (CAMPBELL, 1979). Since 1993, OLEG TITOV (Australian Surveying and Land Information Group, Australia) has been the leader of the OCCAM user community. He was the driving force in developing OCCAM by incorporating the regularly updated IERS Conventions. A few years ago, VOLKER TESMER (Deutsches Geodaetisches Forschungsinstitut DGFI, Germany) and JOHANNES BOEHM (Institute of Geodesy and Geophysics IGG, Vienna University of Technology, Austria) joined their efforts to contribute to various parts of the new version 6.0 of OCCAM, e.g. by adding and improving the least-squares parameter estimation. Since March 2006, IGG has been putting auxiliary files (e.g. ephemerides, EOPs, Vienna Mapping Functions, Terrestrial and Celestial Reference Frames etc.) that are needed by OCCAM, on their webpage⁵⁹. Finally, OCCAM is rather flexible in the sense that it can easily incorporate upcoming improved astronomical and geodynamical models according to the new IERS Conventions.

5.2.2 IGG coordinate time series solutions

With regard to VLBI analysis, we calculated two long-term solutions with VLBI sessions covering more than 20 years. An observation model with conditions between the parameters, as implemented in the OCCAM 6.0 software (TITOV *et al.*, 2001), was used. From November 1981 till June 2004 more than 3800 24-hours X/S-band sessions were observed including 155 stations. Twenty percent of the sessions were discarded for our experiments, e.g., single-baseline sessions, sessions with small (national) networks, and sessions that provided major problems in the analysis. The total number of retained sessions was 3045, containing 50 stations (see Figure 34) that showed small residuals and had stable a priori coordinates (ITRF2000). Our two VLBI solutions differed by one feature: in the first result, we applied atmospheric loading corrections but in the second one, we did not. Source coordinates were fixed to the International Celestial Reference Frame (ICRF ext.1). Station coordinates were estimated within free networks with six no-net-rotation (NNR) and no-net-translation (NNT) conditions, imposed on station coordinates, to work out the singularity of the normal equations. Corrections to the Earth Rotation Parameters (ERP) were estimated for each session. The wet zenith delays were estimated as 1-hour piecewise linear functions using the Vienna Mapping Functions (BOEHM AND SCHUH, 2004). One offset and four six-hour rates, for the north and east components, were estimated per station and session to account for atmospheric gradients.

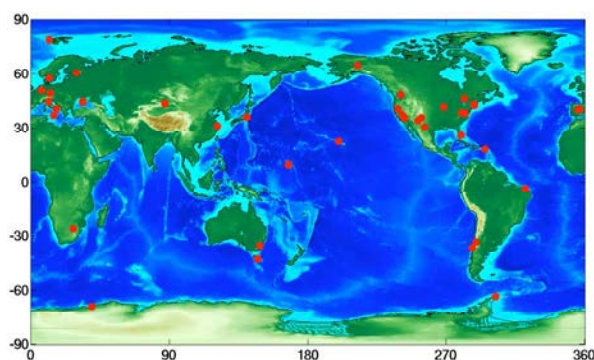


Figure 34: Distribution of 50 chosen VLBI stations.

5.2.3 Baselines

Subsequently, we determined repeatabilities for those baseline lengths that were observed in more than 10 sessions in the period 2000.5-2004.5. First, we determined breaks in the baseline length time series.

⁵⁹ <http://mars.hg.tuwien.ac.at/~vlbi/>

Therefore, we first applied an order 15 one-dimensional median filter (PRATT, 1978) to the baseline length time series. This filter reduced the noise, removed gross outliers and preserved sudden jumps, which would have been detected with the subsequent algorithm. Then, we performed a single-level one-dimensional discrete Haar wavelet decomposition (one approximation and one detail). Sudden changes in the first differenced approximation and first details of the Haar decomposition were indicated by large values of the wavelet coefficients. Breaks or jumps were flagged (see Figure 52a) for coefficients larger than 80% of the maximum value, and for differences in the median filtered data larger than 5 mm. Finally, we constructed a regressor with linear pieces between the flagged jumps. The trends of the coordinate time series were derived from these linear pieces by a weighted robust fit.

These linear pieces were removed from the original baseline lengths, resulting in cleaned baseline lengths b^{clean} , for which statistics (repeatabilities) were computed versus a robust weighted linear fit. The definition of the repeatability is given by r :

$$r = \sqrt{\frac{v^T P v}{n-2}} \quad v = b^{clean} - (kt + d) \quad (5.2.1)$$

We used an iteratively reweighted least-squares algorithm (to determine the parameters k and d , t denoting time), with the weights P at each iteration calculated by applying the bisquare function w to the residuals q from the previous iteration (HOLLAND, 1977):

$$w = (|p| < 1) \cdot (1 - p^2)^2 \quad p = \frac{q}{4.685 \cdot s \cdot \sqrt{1-h}} \quad (5.2.2)$$

The vector h represents the leverage values from the least squares fit, and s is an estimate of the standard deviation of the error term, involving the median absolute deviation of the residuals from their median.

In equation (5.2.1), n denotes the number of observations. This algorithm places less importance to points that do not fit well, i.e. outliers. Figure 35a shows the number of baselines within a certain baseline length, while Figure 35b emphasizes that very few observations (less than 100) are available for a huge number of baselines.

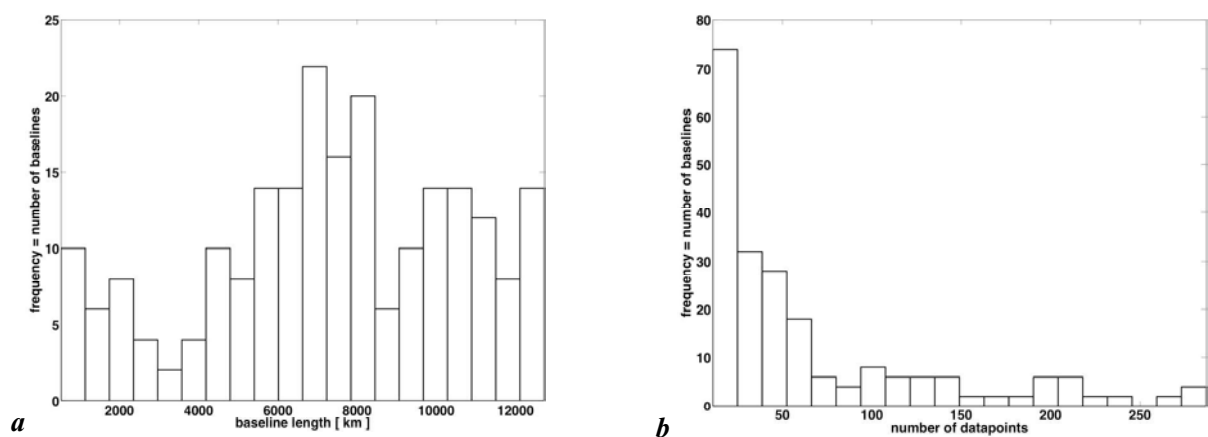


Figure 35: Histogram showing the number of baselines in function of the (a) length and (b) number of datapoints (observations).

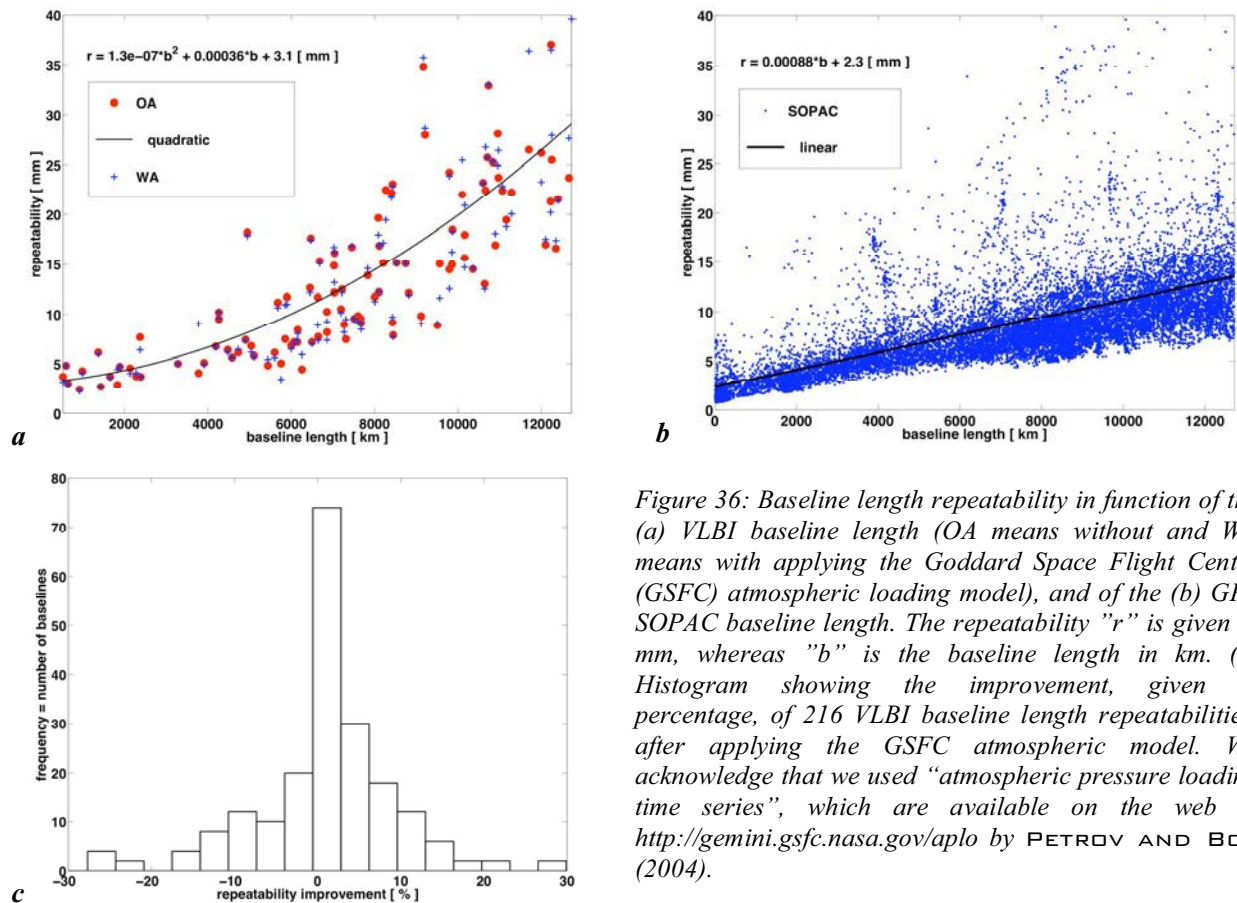


Figure 36: Baseline length repeatability in function of the (a) VLBI baseline length (OA means without and WA means with applying the Goddard Space Flight Centre (GSFC) atmospheric loading model), and of the (b) GPS SOPAC baseline length. The repeatability "r" is given in mm, whereas "b" is the baseline length in km. (c) Histogram showing the improvement, given in percentage, of 216 VLBI baseline length repeatabilities, after applying the GSFC atmospheric model. We acknowledge that we used "atmospheric pressure loading time series", which are available on the web at <http://gemini.gsfc.nasa.gov/aplo> by PETROV AND BOY (2004).

On the one hand, the repeatability [mm] of the resulting 216 VLBI baselines versus baseline length [km] shows a quadratic pattern (see Figure 36a). This feature can be explained by a simple geometrical deduction: At large distances, the sky zone, which can be seen from two telescopes, is continuously reduced. This considerably diminishes the amount of possible common observations. A modest but significant improvement (at a confidence level of 99 %) of the VLBI baseline length repeatability is achieved, after applying the GSFC atmospheric loading model. The median improvement is 1.2 % (see Figure 36c). However, this improvement increases to 3.3 %, when 23 baselines with at least 100 observations instead of 10 are used (MENDES CERVEIRA *et al.*, 2006a). On the other hand, we also calculated baseline length repeatabilities for the GPS technique. Only those baseline lengths of the Scripps Institution of Oceanography solutions were retained that provided more than 10 observations over the period 2000.5-2004.5. The same algorithm for jump search, as for VLBI, was applied. The GPS SOPAC results yield more than 17000 baseline lengths. The dependence between repeatability and baseline length was strongly linear (see Figure 36b), with about 2.3 [mm] + 1 ppb (parts per billion).

5.2.4 Topocentric coordinate time series and trends

In order to check how well the IGG coordinate time series perform with respect to independent external solutions, we obtained minimally-constrained coordinate time series from the GSFC for the VLBI technique, provided by PETROV, already transformed to the ITRF2000, in the SINEX format. In addition, we used the GPS SOPAC coordinate time series to see how well both space geodetic techniques agree on estimating topocentric trends (see Table 8 to Table 10 for the three sites, Wettzell, Westford and Onsala).

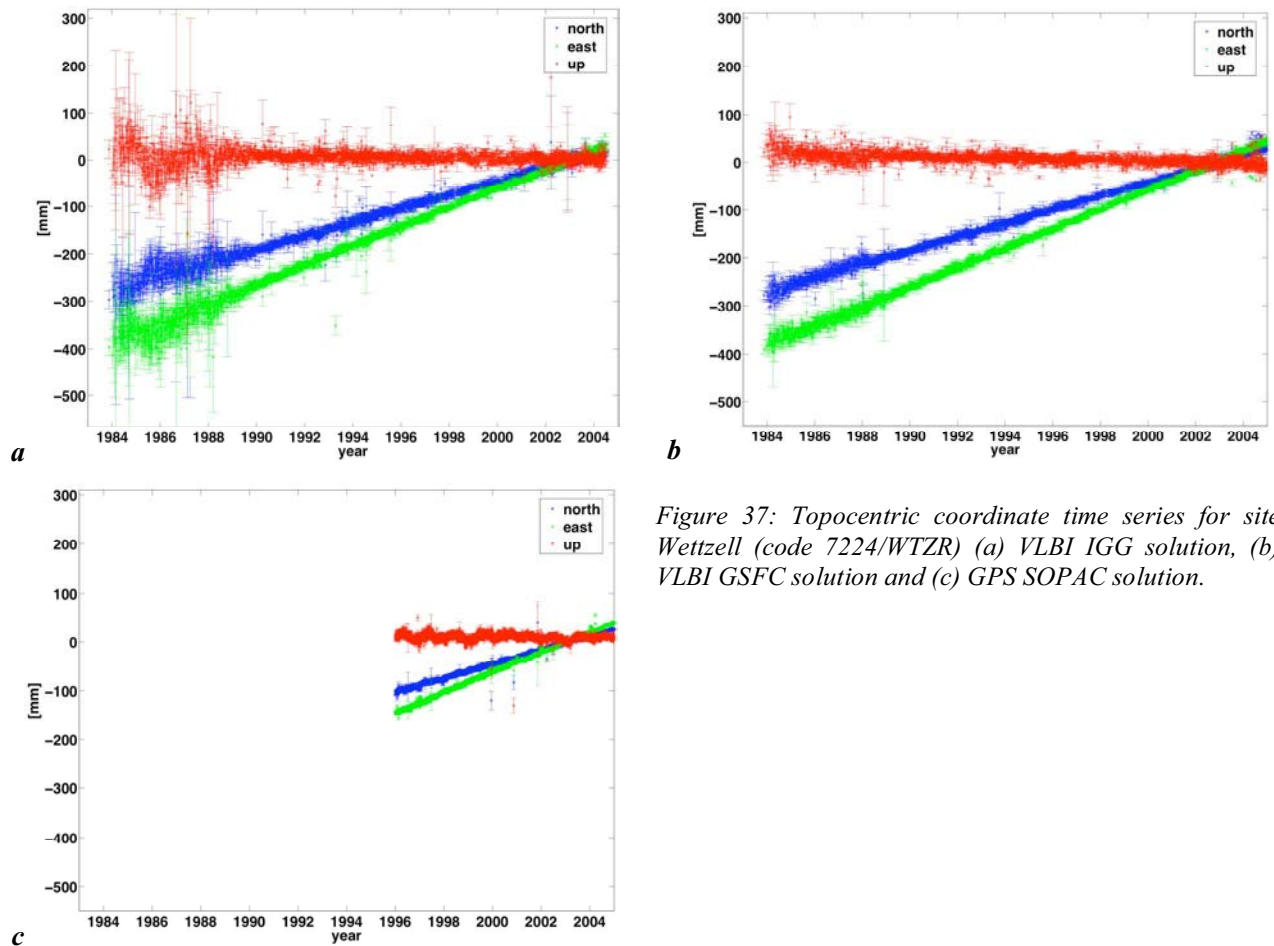


Figure 37: Topocentric coordinate time series for site Wettzell (code 7224/WTZR) (a) VLBI IGG solution, (b) VLBI GSFC solution and (c) GPS SOPAC solution.

Generally, two conclusions can be derived from Figure 37:

- the IGG VLBI solution shows up strong periodic variations from 1984-1989, variations which cannot be perceived on the GSFC solution, but agrees surprisingly well after 1989 with the GSFC solution
- seasonal signals are obviously present in the coordinate time series (being more visible in the GPS SOPAC solution).

Table 8: Trend of topocentric coordinate time series over the years 1996-2004, for the site Wettzell (code 7224/WTZR).

7224/WTZR	IGG OA	IGG WA	GSFC	SOPACI	SOPAC_HP
North [mm/y]	14.30	14.29	14.15	14.51	14.52
sN	0.08	0.08	0.05	0.01	0.11
s0	5.59	5.49	3.80	1.54	1.5
East [mm/y]	19.99	20.00	20.19	20.62	20.44
sE	0.05	0.05	0.05	0.01	0.12
s0	3.77	3.75	3.36	1.86	1.8
Up [mm/y]	-0.49	-0.48	-0.86	-0.52	-0.36
sU	0.14	0.13	0.11	0.04	0.47
s0	9.11	8.50	7.69	5.96	5.2

Table 9: Trend of topocentric coordinate time series over the years 1996-2004, for the site Westford (code 7209/WES2).

7209/WES2	IGG OA	IGG WA	GSFC	SOPAC1	SOPAC_HP
North [mm/y]	4.73	4.72	4.42	4.27	3.62
sN	0.10	0.10	0.09	0.02	0.23
s0	4.28	4.26	3.93	3.20	2.6
East [mm/y]	-14.93	-14.93	-14.86	-16.55	-14.77
sE	0.11	0.11	0.08	0.04	0.26
s0	4.66	4.57	3.89	4.92	3.3
Up [mm/y]	-0.85	-0.82	-0.80	1.04	-1.80
sU	0.21	0.21	0.20	0.05	0.45
s0	8.95	8.80	8.63	7.17	7.8

Table 10: Trend of topocentric coordinate time series over the years 1996-2004, for the site Onsala (code 7213/ONSA).

7213/ONSA	IGG OA	IGG WA	GSFC	SOPAC1	SOPAC_HP
North [mm/y]	14.45	14.47	13.88	13.99	14.05
sN	0.21	0.21	0.13	0.01	0.08
s0	4.83	4.91	3.56	1.43	1.9
East [mm/y]	17.28	17.28	17.27	17.28	17.25
sE	0.14	0.14	0.11	0.01	0.10
s0	3.28	3.27	2.76	1.80	2.2
Up [mm/y]	1.07	0.92	0.71	-0.20	1.61
sU	0.41	0.41	0.35	0.04	0.41
s0	9.41	9.39	9.24	5.46	6.6

From Table 8 to Table 10, sN, sE, and s0 stand for the standard deviation of the trend in the north and east components and for the standard deviation of unity weight, respectively. Huge differences arise in the trends, e.g., in the east component of station WES2, due to small successive jumps in the GPS SOPAC coordinate time series (SOPAC1). A much better agreement is guaranteed between inter-techniques, when using the SOPAC refined model (ΝΙΚΟΛΑΙΔΙΣ, 2002), denoted by SOPAC_HP.

5.3 GPS analysis

5.3.1 Analysis Centres of the IGS

The Analysis Centres (ACs) analyze the IGS station data to form submissions to IGS products such as orbits, clocks, and station positions, while the Global Network Associate Analysis Centres (GNAACs) combine the ACs' submissions to form station positions. Table 11 lists the IGS agencies participating in the release of weekly station positions, which will be studied in detail in this section.

Table 11: Acronyms used for Analysis Centres (ACs) and Global Network Associate Analysis Centres (GNAACs).

Code	Type	Agency Name	City	Location
COD	AC	Centre for Orbit Determination in Europe, CODE	Berne	Switzerland
NRC	AC	Natural Resources Canada, NRCan, formerly EMR	Ottawa, Ontario	Canada
ESA	AC	European Space Operations Centre, ESOC	Darmstadt	Germany
GFZ	AC	GeoForschungsZentrum	Potsdam	Germany
JPL	AC	Jet Propulsion Laboratory	Pasadena, California	USA
SIO	AC	Scripps Institution of Oceanography	San Diego, California	USA
MIT	AC	Massachusetts Institute of Technology	Cambridge, Massachusetts	USA
NGS	AC	National Geodetic Survey	Silver Spring, Maryland	USA
NCL	GNAAC	University of Newcastle-upon-Tyne	Newcastle, England	United Kingdom
mit	GNAAC	Massachusetts Institute of Technology	Cambridge, Massachusetts	USA

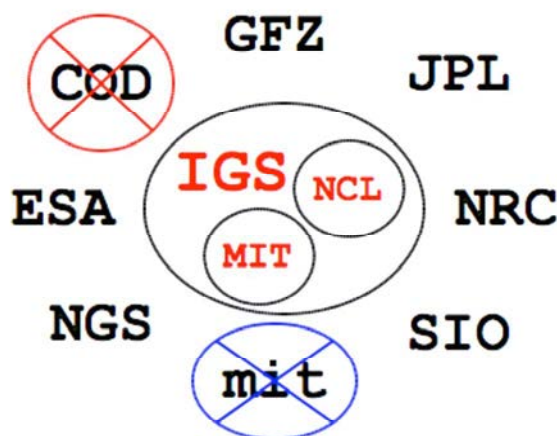


Figure 38: The lowercase solution “mit” has been discarded in the analysis, due to its recent upcoming. The COD solution is questionable due to the error detected in the corrections of the solid Earth tides, in mid-2004. The IGS final solution is a combination of the eight ACs. Presently, the IGS final solution is therefore slightly corrupted by the COD solution, since no reprocessing has been undertaken, yet. NCL and MIT figure as a control for the final IGS solution. Three ACs use a Kalman filtering approach (NRC=EMR, JPL, MIT) to generate the daily coordinate solutions. However, the IGS coordinator does not use a Kalman filter to connect the weekly solutions.

Eight ACs of the IGS (see Figure 38) produce global weekly station coordinate solutions in the SINEX format, which can be downloaded from the Crustal Dynamics Data Information System (CDDIS) server⁶⁰. This format contains parameter vectors, a so-called “full” estimated covariance matrix and for some ACs (e.g. COD, SIO and GFZ) it includes also its a priori covariance matrix. As described in DAVIES AND BLEWITT (2000) and ALTAMIMI *et al.* (2002), these matrices should allow removing a priori constraints to restore a free network solution. For our investigations, all available AC solutions from GPS week 1021 till week 1330 (August 1999 till July 2005) were used. Besides, we also downloaded geocentric daily coordinate solutions (in the ITRF2000) from the Scripps Orbit and Permanent Array Centre (SOPAC⁶¹). We did not choose the topocentric solutions (relative to a mean position), because these did not enable the

⁶⁰ <ftp://cddis.gsfc.nasa.gov/pub/gps/products/>

⁶¹ <ftp://garner.ucsd.edu/pub/timeseries/>

recovering of the geocentric positions of the stations. Only 359 IGS stations were selected for our analysis (see Figure 39a).

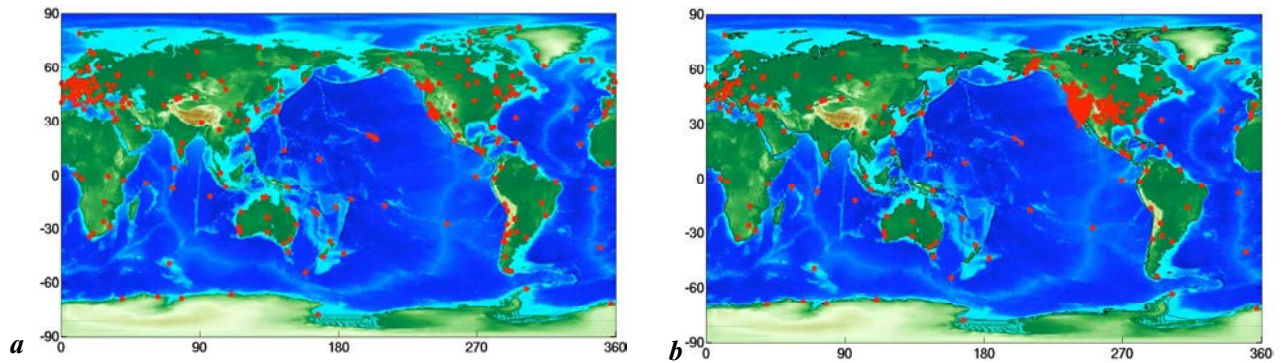


Figure 39: Distribution of (a) 359 IGS stations and (b) 675 SOPAC stations used in this investigation.

5.3.2 Constraints handling

The notion of “loose constraints” lacks a mathematical definition. It is used for non-minimum constraints, and the term “loose” should suggest that the weight of the constraints is so small that we may neglect their distorting effect on the equations or on the solution. In fact, the rigorous reduction of constraints was not rigorously possible for the selected solutions, meaning that these solutions are not completely compatible with the strategy on the level of unconstrained solutions. Nevertheless, we decided to include loosely and tight constrained solutions (e.g. COD, SIO, and GFZ) because of the importance to have “redundancy”. The problems of reducing constraints could be avoided, e.g. preferably if the ACs provided, e.g., SINEX files with unconstrained normal equations.

Unfortunately, the character of individual SINEX files, submitted by several ACs of the IGS, differs completely. For example, the AC at the European Space Agency (ESA) distributes minimally constrained solutions. To remove non-minimal constraints on station coordinates from estimated GPS weekly solutions, provided by the ACs at COD, SIO and GFZ, we subtracted the inverse of the estimated matrices Σ^{est} and the a priori constrained ones Σ^{const} (ALTAMIMI *et al.*, 2002):

$$N^{unc} = \left(\Sigma^{unc} \right)^{-1} = \left(\Sigma^{est} \right)^{-1} - \left(\Sigma^{const} \right)^{-1} \quad (5.2.3)$$

The resulting unconstrained matrix N^{unc} should be singular. Unfortunately, important information to reproduce the results is missing. One assumption in the deconstraining procedure is that the complete covariance matrix (which is not included in the SINEX file) consists of a block diagonal structure. But, as there are high correlations between several estimated parameters (see Figure 42 and Figure 40), the usual deconstraining procedure cannot be rigorous. We were not able to recover three, computationally very small eigenvalues, which would have corresponded to the three degrees of freedom of the unobserved network orientation. As GPS is a differential technique, we would even have expected a rank deficiency of six. Nonetheless, we added minimum constraints to obtain the minimally constrained variance matrix Σ^{mc} (ALTAMIMI *et al.*, 2002), involving appropriate columns of the design matrix of partial derivatives, A , using approximate station positions:

$$A = \begin{pmatrix} 1 & 0 & 0 & 0 & z_i & -y_i \\ 0 & 1 & 0 & -z_i & 0 & x_i \\ 0 & 0 & 1 & y_i & -x_i & 0 \\ \vdots & \vdots & \vdots & \vdots & \vdots & \vdots \end{pmatrix}; \quad B = A^T A$$

$$(\Sigma^{mc})^{-1} = (\Sigma^{unc})^{-1} + B^T B \quad (5.2.4)$$

The resulting deconstrained solution X^{dec} becomes:

$$X^{dec} = \Sigma^{mc} \left[(\Sigma^{est})^{-1} X^{est} - (\Sigma^{const})^{-1} X^{const} \right] \quad (5.2.5)$$

where X^{est} and X^{const} are respectively the estimated and a priori parameter vectors. In the case of loosely constrained solutions, we augmented the estimated covariance matrix by minimum constraints in order to remove the remaining Helmert parameter constraints by using the following equation (ALTAMIMI *et al.*, 2001):

$$\Sigma^{mc} = \Sigma^{est} - \left[\Sigma^{est} B^T (B \Sigma^{est} B^T)^{-1} B \Sigma^{est} \right] \quad (5.2.6)$$

The constraints in the COD solution are generally loose (at a few m level), so they should have a marginal effect on the estimated parameters. Actually, the IGS coordinator uses the following trick to deconstrain the weekly COD solution: He rescales the a priori covariance matrix by ~ 100 ppm to avoid numerical problems. To date, he still has not succeeded in removing constraints on the pole rates of the COD solution, and neither have we. To avoid corrupting the combined weekly IGS solution, those parameters are simply removed before combining the solutions.

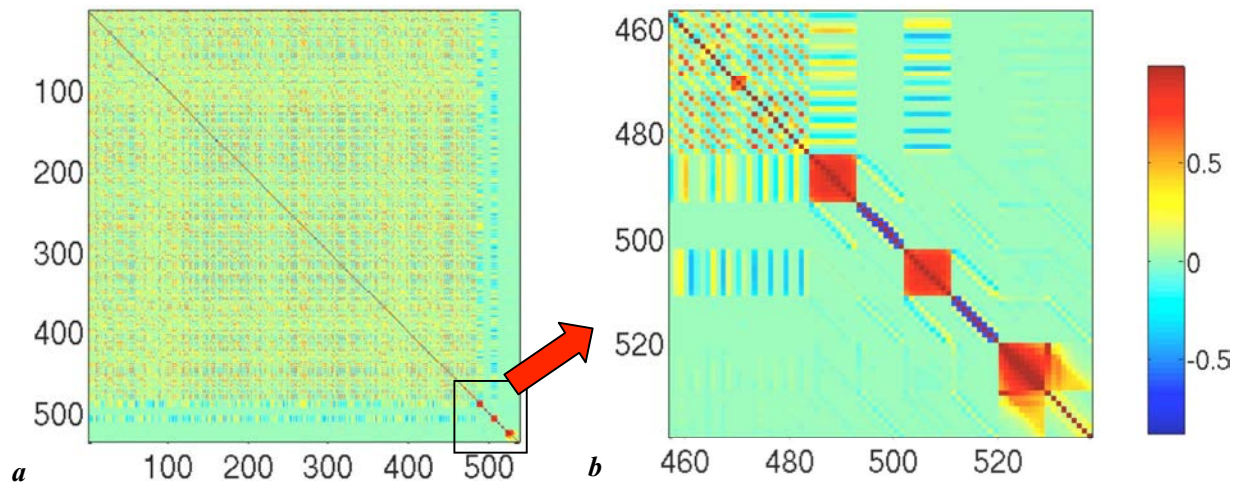


Figure 40: Matrix of correlation coefficients (a) between the 537 parameters (3D geocentric coordinates of 161 stations (block 1-483), daily polar motion offsets and rates, daily UT offsets and daily LOD parameters). Zoom (b) on the Earth orientation parameters (block 484-537) for the COD weekly solution of the GPS week 1321.

As already mentioned, COD applies rather loose constraints at few m level, and the geocentric coordinates corrections reach values of about 6 mm (see Figure 41).

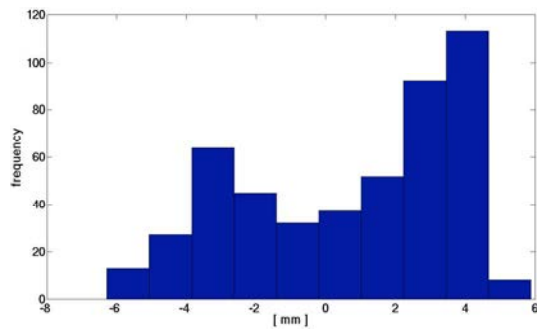


Figure 41: Histogram of the 483 coordinate corrections applied to deconstrain the coordinates of the COD weekly solution of the GPS week 1321. The geocentric coordinate corrections do not exceed 6 mm for the week 1321. The AC at COD applies loose coordinate constraints at the 4 m level.

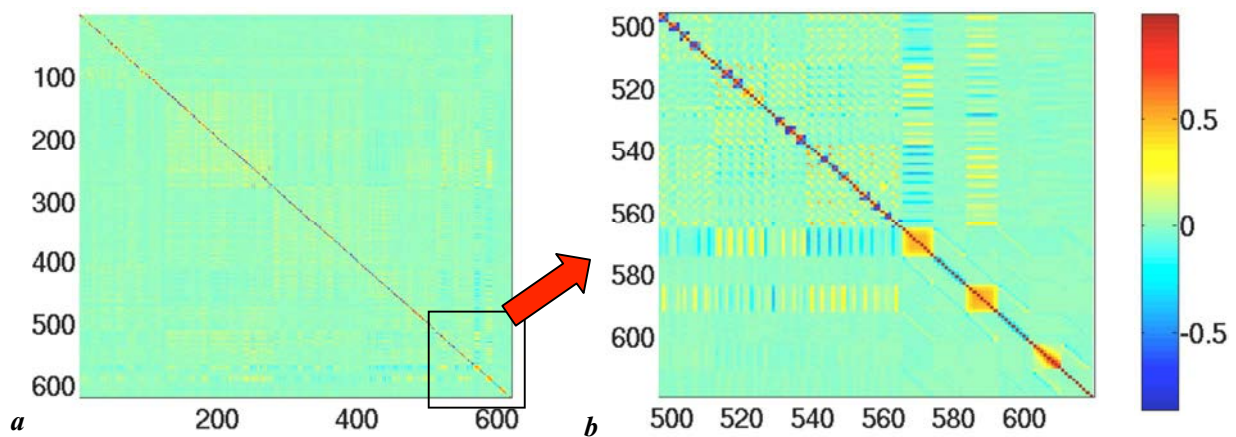


Figure 42: Matrix of correlation coefficients (a) between the 618 parameters, representing 3D geocentric coordinates of 188 stations (block 1-564), daily polar motion offsets and rates, daily UT offsets and daily LOD parameters. Zoom (b) on the Earth orientation parameters (block 565-618) for the GFZ weekly solution of the GPS week 1321.

As GFZ applies very tight coordinate constraints, we would expect much larger corrections from Figure 43. This could be an indication that we did not completely succeed in deconstraining the GFZ solution! No opportunity exists, so far, to check whether the deconstraining process was successful or not. However, one thing is sure: We did not retrieve 6 very small eigenvalues from the singular normal equation matrix N^{unc} . In general, the coordinate corrections remained below the 1 cm level for the solution of GFZ.

Figure 44 shows the histogram of the geocentric coordinate corrections, which enable the deconstraining of the SIO solution for GPS week 1321, and reveals that the geocentric coordinate corrections do not exceed one mm. It is somehow proof, that SIO really applies very loose coordinate constraints (at the 10 m level). Furthermore, three very small eigenvalues could be recovered from the N^{unc} matrix.

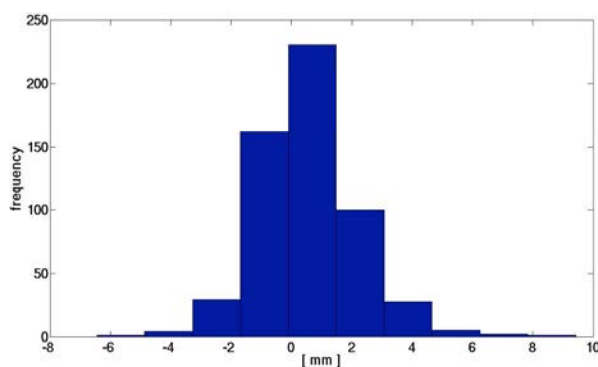


Figure 43: Histogram of the 564 coordinate corrections applied to deconstrain the coordinates of the GFZ weekly solution of the GPS week 1321. The geocentric coordinate corrections do not exceed 6 mm for the week 1321, although the AC at GFZ applies tight coordinate constraints at the sub-cm level.

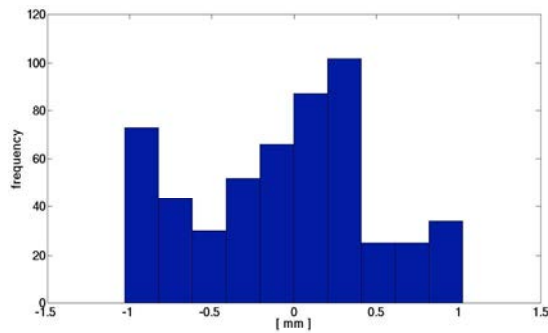


Figure 44: Histogram of the 537 coordinate corrections applied to deconstrain the coordinates of the SIO weekly solution of the GPS week 1321. The geocentric coordinate corrections do not exceed 1 mm for the week 1321. SIO applies very loose coordinate constraints at the 10 m level.

5.3.3 Similarity transformation parameters

For clarity's sake, we refer to the sites used to compute the transformations as “transformation sites”, while the other sites are “remaining sites”. So, we estimated a new set of seven transformation parameters with respect to the updated IGB00 reference frame (RAY *et al.*, 2005), for each GPS week, for each deconstrained AC solution (see Figure 45 to Figure 49, where results of the transformation parameters are only shown for COD, EMR, ESA, IGS, and MIT). The task was to align the weekly AC solutions to the IGB00 reference frame, in order to undertake comparisons. The seven Helmert parameters were estimated using only those stations for which the deviation to their IGB00 position was smaller than 3 cm (this step was done iteratively). This precision limit corresponded to maximum apparent seasonal and transient variations of the GPS coordinate time series. Thus, the number of chosen stations was typically from 40 to 70 out of the 99 possible ones. For the degree-one deformation approach, one should exclude the scale parameter from the estimation process, because it likely absorbs seasonal deformation, originating from surface loading. But, the scale parameter allows resorbing deficiencies due to GPS antenna phase centre offsets and variations etc.

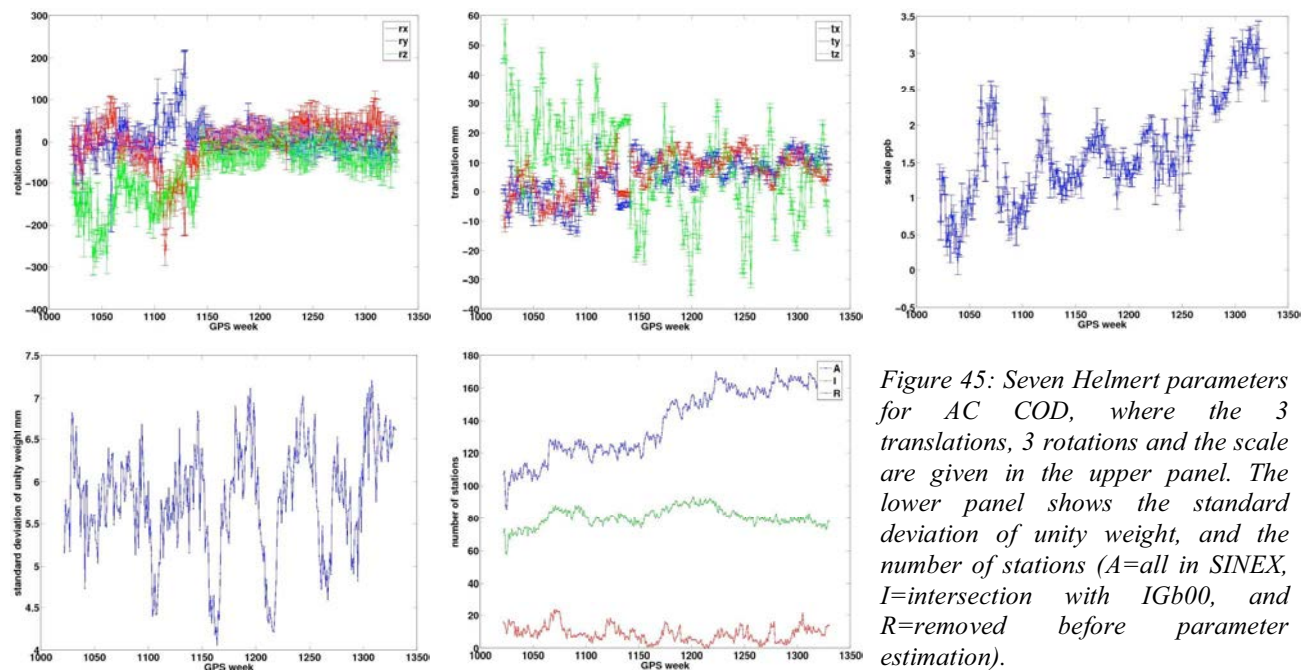


Figure 45: Seven Helmert parameters for AC COD, where the 3 translations, 3 rotations and the scale are given in the upper panel. The lower panel shows the standard deviation of unity weight, and the number of stations (A=all in SINEX, I=intersection with IGB00, and R=removed before parameter estimation).

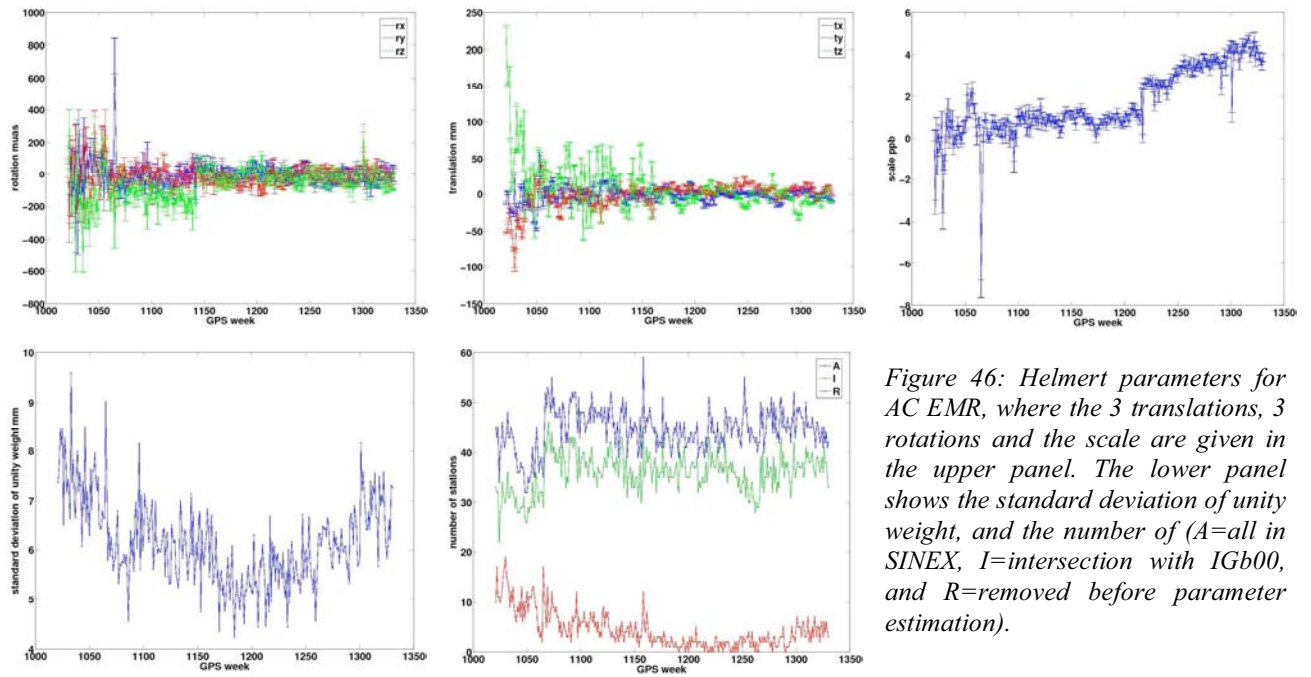


Figure 46: Helmert parameters for AC EMR, where the 3 translations, 3 rotations and the scale are given in the upper panel. The lower panel shows the standard deviation of unity weight, and the number of (A=all in SINEX, I=intersection with IGB00, and R=removed before parameter estimation).

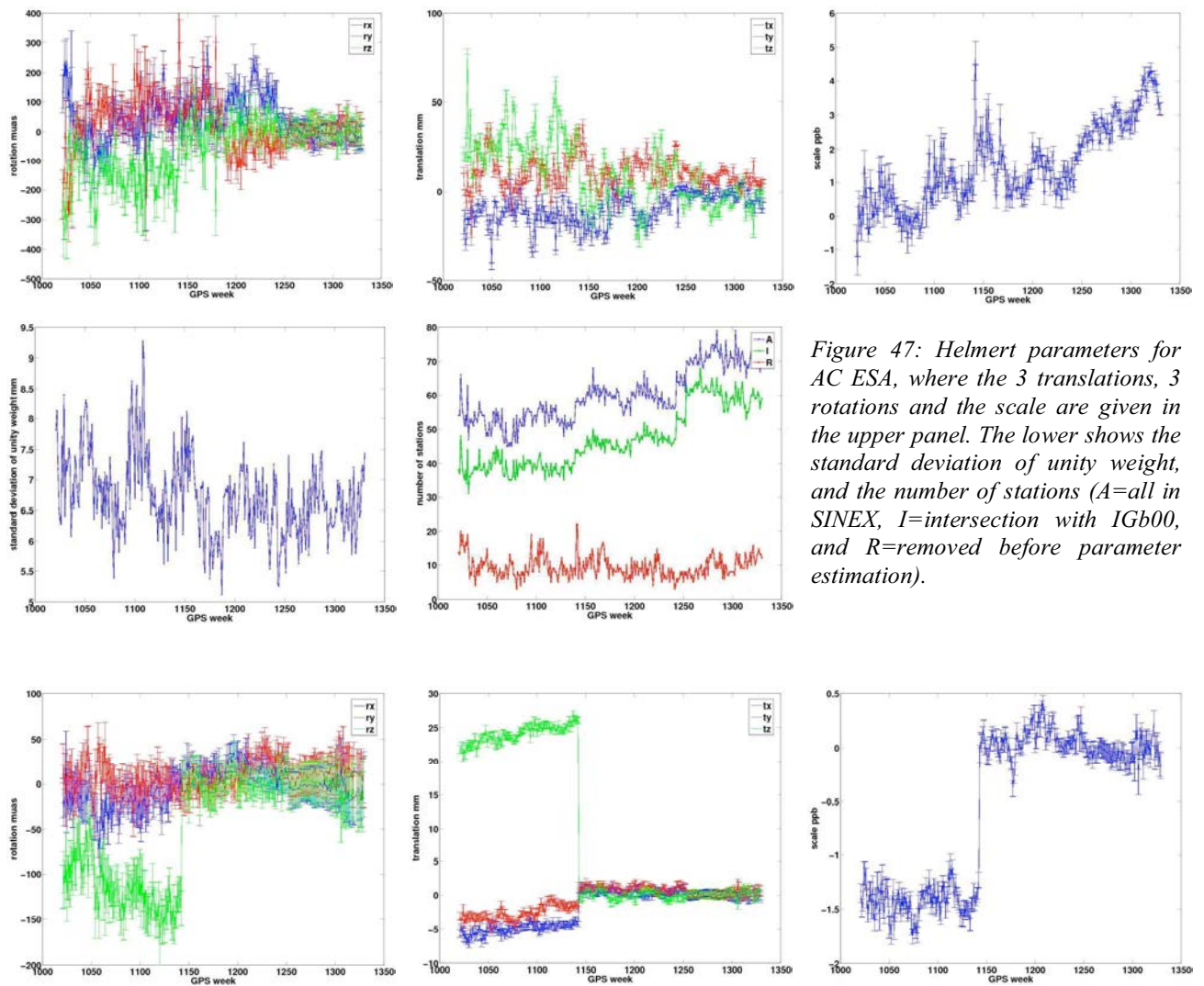


Figure 47: Helmert parameters for AC ESA, where the 3 translations, 3 rotations and the scale are given in the upper panel. The lower shows the standard deviation of unity weight, and the number of stations (A=all in SINEX, I=intersection with IGB00, and R=removed before parameter estimation).

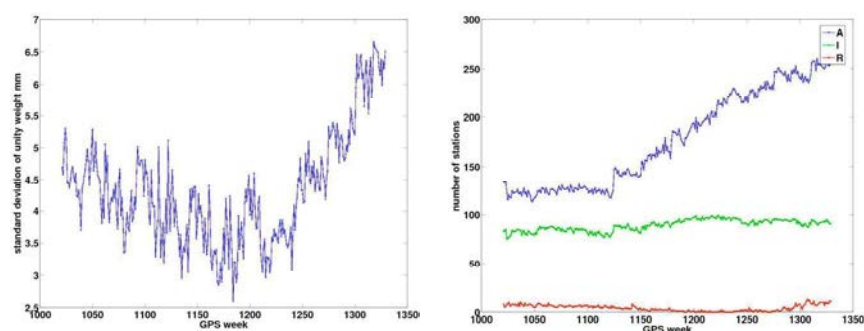


Figure 48: Helmert parameters for the IGS final combined solution, where the 3 translations, 3 rotations and the scale are given in the upper panel. The lower panel shows the standard deviation of unity weight, and the number of stations (*A*=all in SINEX, *I*=intersection with IGB00, and *R*=removed before parameter estimation).

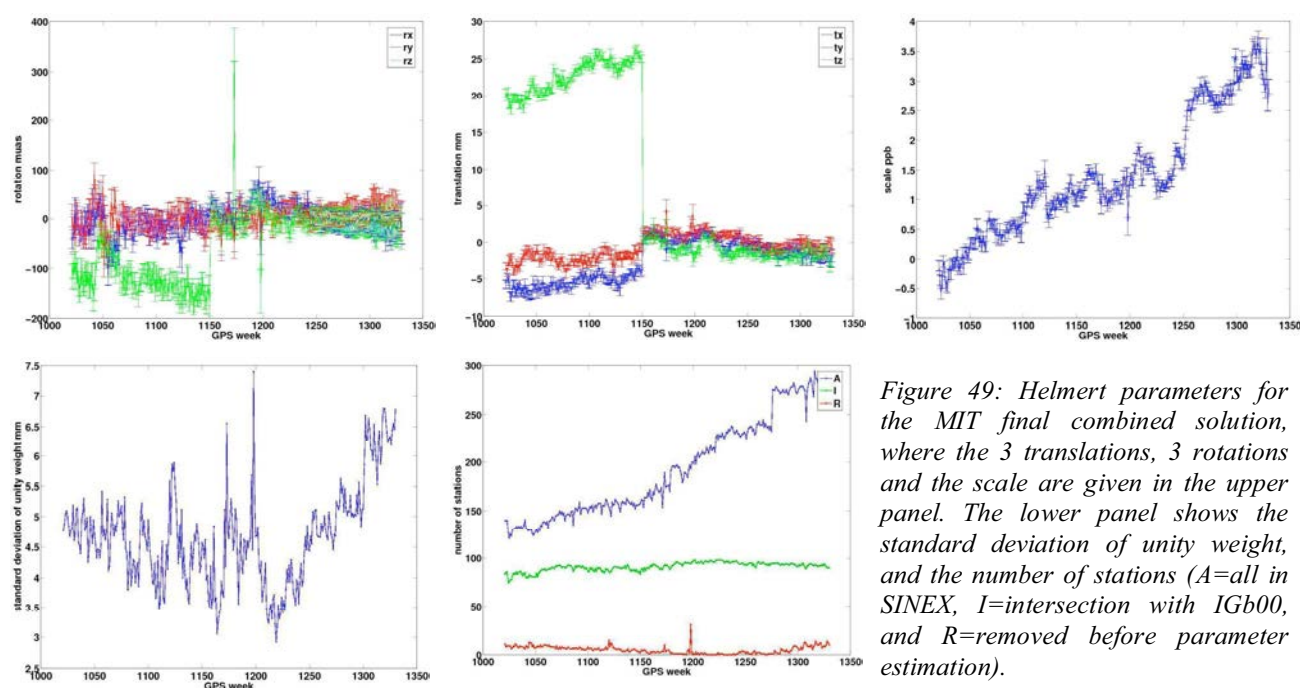


Figure 49: Helmert parameters for the MIT final combined solution, where the 3 translations, 3 rotations and the scale are given in the upper panel. The lower panel shows the standard deviation of unity weight, and the number of stations (*A*=all in SINEX, *I*=intersection with IGB00, and *R*=removed before parameter estimation).

One feature, visible from Figure 45 to Figure 49 in the rotation and translation parameters, is the change of reference frame (from IGS00 to IGB00) at GPS week 1143. A jump of 150 microarcseconds (μs) in the Z-axis rotation and 2.5 cm in Z-axis translation was the consequence. Although the number of stations in the SINEX files has been steadily increasing, the standard deviation of unity weight has been degrading since GPS week 1210. The number of transforming stations, intersecting with the IGB00 frame, is relatively constant over time for all ACs. The use of absolute phase centre offsets and variations (PCV) on the scale parameter is still pending. Its application, in the near future (probably 2006), will intricately stabilize the scale. During the epoch 2000.5-2004.5, the scale parameter was increasing by ca. 0.8 ppb per year for the AC solutions. The IGS final combined solution (see Figure 48) shows a stable scale, with variations of less than 0.4 ppb since GPS week 1143 (representing ca. 3 mm on Earth's surface). The jump of the IGS scale (1.5 ppb) on GPS week 1143 is due to a change from Terrestrial Coordinate Geocentric (TCG) time to Terrestrial Time (TT). It is however interesting that in the MIT combined solution (Figure 49), the scale parameter is still drifting. And finally, the standard deviation of unity weight for the AC at COD (Figure 45) reflects the seasonal variation of the identified error in the displacement of the solid Earth tides corrections.

Another test implies that the effect of the number and quality of stations contributing to realizing the reference frame is often underestimated, i.e., station positions change in a network, depending on which stations have been used in the estimation of the Helmert transformation parameters (see Figure 50 for SIO on GPS week 1321).

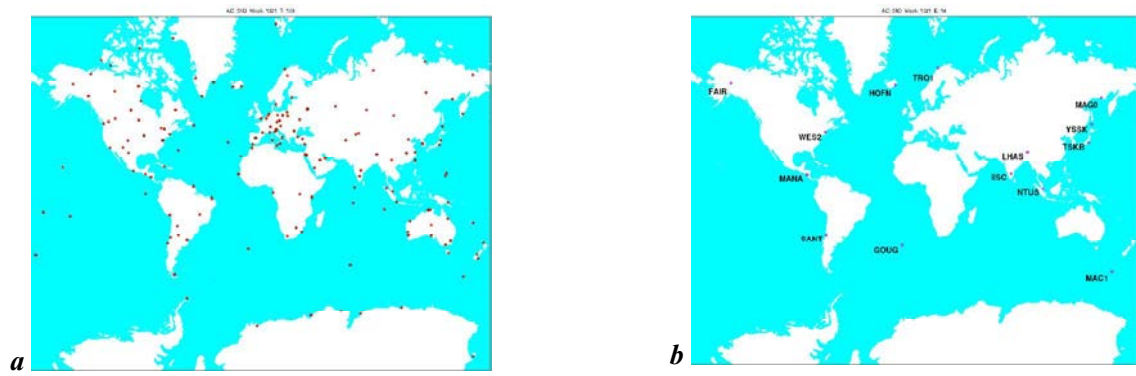


Figure 50: In total, on GPS week 1321, (a) 179 stations were processed at SIO; 87 transforming stations intersected with the IGB00 frame, but (b) 14 stations were removed from the 7-Helmert-parameter estimation process.

As a further test, we sequentially eliminated the worst common station from the estimation process, i.e., the one with the largest deviation versus IGB00 projected to the given epoch, and determined the seven parameters of the similarity transformation at GPS week 1321 for the AC at SIO. Depending on the number of flagged stations for the inversion of the seven Helmert parameters, the scale parameter changed by more than 0.5 ppb, which corresponded to 3 mm variation of the vertical component on Earth's surface (see Figure 51c). Estimated translation parameters varied in the order of 1 cm (see Figure 51b). This transformation process evidently complicates the distinction between real and artificial crustal motion at individual sites. Rotation parameters did not vary more than by 200 microarcseconds (μs) (see Figure 51a).

The transformation parameters obtained at GPS week 1321 for the AC at SIO are the ones shown in Figure 51 for the station number 73 in the horizontal axes ($73=87-14$, see caption of Figure 50).

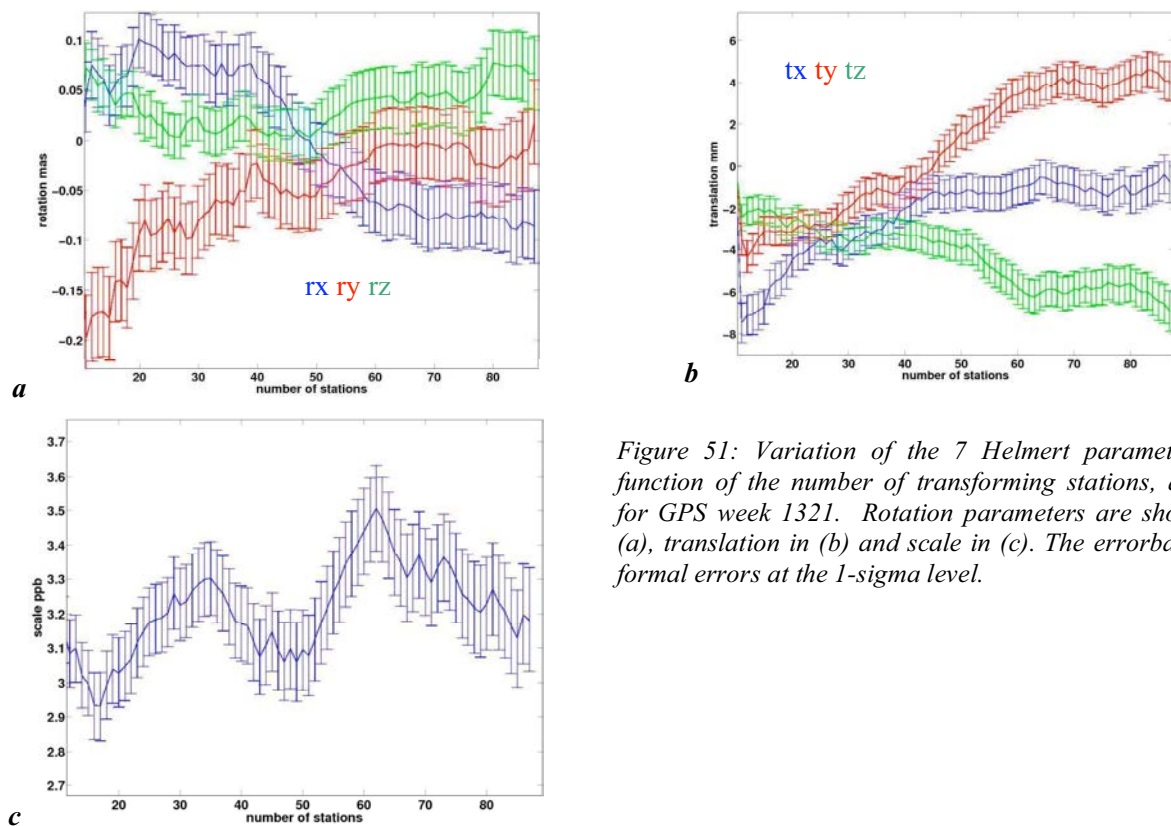


Figure 51: Variation of the 7 Helmert parameters in function of the number of transforming stations, at SIO for GPS week 1321. Rotation parameters are shown in (a), translation in (b) and scale in (c). The errorbars are formal errors at the 1-sigma level.

5.3.4 Data cleaning

After the transformation process, we used the same breaks detection algorithm for the coordinate time series as for the baseline length time series, with only minor changes. Again, we first applied an order 15 one-dimensional median filter (mdf) (PRATT, 1978) to the topocentric coordinate time series. Then, a single-level one-dimensional discrete Haar wavelet decomposition (one approximation and one detail) was applied. Breaks or jumps were flagged (see Figure 52a in pink and red) for coefficients larger than 60% (lateral components) and 80% (vertical components) of the maximum value, and for differences in the median filtered data larger than 4 mm (lateral) and 6 mm (radial). Finally, we constructed a regressor with linear pieces between the flagged jumps (see Figure 52b). Three months after the Sumatra-Andaman earthquake and tsunami of December 2004, another great earthquake, i.e. an aftershock of the 2004 event, the Nias-Simeulue earthquake of magnitude 8.7 was the 6th most powerful earthquake ever recorded (see Figure 52b).

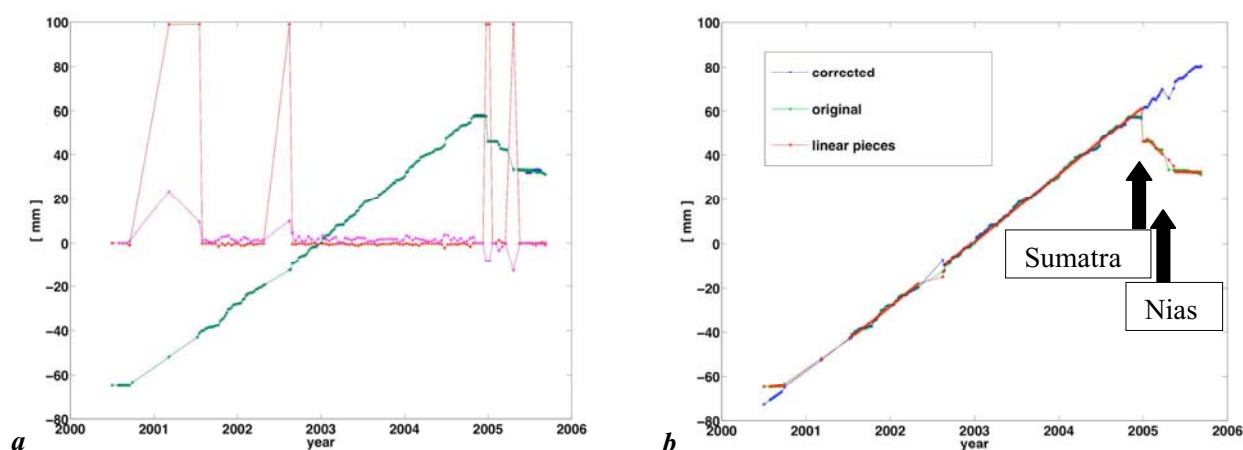


Figure 52: Break detection algorithm tested for the east component of the station NTUS (IGS final solution). The first largest break occurred during the Sumatra earthquake in December 2004 (doy 361), followed by a second one, a few months later, which displaced this station by a few cm in the east component.

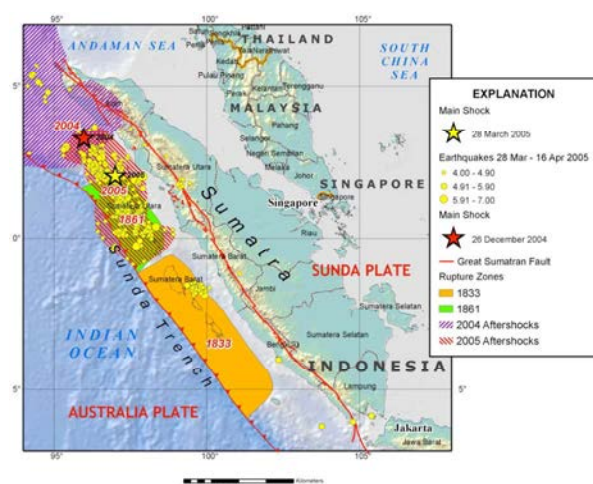


Figure 53: A great earthquake occurred at 16:09:36 (UTC) on Monday, March 28, 2005. The magnitude 8.7 event has been located in northern Sumatra, Indonesia. (source USGS⁶²).

Figure 54 to Figure 58 show the efficacy of the break detection algorithm, applied to selected daily topocentric coordinate time series, from SOPAC, listed in Table 12. Displacements due to earthquakes or receiver and antenna changes are readily identified at the 6 mm level (radial) and 4 mm level (lateral).

⁶² <http://Earthquake.usgs.gov/eqcenter/eqinthenews/2005/usweax/>

The reason for the sudden velocity alteration after a receiver or antenna change (see Figure 56b and Figure 57a), for both stations HOFN and KELY, could not be elucidated. For HOFN, the trend of the vertical component previous to 2001 (doy 264) amounted to 6.4 ± 0.5 [mm/year] at 95% confidence bounds, while afterwards it changed steadily to 13.6 ± 0.5 [mm/year]. The slope is even steeper after mid-2003. SOPAC analysts report one single trend of 10.0 ± 0.8 [mm/year]. For KELY, the trend of the vertical component before 2001 (doy 247) was -2.0 ± 0.3 [mm/year] at 95% confidence bounds, while afterwards it suddenly changed to 1.4 ± 0.4 [mm/year]. Again, SOPAC analysts report one single trend of -1.3 ± 0.7 [mm/year].

Table 12: Station codes.

Code	Station Description	Longitude	Latitude	Height
NTUS	Singapore, Singapore	103 40 47.6	1 20 44.9	79.0
FAIR	Fairbanks, USA	212 30 02.7	64 58 40.8	319.0
MAC1	MacQuarie Island, Southern Ocean	158 56 08.9	-54 29 58.2	-6.7
HOLP	Hollydale, USA	241 49 48.0	33 55 12.0	-6.7
LONG	Irwindale, USA	242 00 00.0	34 06 36.0	74.3
WUHN	Wuhan City, P.R. China	114 21 26.3	30 31 54.1	25.8
HOFN	Hoefn, Iceland	344 48 47.5	64 16 02.2	82.5
KELY	Kangerlussuaq, Greenland	309 03 18.0	66 59 14.3	230.6
HOLB	Holberg, Canada	231 51 54.0	50 38 25.4	560.0
RIOG	Rio Grande, Argentina	292 15 00.0	-53 47 24.0	32.0
BRAZ	Brasilia, Brazil	312 07 19.9	-15 56 50.6	1106.0

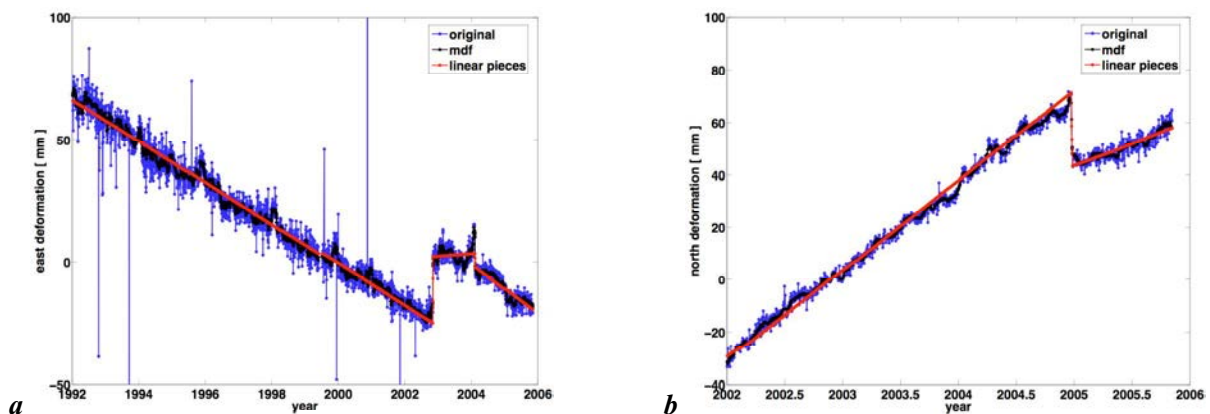


Figure 54: Break detection algorithm applied to the east component of the station (a) FAIR after the Delani earthquake in 2002 (doy 307) and (b) to the north component of the station MAC1 after the Macquarie Island earthquake (M 8.1) in 2004 (doy 358).

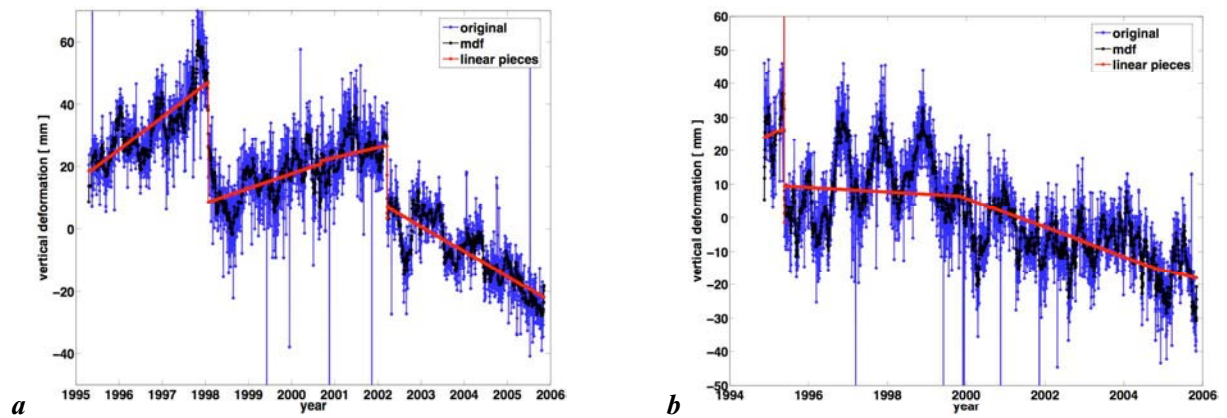


Figure 55: Break detection algorithm applied to the vertical component of the station (a) HOLP showing the Hector Mine earthquake on 1998 (doy 24), and an unknown jump in 2002 (doy 76), and (b) of the station LONG, where an antenna and receiver change occurred in 1995 (doy 139), as well as the Hector Mine earthquake in 1999 (doy 289).

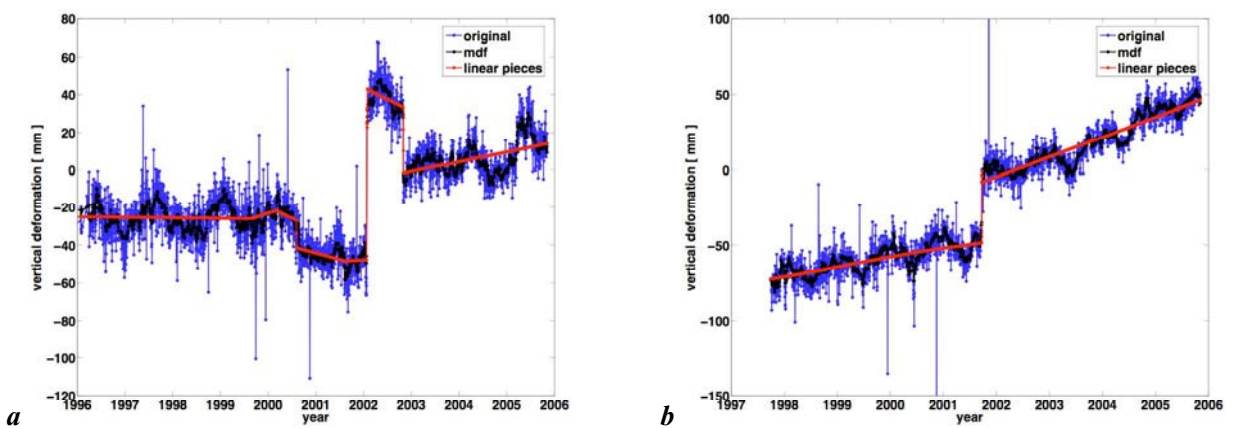


Figure 56: Break detection algorithm applied to the vertical component of the station (a) WUHN with a receiver change in 1999 (doy 265), an antenna offset in 2002 (doy 26) and in 2002 (doy 304) and (b) HOFN with an antenna and receiver change in 2001 (doy 264).

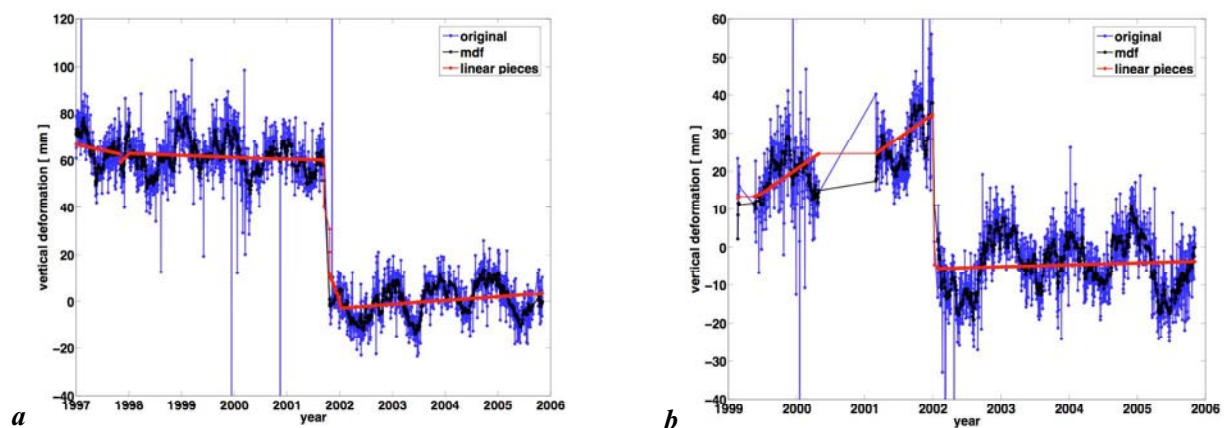


Figure 57: Break detection algorithm applied to the vertical component of the station (a) KELY showing a receiver change in 2001 (doy 257) and (b) HOLB with an antenna and receiver change in 2002 (doy 23).

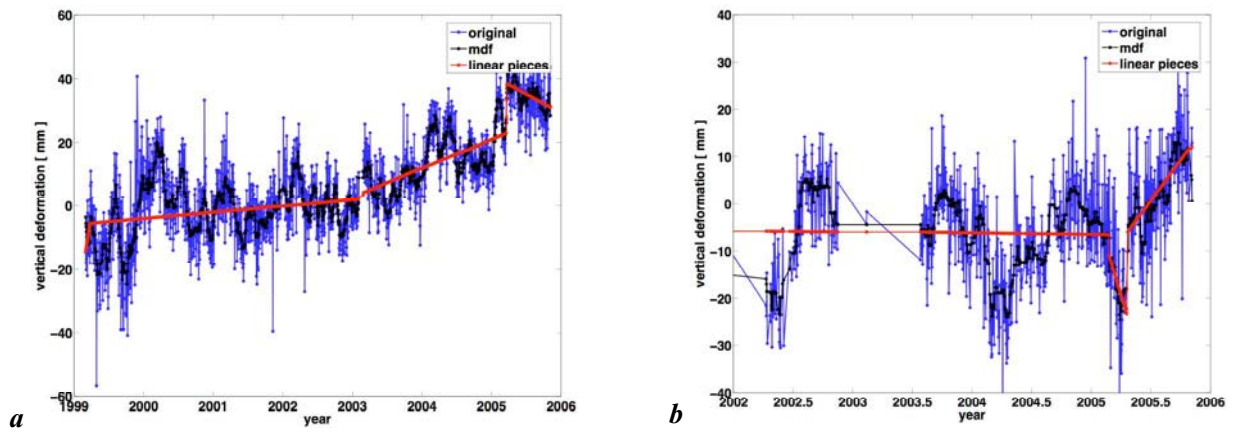


Figure 58: Break detection algorithm applied to the vertical component of the stations (a) RIOG and (b) BRAZ. Small probable breaks of unknown (and unreported) origin were detected.

5.3.5 Model parameters

From the cleaned data, we estimated offsets, trends, annual and semi-annual amplitudes and phases of coordinate time series with respect to GPS week 1021. We implemented a common and efficient linear parameterization to the observed topocentric motion $y(t)$, of each site and each direction, as follows:

$$y(t_i) = a + bt_i + ct_i^2 + d_j \cos(2\pi q_j t_i) + e_j \sin(2\pi q_j t_i) + v_i \quad (5.8.1)$$

where t_i for $i = 1 \dots N$ are the weekly solution in units of years. The first three terms are the site position offset a , linear rate b and quadratic rate c , respectively. Coefficients d_j and e_j describe the amplitudes of the periodic motions, and q_j their respective frequencies (see Table 13). The measurement errors v_i are initially assumed to be independent and randomly distributed with an expectation value of zero $E(v_i) = 0$. The model is linear with respect to the coefficients:

$$\mathbf{x} = [a \quad b \quad c \quad d_j \quad e_j]^T \quad (5.8.2)$$

so that :

$$\mathbf{y}(t) + \mathbf{v} = \mathbf{A}\mathbf{x} \quad (5.8.3)$$

where \mathbf{A} is the design matrix of partial derivatives. The weighted least squares solution yields the best linear unbiased estimates of the unknown parameters. The annual and semi-annual amplitudes and their respective phases are simply a combination of the respective parameters of the unknown vector of coefficients \mathbf{x} .

Table 13: Periods corresponding to the frequencies q_j in the model of parameters.

(Darwinian) symbol	Doodson number	Period [day]	Name
CW		432	Chandler wobble (CW)
Sa	056.554	365.2425	Elliptical tide of first- order to S_0 -solar annual
Ssa	057.555	182.6211	Declinational tide to S_0 -solar semiannual
TA		121.7475	Ter-annual (TA)
QA		91.3106	Quart-annual (QA)
Msf	063.655	31.8119	Evection tide to M_0
Mm	065.455	27.5546	Elliptical tide of first-order to M_0 -lunar fortnightly
Msm	073.555	14.7653	Variation tide to M_0
Mf	075.555	13.6608	Declinational tide to M_0 -lunar fortnightly
Mt	085.455	9.1329	Ter-mensual tide

5.3.6 Comparison between AC solutions

An important step of this work consisted in bearing out anomalies in the different coordinate time series solutions. We started with an example (see Figure 59) indicating at which velocity the station ZIMM (Zimmerwald, Switzerland) is drifting with reference to IGB00 and ITRF2000, for the solution at SIO. The height component is drifting at a velocity of 4.1 mm/year w.r.t. the IGB00 reference frame, but only with 1.9 mm/year w.r.t. ITRF2000.

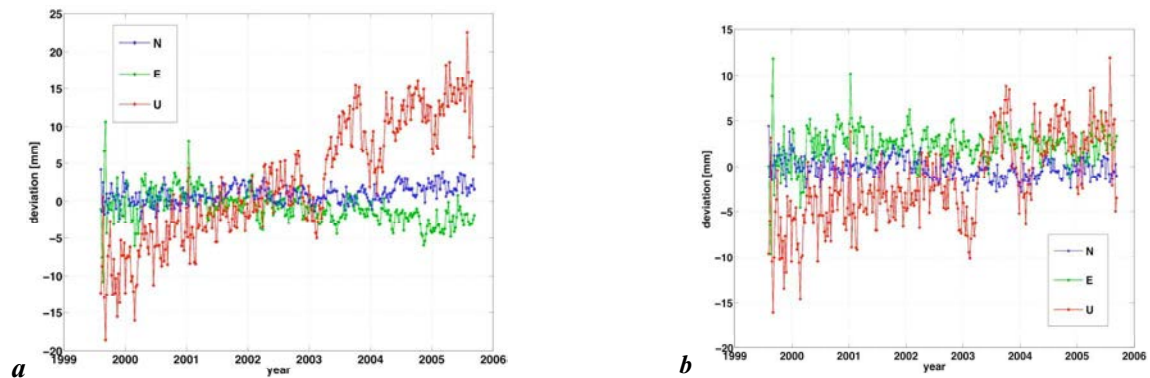


Figure 59: Topocentric coordinate differences between two TRFs and SIO for the station ZIMM located in Zimmerwald, Switzerland. The height component drifts at a velocity of (a) 4.1 mm/year w.r.t. the IGB00 reference frame, while it reaches only (b) 1.9 mm/year w.r.t. ITRF2000.

Figure 60a focuses on the temporal differences in the vertical component of the SIO solution w.r.t. the IGS final solution. The y-axis is labeled for the 359 IGS stations. The differences are seldom (0.5 %) larger than 1 cm. Figure 60b resumes, in a histogram, the topocentric differences for the 359 IGS stations over the period under consideration. 99.5 % of the radial differences are below 1 cm, and 99 % of the lateral (north and east) differences are below 3 mm.

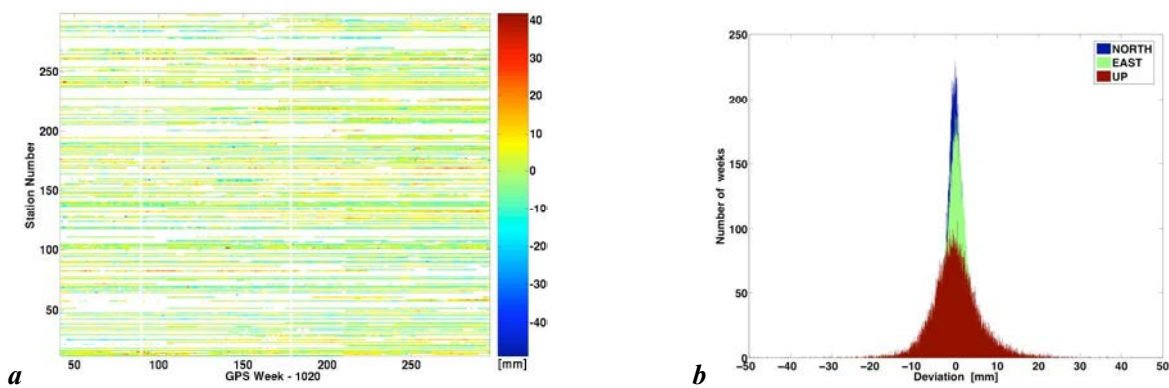


Figure 60: Statistics about the difference IGS minus SIO. The difference in the vertical component for the 359 IGS stations (a). Histogram of the topocentric differences for the 359 stations over the integral time period (b). A cut-off of 50 mm has been enforced.

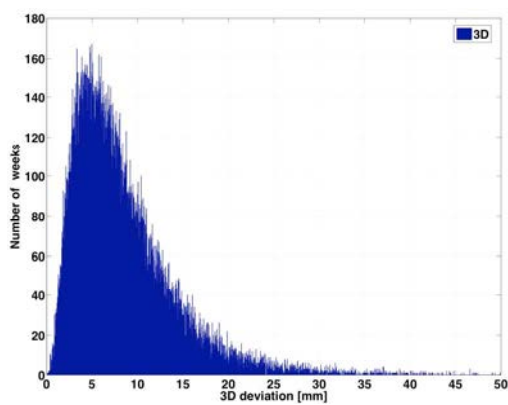


Figure 61: Histogram of the 3D deviation of differences (IGS-SIO) for the 359 stations over the integral time period.

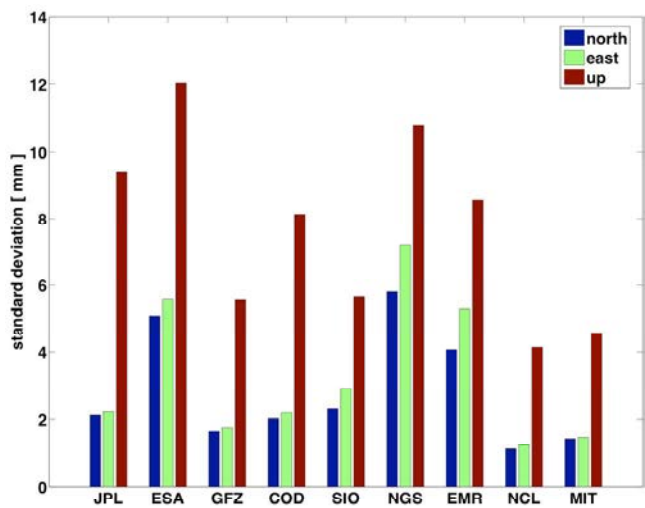


Figure 62: Standard deviation of the difference between the ACs and the IGS final solution, in the three components. A cut-off of 50 mm has been enforced.

Table 14: Mean and standard deviation of the differences w.r.t. the IGS final solution. (N=north, E=east, and U=vertical component).

AC/GNAAC	mean [mm]			standard deviation [mm]		
	N	E	U	N	E	U
JPL	0.3	-0.1	-0.1	2.1	2.2	9.4
ESA	1.1	-0.1	0.6	5.1	5.6	12.0
GFZ	0.1	0.1	0.3	1.7	1.8	5.6
COD	-0.2	-0.3	0.7	2.0	2.2	8.1
SIO	0.3	0.1	0.1	2.3	2.9	5.6
NGS	1.6	-0.1	-0.1	5.8	7.2	10.8
EMR	0.7	0.1	0.5	4.1	5.3	8.6
NCL	-0.2	0.1	0.1	1.1	1.2	4.1
MIT	-0.1	-0.1	0.5	1.4	1.4	4.6

The 3D coordinate difference between the IGS and SIO solutions dilvuges a mode at 5 mm (see Figure 61). The mean and standard deviation of the topocentric coordinate differences has been processed for all ACs w.r.t. the IGS final solution see Figure 62). GFZ is the AC attaining the lowest RMS w.r.t. the IGS final solution. However, due to the difficulties encountered in the deconstraining procedure, this conclusion should be used with precaution. NGS does worst for the lateral components, while ESA displays the highest RMS of 12 mm for the radial component. Figure 62 summarizes Table 14 in a graph.

5.3.7 Seasonal variations

On 15th of July 2004, a significant error in the computation of the solid Earth tides corrections in the Bernese GPS Software was identified. The error affected the computation of the frequency dependent part of the solid Earth tide corrections. The height component of station positions in mid-latitudes showed a once-per-day variation with an amplitude of about 1 cm with a superposed annual variation with an amplitude of another 1 cm. This bug has been fixed successfully, as can be seen in Figure 63 for the station MONP (Laguna Mountains, USA). The station MONP is a good example of how contributions of individual ACs may corrupt the IGS final solution.

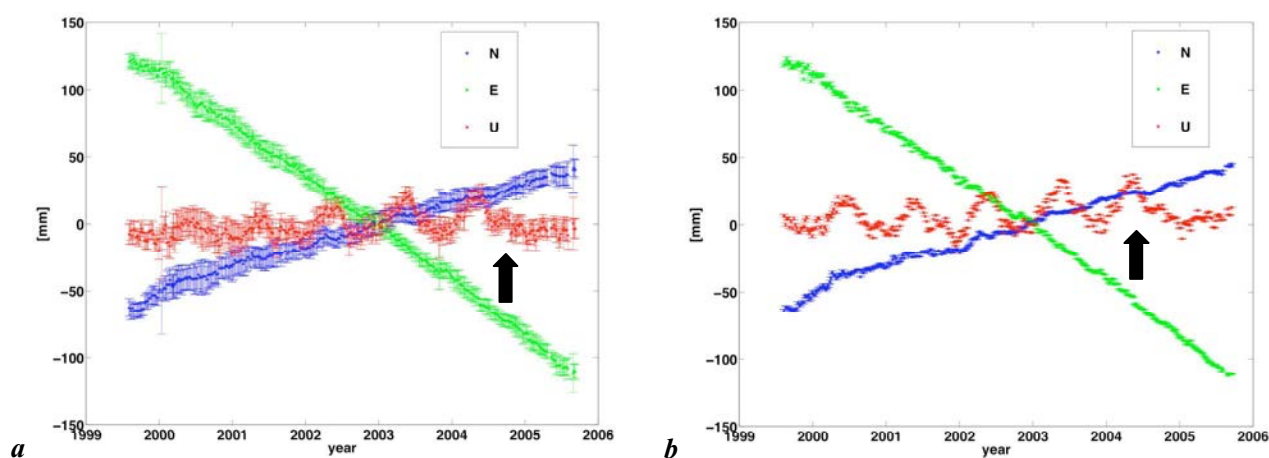


Figure 63: Impact of the COD bug into the IGS final solution for the station MONP in Laguna Mountains, USA for (a) IGS solution and (b) COD solution.

Returning to the seasonal variations (which are hopefully of real geophysical origin), we decided to apply some strict requirements. In deriving Figure 64 to Figure 69, several criteria had to be fulfilled:

- residuals had to follow a normal distribution at a confidence level of 95%
- the standard deviation of unity weight had to be smaller than 6 mm for the vertical component
- at least 156 weeks (3 years) of data had to be available
- the RMS of the phase of the annual component had to be smaller than 3 days

As a result, apparent periodic signals on seasonal timescales in the vertical station coordinates were recovered for all ACs (here, only results for COD and SIO are shown). Due to the above-mentioned bug, the amplitudes derived from the AC at COD showed twice as large annual amplitudes than the average of the other ACs. Regional correlation of the vertical deformation (in amplitude and phase) is clearly demonstrated for the annual signal, while it is less obvious for the semiannual period. In general, the standard deviation of unity weight is smallest for European stations, while other regions being more noisy. Annual signals for other ACs with their respective RMS are given in Appendix B.

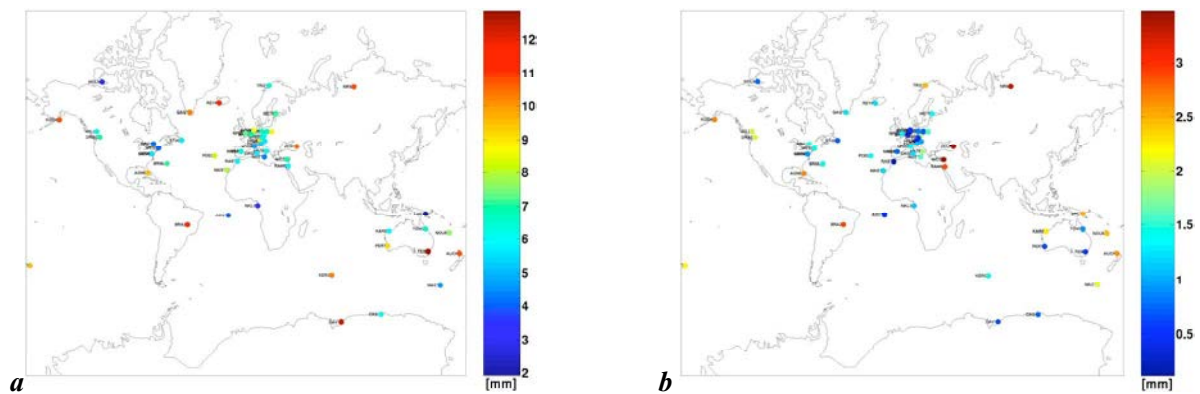


Figure 64: Seasonal amplitudes distribution of the height component at COD for 55 stations that passed the selection criteria (see text): (a) annual amplitudes, (b) semi-annual amplitudes.

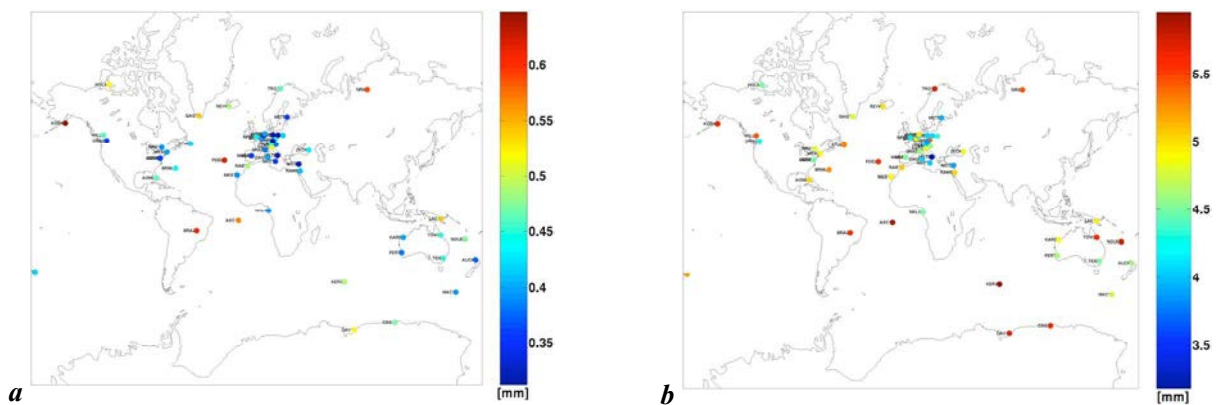


Figure 65: Seasonal amplitudes distribution of the height component at COD for 55 stations that passed the selection criteria (see text): (a) RMS of annual amplitudes, and (b) standard deviation of unity weight.

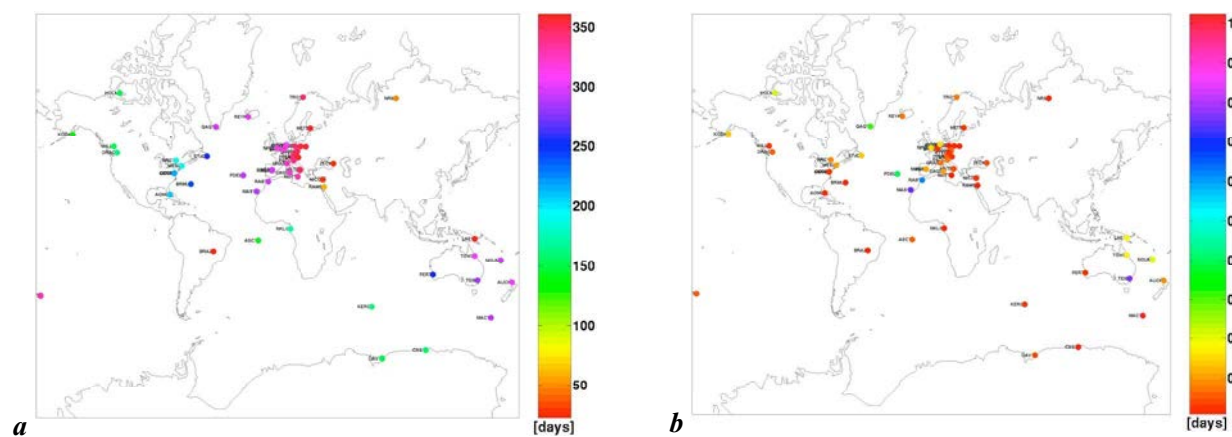


Figure 66: Phase of annual amplitudes distribution of the height component at COD for 55 stations that passed the selection criteria (see text): (a) phase, and (b) RMS of phase.

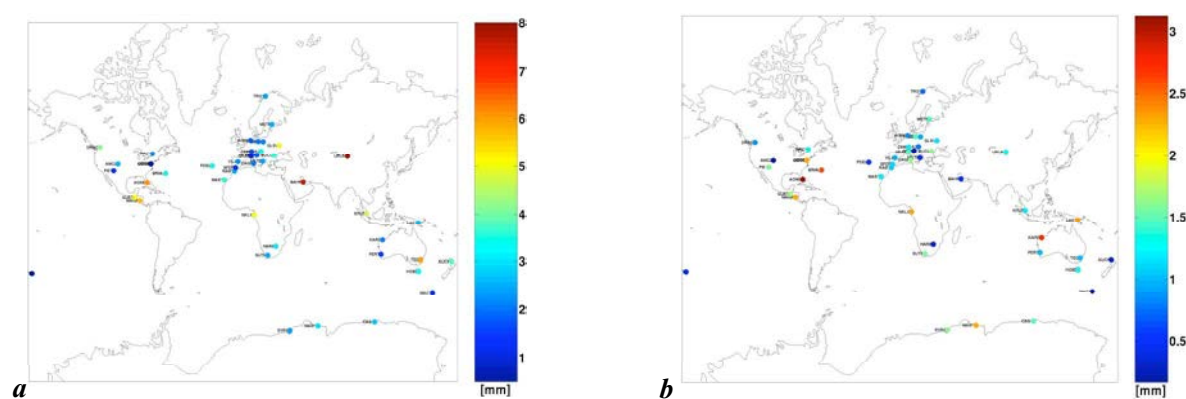


Figure 67: Seasonal amplitudes distribution of the height component at SIO for 45 stations that passed the selection criteria (see text): (a) annual amplitudes, (b) semi-annual amplitudes.

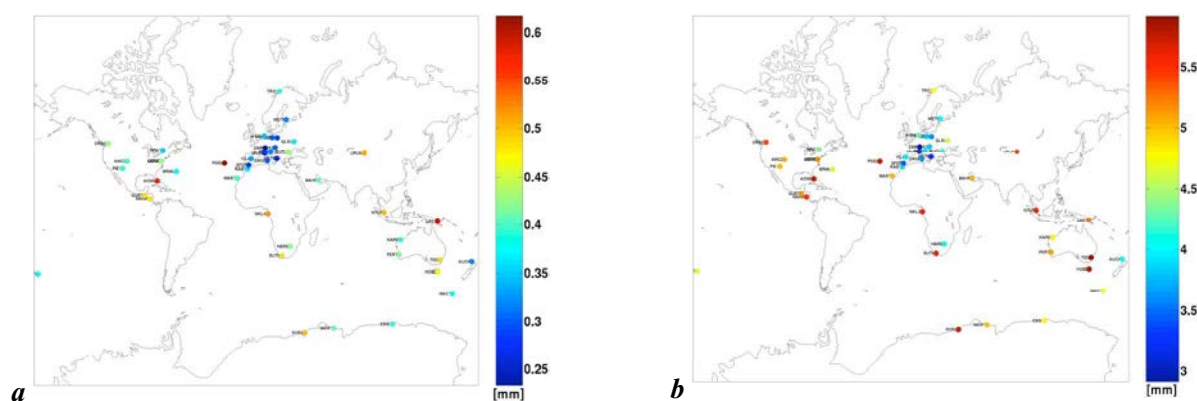


Figure 68: Seasonal amplitudes distribution of the height component at SIO for 45 stations that passed the selection criteria (see text): (a) RMS of annual amplitudes, and (b) standard deviation of unity weight.

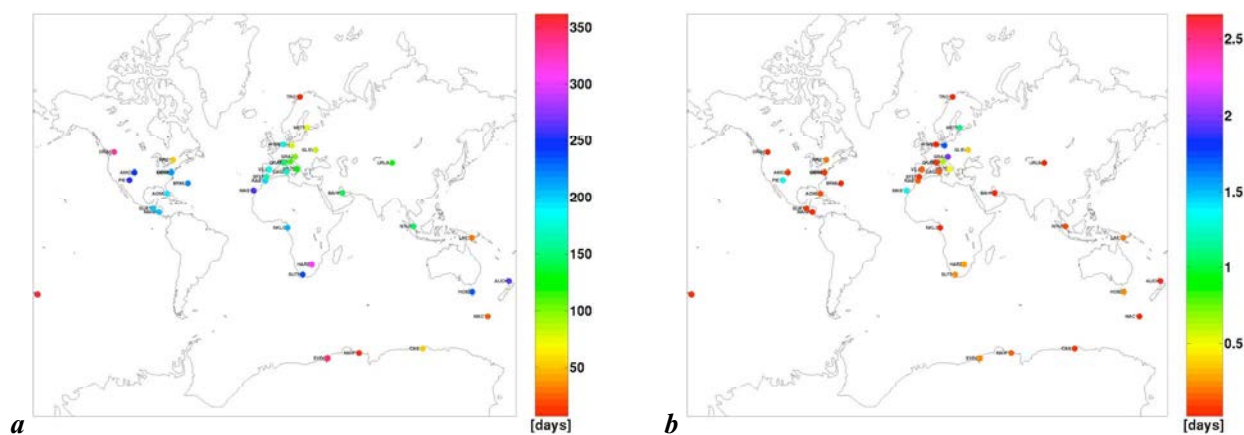


Figure 69: Phase of annual amplitudes distribution of the height component at SIO for 45 stations that passed the selection criteria (see text): (a) phase, and (b) RMS of phase.

5.3.8 Unreported and unexplained offsets

Unreported changes in software models, antenna height changes, and sudden events can make things rather complicated. For example, the model change in resolving ambiguities (fixing to integers) for the carrier phase pseudoranges at the European Space Agency (ESA) AC in November 2003 (personal communication by Dow J., 2004) produced a visible jump of 1 cm in the north component of several stations, e.g., Wettzell (WTZR) or Potsdam (POTS) on GPS week 1243 (see Figure 70). Other unexplained changes occurred at several stations, e.g. QAQ1 located in the south of Greenland (see Figure 71). Although an antenna change took place in 2003 (doy 248), such a change should leave the height variation theoretically unaffected. It is doubtful whether this change really introduced a break of 12 cm in the vertical deformation (see Figure 71b) as recovered by SIO. Another unexplained aspect in Figure 71a is the constant offset by ca. 120 mm of the AC JPL wrt. to other ACs (e.g. GFZ, NGS and COD). Probably, SIO and JPL used (or still use) the wrong height reference for the site QAQ1.

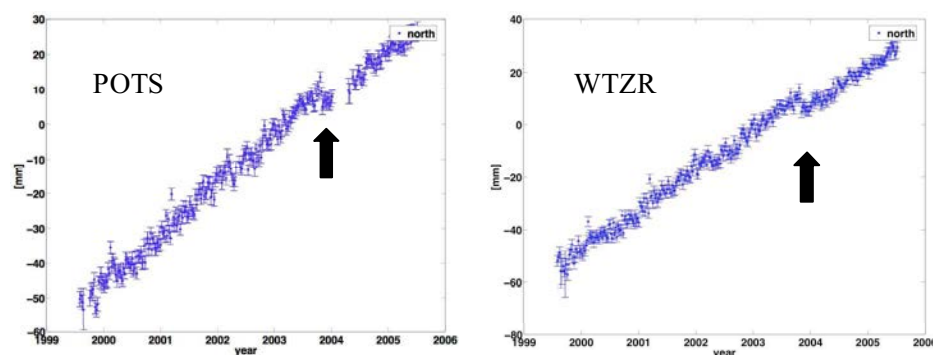


Figure 70: A model change in resolving ambiguities (fixing to integers) for the carrier phase pseudoranges at the European Space Agency (ESA) introduced a jump in the north component of the stations POTS (Potsdam) and WTZR (Wettzell).

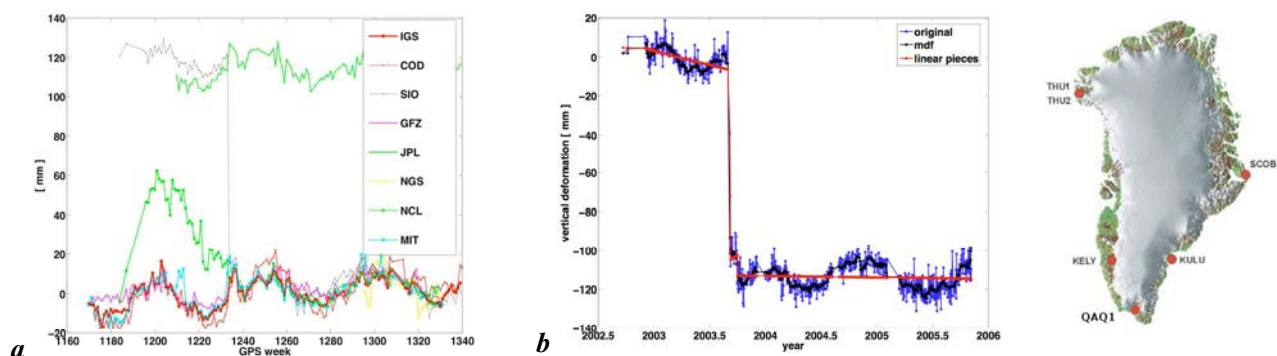


Figure 71: Vertical displacement of station QAQ1⁶³, located in the south of Greenland, as estimated from the available (a) ACs and (b) the daily SOPAC solution.

5.3.9 Very short baselines

Very short baselines help in detecting anomalies due to instrumental problems. For example, two GPS stations NYA1 and NYAL are only separated by 8 m. A common hypothesis is that for such a baseline, the local environment is identical at both stations.

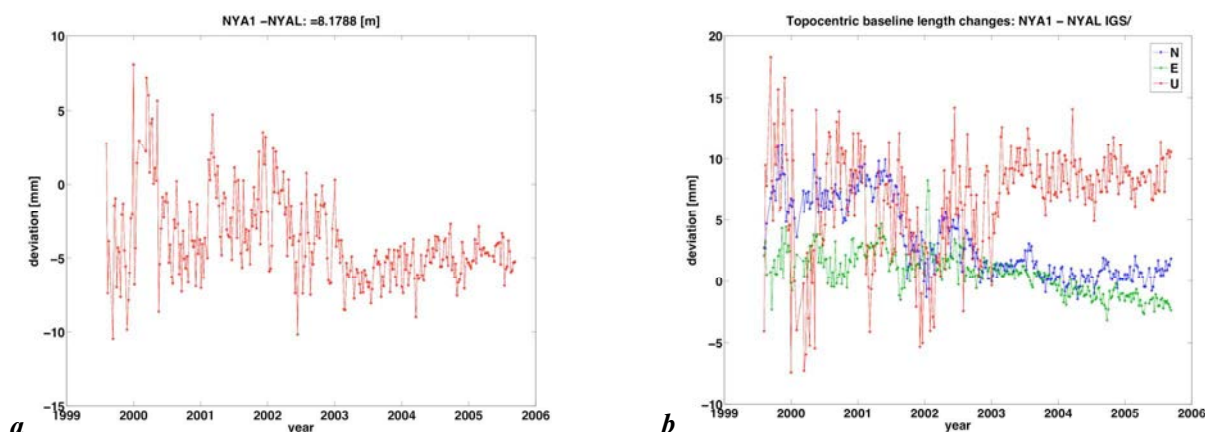


Figure 72: Baseline length variation between NYA1 and NYAL for IGS. The stations are only separated by ca. 8 m.

Figure 72a presents the temporal variation of the baseline length between the latter two stations, while Figure 72b sub-divides the baseline length into the three topocentric components w.r.t. the station NYAL. Since the year 2003, there has been an obvious increase in stability. The height difference is constant, but it seems that the lateral components are likely to be drifting apart at a slow pace. Two other stations, TROM and TRO1 separated by only 51 m, have been analysed for the baseline length. Up to 2004 (doy 195), an apparent drift of 3 mm per year could be measured for this baseline length. However, this trend proved to be misleading, after replacement of the GPS antenna at TRO1 (see Figure 73). Since then, the baseline length has gained in stability.

⁶³ <http://research.kms.dk/~geod/REFSTA/ref.html>

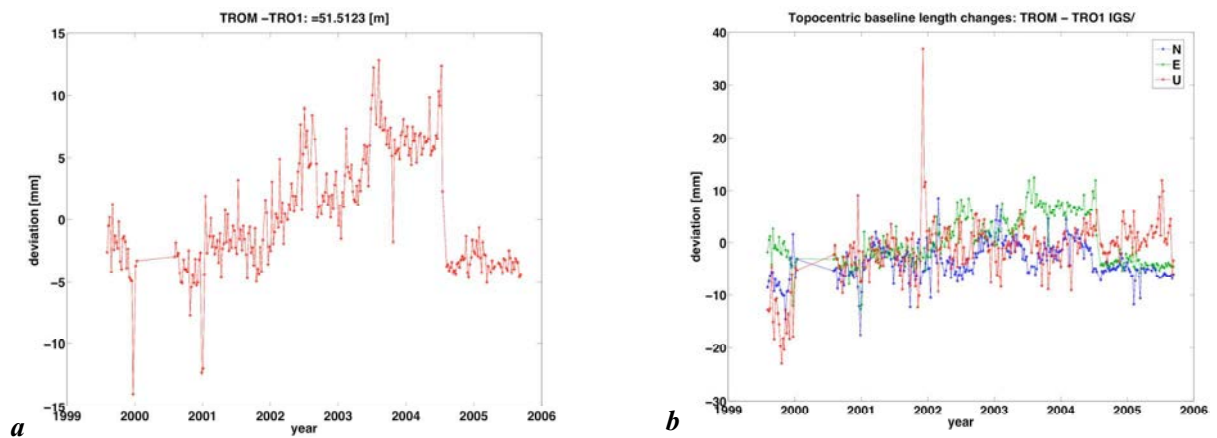


Figure 73: Baseline length variation between TROM and TRO1 for IGS. The stations are only separated by ca. 51 m.

5.3.10 Comparison with atmospheric loading displacements

One crucial question remains: How well do displacements caused by atmospheric pressure loading explain the measured geometric deformation, as derived by GPS on the result level? From now onwards, we will choose the SOPAC coordinate time series, as we know that the combined International GNSS Service (IGS) coordinate solutions show evident seasonal irregularities and aliasing effects (MENDES CERVEIRA *et al.*, 2006a). Moreover, the weekly SIO coordinate time series, transformed to Igb00, correspond completely to the daily SOPAC coordinate time series (see Figure 74).

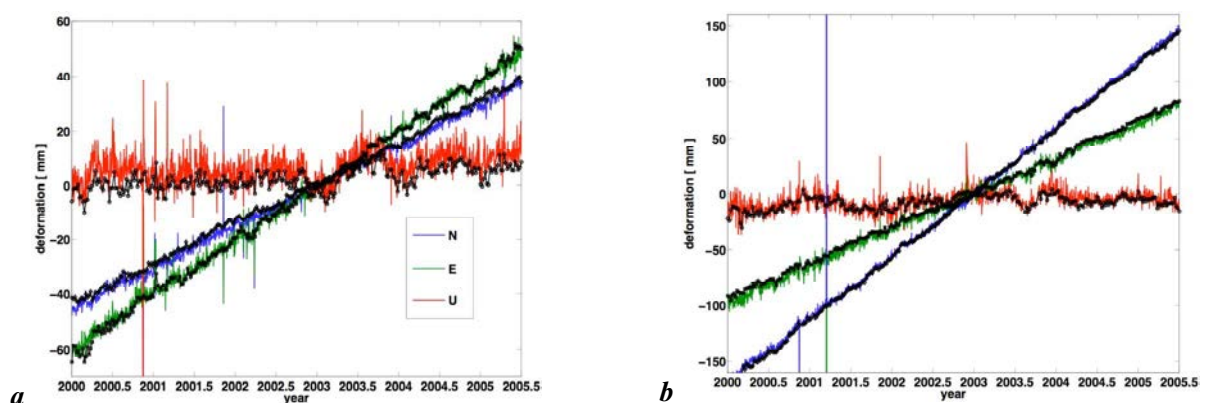


Figure 74: Daily versus weekly topocentric coordinate time series from SOPAC and SIO respectively. Station (a) ZIMM, Zimmerwald, Switzerland and (b) ALIC, Alice Springs, Australia. The black curves show the weekly SIO solution, while red (vertical), blue (north) and green (east) show the topocentric daily SOPAC coordinate time series.

The station displaying the highest correlation coefficient (between measured and modelled) is BAHR, located in Bahrain (see Figure 75a). Figure 76 to Figure 83 present the spectral and aperiodic decomposition of the vertical deformation, as measured by SOPAC and modelled by APLO (induced by atmospheric pressure loading).

The black circle in Figure 76 points out a common aperiodic deformation observed at the beginning of the year 2003 at many central-European stations (e.g. POTS, GRAZ and BOR1).

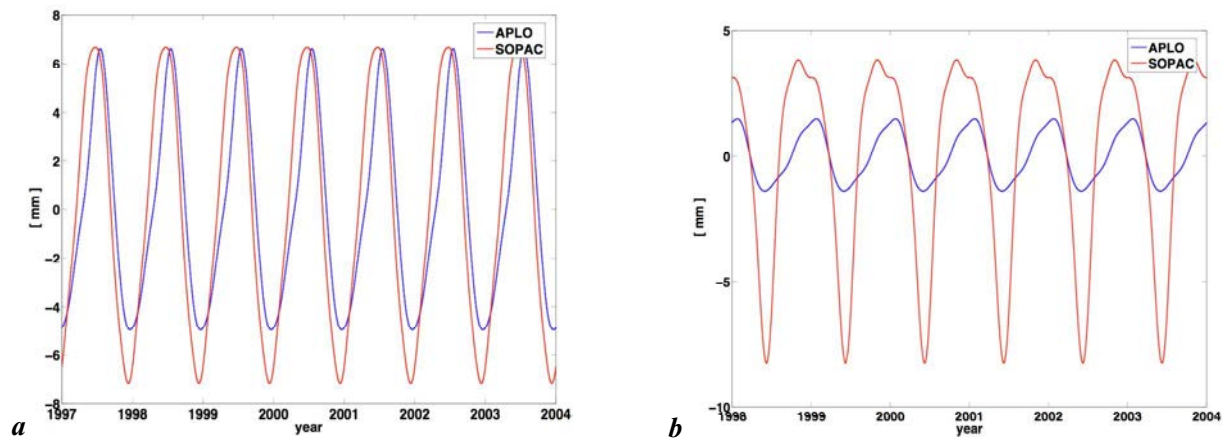


Figure 75: Periodic vertical deformation of the stations (a) BAHR (Bahrain) and (b) HOFN (Iceland), derived from SOPAC and from the modelled deformation calculated by APLO, due to atmospheric pressure loading. 70% of the deformation can be explained by atmospheric loading for the station BAHR, however only 30% of the amplitude is recovered for the station HOFN.

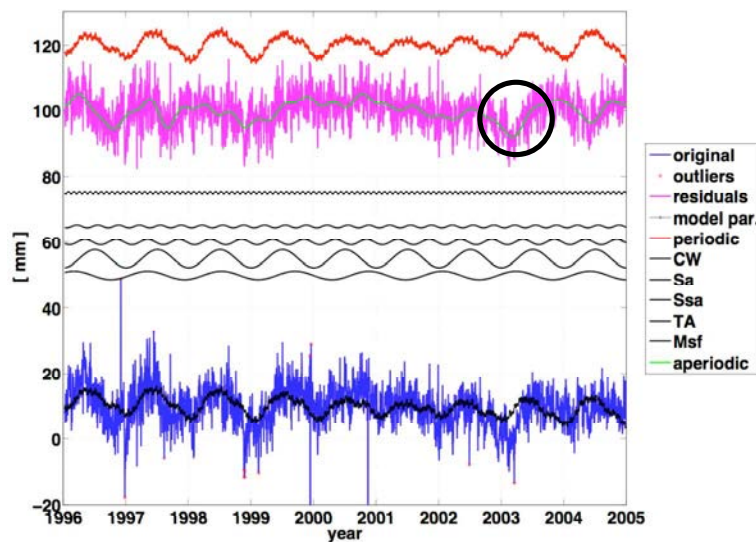


Figure 76: Spectral and aperiodic decomposition of the vertical component of the station WTZR (Wetzell) from SOPAC. ($n_{out}=16$, $s_o=5.6$ mm, $s_0=5.0$ mm, $s_{02}=4.2$ mm). The black circle points to a common aperiodic deformation observed at the beginning of the year 2003 at many central-European stations (e.g. POTS, GRAZ and BOR1). Offsets are applied for better visibility. See Table 13 for the acronyms on the legend.

n_{out} =number of outliers, s_o =RMS of detrended original signal, s_0 =RMS of residuals, and s_{02} =RMS of the reduced residuals by the aperiodic signal.

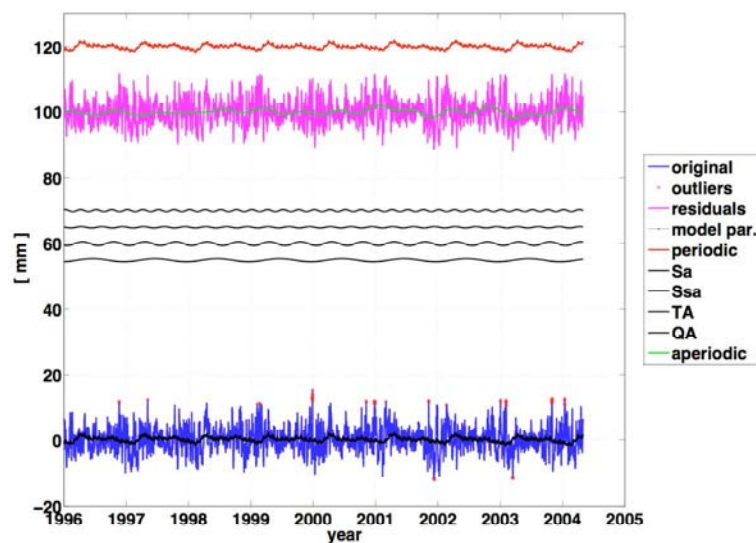


Figure 77: Spectral and aperiodic decomposition of the vertical component of the station WTZR (Wetzell) from APLO. ($n_{out}=115$, $s_o=3.7$ mm, $s_0=3.6$ mm, $s_{02}=3.6$ mm).

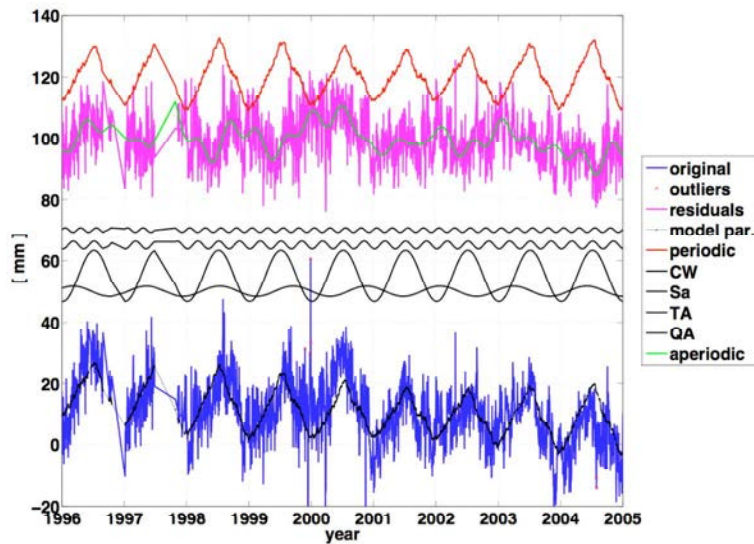


Figure 78: Spectral and aperiodic decomposition of the vertical component of the station IRKT (Irkutsk) from SOPAC. ($n_{out}=12$, $s_o=10.0$ mm, $s_0=7.9$ mm, $s_{02}=6.3$ mm).

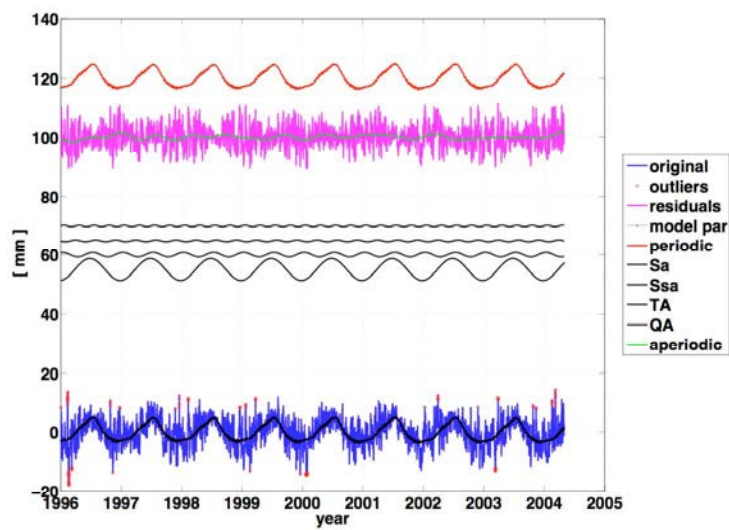


Figure 79: Spectral and aperiodic decomposition of the vertical component of the station IRKT (Irkutsk) from APLO. ($n_{out}=126$, $s_o=4.3$ mm, $s_0=3.4$ mm, $s_{02}=3.3$ mm).

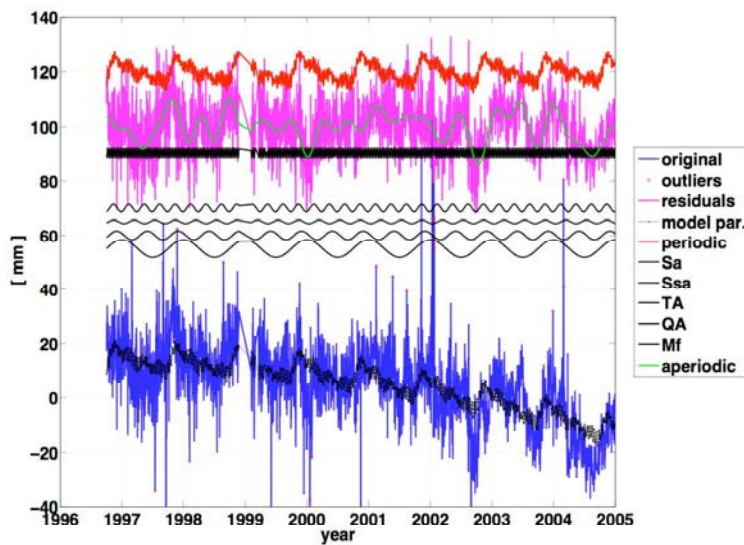


Figure 80: Spectral and aperiodic decomposition of the vertical component of the station MKEA (Hawaii) from SOPAC. ($n_{out}=30$, $s_o=10.0$ mm, $s_0=9.5$ mm, $s_{02}=8.0$ mm).

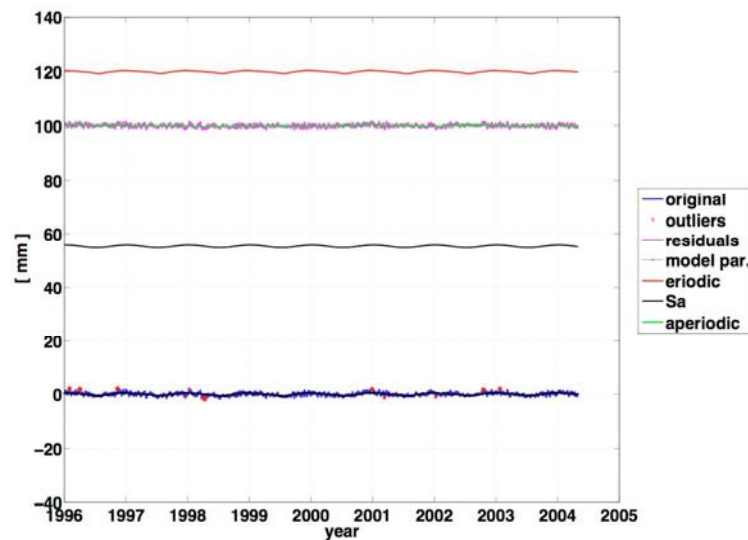


Figure 81: Spectral and aperiodic decomposition of the vertical component of the station MKEA (Hawaii) from APLO. ($n_{out}=102$, $s_o=0.5$ mm, $s_0=0.4$ mm, $s_{02}=0.4$ mm).

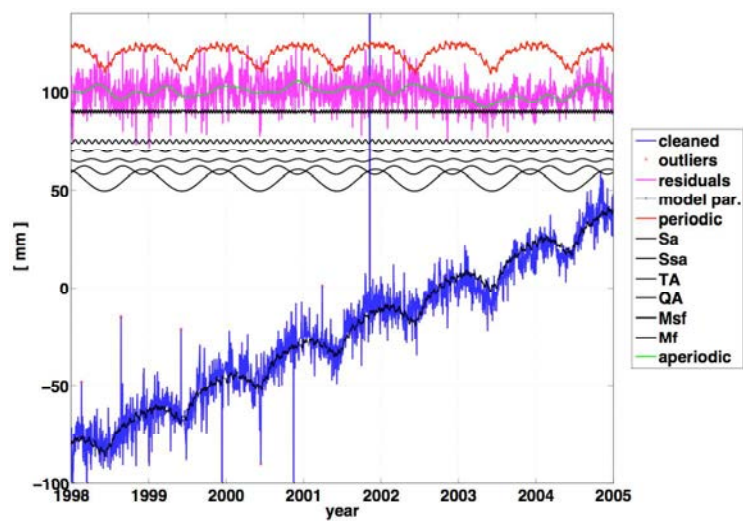


Figure 82: Spectral and aperiodic decomposition of the vertical component of the station HOFN (Iceland) from SOPAC. ($n_{out}=30$, $s_o=10.0$ mm, $s_0=9.5$ mm, $s_{02}=8.0$ mm).

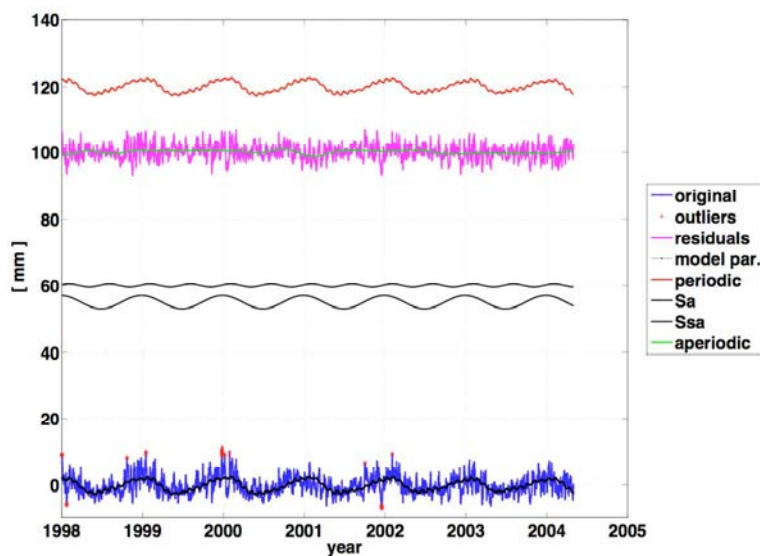


Figure 83: Spectral and aperiodic decomposition of the vertical component of the station HOFN (Iceland) from APLO. ($n_{out}=112$, $s_o=2.7$ mm, $s_0=2.2$ mm, $s_{02}=2.1$ mm).

The station MKEA (Hawaii) indicates a pronounced declinational tide (Mf-lunar fortnightly), with a significant amplitude of about 2 mm, in the SOPAC vertical deformation (see Figure 80). In general, on a seasonal level, APLO only recovers 20% of the vertical deformation as estimated by SOPAC (609 stations

were analysed). The inverted barometer assumption of stations located on islands (e.g. HOFN, MKEA etc.) is rather critical. The prognosticated vertical deformation of APLO, due to atmospheric pressure loading is quasi non-existent for the station MKEA (see Figure 81). However, the periodic deformation derived from SOPAC points out a regular step function. Future work needs to be done for similar stations. Near coastlines, and most GPS stations have been established near the sea, the land-ocean mask seems to be the major source of fundamental discrepancies.

A pronounced Mf-tide of 8.3 mm is visible from the SOPAC data before December 2000 (Figure 84a), at station MAS1 (Las Palmas, Spain). In fact, ocean loading and pole tides were only modelled at SOPAC after November 26th, 2000. A superposition of the ocean tide loading model GOTIC2 (MATSUMOTO *et al.*, 2000), taking 16 major and 33 minor short-period as well as 7 long-period constituents into account, with the recovered tidal signal in the SOPAC vertical component time series is shown in Figure 85.

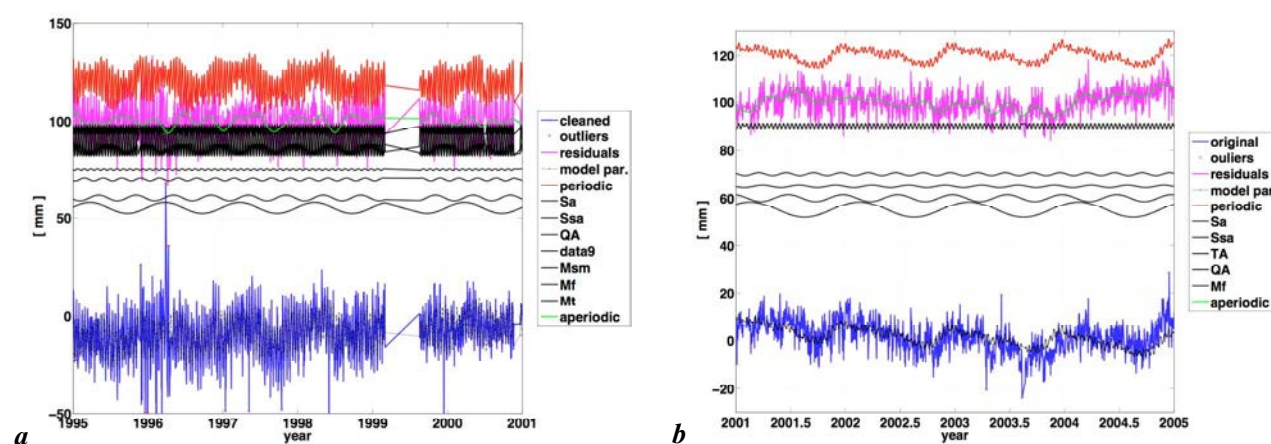


Figure 84: Spectral and aperiodic decomposition of the vertical component of the station MAS1 (Las Palmas, Spain) from SOPAC: (a) before 2001 and (b) after November 2000.

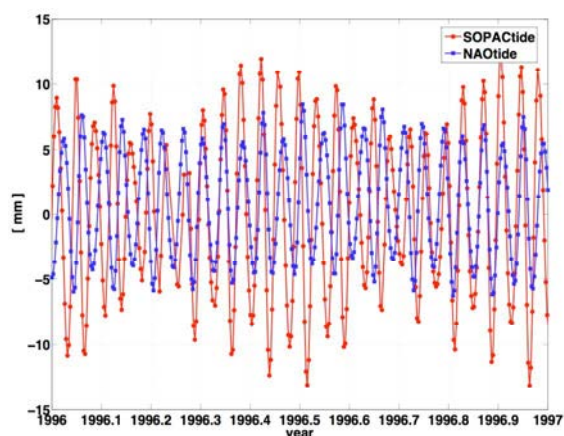


Figure 85: Tidal signal of the vertical component of the station MAS1 (Las Palmas, Spain) from SOPAC (red) and ocean tide loading model GOTIC2⁶⁴ from MATSUMOTO *et al.* 2000.

In fact, most carefully prepared atmospheric and ocean (tide) loading models still differ from actual observations because of weather effects (e.g. wind) and other factors. Meteorological disturbances, usually largest in northern hemisphere winter, have the largest effect on shallow seas. The total level can induce coastal flooding when coinciding with high water. Two other effects may have an immediate impact on sea level. There are local resonant oscillations, called seiches, and waves caused by sub-marine seismic events, called tsunamis. Both seiches and tsunamis are influenced by the local water depths and the shapes of the

⁶⁴ http://www.miz.nao.ac.jp/staffs/nao99/index_En.html

coastlines which they impact. The response of sea-level to wind stress on a rotating Earth turns out to be rather complicated in practice. The water level differences, caused by the so-called Ekman volume transport, have their own influence on water movements. The latter distort the simplicity of Ekman transport dynamics. Well-studied regions showing large surges are, e.g., the North Sea, the west coast of the British Isles, the Atlantic coast of North America, the Bay of Bengal, Japan, the Adriatic, the Baltic Sea, Argentina and Brazil, the coasts of southern China, Hong Kong, the Philippines, Indonesia, Northern Australia and the Queensland coast. Seiches happen in the south coast of Tasmania, the Indian Ocean (e.g. the Seychelles), several Mediterranean ports (e.g. Malta) and the Falkland, being particularly strong because of prevailing winds. The causes of Tsunamis include sub-marine earthquakes, landslides into the sea and sub-marine slumping (PUGH, 2004).

Chapter 6

Inversion for ratios of Load Love Numbers

On the one hand, the Gravity Recovery and Climate Experiment (GRACE) spherical harmonic solutions divulge hydrological-induced signals over continental areas on monthly intervals with a spatial resolution of about 1000 km (WAHR *et al.*, 2004; TAPLEY *et al.*, 2005; LUTHEKE *et al.*, 2006). On the other hand, space geodetic techniques, e.g. GPS and VLBI, allow for an inversion of equivalent load height column changes via estimated station coordinate displacements (BLEWITT AND CLARKE, 2003; KUSCHE AND SCHRAMA, 2005), and additionally, via Earth rotation data (GROSS *et al.*, 2004). In this chapter, we present aspects concerning geoid height changes and geometrical station displacements (lateral and radial) in a separate inversion for spatio-temporal load height column variations closely related to Load Love Numbers. The Load Love Numbers are taken azimuth-dependent to ensure uniqueness and consistency. The goal of this chapter is to set up the theoretical basis that allows one to assess and corroborate the stochastic geometrical model of GPS or VLBI spectral deformation coefficients.

6.1 Introduction

Considering that most mass transports occur on the Earth's surface, at annual and sub-annual time scales, it is possible to invert gravity changes into surface mass redistribution via instantaneous (monthly) geoid height changes (CHAD, 2005). The atmospheric pressure contribution can be modelled and reduced through numerical weather models, e.g. provided by NCEP or ECMWF. Thus, large-scale hydrological mass variations over land areas remain. These can be monitored within a joint integrated or separate inversion of GRACE and GPS data, by using the classical Gauss-Markov least-squares algorithms. The importance of VLBI data lies in the crosschecking for GPS seasonal station displacements at co-located sites. GRACE, polar motion and length of day data offer the possibility of relieving constraints commonly used in the inversion of GPS-derived geometrical displacements (see Figure 86).

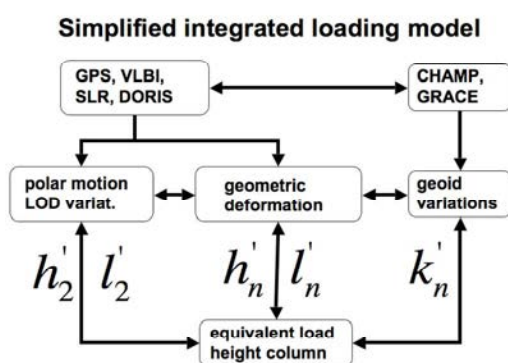


Figure 86: Simplified integrated loading model. On the one hand, space geodetic techniques allow one to derive polar motion and length of day (LOD) variations as well as geometric deformations. These changes can be related to the so-called equivalent load height column (ELHC) through the LLNs h' and l' . On the other hand, satellite gravity missions produce height anomaly variations. These variations are, once again, related to the same ELHC through the LLNs k' . These LLNs are usually only zonal.

6.2 Theoretical aspects

Following the succinct notations of BLEWITT AND CLARKE (2003), let us consider a network of geodetic stations located at geographical positions Ω_i (latitude φ_i , longitude λ_i), which provide time series of

station coordinate 3D-displacements $\mathbf{D}(\Omega_i)$ in the ITRF2000 reference frame. The geocentric displacement function $\mathbf{D}(\Omega_i)$, under the Love-Shida hypothesis that no toroidal displacements exist under a surface-normal load, can be decomposed solely into poloidal components (in a spherical coordinate system, see) e.g. BLEWITT AND CLARKE (2003):

$$D_j(\Omega_i) = \partial_j \Psi(\Omega_i) + H_j(\Omega_i) = \left[\frac{1}{\cos \varphi_i} \partial_\lambda \Psi(\Omega_i) \right] \hat{\lambda} + [\partial_\varphi \Psi(\Omega_i)] \hat{\phi} + [H(\Omega_i)] \hat{\mathbf{r}} \quad (6.2.1)$$

where $\hat{\lambda}$, $\hat{\phi}$ and $\hat{\mathbf{r}}$ are unit vectors pointing eastward, northward and radial, respectively. The functions $\Psi(\Omega_i)$ and $H(\Omega_i)$ are the lateral and radial poloidal scalar respectively. If we assume that the displacements $\mathbf{D}(\Omega_i)$ are harmonic, the poloidal functions can be represented as surface spherical harmonic (SSH) expansions Y_{nm}^Φ :

$$\begin{aligned} \Psi(\Omega) &= \sum_{n=1}^{\infty} \sum_{m=0}^n \sum_{\Phi} Y_{nm}^\Phi(\Omega) \Psi_{nm}^\Phi \\ \underbrace{E(\Omega)}_{\mathbf{I}_E} &= \sum_{n=1}^{\infty} \sum_{m=1}^n \sum_{\Phi} \underbrace{\frac{\partial_\lambda Y_{nm}^\Phi(\Omega)}{\cos \varphi}}_{\mathbf{A}_E} \underbrace{\Psi_{nm}^\Phi}_{\mathbf{x}_{E,N}} \\ \underbrace{N(\Omega)}_{\mathbf{I}_N} &= \sum_{n=1}^{\infty} \sum_{m=0}^n \sum_{\Phi} \underbrace{\partial_\varphi Y_{nm}^\Phi(\Omega)}_{\mathbf{A}_N} \underbrace{\Psi_{nm}^\Phi}_{\mathbf{x}_{E,N}} \\ \underbrace{H(\Omega)}_{\mathbf{I}_H} &= \sum_{n=1}^{\infty} \sum_{m=0}^n \sum_{\Phi} \underbrace{Y_{nm}^\Phi(\Omega)}_{\mathbf{A}_H} \underbrace{H_{nm}^\Phi}_{\mathbf{x}_H} \end{aligned} \quad (6.2.2)$$

where $E(\Omega)$, $N(\Omega)$, and $H(\Omega)$ represent the longitudinal, latitudinal and radial deformation in units of [m] respectively. $\Phi \in \{C, S\}$ identify the cosine and sine components of the SH expansion. Here, we simply ignore the issue of the degree-0 coefficients and refer to MENDES CERVEIRA *et al.* (2006b).

Next we consider a surface load mass distribution $T(\Omega)$, in units of [kg/m²], expanded into SSH:

$$T(\Omega) = \rho_s \sum_{n=1}^{\infty} \sum_{m=0}^n \sum_{\Phi} T_{nm}^\Phi Y_{nm}^\Phi(\Omega) \quad (6.2.3)$$

The surface load SH coefficients T_{nm}^Φ , also called the equivalent load height column coefficients (ELHCC), are given in units of [m], corresponding to a height of a column of seawater (see Figure 87). The density of seawater has the value $\rho_s = 1025$ [kg/m³]. Herein, we assume that $T(\Omega)$ represents the sea level over the oceans and the continental water over the land. Following FARRELL (1972), and BLEWITT AND CLARKE (2003), such a surface load changes the gravitational potential on the Earth's surface by an amount $V_T(\Omega)$:

$$V_T(\Omega) = \sum_{n=1}^{\infty} \sum_{m=0}^n \sum_{\Phi} \frac{3g\rho_s}{(2n+1)\rho_E} T_{nm}^\Phi Y_{nm}^\Phi(\Omega) \quad (6.2.4)$$

where $g = 9.81$ [m/s²] is the mean gravity acceleration on Earth's surface, while $\rho_E = 5517$ [kg/m³] is the mean density of the Earth.

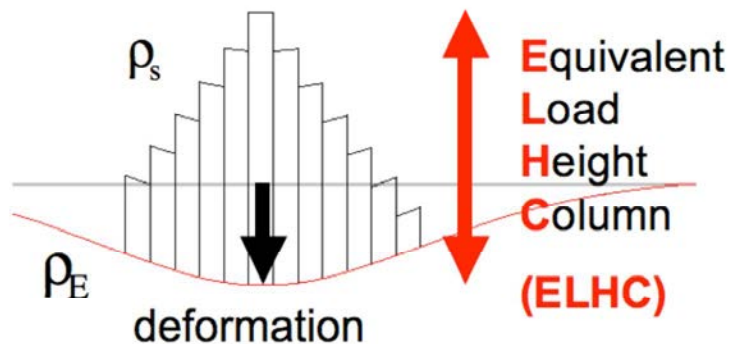


Figure 87: Determination of the height of the load (red arrow), given a measured deformation (black arrow).

On the one hand, the height of the instantaneous geoid variation $R(\Omega)$ above a reference surface (initial or mean geoid, derived from GRACE), is composed of the gravitational potential $V_T(\Omega)$ plus the additional potential $V_K(\Omega) = k'_{nm} V_T(\Omega)$ due to the load-induced deformation:

$$R(\Omega) = \frac{V_T(\Omega) + V_K(\Omega)}{g} = \sum_{n=1}^{\infty} \sum_{m=0}^n \sum_{\Phi} (1 + k'_{nm}) \frac{3\rho_s}{(2n+1)\rho_E} T_{nm}^{\Phi} Y_{nm}^{\Phi}(\Omega) \quad (6.2.5)$$

where k'_{nm} are unitless azimuth-dependent geoid height Load Love Numbers. On the other hand, $R(\Omega)$ may also be expanded into SSH:

$$R(\Omega) = \sum_{n=1}^{\infty} \sum_{m=0}^n \sum_{\Phi} R_{nm}^{\Phi} Y_{nm}^{\Phi}(\Omega) \quad (6.2.6)$$

Equating equations (6.2.5) and (6.2.6), the monthly-reduced geoid geopotential coefficients R_{nm}^{Φ} may be related to the surface load SH coefficients T_{nm}^{Φ} by:

$$R_{nm}^{\Phi} = (1 + k'_{nm}) \frac{3\rho_s}{(2n+1)\rho_E} T_{nm}^{\Phi} = a_{nm} T_{nm}^{\Phi} \quad (6.2.7)$$

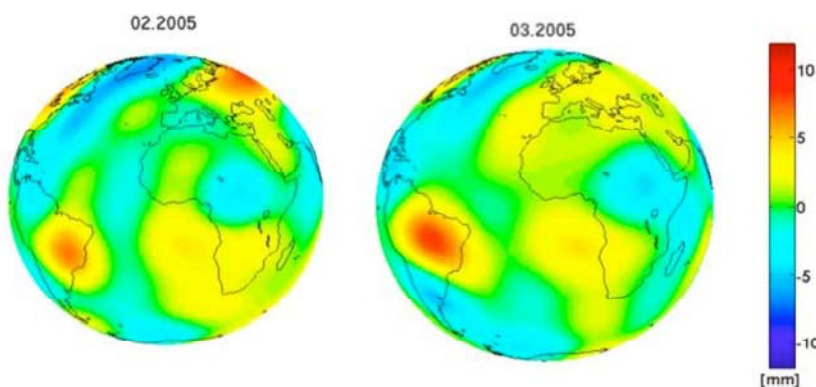


Figure 88: Monthly height anomaly variations derived from the Jet Propulsion Laboratory JPL⁶⁵ constrained geopotential coefficients for February and March 2005.

On the other hand, the geometric displacement coefficients (derived from GPS supported by VLBI coordinate time series at co-located sites) may be related to the equivalent load height column coefficients (e.g. BLEWITT AND CLARKE, 2003):

⁶⁵ http://podaac.jpl.nasa.gov/grace/data_access.html

$$\begin{aligned}
H(\Omega) &= \sum_{n=1}^{\infty} \sum_{m=0}^n \frac{h'_{nm} V_{T,nm}(\Omega)}{g} = \sum_{n=1}^{\infty} \sum_{m=0}^n \sum_{\Phi} h'_{nm} \frac{3\rho_s}{(2n+1)\rho_E} T_{nm}^{\Phi} Y_{nm}^{\Phi}(\Omega) \\
\Psi(\Omega) &= \sum_{n=1}^{\infty} \sum_{m=0}^n \frac{l'_{nm} V_{T,nm}(\Omega)}{g} = \sum_{n=1}^{\infty} \sum_{m=0}^n \sum_{\Phi} l'_{nm} \frac{3\rho_s}{(2n+1)\rho_E} T_{nm}^{\Phi} Y_{nm}^{\Phi}(\Omega)
\end{aligned} \tag{6.2.8}$$

The radial H_{nm}^{Φ} and lateral Ψ_{nm}^{Φ} poloidal coefficients follow as:

$$\begin{aligned}
H_{nm}^{\Phi} &= h'_{nm} \frac{3\rho_s}{(2n+1)\rho_E} T_{nm}^{\Phi} = b_{nm} T_{nm}^{\Phi} \\
\Psi_{nm}^{\Phi} &= l'_{nm} \frac{3\rho_s}{(2n+1)\rho_E} T_{nm}^{\Phi} = c_{nm} T_{nm}^{\Phi}
\end{aligned} \tag{6.2.9}$$

where h'_{nm} and l'_{nm} are height and lateral unitless azimuth-dependent LLN. The latter, usually only degree-dependent, are taken here in the centre of figure (CF) frame (e.g., BLEWITT, 2003) for the Gutenberg-Bullen GB-A Earth model.

Another area for consideration is the Earth rotation parameters. After some rearrangements, the following degree-2 radial spectral coefficients H_{20}^C , H_{21}^C and H_{21}^S can be related (GROSS *et al.*, 2004) to Earth rotation data:

$$\begin{aligned}
H_{20}^C &= -\frac{h'_{20}}{\rho_E} \frac{3}{5} \frac{1}{0.756} \frac{15}{8\pi} \frac{C_m}{R^4} \left[\frac{\Delta\Lambda}{\Lambda_0} - \frac{\Delta h_z}{\Omega C_m} \right] \\
H_{21}^C + jH_{21}^S &= -\frac{h'_{21}}{\rho_E} \frac{3}{5} \frac{1.44}{1.614} \frac{5}{4\pi} \frac{C-A}{R^4} \left[\chi - 1.61 \frac{\Delta \mathbf{h}}{\Omega(C-A)} \right] \\
\chi &= \mathbf{p} + j \frac{1}{\sigma_{CW}} \dot{\mathbf{p}} \quad \mathbf{p} = p_x - jp_y \quad \Delta \mathbf{h} = \Delta h_x + j\Delta h_y
\end{aligned} \tag{6.2.10}$$

where j denotes the imaginary unit, p_x and p_y are the coordinates of the rotation pole, σ_{CW} is the complex-valued frequency of the Chandler wobble, and C_m is the polar moment of inertia of the Earth's crust and mantle. Accordingly, $C-A$ is the difference between polar and equatorial moments of inertia of the whole Earth, Λ_0 is the nominal length of day (LOD) of 86400 seconds, $\Delta\Lambda$ is the variation of LOD, $\Delta h_{x,y,z}$ are changes of relative angular momentum, and Ω is the mean angular speed of the Earth and R is Earth's mean radius.

Similar equations to (6.2.10) can be set up for the degree-2 lateral spectral coefficients Ψ_{20}^C , Ψ_{21}^C and Ψ_{21}^S . But accordingly, the Load Love Numbers l'_{20} and l'_{21} have to be used instead of h'_{20} and h'_{21} , respectively.

Table 15: Azimuth-independent ($m=0$) theoretical conversion factors a_{n0} , b_{n0} and c_{n0} up to degree-11, in the centre of figure frame (CF) for the Gutenberg-Bullen GB-A Earth model.

degree-n	a_{n0}	b_{n0}	c_{n0}	a_{n0} / b_{n0}	a_{n0} / c_{n0}	b_{n0} / c_{n0}
1	0.190	-0.050	0.0250	-3.8000	7.6000	-2.0000
2	0.077	-0.112	0.0032	-0.6875	24.0625	-35.0000
3	0.064	-0.084	0.0060	-0.7619	10.6667	-14.0000
4	0.054	-0.065	0.0038	-0.8308	14.2105	-17.1053
5	0.045	-0.055	0.0025	-0.8182	18.0000	-22.0000
6	0.039	-0.049	0.0018	-0.7959	21.6667	-27.2222
7	0.034	-0.046	0.0014	-0.7391	24.2857	-32.8571
8	0.030	-0.042	0.0011	-0.7143	27.2727	-38.1818
9	0.027	-0.040	0.0009	-0.6750	30.0000	-44.4444
10	0.025	-0.038	0.0008	-0.6579	31.2500	-47.5000
11	0.023	-0.037	0.0007	-0.6216	32.8571	-52.8571

When estimating the coefficients N_{nm}^Φ , H_{nm}^Φ , and Ψ_{nm}^Φ from monthly GRACE geopotential coefficient variations and GPS- and VLBI-derived coordinate time series variations, it is possible to calculate ratios between LLN k'_{nm} , h'_{nm} and l'_{nm} , and compare these ratios to the theoretical ones, which are usually assumed to be solely degree-dependent on the Earth's surface (i.e., k'_n , h'_n and l'_n):

$$\frac{N_{nm}^\Phi}{H_{nm}^\Phi} = \frac{(1 + k'_{nm})}{h'_{nm}}, \quad \frac{N_{nm}^\Phi}{\Psi_{nm}^\Phi} = \frac{(1 + k'_{nm})}{l'_{nm}}, \quad \frac{H_{nm}^\Phi}{\Psi_{nm}^\Phi} = \frac{h'_{nm}}{l'_{nm}} \quad (6.2.11)$$

The part related to Earth rotation and gravity data will not be examined further throughout this thesis. We will only focus on the last item of the equation (6.2.11), which leads to the following remarks:

- it provides formal errors on ratios of LLN
- it allows to check whether the order- m dependence in the LLN is significant
- it examines whether the assumptions (Love-Shida hypothesis) are true for the real Earth
- it enables to estimate the quality of GPS-derived coefficients
- it verifies whether the GPS time series are in a CF frame or not.

Finally, there is no need to know either the density or the kind of the load, as long as a surface-normal load is active.

6.3 Inversion related issues

Due to the no-net translation (NNT) condition imposed on station coordinate variations, as demonstrated in equation (11) by BLEWITT AND CLARKE (2003), the quotient $H_{1m}^\Phi / \Psi_{1m}^\Phi = h'_{1m} / l'_{1m} = -2$ should be satisfied for all orders- m of degree-1, in a CF frame. We remind, however, that e.g. the ratio h'_{1m} / l'_{1m} , when given in a CE (center of mass of the solid Earth) frame for a GB-A Earth model, is approximately -2.57. Thus, only in a CF frame, the geocentric degree-1 displacement $\mathbf{D}_{1G}(\Omega_i)$ reads:

$$\begin{aligned}
\mathbf{D}_{1G}(\Omega_i) &= (\hat{\lambda}\hat{\lambda}^T + \hat{\phi}\hat{\phi}^T) \Psi_1 + \hat{\mathbf{r}}\hat{\mathbf{r}}^T \mathbf{H}_1 \\
&= \left(\underbrace{\hat{\lambda}\hat{\lambda}^T + \hat{\phi}\hat{\phi}^T + \hat{\mathbf{r}}\hat{\mathbf{r}}^T}_{G_1^T G = \mathbf{E}} \right) \Psi_1 - \hat{\mathbf{r}}\hat{\mathbf{r}}^T \Psi_1 + \hat{\mathbf{r}}\hat{\mathbf{r}}^T \mathbf{H}_1 \\
&= \mathbf{E} \Psi_1 + \hat{\mathbf{r}}\hat{\mathbf{r}}^T [\mathbf{H}_1 - \Psi_1] = (\mathbf{E} - 3\hat{\mathbf{r}}\hat{\mathbf{r}}^T) \Psi_1 \\
&= (\hat{\lambda}\hat{\lambda}^T + \hat{\phi}\hat{\phi}^T - 2\hat{\mathbf{r}}\hat{\mathbf{r}}^T) \Psi_1 = G_1^T F G_1 \Psi_1
\end{aligned} \tag{6.3.1}$$

where $\Psi_1 = (\Psi_{11}^C \quad \Psi_{11}^S \quad \Psi_{10}^C)^T$, $\mathbf{H}_1 = (H_{11}^C \quad H_{11}^S \quad H_{10}^C)^T$, the superscript T denoting the transpose, and

$$G_1^T(\Omega_i) = \begin{pmatrix} -\sin \lambda_i & -\cos \lambda_i \sin \varphi_i & \cos \lambda_i \cos \varphi_i \\ \cos \lambda_i & -\sin \lambda_i \sin \varphi_i & \sin \lambda_i \cos \varphi_i \\ 0 & \cos \varphi_i & \sin \varphi_i \end{pmatrix} \quad F = \begin{pmatrix} 1 & 0 & 0 \\ 0 & 1 & 0 \\ 0 & 0 & -2 \end{pmatrix} \tag{6.3.2}$$

The topocentric degree-1 displacement is $\mathbf{D}_{1T}(\Omega_i) = G_1 \mathbf{D}_{1G}(\Omega_i) = F G_1 \Psi_1 = -0.5 F G_1 \mathbf{H}_1$. An elegant way to deal with the NNT condition $2\Psi_{1m}^\Phi + H_{1m}^\Phi = 0$ (containing three equations), is to formulate a least-squares adjustment for the observation equation in the presence of a condition. One could also minimize the Lagrange function Γ :

$$\begin{aligned}
\Gamma &= \mathbf{v}^T \mathbf{P} \mathbf{v} + 2\mathbf{k}^T (\mathbf{B}^T \mathbf{x}) \doteq \min \\
\mathbf{v} + \mathbf{l} &= \mathbf{A} \mathbf{x}
\end{aligned} \tag{6.3.3}$$

where \mathbf{v} is the residuals column vector of the detrended topocentric displacement $\mathbf{D}_{1T}(\Omega_i)$, \mathbf{P} is the weight matrix of the observations \mathbf{l} (detrended $\mathbf{D}_{1T}(\Omega_i)$), \mathbf{B} designates the condition matrix, \mathbf{k} the Lagrange factor (the superscript T denoting again the transpose), and \mathbf{x} is the vector of the unknown coefficients H_{nm}^Φ and Ψ_{nm}^Φ . Each detrended topocentric component of $\mathbf{D}_{1T}(\Omega_i)$ can be taken separately as an observation equation under the control of the NNT condition $2\Psi_{1m}^\Phi + H_{1m}^\Phi = 0$. The trivial solution is given by:

$$\begin{pmatrix} \mathbf{x} \\ \mathbf{k} \end{pmatrix} = \begin{pmatrix} \mathbf{A}^T \mathbf{P} \mathbf{A} & \mathbf{B} \\ \mathbf{B}^T & \mathbf{0} \end{pmatrix}^{-1} \begin{pmatrix} \mathbf{A}^T \mathbf{P} \mathbf{l} \\ \mathbf{0} \end{pmatrix} \tag{6.3.4}$$

For instance, the exclusion of the condition $2\Psi_{1m}^\Phi + H_{1m}^\Phi = 0$ from the equation system (6.3.4) enables one to verify a posteriori whether the GPS coordinate time series (given in the ITRF2000 reference frame) correspond to a CF frame.

For a truncation degree n , there are $2n(n+2)-3$ independent spectral coefficients H_{nm}^Φ and Ψ_{nm}^Φ (see Figure 89), if the complete detrended topocentric displacement $\mathbf{D}_{1T}(\Omega_i)$ is considered. Each station s provides a 3D-displacement with three observations, thus, the minimum number of stations for a non-degenerate network is (see Table 16):

$$s \geq \text{int} \left[\frac{2}{3}n(n+2) - 1 \right] \quad (6.3.5)$$

where int represents the largest integer greater or equal to its argument. Considering the present number and distribution of GPS stations, an expansion till degree and order 11 seems realistic (e.g. MENDES CERVEIRA *et al.*, 2006b). In the case that only detrended east $E(\mathbf{\Omega})$ components are used, then $n(n+1)$ independent coefficients can be estimated. For the north $N(\mathbf{\Omega})$ and for the vertical $H(\mathbf{\Omega})$ components, there remain $n(n+2)$ coefficients respectively (see Figure 89).

Table 16: Minimum number s of well distributed stations in function of the truncation degree n .

n	1	2	3	4	5	6	7	8	9	10	11
s	1	5	9	15	23	31	41	53	65	79	95

As already indicated, the lateral poloidal coefficients Ψ_{nm}^Φ can be estimated twofold, namely from the east and the north components of station coordinate variations, thus enabling a technique-internal cross-validation. The partial derivatives of the longitudinal displacement are trivial as shown in equation (6.3.6). We noted that the east component $E(\mathbf{\Omega})$ was not sensitive to zonal coefficients ($m = 0$):

$$\underbrace{E(\mathbf{\Omega}) + \mathbf{v}_E}_{\mathbf{l}_E} = \sum_{n=1}^{\infty} \sum_{m=1}^n \underbrace{\frac{m}{\cos \varphi_i} P_{nm}(\sin \varphi_i) \begin{bmatrix} -\sin(m\lambda_i) & \cos(m\lambda_i) \end{bmatrix}}_{\mathbf{A}_E} \underbrace{\begin{bmatrix} \Psi_{nm}^C \\ \Psi_{nm}^S \end{bmatrix}}_{\mathbf{x}_E} \quad (6.3.6)$$

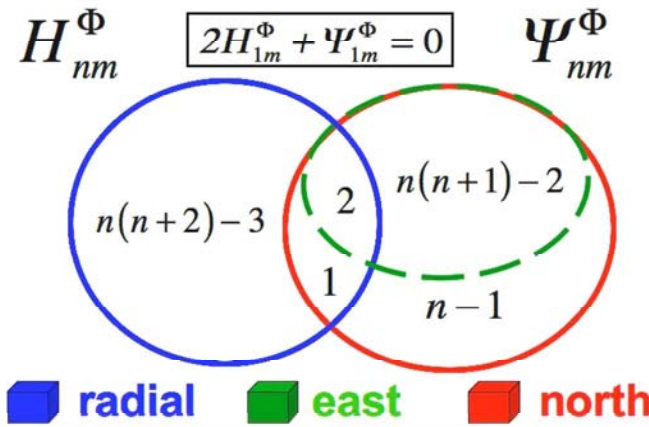


Figure 89: Generally, for a truncation degree n , there are $n(n+2)$ radial poloidal coefficients H_{nm}^Φ sensitive to the radial deformation (in blue), $n(n+1)$ lateral poloidal coefficients Ψ_{nm}^Φ sensitive to the deformation of the east component (in green), and $n(n+2)$ lateral poloidal coefficients Ψ_{nm}^Φ sensitive to the deformation of the north component (in red). So, in total, there are 6 degree-1 poloidal coefficients. However, in a centre of figure frame, where a no-net-translation condition $2\Psi_{1m}^\Phi + H_{1m}^\Phi = 0$ is imposed on station coordinates, the six degree-1 poloidal coefficients melt into one set of three coefficients.

For computing the latitudinal derivatives \mathbf{A}_N of the Legendre functions $P_{nm}(\sin \varphi_i)$, the following 4π -normalized recursion formulas were used (with $t = \sin \varphi$), e.g. HOBSON (1955) or SCHRAMA (1984):

$$\begin{aligned} \bar{P}_{nm}(t) &= \sqrt{(2 - \delta_{0m})(2n+1)} \frac{(n-m)!}{(n+m)!} P_{nm}(t) \\ \frac{\partial \bar{P}_{00}(t)}{\partial t} &= 0 \quad \frac{\partial \bar{P}_{11}(t)}{\partial t} = \frac{-\sqrt{3}t}{\sqrt{1-t^2}} \end{aligned} \quad (6.3.7)$$

$$\frac{\partial \bar{P}_{nm}(t)}{\partial t} = \sqrt{\frac{2n+1}{2n}} \left[\frac{-t}{\sqrt{1-t^2}} \bar{P}_{n-1,n-1}(t) + \sqrt{1-t^2} \frac{\partial \bar{P}_{n-1,n-1}(t)}{\partial t} \right] \quad (6.3.8)$$

$$\begin{aligned}
\frac{\partial \bar{P}_{n,n-1}(t)}{\partial t} &= \sqrt{2n+1} \left[\bar{P}_{n-1,n-1}(t) + t \frac{\partial \bar{P}_{n-1,n-1}(t)}{\partial t} \right] \\
\frac{\partial \bar{P}_{n,m}(t)}{\partial t} &= \sqrt{\frac{(2n+1)(2n-1)}{(n-m)(n+m)}} \left[\bar{P}_{n-1,m}(t) + t \frac{\partial \bar{P}_{n-1,m}(t)}{\partial t} \right] \dots \\
&\quad - \sqrt{\frac{(2n+1)(n+m-1)(n-m-1)}{(n-m)(n+m)(2n-3)}} \frac{\partial \bar{P}_{n-2,m}(t)}{\partial t}
\end{aligned} \tag{6.3.9}$$

It is remarkable that one single 3D-displacement of one single station is theoretically sufficient to determine degree-1 coefficients H_{1m}^Φ , if higher degrees (especially correlations due to the degenerate network) are ignored:

$$\begin{pmatrix} H_{11}^C \\ H_{11}^S \\ H_{10}^C \end{pmatrix} = -2G_1^T F^{-1} \begin{pmatrix} E_i \\ N_i \\ H_i \end{pmatrix} = \begin{pmatrix} 2 \sin \lambda_i & 2 \cos \lambda_i \sin \varphi_i & \cos \lambda_i \cos \varphi_i \\ -2 \cos \lambda_i & 2 \sin \lambda_i \sin \varphi_i & \sin \lambda_i \cos \varphi_i \\ 0 & -2 \cos \varphi_i & \sin \varphi_i \end{pmatrix} \begin{pmatrix} E_i \\ N_i \\ H_i \end{pmatrix} \tag{6.3.10}$$

Differences in amplitude and phase of the equivalent load coefficients T_{nm}^Φ between GRACE and GPS (and Earth rotation data derived coefficients) have been reported (e.g., KUSCHE AND SCHRAMA, 2005). Such differences should be investigated first before being absorbed by a combined all-in-one least-squares adjustment seeking for the height load coefficients T_{nm}^Φ . In fact, we noticed from the equations (6.2.7) and (6.2.8), that there are four ways (when neglecting Earth rotation data) of deriving equivalent load height coefficients T_{nm}^Φ , bearing in mind, however, that the east component does not give a result for zonal coefficients.

For crosschecking purposes, we derived the analytical form of the partial derivatives of the geometric deformation w.r.t. the radial (U) and lateral (E,N) degree-2 poloidal coefficients (PC) (see Table 17 and Table 18). In this way, persistent numerical bugs in deriving the partial derivatives in latitude could be checked, verified and corrected.

Table 17: Partial derivatives of the geometric deformation w.r.t. the radial degree-2 poloidal coefficients (PC), which are only sensitive to the radial deformation U.

PC	H_{20}^C	H_{21}^C	H_{22}^C	H_{21}^S	H_{21}^S
U	$\frac{1}{2}(3 \sin^2 \varphi - 1)$	$\frac{3}{2} \sin 2\varphi \cos \lambda$	$3 \cos^2 \varphi \cos 2\lambda$	$\frac{3}{2} \sin 2\varphi \sin \lambda$	$3 \cos^2 \varphi \sin 2\lambda$

Table 18: Partial derivatives of the geometric deformation w.r.t. the lateral degree-2 poloidal coefficients (PC), which are only sensitive to the east (E) and north (N) deformation.

PC	Ψ_{20}^C	Ψ_{21}^C	Ψ_{22}^C	Ψ_{21}^S	Ψ_{21}^S
E	0	$-3 \sin \varphi \sin \lambda$	$-6 \sin \varphi \sin 2\lambda$	$3 \sin \varphi \cos \lambda$	$6 \cos \varphi \cos 2\lambda$
N	$3 \cos \varphi \sin \varphi$	$3 \cos 2\varphi \cos \lambda$	$-3 \sin 2\varphi \cos 2\lambda$	$3 \cos 2\varphi \sin \lambda$	$-3 \sin 2\varphi \sin 2\lambda$

Chapter 7

Spectral approximation

This chapter is devoted to estimating stable deformation coefficients, which, in turn, can be converted into equivalent height coefficients T_{nm}^{Φ} of a column of seawater. Moreover, we will estimate the ratios of low-degree poloidal coefficients to check Earth's mechanical properties. To achieve our goal, the data of 675 stations were obtained from the Scripps Orbit and Permanent Array Centre (SOPAC). We chose the SOPAC data, because the combined International GNSS Service (IGS) data showed evident seasonal irregularities and aliasing effects (MENDES CERVEIRA *et al.*, 2006a). As mentioned in Chapter 5, the contribution of COD to the combined IGS coordinate time series is not negligible, but re-processing of the combined IGS solution has not been performed so far. To overcome aliasing effects, high-frequency spatial local variations, and high correlations between the estimated harmonic coefficients, we adopted an iterative 2D-interpolation approach, based on input from low-degree spherical harmonic coefficients with a spatial resolution of 10 degrees for longitude and latitude. Considering the assumption that the radius of a spherically symmetric Earth model is not supposed to change because of the Earth's constant mass, we tested two options: one with and one without setting degree-0 to zero. One half of the amplitude of degree-0 coefficient will be absorbed by the zonal degree-2 coefficient, if the former is not estimated.

7.1 Background

BLEWITT *et al.* (2001) presented a new global mode of Earth deformation using five years of GPS data, acquired by 66 stations of the IGS network. Free network solutions (HEFLIN *et al.*, 1992) in the centre of mass (CM) frame were analyzed to produce site coordinate time series in the centre of figure (CF) frame. In that paper, a maximum downward deformation of 3mm was found, pointing close to the North Pole during February to March, and to the South Pole during August to September. WU *et al.* (2002) have pointed out that the CF approximation for the centre of network (CN) in the inversion for load coefficients introduces non-negligible errors. Moreover, they have shown that it is difficult to retrieve all significant harmonics when using a sparse and uneven GPS network lacking of coverage in the polar areas, oceans and southern hemisphere. In addition, they stated that if load-induced deformation components of higher degrees are not estimated, the inverted results for the degree-1 load and geocentre motion are contaminated. BLEWITT AND CLARKE (2003) used the published empirical seasonal model of degree-1 deformation, described in BLEWITT *et al.* (2001), to weigh sea level in static equilibrium with surface mass redistribution.

Recently, KUSCHE AND SCHRAMA (2005) used a different method to deal with the problem of lacking of coverage, where pseudodata is replaced by an analytical augmentation of the least squares cost functional, i.e., using an ocean load variability constraint. In their paper, they find similar patterns of annual variations of continental mass redistribution from IGS and GRACE data, as well as from a global hydrology model. Nevertheless, they also point out systematic differences between these three data sets.

7.2 Approach

The SOPAC model takes into account coordinate offsets (e.g. co-seismic) and linear velocities. Additionally, SOPAC analysts estimate annual and semi-annual fluctuations for stations that have at least one and two years' worth of data, respectively, which are updated on a regular basis. The input data for their model are the daily processed site positions calculated at SOPAC by using the GAMIT and GLOBK software packages (KING AND BOCK, 2005).

No changes and no additional transformations were applied to the SOPAC data. Annual and semi-annual amplitudes and their phases were taken as provided by SOPAC. These were used to derive synthetic station coordinate time series, as input for the SH expansion. Besides, we also took a few SOPAC coordinate time series, but only for the purpose of investigating temporal aliasing effects (see section 7.3). For extensive details concerning the pre-processing and processing of the GPS data at SOPAC, we referred to the thesis of NIKOLAIDIS (2002) that can be downloaded from the SOPAC homepage⁶⁶.

We thus choose a global network (see Figure 90a) of 609 GPS stations among 675 (downloaded from SOPAC on August 7th, 2005) fulfilling the requirements that, for that specific epoch,

- the standard deviations of annual amplitudes in the horizontal components (north and east) are smaller than 1 mm (see Figure 90b), and, in the vertical component, smaller than 2.5 mm
- the standard deviations of semi-annual amplitudes in the horizontal components are smaller than 0.75 mm, and in, the vertical component, smaller than 1.75 mm.

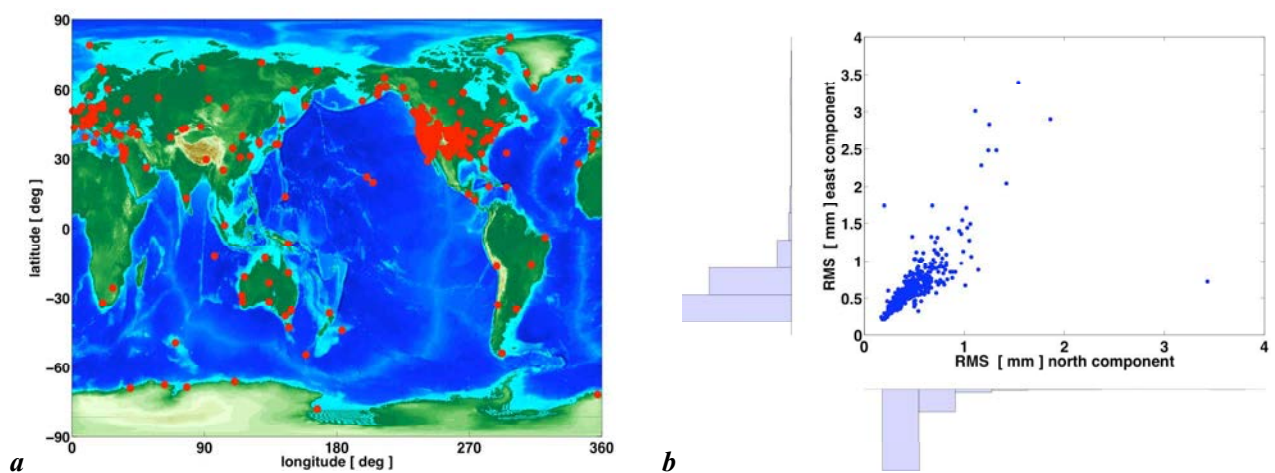


Figure 90: Selected station distribution (609 SOPAC stations) fulfilling specific requirements (see text) (a), and RMS of lateral annual amplitudes (b).

In order to overcome spatial aliasing effects mentioned in Wu *et al.* (2002, 2003), we performed an iterative 2D-interpolation approach with a spatial resolution of 10 deg for longitude and latitude. This iterative approach consisted of three main steps: Firstly, we estimated degree-1 spectral coefficients from the irregular sampled data. Secondly, we performed a gridded 2D-interpolation with a spatial resolution of 10 degrees, based upon the degree-1 coefficients, which were estimated previously. Thirdly, we added the irregular sampled vertical components to this 2D-grid, and estimated degree-2 coefficients. The iteration was carried out till degree-11. These 2D-interpolation pseudo-data formed our constraints. By this method, the 1827 ($=3 \times 609$) GPS coordinate time series (in the ITRF2000) were inverted into monthly spherical harmonics series up to degree- and order-11. The pseudo-observations obtained from the 2D-interpolation were weighted by unity, whereas the synthetic real SOPAC data were weighted by two. In order to evaluate the effect of truncation at a lower degree, a comparison of the previously estimated coefficients versus the coefficients derived from an expansion till degree and order seven shows maximum differences of 0.3 mm. Moreover, a comparison of this degree-11 expansion versus the point-by-point SOPAC data does not show any abnormal aliasing effects. A spatial resolution of 10 degrees spacing is a judicious choice, as the role of the pseudodata should only convey the stabilization of the normal equation system. With respect to a ten-degree spacing, a five-degree spacing experiment shows apparently the same pattern in the variation of

⁶⁶ <http://sopac.ucsd.edu/>

coefficients. However, there is a maximum increase of 0.4 mm in the amplitude spectrum of degree-1, as well as a maximum decrease of 0.3 mm in the degree-2 and degree-5 spectrum. Other spectrum degrees are not influenced by more than 0.2 mm. In fact, the horizontal displacement components show a random spatial pattern. However, the horizontal deformation is also the gradient of the lateral poloidal function.

7.3 Temporal aliasing effects

PENNA AND STEWART (2003), and STEWART *et al.* (2005) argue that temporal aliasing effects are mainly a function of the design of the GPS constellation, the length of the processing session and the quality of tidal models applied in the GPS data processing procedure. They give evidence that this kind of aliasing effects might result in incorrect conclusions drawn from GPS coordinate time series, regarding the presence of seasonal crustal motions. A heuristic spectral analysis of SOPAC height time series, using a software routine provided by MAUTZ (2001), revealed significant energy for around 13.66 days. This period was also obtained from a Fourier analysis (see Figure 91a for station BAHR, Bahrain). This period is also predicted from the GPS sidereal orbit aliasing effect for both M_2 and O_1 tidal constituents. However, this period could also be attributed to the lunar fortnightly M_f tidal constituent. In NIKOLAIDIS (2002) we found out that ocean tide loading and pole tide were only modelled after November 26th, 2000. However, the 13.66-day period also shows up for sites far from the coast (see Figure 91b for station WTZR, Wettzell). This brings us to the conclusion that this period cannot uniquely be attributed to unmodelled ocean loading. It is not within the scope of this thesis to provide further explanation for this phenomenon.

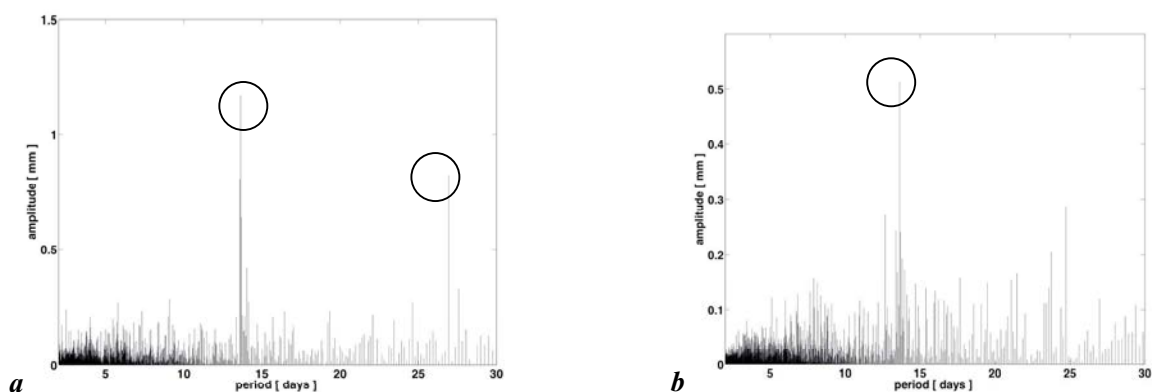


Figure 91: Fourier analysis of the vertical deformation for the stations (a) BAHR and (b) WTZR. The period window is limited from two to thirty days.

Another investigation, of the tidal potential catalogue made available by KUDRYAVTSEV (2004) including 28806 waves, was carried out to check which frequencies of the tidal potential alias into longer periods due to the 24-hour GPS processing and the period of the GPS repeat orbit (23.93444 hours), using the following formula (PENNA AND STEWART, 2003):

$$f' = \left| f - \frac{1}{\Delta t} \text{integer}(f\Delta t + 0.5) \right| \quad (7.3.1)$$

where f' is the aliased frequency, f is the original frequency of the signal, Δt is the sampling interval, and the “integer” function returns the largest integer less than or equal to its argument.

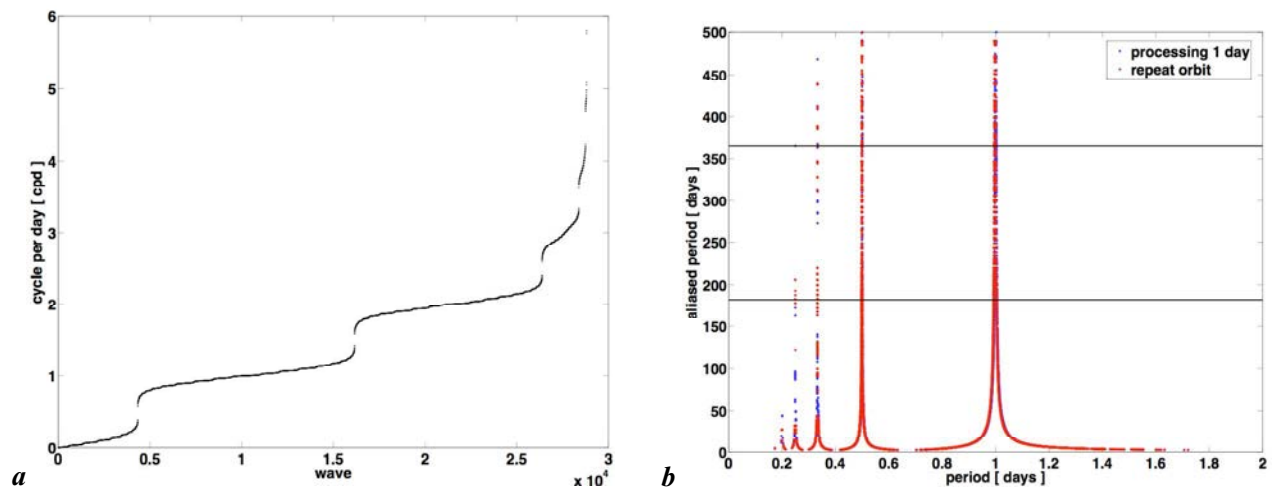


Figure 92: Tidal waves (28806) of the tidal potential catalogue (KSM) of KUDRYAVTSEV (2004) (a), and (b) aliased periods derived from the KSM tidal catalogue with the 24-hours-processing period (blue) and GPS repeat orbit period (red).

One result of this investigation is that many waves around 1 cycle per day (cpd) alias into annual and semiannual periods, due to the 24-hours processing strategy and the sidereal repeat orbit of GPS satellites (see Figure 92).

7.4 Degree-0 investigation

The degree-0 coefficient H_{00}^C represents an apparent scale variation in the GPS SOPAC coordinate time series. LAVALLEE AND BLEWITT (2002), BLEWITT AND CLARKE (2003), and GROSS *et al.* (2004) start the expansion of the height function H_{nm}^Φ with degree-1, stating that the existence of a degree-0 would imply an average change of the Earth's radius and a degree-0 load different from zero. In theory, e.g., in a SNREI Earth model, such a radial variation is not permitted, with the assumption that the total surface mass (i.e. oceans and atmosphere) is constant because of the conservation of mass. But, on a real Earth, nothing prevents the Earth's radius from shrinking or expanding. Here, the meaning of H_{00}^C differs completely from the meaning of the coefficient derived from the gravitational potential. In the latter case, the degree-0 coefficient is effectively a function of the Earth's mass. Geometry and matter are related by density. If the volume changes, the density may change proportionally, without affecting the mass. We investigated two options: one with and one without setting degree-0 to zero, first to evaluate the pattern of H_{00}^C , and second to test its effect on the zonal degree-2 coefficient H_{20}^C .

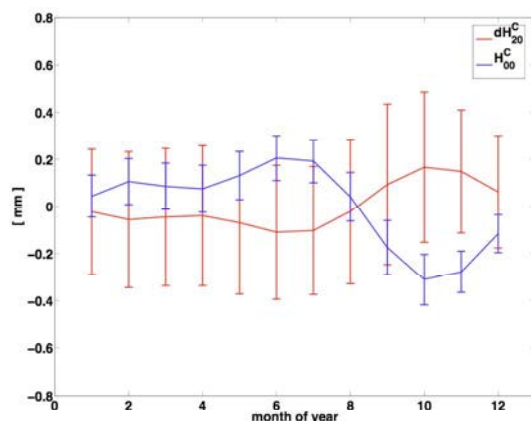


Figure 93: Temporal variation of the radial degree-0 poloidal coefficient in blue (a), and of the (b) difference of the radial zonal degree-2 coefficient in red (by fixing degree-0 to zero or not fixing it). The coefficient H_{20}^C absorbs approximately one half of the amplitude of coefficient H_{00}^C , if the latter is not estimated.

From Figure 93 we may derive that the Earth's radius apparently seems to be shrinking from October to November (-0.3 mm), w.r.t. ITRF2000. However, the degree-0 coefficients are possibly biased due to Helmert transformations applied to the SOPAC data set. Hence, degree-0 is subject to frame-related errors. Systematic errors of the orbit models may be removed by applying seven- or fourteen-parameter transformations, but the latter also remove the apparent scale due to loading signals, that are aliased by the uneven and sparse GPS network. Such transformations lead to frame errors and may bias the load signals. From inspecting Figure 93 it appears that coefficient H_{20}^C absorbs approximately one half of the amplitude of coefficient H_{00}^C , if the latter is not estimated.

7.5 Degree-1 investigation

Degree-1 conveys a real (seasonal) motion of the solid Earth's centre of mass. As pointed out by *WU et al.* (2002) degree-1 deformation may be considered as equivalent to geocentre motion. In the same paper they argue that degree-1 is insufficient to represent surface loading deformations: the SH expansion should be done at least to degree and order six. *FARRELL* (1972) and, subsequently, *BLEWITT AND CLARKE* (2003) derive that degree-1 deformation (from a surface displacement field in poloidal functions) is not a pure translation, because only three out of six coefficients are independent due to the no-net translation condition imposed on station coordinates (see Figure 89). However, we interpret the degree-1 height displacement coefficients as a translation. Figure 94 shows the temporal variation of the degree-1 coefficients. Before the seven-parameter transformation is applied to the station coordinates, the degree-1 gravity coefficients are set to zero for GPS orbital integration. Thus the fiducial-free solution is in the centre of mass of the Earth's system (CM) frame. But the CM link is rather weak, which is reflected by the large uncertainties in such solutions (personal communication *WU*, 2005). After the 7-parameter transformation, the coordinate origin is then fixed to the ITRF2000 origin, which is realized by constant and linear coordinates of the ITRF2000 coordinates. At the seasonal scale, since no motion is allowed for the ITRF2000 stations, the ITRF2000 origin is closer to the centre of network (CN) than to the CM frame. Having used coordinates in the ITRF2000 (considered as a CF frame), we deduce from Figure 94 that a local minimal z-shift of -1.8 mm takes place from March to April, a maximum x-shift of 1.5 mm from August to September, and a maximum y-shift of 0.8 mm from July to August. This y-shift points towards the Asian continent where large positive vertical seasonal deformations occur at that epoch.

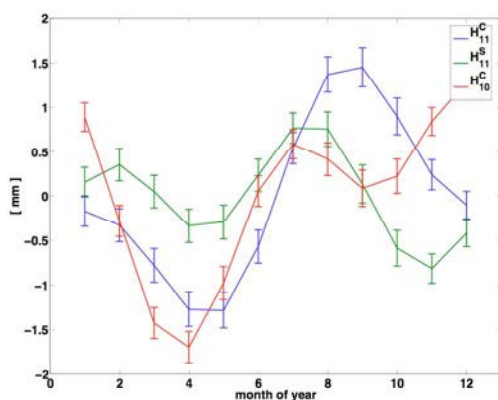


Figure 94: Temporal variation of the radial degree-1 poloidal coefficients.

Table 19 shows the discrepancy of our radial degree-1 poloidal coefficients w.r.t. the ones published in *BLEWITT AND CLARKE* (2003). In our study, the annual amplitude of the sectorial coefficients H_{11}^Φ is larger than that of the zonal coefficient H_{10}^C . A probable cause for this difference could originate from the different epochs under consideration. *BLEWITT AND CLARKE* (2003) used IGS data from 1996 to 2001. A

surprising diminution in amplitude of the variation in the z-component of the load moment vector from 2002 upwards is obvious in Figure 3 of KUSCHE AND SCHRAMA (2005), which seems to validate present results.

Table 19: Comparison of degree-1 coefficients H_{lm}^Φ from GPS inversion between BLEWITT AND CLARKE (2003) (denoted by BaC) and our study (OS). AA=Annual Amplitude [mm], SA=Semi-annual Amplitude [mm], AP=Annual Phase [deg], SP=Semi-annual Phase [deg], using the same conventions as BLEWITT AND CLARKE (2003). Here, only the radial deformation has been used.

		AA	AP	SA	SP
BaC	H_{10}^C	2.97 ± 0.12	236 ± 2	0.67 ± 0.12	27 ± 10
	H_{11}^C	0.90 ± 0.15	266 ± 9	0.31 ± 0.15	249 ± 26
	H_{11}^S	1.30 ± 0.13	165 ± 6	0.27 ± 0.12	121 ± 25
OS	H_{10}^C	1.22	279.56	0.37	74.38
	H_{11}^C	1.61	171.77	0.70	95.25
	H_{11}^S	2.22	156.61	0.57	44.16

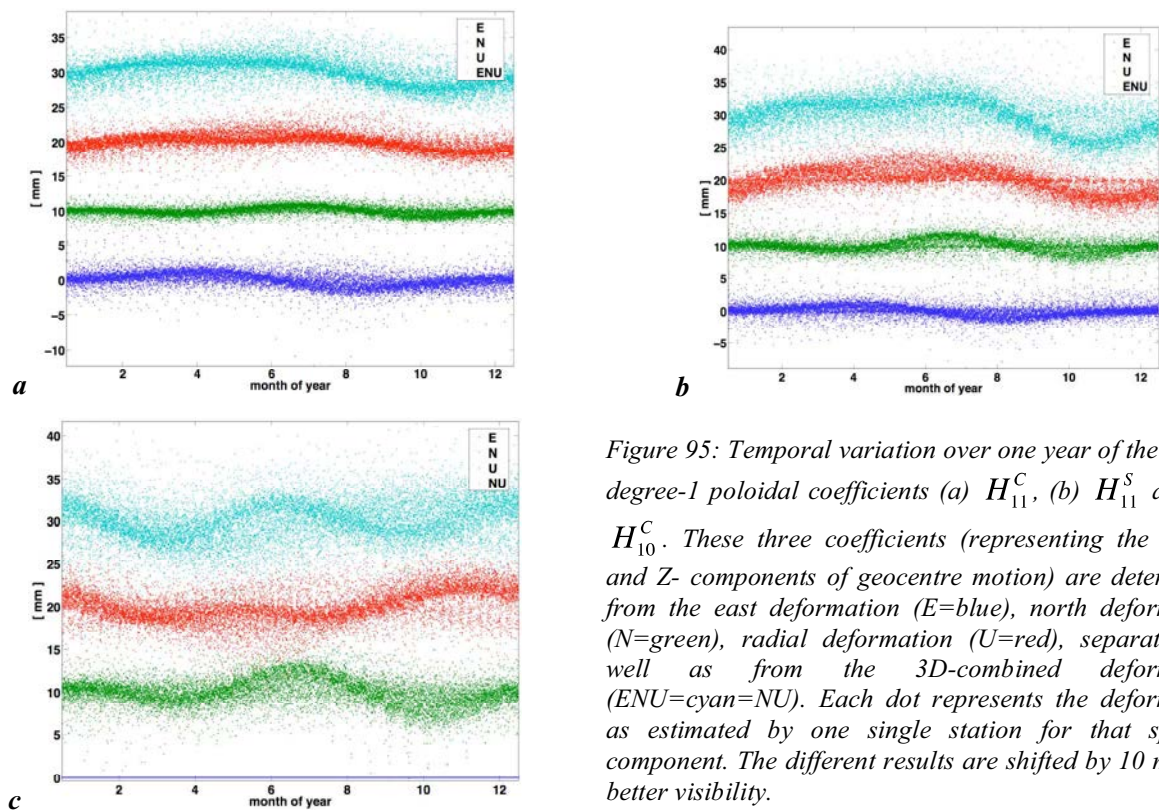


Figure 95: Temporal variation over one year of the radial degree-1 poloidal coefficients (a) H_{11}^C , (b) H_{11}^S and (c) H_{10}^C . These three coefficients (representing the X-, Y- and Z- components of geocentre motion) are determined from the east deformation (E=blue), north deformation (N=green), radial deformation (U=red), separately as well as from the 3D-combined deformation (ENU=cyan=NU). Each dot represents the deformation as estimated by one single station for that specific component. The different results are shifted by 10 mm for better visibility.

Figure 95 shows the temporal variation of the three radial degree-1 poloidal coefficients over one year, estimated from geometric deformations using equation (6.3.10) of 609 SOPAC stations. The results are shown site by site, for each component separately, and combined. Obviously, the radial deformation rules the degree-1 poloidal coefficients, while the lateral deformation mainly adds noise. Each dot represents the deformation as estimated by one single station for that specific component.

7.6 Degree-2 investigation

The degree-2 coefficients H_{2m}^Φ are related to the Earth's inertia tensor (postulating a constant density), and hence to changes in Earth rotation (VARGA *et al.*, 2004). Changes in H_{20}^C can be referred to variations in length-of-day (LOD), changes in H_{21}^C and H_{21}^S to polar motion excitation. Thus, these GPS-derived height displacement coefficients allow a comparison with observed Earth rotation changes, after removing tidal and motion effects, e.g., winds and currents. GROSS *et al.* (2004) investigate degree-2 mass loads from GPS. They state that low-degree SH coefficients determine the surface density (mass load) that is acting to change the Earth's shape. But, on the other hand, if a load variation is known, then Load Love Numbers may be computed to test Earth's mechanical properties (BLEWITT *et al.* 2001; BLEWITT AND CLARKE, 2003). Figure 96ab shows the temporal variation of radial and lateral degree-2 poloidal coefficients. The flattening of the Earth, described by H_{20}^C , is maximal from September to October (4 mm) and should theoretically slow down the angular speed of Earth's rotation axis during that month. Generally, the variation of coefficient H_{22}^C represents an asymmetry of the equatorial axis with regard to the rotational axis or in other words an ellipticity of the equator, and the variation of coefficient H_{22}^S indicates that the principal axes of the vertical deformation oscillate around the conventional X (Greenwich meridian) and Y directions. Figure 97 presents the angular variation α of the principal axes of the vertical deformation, w.r.t. the Greenwich meridian, estimated by:

$$\alpha = \frac{1}{2} \operatorname{atan} \left(\frac{H_{22}^S}{H_{22}^C} \right) \quad (7.6.1)$$

A rapid angular variation α is noticed from February to April.

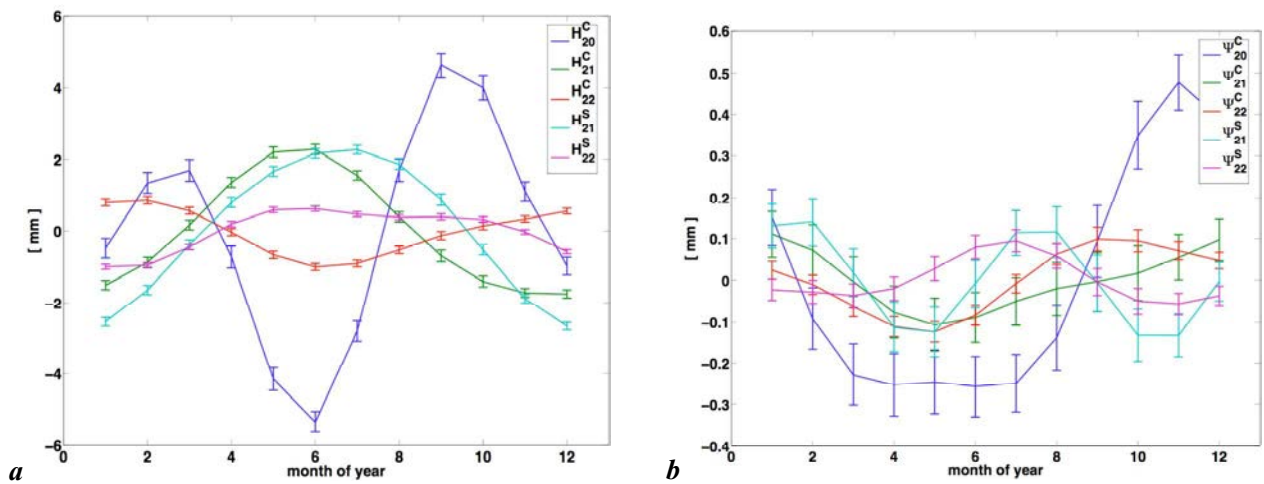


Figure 96: Temporal variation of (a) the radial and (b) the lateral degree-2 poloidal coefficients.

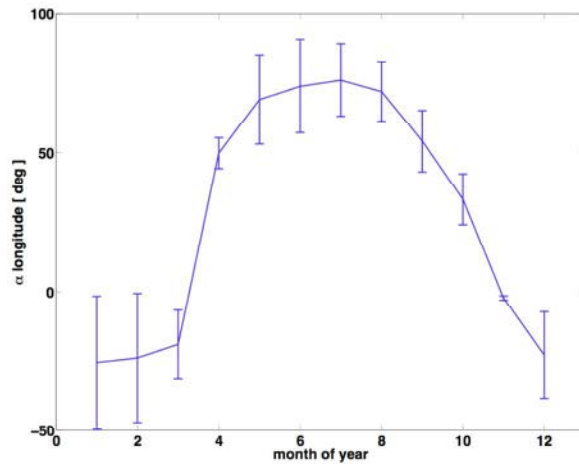


Figure 97: Angular variation of the principal axes of the vertical deformation w.r.t. the Greenwich meridian.

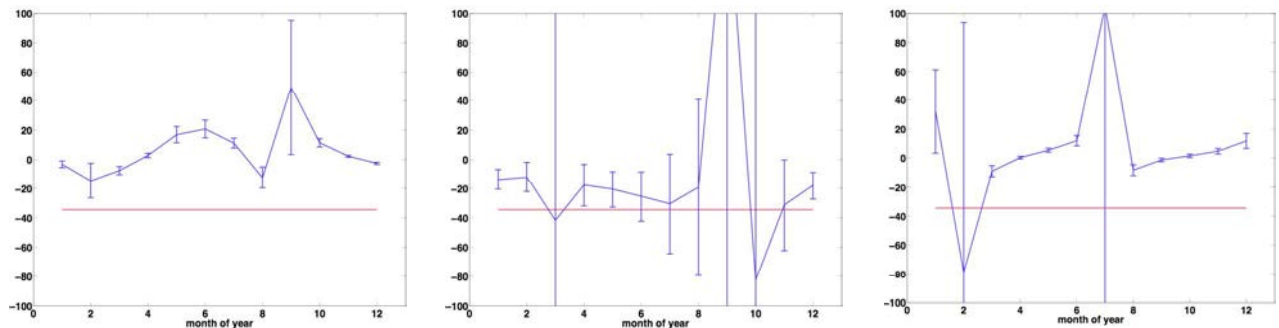
7.7 Ratios of degree-2 poloidal coefficients

Generally, if the load is available, and assuming known mechanical properties of the Earth, then the geometric displacement can be computed. If the deformation is measured, assuming known mechanical properties, then the load may be recovered. If the load and the deformation are known, then the mechanical properties of the Earth can be tested. But, what can be deduced when only the deformation is measured? In that case, we can test Earth's mechanical properties by estimating the ratios of the radial and lateral poloidal coefficients H_{nm}^{Φ} and Ψ_{nm}^{Φ} . We do not need to know:

- the density of the load
- the kind of the load (arising due to atmospheric pressure loading, ocean tide loading etc.)

as long as a surface-normal load is at the origin of the deformations.

In a first attempt, results will be presented for the ratios of the degree-2 poloidal coefficients (see Figure 98). The expected value of these ratios is -35.0 for a Gutenberg-Bullen (GB-A) Earth model in a centre of figure (CF) frame. First, we conjecture that, presently, the ratios of LLNs are much more stable than the ratios of PC can ever be. Special attention is given to the ratios of the cosine tesseral degree-2 PC, which show by far the largest formal errors. The discrepancy of the estimated ratios with regard to a theoretical Earth model, should be a sign that something is partly wrong in the poloidal coefficients of the spectral deformation derived from GPS. One potential explanation can be given on hindsight: the lateral poloidal coefficients could be at the origin, due to the spatial chaotic pattern in the lateral deformation.



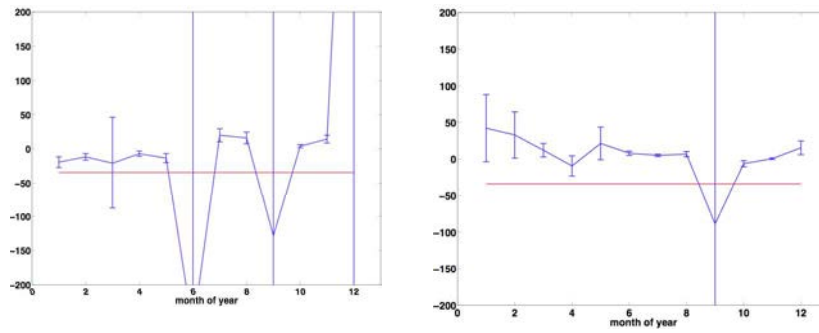


Figure 98: Ratios of degree-2 poloidal coefficients H_{20}^C / Ψ_{20}^C , H_{21}^C / Ψ_{21}^C , H_{22}^C / Ψ_{22}^C , H_{21}^S / Ψ_{21}^S and H_{22}^S / Ψ_{22}^S (from left to right, from top to bottom). The y-axis is unitless. The red line is the ratio of the height and lateral degree-2 LLNs, for a GB-A Earth model, in a CF frame.

Chapter 8

Conclusions

8.1 Summary of results and remarks

One global target of space geodesy is to monitor mass transports occurring on the Earth's surface. These mass transfers are closely related to geometric deformations through special factors, commonly called Load Love Numbers. Starting with the tidal potential, the basic theory on Love Numbers, and Load Love Numbers, has been presented in Chapter 3.

Thereafter, we made a thorough comparison of deformations computed from available atmospheric loading models. The largest uncertainty of such models can be attributed to the inability to correctly verify over which oceans the inverted barometer assumption holds. Presently, only the IB or NIB assumptions are taken for granted, without allowing for intermediate steps in the response of the oceans and seas.

We demonstrated in Chapter 5 that we were not able to evaluate the effect of constraints on station coordinates and baseline lengths for those GPS ACs that provide constrained coordinate solutions. Moreover, the number and location of transforming stations influences, up to the cm level, station coordinate solutions. The determination of the various centres of frame will be a point of discussion in the next decades to come. The determination of geocentre motion is not yet a fully closed chapter. On a global level, the ten GPS coordinate solutions agree at the sub-cm level RMS. Prior to summer 2004, the COD vertical coordinate time series divulged large apparent seasonal signals in the vertical component in the order of 2 cm that are now proved to be non-existent. The improvement of repeatability from baseline lengths after applying atmospheric loading models is tiny due to many aliasing effects (TREGONING AND VAN DAM, 2005b). Atmospheric loading effects exist and there is good evidence that not all of the applied loading corrections actually change the station coordinates (and, accordingly, the baseline lengths). The repeatability of baseline lengths includes a mixture of noise, signals and, to some degree, undetected small breaks. Investigating repeatabilities versus a weighted best-fit straight line does not separate information of seasonal signals from noise.

The seasonal deformation of coordinate time series is closely connected to variations of a so-called equivalent load height column. The theoretical approach, including the relation between geometric deformations, height anomaly, polar motion and LOD variations, has been discussed in Chapter 6. In artificial cases, i.e. when mass redistribution compensates the effect of height displacement, it is possible to obtain a non-zero LLN h'_0 (VARGA, 1983). However, as the LLN h'_0 practically does not influence the results of load-induced deformations, most authors simply disregard it.

Despite the low magnitude of lateral Load Love Numbers l'_n , the relative information of horizontal displacements is usually assumed to be significant, as horizontal variances are typically ten times smaller than vertical variances for global referenced station coordinates. However, due to the random spatial distribution, we emphasize in Chapter 7 that, so far, the deformation in the lateral components mainly adds noise. This topic needs to be more widely researched in future. Our iterative 2D-interpolation approach is one possibility to obtain stable spectral coefficients from a sparse and uneven GPS network lacking coverage in many areas. We showed that conservation of the Earth's mass influences the zonal degree-2 coefficient H_{20}^C significantly in the order of 0.5 mm. However, it must be emphasized that our results are only valid under the assumption that other error sources with seasonal periods, which might cause apparent geophysical deformations, e.g., deficiencies in the used mapping functions for high latitudes (BOEHM AND SCHUH, 2004), have been completely removed prior to our analysis. In this context, very recent studies (BOEHM *et al.*, 2006b) show that the impact of the new Vienna Mapping Functions 1 (VMF1) reduces

seasonal signals in station height time series significantly over many regions of the globe. However, these new mapping functions are not yet routinely used in GPS software analysis packages.

The values of the estimated ratios of poloidal coefficients, which disagree versus the ones computed for the GB-A Earth model, could be an indication that the deformations derived by GPS do not yet match the requirements of the Love-Shida hypothesis. On the whole, a thorough combination of space geodetic observations including information from recent gravity missions must be the dedicated goal of the space geodetic community.

8.2 Directions for future research

Currently, the Gravity Recovery and Climate Mission (GRACE) is considered as one of the key scientific instruments for the determination of superficial mass transports. In the future, the aim should consist in developing a consistent strategy for an inter-technique joint inversion. In clarity, the observables for this joint inversion should, in that perspective, contain:

- time series of site deformations from space geodetic techniques GPS, VLBI, SLR and the Doppler Orbitography and Radiopositioning Integrated by Satellite (DORIS)
- height variations of the ocean seafloor obtained from ocean bottom pressure (OBP) measurements from hydrographic and oceanographic data sources
- temporal height anomaly variations derived from combined GRACE geopotential coefficients
- Earth rotation data, i.e. polar motion and length of day (LOD) variations, as degree-2 constraints

One assumption in using the time series of site deformations is that the remaining deformations are solely due to surface-normal loads. The impact of the tidal and non-tidal atmospheric contributions can readily be removed by using numerical weather models. Tidal mass variations are pre-reduced from the raw observables of GPS and GRACE. In the deeper Earth, mass redistribution occurs on much larger timescales. Thus, one conjecture is that the remaining mass variations uniquely stem from oceanic and hydrologic origins. OBP variations deform the ocean floor and the continental crust near the coasts, and should be a measurable quantity in GPS deformations. Height anomaly variations, directly linked to the gravity field as a first integral, sense mass redistributions instantaneously. In addition, GPS site load-induced deformations are sensitive to the loading of the Earth. One shortcoming of GPS, VLBI, SLR and DORIS is that sites are sparse for ocean areas and heterogeneous on continental areas. However, a consistent combination, in a joint inversion of geometric surface deformation from GPS site deformation, OBP information, height anomaly variations, and Earth rotation data is expected to substantially improve the detection of mass redistribution on all spatial scales. Furthermore, it allows for intra and inter-technique cross-validations on a statistical basis. In addition, we single out one major advantage of the GPS inversion technique: It is along with SLR a technique sensitive to geocentre motion. The dedicated target in the next decade should be to significantly extend the degree of spherical harmonics sensitive to global mass redistribution up to degree 15. A combined inversion should avoid the flaws of individual solutions as far as possible, by accounting for data variance-covariance information, site distribution and the individual sensitivities of GPS, OBP and GRACE. For areas of dense site distribution, regional modelling approaches, based on wavelet analysis, could prevent the aliasing effects corrupting estimated global spherical harmonics. Ocean circulation models evaluate the change in volume of the ocean, but seem to be less reliable with respect to the mass-flux related to sea level change. If continental hydrologic loading is the focus of interest, then the ocean-related deformation represents a "noise" signal and can be removed by using e.g. the ECCO (Estimating the Circulation and Climate of the Ocean) model.

Appendix A

Acronyms

ACs	Analysis Centres
APL	Atmospheric Pressure Loading
APLO	Atmospheric Pressure Loading Service
CALC/SOLVE	VLBI software
CDDIS	Crustal Dynamics Data Information System
CE	Centre of solid Earth frame
CEDIES	Centre de Documentation et d'Information sur l'Enseignement Supérieur
CF	Centre of figure frame
CM	Centre of Earth frame (solid Earth plus fluid and gaseous envelope)
CN	Centre of network frame
COD	Centre for Orbit Determination in Europe (CODE)
DORIS	Doppler Orbitography and Radiopositioning Integrated by Satellite
ECGS	European Centre for Geodynamics and Seismology
ECMWF	European Centre for Medium-Range Weather Forecasts
ELHC	Equivalent load height column
ELHCC	Equivalent load height column coefficients
EOPs	Earth Orientation Parameters
ERPs	Earth Rotation Parameters
ESA	European Space Agency
ESOC	European Space Operations Centre
FE	Fluid and gaseous envelope
GB	Gutenberg-Bullen
GC	Global convolution
GFZ	GeoForschungsZentrum Potsdam
GGOS	Global Geodetic Observing System
GLONASS	Russian Global Navigation Satellite System
GNAACs	Global Network Associate Analysis Centres
GNSS	Global Navigation Satellite System
GPS	Global Positioning System
GRACE	Gravity Recovery and Climate Experiment
GSFC	Goddard Space Flight Centre
GSWP	Global Soil Wetness Project
HGS	Hans-Georg Scherneck
IAG	International Association of Geodesy

IAU	International Astronomical Union
IB	Inverted barometer
ICRF	International Celestial Reference Frame
IERS	International Earth Rotation and Reference Systems Service
IGb00	GPS specific TRF
IGG	Institute of Geodesy and Geophysics
IGS	International GNSS Service
ITRF	International Terrestrial Reference Frame
ITRF2000	ITRS realization 2000
ITRS	International Terrestrial Reference System
IVS	International VLBI Service for Geodesy and Astrometry
JPL	Jet Propulsion Laboratory
LLNs	Load Love Numbers
LOD	Length of day
MIT	Massachusetts Institute of Technology
NCEP	National Centres for Environmental Prediction
NCL	University of Newcastle-upon-Tyne
NDFW	Nearly Diurnal Free Wobble
NGS	National Geodetic Survey
NIB	Non-inverted barometer
NMC	National Meteorological Centre
NNR	No-net rotation
NNT	No-net translation
NOAA	National Oceanic and Atmospheric Administration
NRC	Natural Resources Canada
OA	Without atmospheric pressure loading correction
OBP	Ocean bottom pressure
OCCAM	VLBI geodetic software
OTL	Ocean tide loading
PG	Pascal Gegout
PREM	Preliminary Reference Earth Model
REM	Reference Earth Model
RMS	Root mean square
ROB	Royal Observatory of Belgium
SBL	Special Bureau for Loading
SFCP	Surface pressure
SH	Spherical harmonics

SINEX	Software Independent Exchange format
SIO	Scripps Institution of Oceanography
SIRGAS	Sistema de Referencia Geocéntrico para las Américas
SLP	Sea-level pressure
SNREI	Spherical non-rotating elastic and isotropic
SOPAC	Scripps and Orbit Permanent Array Centre
SSH	Surface spherical harmonics
TRF	Terrestrial reference frame
TVD	Tonie van Dam
USNO	U.S. Naval Observatory
UT1	Universal Time
VLBI	Very Long Baseline Interferometry
WA	With atmospheric pressure loading corrections

Appendix B

Estimated vertical site rates [mm/y] and RMS of selected ACs

STAT	COD		SIO		GFZ		ESA		JPL		IGS	
ALBH	-2.99	0.22	-1.47	0.22			0.24	0.38	-2.14	2.63	-3.12	0.21
ALGO	2.42	0.16	1.40	0.21	2.07	0.15	0.79	0.26	2.96	0.40	1.55	0.13
ALIC	3.53	0.18	2.34	0.21	4.00	0.46	8.33	9.55	2.76	0.23	2.33	0.16
ALRT	10.99	0.71	7.57	0.84	7.92	0.63			10.91	1.13	9.13	0.59
AMC2	1.26	0.23	1.43	0.16					-2.81	0.46	-0.15	0.15
AMMN			-8.16	0.84								
ANKR	-0.31	0.22	-0.28	0.16			3.17	0.69	0.03	0.62	0.77	0.22
AOML	0.22	0.24	0.59	0.36	-3.84	0.29			-0.95	0.37	-2.26	0.21
AREQ	-0.87	0.31	-0.79	0.42	-2.89	0.37	-3.66	0.34	-1.90	0.34	-1.76	0.32
ARTU	-1.74	0.24	-1.02	0.24	-3.34	0.28	-4.47	2.72	0.21	0.21	-1.01	0.18
ASC1	4.12	0.24	0.40	0.27	0.68	0.26	-0.22	0.56	0.00	0.23	1.03	0.19
AUCK	2.32	0.15	1.70	0.13	2.08	0.33	0.89	0.34	1.72	0.15	2.05	0.11
AZU1												
BAHR	0.68	0.21	0.82	0.17	1.64	0.19	-3.10	0.37	-0.17	0.16	0.72	0.12
BAKE			6.79	0.73							6.20	0.72
BAKO	4.46	0.41	0.16	0.53	-14.21	1.14					7.59	0.56
BAN2			3.14	0.89	2.42	0.65			5.06	1.08	1.25	0.45
BARH					-4.31	0.36					-4.24	0.34
BILI	-1.11	0.31	0.08	0.35	0.51	0.30	5.81	2.16	0.03	0.48	0.53	0.34
BJFS	-0.83	0.52	2.91	0.37	6.99	0.35			3.25	0.28	5.19	0.21
BOGT	-41.37	1.43	-40.86	1.60	-41.51	0.89	-38.91	1.56	-39.45	1.34	-41.42	0.81
BORI	0.17	0.13	-0.31	0.12	2.00	0.45	-1.38	0.45	1.42	1.64	0.15	0.11
BRAZ	0.21	0.44	1.40	0.48	1.37	0.36			0.91	0.55	1.53	0.30
BREW									-1.30	0.97	-1.05	0.57
BRMU	-3.70	0.18	-2.60	0.15	-6.21	0.19	-7.50	1.41	-4.26	0.27	-5.09	0.12
BRST	2.02	0.63							2.52	0.68	1.76	0.42
BRUS	1.15	0.16	1.10	0.11	3.83	0.47			4.66	3.89	0.98	0.11
BUCU			0.77	0.16					1.04	1.20	1.82	0.34
CAGL	0.68	0.24	0.17	0.12	1.00	0.35			-0.21	1.98	0.22	0.11
CAGS			-2.39	0.45							-1.52	0.47
CAGZ	3.72	0.87							1.88	2.87	2.47	0.74
CASI	0.38	0.20	3.70	0.16	6.86	0.21	4.16	0.33	2.08	0.22	3.07	0.12
CEDU	1.82	0.23	0.82	0.20	-0.20	0.43	-1.40	1.05	0.17	0.36	1.31	0.16
CFAG					5.47	1.92					3.85	1.46
CHAT	1.74	0.17	1.46	0.15	3.54	0.17	4.75	1.32	3.09	0.19	2.75	0.13
CHPI	-2.21	1.97	8.01	1.77							-1.89	1.68
CHUM					0.29	0.49			-1.31	1.97	-0.66	0.48
CHUR	8.21	0.20	9.12	0.17	8.78	0.51	12.44	14.62	9.62	1.35	7.49	0.16
CICI					-7.67	0.53			-0.37	0.30	-0.41	0.25
COCO	5.21	0.20	2.28	0.23	-1.81	0.27	-3.08	0.52	2.20	0.21	1.13	0.17
CONZ	2.73	0.85	51.21	3.28	7.50	0.87			0.80	1.25	4.46	0.60
CORD	2.07	0.40	2.48	0.47	3.18	0.39	-18.62	6.02	3.42	1.08	9.32	0.34
CROI	-4.83	0.30	-2.95	0.25	-5.84	0.71	-1.42	0.43	0.05	0.36	-3.62	0.22
DAEJ	-1.96	0.22	-0.51	0.24	2.11	0.42			0.92	0.44	1.08	0.17
DARR	3.35	0.74							3.78	1.31	-1.85	2.47
DARW	4.11	0.43	0.78	0.23	-0.43	0.50	-10.03	2.75	1.43	0.34	0.84	0.19
DAV1	-2.71	0.22	2.03	0.16	4.16	0.21	-1.46	1.02	0.04	0.20	1.38	0.13
DAVR	10.30	1.15							2.32	2.58	0.75	2.97
DGAR	6.19	0.24	2.77	0.22	-0.29	0.26	4.17	0.35	2.01	0.20	1.73	0.15
DRAG			-0.89	0.91	1.06	0.60			0.01	1.57	2.42	0.45
DRAO	1.38	0.15	1.35	0.17	0.48	0.14	1.56	0.19	0.98	0.94	0.38	0.13
DUBO	-0.97	0.24	-0.12	0.23	-6.56	0.52			-2.43	0.45	-1.66	0.20
DWHI	-9.49	0.70			-4.38	0.55			-4.75	0.74	-3.55	0.76
EBRE									-3.00	3.66	-5.33	3.67
EISL	-0.81	0.54	-2.28	0.47	-1.74	0.44	-2.33	0.93	-0.91	0.42	-0.01	0.38
EPRT			-4.07	1.01	-5.32	0.72					-3.38	0.52
EURK									10.63	1.16	7.68	1.17
FAIR	2.96	0.27	3.82	0.24	3.85	0.29	9.84	0.52	5.28	0.29	4.18	0.23
FLIN	1.21	0.21	1.83	0.22	-1.91	0.51	6.25	1.39	-2.26	1.18	0.45	0.19
FORT	-0.71	0.37	2.58	0.30	-0.95	0.34	-2.29	0.60	1.31	0.29	1.01	0.22
GENO					0.81	0.36					0.29	0.29
GLPS	0.18	0.43	0.50	0.54	1.68	0.51	1.26	2.36	3.12	0.73	-0.79	0.41
GLSV	-0.74	0.16	-1.01	0.15	5.68	0.54			-1.24	0.65	-0.14	0.13
GODE	-2.27	0.17	-3.23	0.16	-5.40	0.35	-1.78	0.26	-2.21	1.56	-4.36	0.13
GODZ	4.06	1.43										
GOL2	7.79	8.14	2.25	0.22	0.89	5.67	-1.41	0.70	1.74	4.72		
GOLD	1.29	0.30			0.67	0.27	-4.55	0.76			0.73	0.18
GOPE	1.81	0.18	3.27	0.26	1.60	0.47	-5.27	3.51			2.77	0.18
GOUG	-15.47	0.44	-12.37	0.49	-14.80	0.42			-13.85	0.46	-12.87	0.35
GRAS	1.52	0.15	1.29	0.11	6.85	0.48					1.33	0.11
GRAZ	0.79	0.15	0.43	0.12	3.62	0.89	-0.54	0.37	1.33	1.00	0.60	0.11
GUAM	-1.90	0.25	-1.07	0.23	-2.36	0.32	0.02	0.43	-2.88	0.24	-1.94	0.19
GUAO									2.76	0.50	1.26	0.57
GUAT	0.54	0.85	2.28	0.24	-2.11	0.56			3.29	0.32	1.25	0.27
HARB	0.37	0.31	2.10	0.20	2.77	0.29			2.77	0.69	2.61	0.19
HARV					-13.71	1.32			-5.57	0.40	-7.87	0.35
HERS	-1.01	0.31	-2.51	0.16							-2.50	0.14
HERT	2.97	0.71									2.55	0.49
HFLK	2.24	0.17									2.00	0.16
HIL0					1.63	1.08			-10.81	9.91	0.72	0.68
HLFX									-9.77	6.09	-3.49	0.65
HNLC					3.59	0.74			1.25	1.32	4.81	0.53
HNPT					-2.65	0.35					-2.84	0.34
HOB2	3.72	0.20	3.33	0.19	4.63	0.18	-0.95	0.42	1.37	0.18	2.68	0.15
HOFN	13.15	0.70	12.70	0.44	12.95	0.52					12.39	0.48
HOLB					-2.44	0.43			-11.70	2.10	-7.72	0.31
HOLM	4.29	0.41	3.71	0.55	4.92	0.51			2.25	3.61	3.68	0.41
HRAO	-0.13	0.23	-0.01	0.21	2.02	0.63	-1.53	0.34	1.52	0.21	0.56	0.18

HYDE	-0.57	0.49	4.68	0.64					-0.60	1.64	0.45	0.37
IISC	2.60	0.26	2.78	0.25	1.70	0.27	3.02	0.37			3.24	0.23
INVK	-8.27	0.92	-10.18	1.08	-9.60	0.71					-9.46	0.69
IRKJ	-3.38	1.27							-1.66	1.42	-4.66	1.20
IRKT	-2.41	0.33	-1.51	0.24	0.35	0.21	0.13	0.29	0.80	0.20	-0.11	0.16
ISTA			4.18	0.72					0.46	0.51	2.63	0.66
JAB1	4.63	0.25	-2.14	0.74	2.37	0.81	18.27	14.01	-0.82	0.36	0.59	0.23
JAMA	2.06	0.46	1.91	1.05	0.15	3.96			-1.93	1.03	1.40	1.55
JOZ2	2.20	0.90									1.59	0.78
JOZE	1.04	0.26	1.04	0.15	-3.79	1.17					1.89	0.15
JPLM			1.15	0.19	0.94	0.22			0.95	0.59	0.31	0.17
KARR	6.09	0.16	3.98	0.16	2.11	0.51	5.05	2.90	4.27	0.32	3.57	0.14
KELY	-13.02	0.69	-13.11	0.56	1.67	0.40	-3.80	1.21	-7.81	0.89	-13.81	0.43
KERG	1.75	0.20	4.66	0.18	2.71	0.19	6.60	1.02	2.50	0.20	2.85	0.14
KGN0					2.69	0.48			0.87	0.48	1.36	0.29
KHAJ	-3.97	1.43							0.09	0.74	-7.55	0.97
KIRU	1.64	0.64	6.77	0.34	11.82	0.82	8.29	0.44	6.07	1.05	7.24	0.29
KIT3	-5.77	0.32	-3.17	0.29	-3.81	0.27	-2.28	0.37	-3.14	0.22	-2.52	0.23
KODK	7.86	0.36	10.24	0.34	9.37	0.27			7.81	0.74	8.97	0.41
KOKB	0.98	0.20	2.46	0.44	3.61	0.32	-2.09	0.48	0.07	0.26	2.11	0.22
KOSG	0.47	0.13	-0.64	0.11	1.14	0.15	-1.04	0.30			0.04	0.09
KOU1	2.62	0.67							4.14	1.27	2.56	0.63
KOUR	1.33	0.34	1.77	0.26	-0.47	0.28	2.54	0.33	-0.44	0.91	1.65	0.22
KR0G											9.39	0.51
KSMV									5.23	3.62	4.11	3.84
KSTU	-3.11	0.37	-2.85	0.35	-1.20	0.29			-0.16	0.52	-1.10	0.28
KUNM	1.39	0.36	3.18	0.30	1.97	0.67			5.16	0.32	4.21	0.24
KUUJ									3.36	3.23	-0.11	2.41
KWJ1	-3.84	1.70	-3.64	1.35	-10.67	1.52			-5.99	1.43	-7.08	1.16
LAE1	-4.01	0.28	-3.46	0.30	-1.50	0.37			-3.62	0.31	-0.52	0.41
LAMA	-1.20	0.19	-1.84	0.18					-8.31	5.08	-1.05	0.18
LEIJ												
LHAS	0.52	0.34	1.04	0.22	2.91	0.22	4.31	0.46	3.18	0.22	2.44	0.16
LHAZ	1.42	1.01							2.52	1.07	3.59	0.79
LHUE					-0.90	1.39			-2.50	1.59	3.16	1.33
LPGS	3.40	0.27	1.94	0.29	1.31	0.22	4.57	0.38	1.85	0.34	3.23	0.25
LROC					0.78	0.33			0.31	0.96	0.67	0.27
MAC1	-1.76	0.17	-0.84	0.15	-0.53	0.16	-3.06	1.77	-2.08	0.45	-0.46	0.12
MAD2			3.89	0.25					3.48	0.42		
MADR	4.41	0.45	4.31	0.38	1.68	0.25			11.55	3.71	3.49	0.20
MAG0	-3.52	0.28	-0.85	0.26	3.91	0.43			-1.34	0.24	-1.24	0.19
MALD	4.13	1.94	10.07	2.68	3.45	1.78					2.96	1.11
MALI	1.71	0.34	2.18	0.31	-0.67	0.31	4.57	0.52	5.23	0.97	2.13	0.24
MANA			2.50	0.22	-2.63	0.65			2.50	0.56	-0.34	0.37
MAS1	0.28	0.16	0.07	0.16	0.10	0.15	-1.08	0.33	0.53	0.17	-0.10	0.12
MAT1	0.34	0.72									-0.34	0.56
MATE	1.23	0.21	0.59	0.11	0.45	0.14	0.51	0.44	0.64	0.40	0.66	0.09
MAUI					0.06	0.68			-2.25	2.55	1.12	0.69
MAW1	-0.77	0.18	3.28	0.16	2.79	0.48	10.77	2.46	0.79	0.34	1.42	0.12
MBAR	5.40	0.25	9.69	1.31	7.59	0.28			3.03	0.30	5.56	0.31
MCM4	-7.58	0.55	-2.68	0.22	-2.77	0.30	0.23	0.85	1.62	0.31	-1.96	0.21
MD01	-2.25	0.26	-1.06	0.23	-2.23	0.21	0.17	0.41	-1.51	0.55	-1.90	0.21
MDVJ	2.80	0.87							-1.43	1.90	0.75	1.10
MDVO	2.46	0.75	7.66	2.79			-92.51	468.69			0.55	0.53
MEDI	-2.54	0.14	-2.74	0.13					-2.18	0.82	-2.66	0.11
METS	4.64	0.16	4.58	0.13	5.02	0.15			4.28	0.46	4.98	0.12
METZ	6.22	0.79									5.79	0.73
MKEA	-5.23	0.23	-3.98	0.25	-0.69	0.43	-3.11	0.28	-4.83	0.78	-3.43	0.17
MOBN			6.14	1.02					-0.09	0.51	0.80	0.48
MOBS			-0.06	0.44							-0.31	0.43
MONP	1.07	0.22							-8.39	10.84	1.37	0.20
MORP	1.18	0.65							1.63	2.77	0.46	0.58
MSKU	4.73	0.78	-8.54	1.66	4.97	0.56			5.72	0.72	4.55	0.59
MTKA	-1.22	1.08									-0.89	0.98
NAIN					-1.64	0.70			8.88	3.25	-0.78	0.61
NANO					-2.02	0.42					-1.23	0.28
NICO	-1.70	0.14	-3.22	0.47	1.88	0.43	-1.00	3.24	-0.41	0.32	-0.58	0.14
NKLG	1.13	0.18	0.51	0.23	-2.56	0.35	1.66	0.81	0.11	0.25	1.10	0.22
NLIB	-2.02	0.30	-0.23	0.23	-1.79	0.27	-1.29	0.76	0.10	0.72	-2.14	0.22
NNOR			0.70	0.70			1.70	0.75	1.80	0.97	-2.75	0.41
NOT1	0.48	0.18	0.87	0.53					0.45	0.34	0.00	0.20
NOUM	0.58	0.19	-1.98	0.28	-1.23	0.23			4.65	0.32	0.46	0.18
NPLD	2.22	0.20			2.39	0.51			0.36	0.65	1.76	0.19
NRC1	2.57	0.16	2.63	0.14	0.35	0.33	2.93	0.23	0.91	0.63	1.40	0.11
NRC2									2.63	0.79		
NRIL	4.08	0.45	1.79	0.27	1.79	0.31			2.65	0.28	3.10	0.29
NISSP	-0.47	0.35							-0.66	0.87	-0.59	0.30
NTUS	5.00	0.28	2.62	0.20	-1.10	0.29	-2.79	0.46	2.82	0.21	1.56	0.17
NYSK			1.85	0.52	-11.04	1.26					-0.10	0.75
NYA1	8.08	0.26	9.24	0.24	11.12	0.20			9.34	0.30	9.40	0.20
NYAL			10.46	0.43	14.26	0.46	9.09	0.31	6.80	0.34	10.12	0.22
OBE2					1.84	0.27					1.49	0.26
OBET					-3.65	1.17					-3.35	1.06
OH12			16.45	1.61	11.46	0.46			7.28	0.60	12.48	0.48
ONSA	3.21	0.14	2.51	0.11	2.94	0.12	5.12	0.20	3.14	0.14	3.20	0.10
OPMT	0.05	0.84			0.18	1.20					-1.43	0.59
OUS2					-1.23	0.30			-1.88	0.72	-0.77	0.24
PADO	-0.99	0.34									-1.02	0.27
PDEL	-1.26	0.46	-3.04	0.47	-0.26	0.48			0.01	0.46	-1.78	0.32
PENC	-2.28	0.25									-2.72	0.16
PERT	-3.61	0.16	-3.99	0.17	-3.81	0.39	-5.42	0.33	-2.21	0.25	-5.19	0.13
PETP	-6.15	0.30	-1.82	0.20	-0.90	0.15	-8.52	9.22	-3.33	0.23	-1.67	0.15
PIE1	0.39	0.20	0.53	0.16	-3.48	0.56	4.28	0.28	1.89	1.11	-0.00	0.15
PIMO	1.85	0.41	0.96	0.37	-1.20	0.35			1.69	0.37	1.66	0.37
POL2	-1.44	0.23	-0.69	0.18			-2.45	0.24	-0.35	0.34	0.42	0.15
POLV					-0.17	0.44			-2.70	0.80	-0.76	0.33
POTS	0.41	0.13	-0.25	0.12	-0.05	0.13	1.51	0.22			0.20	0.11
PRDS			-0.83	0.24	-12.53	0.67					-2.56	0.20
PTBB	-0.42	0.42									4.69	0.33

QAQI	6.27	0.41			2.90	0.34			1.92	0.48	2.94	0.30
QUIN	2.50	0.41									2.54	0.35
RABT	1.10	0.28	0.39	0.19	-0.76	0.37			2.60	0.41	-0.41	0.20
RAMO	-1.12	0.16	-1.18	0.59	-0.07	0.49			-0.61	0.28	0.93	0.18
RBAY	-2.48	0.50	3.37	0.40	1.63	0.70			4.87	0.99	1.99	0.36
RESO	7.74	0.35	5.88	0.75	5.44	0.28			5.50	0.62	5.51	0.30
REYK	-6.00	0.30	-3.29	0.17	-3.99	0.21	-6.25	0.61	-6.75	0.30	-4.27	0.17
REYZ	7.69	0.81			0.98	2.25			8.61	1.50	8.18	0.64
RIOG	4.54	0.27	5.24	0.25	8.02	0.15	6.92	0.66	4.74	0.18	8.69	0.25
SACH			3.03	0.68	1.02	0.94			4.22	0.71	3.45	0.56
SANT	5.71	0.24	2.82	0.35	4.04	0.23	3.08	0.39	4.32	0.24	4.18	0.20
SCH2	8.22	0.25	9.88	0.27	5.87	0.48			7.74	0.44	7.99	0.23
SCIP									-1.36	1.17	-4.21	1.94
SCUB	-2.57	0.76	-2.09	1.21	-2.57	0.57			2.92	0.60	-2.27	0.51
SELE	-2.54	0.24	-1.16	0.22			-1.10	0.92	-0.51	0.26	-0.38	0.15
SEY1	-1.24	0.89	-1.71	0.62	-3.55	0.49	1.96	2.26			-1.57	0.49
SFER			2.15	0.11	2.09	0.34	-2.63	0.85	4.05	0.40	1.67	0.12
SHAO	-2.82	0.28	-1.89	0.34			-2.64	0.62	-1.21	0.49	-1.07	0.25
SIMO	-3.16	0.81			1.51	1.25			3.19	0.85	-8.92	1.35
SIO3					-3.38	0.43					-4.73	0.38
SN11									-2.30	1.03	-2.94	1.09
SOFI					0.88	0.58	-6.35	2.26	7.46	4.25	0.08	0.35
SOLI					-3.04	0.52					-3.27	0.47
SPT0											5.52	0.73
SSIA	2.10	0.72	3.46	0.52	5.27	0.62			4.35	1.01	2.48	0.48
STJO	-1.27	0.17	0.56	0.15	-0.77	0.15	-1.91	0.27	-2.10	0.42	-0.28	0.12
STR1									4.57	0.55	3.75	0.29
STR2	-2.03	1.00									-0.84	1.01
SUTH	3.61	0.23	1.92	0.20	7.57	0.29	-7.14	0.92	0.88	0.52	4.32	0.17
SUTM			4.91	0.75	2.65	0.37			5.68	1.15	3.12	0.29
SUWN	-2.67	0.26	-1.24	0.32	4.32	0.84			3.91	0.77	0.50	0.24
SYOG	0.19	0.25	2.95	0.22	4.29	0.24	18.73	2.88	3.18	0.25	3.96	0.18
TCMS			6.28	0.55							5.84	0.57
TH11	-1.78	0.30	-1.17	0.29	-4.12	0.36	-3.24	0.95	-1.86	0.25	-1.73	0.21
THU3	5.87	0.50	4.95	0.58	4.00	0.40					4.48	0.30
TID2	1.57	9.56	3.18	0.19	1.08	0.17	4.56	0.51	3.47	0.53		
TIDB	2.11	0.25	-0.33	0.37	1.28	0.16	3.23	0.56			1.90	0.13
TIX1	-1.12	0.24	0.05	0.27	0.88	0.18	9.61	1.82	0.95	0.24	0.53	0.20
TLSE	-0.79	0.23	-0.51	0.88	0.37	0.42			-0.19	0.86	-1.26	0.19
TNML			4.47	1.04					-0.86	1.45	2.54	0.82
TOW2	5.84	0.18	3.08	0.17	5.28	0.32			2.20	0.19	3.29	0.14
TRAB					-0.16	0.39			-1.23	0.25	-0.46	0.27
TRO1	3.47	0.18	4.29	0.16	5.64	0.15					4.65	0.14
TROM			6.06	0.45			2.92	0.37			3.21	0.21
TSKB	0.50	0.27	2.29	0.21	0.21	0.20	-0.94	0.40	0.86	0.19	1.36	0.18
TUBI									-0.40	0.72	-0.92	0.86
TWTF	-0.81	0.80	9.65	1.34	-5.36	0.48			-5.38	0.48	-3.63	0.53
ULAB					1.25	0.30			0.71	0.52	1.29	0.32
UNB1	-0.41	0.77									-1.11	0.68
UNSA	0.04	0.30	1.28	0.44	0.83	0.28	-3.00	1.92	1.60	0.77	1.51	0.22
URUM	2.86	0.25	2.32	0.24	3.69	0.17			2.90	0.44	3.38	0.21
USNA					-8.27	0.49					-8.05	0.48
USNO	-2.29	0.15	-2.68	0.17			-1.81	0.30	-3.46	0.57	-3.59	0.13
USUD	-4.10	0.34	-2.47	0.28	-2.97	0.28	-3.46	0.44	-0.89	0.72	-2.27	0.24
UZHL					1.07	0.47					-0.24	0.40
VE NE			-0.96	0.44	0.12	0.30					-0.10	0.25
VESL	-1.40	0.45	1.53	0.33	6.69	0.26			1.73	0.41	3.24	0.29
VILL	-0.35	0.15	-0.55	0.13	-1.35	0.13	-1.78	0.22			-1.48	0.11
WES2	-2.23	0.16	-1.48	0.23	-3.05	0.19					-2.93	0.19
WHIT	1.08	0.26	2.47	0.24	3.06	0.54			4.28	0.45	1.63	0.24
WILL	1.86	0.18	1.29	0.92	-2.33	0.42					1.07	0.15
WROC											1.54	0.68
WSRT	1.64	0.16	-0.08	0.14	1.43	0.16	-9.62	0.86			0.29	0.12
WTZR	0.42	0.12	-0.14	0.11	0.97	0.13	-0.32	0.18	-0.99	0.16	0.08	0.10
WTZZ	-0.05	1.03									-0.19	0.76
YAKT	-1.02	0.76	2.13	0.43	1.91	0.90	2.45	3.98	0.96	0.57	1.36	0.39
YAKZ	-0.26	1.03	-4.96	0.93								
YARI	5.44	0.62	3.10	0.50	2.69	0.60	3.21	0.90	3.55	0.53	4.62	0.15
YARR	7.38	0.74							5.24	3.09	6.33	0.47
YE BE									4.33	1.04	2.90	0.45
YELL	3.20	0.20	5.26	0.20	4.93	0.20	3.99	0.27	4.83	0.21	4.29	0.18
YKRO	0.97	1.38	3.57	1.23	0.67	1.38			5.48	1.03	2.63	0.67
YSSK	0.34	0.21	1.71	0.21	2.07	0.17			2.54	0.62	2.35	0.15
ZAMB	5.46	0.70	5.73	0.66	1.71	0.62			7.67	0.98	4.34	0.99
ZECK	0.39	0.18	-0.13	0.39	1.22	0.17			1.98	0.30	1.83	0.15
ZIMJ	0.59	0.94							-3.15	5.95	0.10	0.88
ZIMM	2.02	0.13	1.48	0.09	4.22	0.39	0.49	1.34			2.01	0.09
ZWEN	-1.49	0.40	0.92	0.44	1.21	0.47	1.69	0.49	-1.19	0.94	0.80	0.36

Appendix C

Observed annual signals [mm] and RMS in vertical component for selected ACs

STAT	COD		SIO		GFZ		ESA		JPL		IGS	
ALBH	9.42	0.54	2.02	0.55	1.47	0.52	6.16	0.60	0.45	1.41	0.58	0.52
ALGO	4.28	0.39	2.59	0.52	2.48	0.36	5.82	0.63	3.41	0.92	2.23	0.33
ALIC	9.35	0.45	2.71	0.52	5.98	0.54			6.66	0.52	5.27	0.39
ALRT	5.19	0.77	5.96	0.90	5.10	0.63			5.73	0.94	4.81	0.63
AMC2	7.46	0.57	2.64	0.40	4.11	0.47			6.09	0.67	3.60	0.37
ANKR	7.57	0.54	3.08	0.37	5.88	0.57	4.59	1.20			4.00	0.48
AOML	9.54	0.46	6.07	0.58	3.06	0.55			3.47	0.75	5.45	0.40
AREQ	11.71	0.77			4.24	0.92	3.22	1.00	3.15	0.85	3.52	0.84
ARTU	11.88	0.59	6.53	0.58	7.41	0.65			11.40	0.50	8.18	0.44
ASC1	3.96	0.57	5.43	0.66	2.71	0.61	3.59	1.14	5.72	0.55	2.93	0.48
AUCK	10.70	0.37	3.77	0.32	5.64	0.39	8.80	0.75	3.44	0.36	4.42	0.27
BAHR	6.91	0.51	7.53	0.41	9.22	0.46	6.14	0.84	6.82	0.38	7.05	0.30
BAKE			7.23	0.61							6.03	0.58
BAN2			6.93	0.76	4.77	0.69			8.44	1.14	5.92	0.50
BARH					2.01	0.42					1.71	0.42
BILI	13.47	0.64	4.06	0.74	2.26	0.59			8.28	0.75	3.43	0.54
BJFS	14.41	0.82	9.12	0.81	8.69	0.77			6.27	0.69	7.68	0.50
BOGT					10.35	1.79			9.44	2.05	9.26	1.78
BORI	6.85	0.32	2.15	0.29	0.82	0.45	3.29	0.73			2.42	0.27
BRAZ	11.05	0.61	8.42	0.67	12.73	0.46			11.86	0.62	11.11	0.42
BREW											2.55	0.93
BRMU	7.12	0.44	3.50	0.38	1.98	0.46	3.58	1.06	1.83	0.63	3.36	0.29
BRST	6.44	0.66							2.25	0.60	4.58	0.42
BRUS	6.96	0.39	0.69	0.26	2.18	0.47					1.38	0.29
BUCU			3.56	0.43					2.85	0.80	3.20	0.56
CAGL	5.74	0.40	2.00	0.30	1.86	0.41			4.64	4.35	0.99	0.28
CAGS			3.35	0.50							2.48	0.53
CAGZ	5.62	0.82							6.72	1.69	4.06	0.68
CASI	6.09	0.47	2.74	0.39	0.70	0.50	6.92	0.74	1.87	0.49	1.72	0.29
CEDU	10.95	0.56	3.93	0.42	6.67	0.50	14.30	1.09	8.01	0.50	5.91	0.40
CHAT	9.53	0.42	0.43	0.38	1.05	0.42			2.18	0.51	2.58	0.31
CHUM					8.39	0.62					7.09	0.66
CHUR	5.06	0.50	2.95	0.44	3.96	0.58					1.31	0.40
CICI					3.35	0.53			3.22	0.74	1.95	0.58
COCO	3.34	0.51	2.63	0.57	2.69	0.66	1.31	0.90	3.72	0.52	1.62	0.43
CONZ	4.67	0.80			3.48	0.95			9.18	1.36	2.08	0.70
CORD					2.96	1.00					3.07	0.62
CROI	6.73	0.65	5.01	0.56	3.90	0.72	7.85	0.94	2.91	0.78	4.61	0.49
DAEJ	15.37	0.55	6.38	0.59	5.23	0.48			6.62	1.09	6.06	0.41
DARR	5.43	0.70							4.94	0.80		
DARW	1.70	0.74	3.82	0.57	5.75	0.59	4.70	1.75	3.07	0.81	3.93	0.48
DAV1	12.27	0.52	1.61	0.40	0.88	0.48	5.01	1.26	1.98	0.44	1.68	0.31
DGAR	1.46	0.69	5.26	0.65	6.01	0.74	3.64	1.02	4.42	0.59	4.58	0.45
DRAG			4.63	0.71	7.49	0.58			5.71	2.84	5.96	0.71
DRAO	6.94	0.36	4.20	0.43	4.58	0.35	6.56	0.43	8.78	1.20	3.50	0.33
DUBO	6.03	0.58	1.83	0.56	1.56	0.60			4.27	0.63	0.70	0.49
DWHI	5.84	0.71			5.64	0.55			6.30	0.73	0.53	0.82
EISL			5.22	0.82	1.56	0.88	8.19	1.62	4.24	0.73	3.56	0.66
EPRT					1.58	0.78					1.39	0.63
EURK									2.30	0.90	2.84	0.97
FAIR	7.01	0.68	4.58	0.63	2.70	0.69	0.90	1.21	0.96	0.71	3.54	0.57
FLIN	7.08	0.54	1.47	0.55	0.78	0.60	7.11	1.66			0.63	0.47
FORT	2.86	0.86	3.86	0.75	8.02	0.84	4.05	1.46	7.74	0.71	5.03	0.56
GENO					1.06	0.42					0.76	0.35
GLPS	1.19	0.44	1.66	0.49	2.53	0.47	1.79	1.35	1.80	0.61	1.27	0.35
GLSV	8.66	0.39	4.98	0.37	2.92	0.54			6.20	1.77	5.32	0.32
GODE	7.00	0.36	0.49	0.41	2.33	0.40	1.14	0.64			2.00	0.33
GODZ	1.29	0.74										
GOLD	11.59	0.64			4.34	0.55	2.10	0.79			3.78	0.43
GOPE	5.86	0.44	1.31	0.60	0.49	0.47					1.75	0.43
Goug					6.33	1.01			4.92	1.12	4.83	0.86
GRAS	4.66	0.38	1.00	0.27	1.86	0.58					0.16	0.26
GRAZ	5.64	0.38	3.38	0.30	5.51	0.98	5.74	0.65			2.61	0.27
GUAM	6.39	0.59	2.79	0.58	1.46	0.71	6.01	1.38	1.80	0.58	2.80	0.48
GUAO									3.43	0.51	4.11	0.51
GUAT	9.84	0.72	5.20	0.48	7.26	0.65			6.39	0.59	6.41	0.46
HARB	4.23	0.63	3.13	0.42	2.19	0.53			7.17	1.17	2.27	0.34
HARV					1.45	0.69			6.13	1.02	2.72	0.71
HERS	7.99	0.56	1.79	0.41							0.52	0.37
HERT	5.87	0.66									4.63	0.45
HFLK	9.28	0.43									7.84	0.40
HILO					5.47	0.88					2.58	1.10
HLFX											0.51	0.47
HNLC					5.63	0.79			5.10	3.07	4.35	0.69
HNPT					3.53	0.42					3.60	0.45
HOB2	9.58	0.49	3.24	0.47	5.01	0.44	10.25	1.01	5.55	0.45	4.49	0.37
HOLB					3.48	0.50			3.25	2.97	3.01	0.76
HOLM	3.04	0.52	5.02	0.60	3.76	0.49					2.04	0.46
HRAO	7.21	0.58	2.32	0.52	5.57	0.73	4.52	0.81	4.76	0.54	2.97	0.45
HYDE	4.57	0.56	7.10	0.57					4.44	1.62	5.36	0.43
IISC	5.05	0.54	5.30	0.63	6.19	0.66	6.37	0.90			3.90	0.60
INEG	8.22	0.90	2.38	0.86	3.05	0.99					2.68	0.93
IRKT	20.46	0.63	8.46	0.59	8.45	0.51	13.44	0.70	8.01	0.48	8.42	0.40
ISTA			5.26	0.57					1.68	1.06	3.80	0.52
JAB1	4.87	0.62	3.03	0.61	4.03	0.85			6.51	0.90	4.52	0.58

JAMA	7.76	0.68			5.34	1.87			1.30	1.24	6.42	1.25
JOZ2	5.65	0.82									5.10	0.70
JOZE	8.78	0.42	2.19	0.39	1.96	1.19					3.80	0.38
JPLM			2.62	0.47	2.61	0.53			3.36	1.09	2.64	0.42
KARR	6.02	0.40	2.20	0.39	4.98	0.59	5.26	1.69	5.00	0.67	4.45	0.34
KERG	10.18	0.49	2.56	0.45	1.81	0.44	6.76	1.58	2.38	0.48	0.74	0.35
KGNO					4.80	0.49			3.57	0.63	4.03	0.42
KGNI												
KIT3	6.37	0.71	2.08	0.68	3.13	0.61	6.01	0.83	2.34	0.52	1.61	0.54
KODK	10.82	0.65	3.61	0.81	5.28	0.45			8.09	1.27	1.92	0.57
KOKB	9.86	0.54	4.60	0.70	2.61	0.81	3.89	1.03	6.66	0.66	4.82	0.56
KOSG	6.87	0.33	1.34	0.26	0.31	0.35	2.41	0.49			0.77	0.24
KOU1	7.08	0.52							7.13	0.94	6.30	0.87
KOUC												
KOUR	4.31	0.70	5.51	0.64	6.94	0.65	6.66	0.82	4.17	2.09	5.21	0.54
KUNM	8.34	0.77	8.22	0.71	9.31	0.78			7.24	0.78	6.50	0.56
LAE1	1.84	0.54	2.66	0.60	4.09	0.66			5.35	0.61	3.68	0.65
LAMA	7.48	0.46	3.49	0.44							3.48	0.42
LHAS	4.93	0.60	7.16	0.53	6.00	0.51	8.19	0.74	3.53	0.50	4.95	0.39
LHAZ	2.07	0.83							4.74	0.80	2.27	0.64
LHUE					6.77	0.79			12.13	1.39	8.55	0.87
LPGS	7.86	0.70	3.44	0.71	3.48	0.53	2.88	1.20	5.15	0.90	3.10	0.63
LROC					1.13	0.37			4.66	1.36	1.16	0.34
MAC1	4.62	0.39	1.42	0.38	1.91	0.39	2.92	1.24	0.42	1.10	0.72	0.29
MAD2			2.65	0.60					1.76	1.03		
MADR	6.94	0.60	2.19	0.67	1.80	0.50					1.49	0.45
MAG0	13.99	0.70	1.55	0.65	1.68	0.49			1.95	0.57	2.40	0.47
MALI	6.07	0.75	1.34	0.75	1.68	0.71	1.79	1.27	0.88	1.42	2.45	0.58
MANA			5.69	0.48	4.14	0.64			5.08	1.21	5.22	0.53
MASI	8.01	0.39	3.59	0.40	3.06	0.31	4.26	0.61	1.89	0.43	2.86	0.30
MAT1	4.50	0.70									2.94	0.54
MATE	6.23	0.32	2.41	0.26	2.33	0.35	2.75	1.08	3.40	1.14	1.54	0.22
MAW1	11.42	0.45	3.04	0.41	1.15	0.55	1.25	1.23	1.35	0.97	1.40	0.28
MBAR	1.02	0.55	4.32	0.67	0.82	0.55			1.29	0.62	1.72	0.55
MCM4	7.94	0.87	6.92	0.55	6.51	0.72	2.53	2.16	3.09	0.73	5.46	0.52
MDO1	7.60	0.65	0.52	0.58	2.44	0.50	3.81	0.89	3.82	1.60	0.65	0.52
MDVO											4.99	0.73
MEDI	5.92	0.36	1.80	0.32					1.67	2.17	1.75	0.28
METS	7.17	0.36	2.48	0.32	2.39	0.35			1.68	1.14	2.00	0.30
METZ	4.62	0.71									4.58	0.62
MIZU					1.73	0.60			2.50	1.55	0.49	0.58
MKEA	8.78	0.55	2.98	0.62	6.17	0.49	5.52	0.66	4.09	2.03	2.63	0.43
MOBN			6.21	0.84					2.38	0.72	4.04	0.66
MOBS			4.34	0.35							5.86	0.33
MONP	10.01	0.55									6.63	0.49
MORP	9.21	0.78							5.96	2.41	7.07	0.68
MTKA	8.83	1.00									5.96	0.90
NAIN					1.04	0.51			5.31	3.48	1.51	0.48
NANO					2.11	0.47					1.33	0.44
NICO	6.93	0.32	3.94	0.50	6.20	0.47	3.39	2.65	4.11	0.73	4.46	0.32
NKLG	3.28	0.39	5.11	0.52	3.34	0.74	4.09	1.17	2.81	0.57	4.15	0.37
NLIB	6.51	0.75	3.08	0.56	5.56	0.64	7.57	1.28	3.75	1.47	2.88	0.54
NNOR			5.18	0.56			13.88	0.90	8.95	1.01	5.78	0.51
NOT1	4.38	0.36	0.59	0.44					2.59	0.55	2.05	0.33
NOUM	7.61	0.47	7.72	0.69	5.08	0.52			7.10	0.81	6.30	0.45
NPLD	7.23	0.44			3.25	0.48			2.20	1.20	5.26	0.36
NRC1	4.21	0.39	2.18	0.35	1.34	0.38	5.14	0.55	5.90	0.75	1.96	0.28
NRC2									6.15	0.61		
NRIL	10.74	0.59	4.98	0.55	3.19	0.55			5.65	0.56	4.89	0.49
NSSP	7.32	0.64							4.01	0.76	6.67	0.57
NTUS	4.77	0.66	4.63	0.50	6.50	0.69	6.51	1.47	5.64	0.52	5.78	0.43
NYSK			5.95	0.93							8.00	1.07
NYA1	6.14	0.64	4.13	0.58	1.36	0.47			2.05	0.76	3.58	0.50
NYAL			4.24	0.78	2.65	0.53	3.57	0.73	3.09	0.59	3.72	0.54
OBE2					0.96	0.43					0.91	0.38
OBET					3.53	0.85					3.95	0.75
OH12					1.62	0.65	10.92	1.80	1.80	0.77	6.11	0.69
ONSA	5.63	0.34	0.78	0.27	1.15	0.28	2.26	0.48	1.49	0.35	0.39	0.25
OPMT	3.68	0.90			0.59	0.60					1.87	0.62
OUS2					2.53	0.38			2.09	0.70	2.77	0.32
PADO	5.37	0.51									3.69	0.41
PDEL	8.17	0.62	3.31	0.62	2.80	0.52	2.74	2.51	1.80	0.57	4.20	0.42
PENC	6.46	0.45									3.58	0.40
PERT	9.24	0.38	1.53	0.42	5.19	0.43	11.62	0.77	3.96	0.49	3.98	0.33
PETP	14.16	0.66	2.97	0.51	3.05	0.37			0.07	0.58	2.94	0.37
PICL												
PIE1	9.45	0.49	1.30	0.40	3.70	0.56	2.34	0.64	4.07	1.49	1.91	0.37
PIMO	7.48	0.88	3.48	0.86	5.17	0.87			5.76	0.88	2.55	0.92
PIN1												
POL2	10.47	0.60	2.54	0.47			6.31	0.72	5.15	0.81	3.22	0.39
POLV					3.51	0.51			1.59	1.07	3.66	0.44
POTS	6.78	0.32	2.01	0.30	1.35	0.30	4.01	0.52			1.71	0.27
PRDS			4.30	0.61	3.06	0.63					3.70	0.52
PTBB	7.80	0.77									6.52	0.46
QAQ1	10.20	0.54			5.35	0.42			7.18	0.51	7.13	0.40
QUIN	9.07	0.88									4.97	0.78
RABT	5.67	0.49	2.51	0.37	1.49	0.43			2.56	0.78	2.74	0.33
RAMO	5.90	0.41	8.15	0.62	9.69	0.54			4.70	0.73	5.30	0.44
RBAY	6.72	0.85	2.86	0.68	1.95	0.80			5.29	1.46	0.85	0.62
RESO	1.49	0.49	6.36	0.83	5.06	0.43			4.86	0.79	4.54	0.49
REYK	11.35	0.49	6.45	0.43	6.24	0.51	4.43	1.01	4.68	0.75	5.85	0.43
RIOG	12.06	0.65	5.41	0.60	1.03	0.37	11.00	1.19	2.97	0.47	2.03	0.43
SACH			5.67	0.72	3.94	0.75			4.60	0.68	4.33	0.58
SANT	9.58	0.57	0.82	0.85	3.00	0.56	3.05	0.93	5.89	0.54	3.15	0.51
SCH2	3.40	0.63	3.92	0.70	3.24	0.55			4.61	0.55	0.96	0.58
SCUB	5.79	0.93	4.39	0.99	4.36	0.80			4.27	0.75	4.47	0.70
SELE	11.39	0.59	3.38	0.54			9.72	1.05	6.68	0.56	4.61	0.37
SFER			1.18	0.28	2.00	0.40	2.26	0.81	3.20	1.05	1.29	0.29
SHAO	13.07	0.69	4.66	0.86			9.00	1.39	10.69	1.34	3.82	0.59

SIMO	11.27	0.84			1.32	0.82			3.01	0.92	1.39	1.08
SIO3					5.07	0.50					4.79	0.44
SNH									5.73	0.90	5.47	0.75
SOFI					2.74	0.57	9.72	1.97	3.64	2.77	3.08	0.50
SOL1					2.93	0.62					2.67	0.60
SPT0											3.23	0.50
STJO	5.70	0.42	1.57	0.38	0.68	0.36	1.98	0.66	2.31	1.05	0.88	0.29
STR1									7.59	1.71	5.97	0.79
STR2	3.78	0.71									4.05	0.70
SUTH	10.11	0.57	2.50	0.48	2.22	0.69	4.15	1.19	3.69	1.25	1.29	0.41
SUTM			5.62	0.64	4.96	0.49			6.36	1.26	4.63	0.42
SUWN	16.65	0.63	6.93	0.79	8.22	0.82			4.90	0.77	6.00	0.60
SYOG	9.59	0.57	2.37	0.50	2.45	0.55	4.86	1.88	0.97	0.54	1.90	0.43
TCMS			5.69	0.71					3.03	2.40	5.01	0.67
THTI	5.52	0.74	0.81	0.71	1.53	0.79	5.49	1.22	1.44	0.61	1.16	0.51
THU2	4.42	0.60	5.69	0.81								
THU3	1.78	0.72	6.09	0.74	3.47	0.46	4.49	1.06			4.12	0.38
TID1					5.30	0.44			3.83	1.11		
TIDB	12.93	0.45	3.65	0.54	5.95	0.31	13.02	0.79	6.23	2.62	6.05	0.32
TIXI	12.08	0.61	4.07	0.68	3.78	0.45	8.83	1.12	5.10	0.60	4.31	0.49
TLSE	5.69	0.42	0.35	0.56	0.06	0.42			0.97	1.56	2.69	0.31
TNML									0.93	1.33	5.19	0.84
TOW2	6.67	0.45	1.88	0.43	5.51	0.64	7.29	1.04	6.53	0.47	3.84	0.34
TRAB					1.64	0.45			2.72	0.54	1.90	0.41
TROI	6.35	0.46	2.45	0.39	1.17	0.37			3.50	0.87	2.58	0.34
TROM			4.16	0.55			3.54	0.65			4.28	0.51
TSKB	7.46	0.66	7.42	0.52	10.07	0.46	4.19	0.95	7.45	0.46	5.98	0.44
TUBI									3.45	1.92	3.65	1.97
TWTF	7.45	1.01			5.39	0.72			4.40	0.77	3.86	0.78
ULAB					5.40	0.49			6.28	0.81	5.72	0.48
UNB1	2.44	0.75									1.96	0.65
UNSA	8.82	0.65	2.44	0.87	3.76	0.56	6.76	1.19	2.09	0.88	3.72	0.47
URUM	16.30	0.57	8.07	0.51	7.97	0.39			10.76	0.84	8.75	0.50
USNA					3.11	0.56					3.23	0.59
USNO	5.64	0.36	0.42	0.43			2.70	0.58	3.02	0.83	1.24	0.32
USUD	14.15	0.81	1.84	0.66	1.98	0.67	3.88	1.32	1.98	1.04	3.84	0.57
UZHL					3.70	0.56			2.74	3.27	3.01	0.50
VEVE			2.90	0.36	1.13	0.34					1.65	0.30
VESL			4.67	0.77	2.88	0.64			2.60	0.95	6.05	0.71
VILL	6.38	0.36	2.32	0.33	1.75	0.31	3.10	0.55			2.06	0.28
WES2	4.01	0.40	1.10	0.58	0.82	0.49	3.36	1.29			1.55	0.47
WHIT	4.34	0.66	7.17	0.59	5.36	0.63			8.58	1.00	6.20	0.61
WILL	6.35	0.46	4.04	0.63	2.58	0.46					0.51	0.38
WROC											0.78	0.45
WSRT	8.76	0.40	1.79	0.34	2.26	0.38	5.14	0.73			1.53	0.30
WTZR	6.48	0.31	1.55	0.28	1.53	0.31	3.57	0.43	1.63	0.36	1.35	0.24
WTZZ	4.80	0.76									4.11	0.55
YAKT	13.84	0.98	5.15	0.78	3.51	1.04	11.21	2.57	8.04	0.95	6.86	0.68
YAKZ	17.87	0.74	4.81	0.67					9.49	1.77		
YAR1	10.69	0.73	3.63	0.57	7.73	0.70	12.74	1.03	6.56	0.60	5.51	0.38
YAR2	13.37	0.51	6.21	0.67	7.06	0.46			3.93	2.55		
YARR	7.42	0.62							9.39	3.73	6.92	0.42
YEVE									2.02	1.46	0.53	0.53
YELL	5.47	0.51	4.21	0.51	4.60	0.49	2.49	0.65	5.71	0.51	3.84	0.45
YSSK	18.23	0.51	5.74	0.51	4.76	0.38			2.27	0.77	7.35	0.38
ZAMB	6.49	0.77	5.45	0.66	6.45	0.63			6.71	0.74	5.34	0.81
ZECK	10.67	0.43	5.83	0.46	4.00	0.39			4.85	0.72	6.12	0.35
ZIMJ	4.79	0.91									3.43	0.85
ZIMM	5.79	0.31	1.70	0.23	1.04	0.39	2.21	1.35			1.44	0.21
ZIMZ	2.72	0.63									3.20	0.55
ZWEN	9.95	0.92	5.20	0.96	5.79	1.01	9.16	1.08	5.05	2.07	6.21	0.77

Bibliography

- ALTAMIMI *et al.*, (2001). The Terrestrial Reference Frame and the Dynamic Earth, *EOS Trans AGU*, 82(25), pp. 273-379.
- ALTAMIMI Z., P. SILLARD, AND C. BOUCHER, (2002). ITRF2000: A New Release of the International Terrestrial Reference Frame for Earth Science Applications, *J. Geophys. Res.*, 107 (B10), 2214, DOI: 10.1029/2001JB000561.
- AMBROSIUS, B., G. BEUTLER, G. BLEWITT, AND R.E. NEILAN, (1998). The Role of GPS in the WEGENER Project, *Journal of Geodynamics*, Vol. 25, pp. 213-240.
- AWANGE, J.L., AND E.W. GRAFAREND, (2005). Solving Algebraic Computational Problems in Geodesy and Geoinformatics, The Answer to Modern Challenge, *Springer*, XVII.
- BAKER, T.F., D.J. CURTIS, A.H. DODSON, (1995). Ocean Tide Loading and GPS, *GPS World*, March, pp. 54-59.
- BEUTLER, G., M. ROTHACHER, S. SCHAEER, T.A. SPRINGER, J. KOUBA, AND R.E. NEILAN, (1999). The International GPS Service (IGS): An Interdisciplinary Service in Support of Earth Sciences, *Advances in Space Research*, Vol. 23, No. 4, pp. 631-635.
- BEUTLER, G., (2005). Methods of Celestial Mechanics, Volume I&II, in cooperation with Prof. Leos Mervart and Dr. Andreas Verduin, *Astronomy and Astrophysics Library*, Springer.
- BLEWITT, G., (1989). Carrier Phase Ambiguity Resolution for the Global Positioning System Applied to Geodetic Baselines up to 2000 km, *Journ. Geophys. Res.*, Vol. 94, No. B8, pp. 10187-10283.
- BLEWITT, G., (1991). Measuring the Earth to Within an Inch Using GPS Satellites, *Geophysics News* 1991, pp. 19-20, American Geophys. Union, Washington D.C.
- BLEWITT, G., M.B. HEFLIN, F.H. WEBB, U.J. LINDQWISTER, AND R.P. MALLA, (1992). Global Coordinates with Centimeter Accuracy in the International Terrestrial Reference Frame Using the Global Positioning System, *Geophys. Res. Lett.*, 19, pp. 853-856.
- BLEWITT, G., (1993). Advances in Global Positioning System Technology for Geodynamics Investigations, in *Contributions of Space Geodesy to Geodynamics: Technology*, Ed. by D.E. Smith and D.L. Turcotte, pp. 195-213, Pub. by American Geophysical Union (Geodynamics Series Vol. 25), Washington DC.
- BLEWITT, G., Y. BOCK, AND J. KOUBA, (1994). Constraining the IGS Polyhedron by Distributed Processing, workshop proceedings : Densification of ITRF through Regional GPS Networks, held at JPL, Nov30-Dec 2, pp. 21-37.
- BLEWITT, G., (1997). Basics of the GPS Technique: Observation Equations, in *Geodetic Applications of GPS*, pp. 10-54, ed. B. Johnson, Nordic Geodetic Commission, Sweden.
- BLEWITT, G., (1998a). Global Positioning Satellites, in *Macmillan Encyclopedia of the Earth Sciences*, pp. 432-436, Macmillan, New York.
- BLEWITT, G., (1998b). GPS Data Processing Methodology: From Theory to Applications, in *GPS for Geodesy*, pp. 231-270, Eds. P.J.G. Teunissen and A. Kleusberg, Springer-Verlag, Berlin.
- BLEWITT, G., (2000). Geodetic Network Optimization for Geophysical Parameters, *Geophys. Res. Lett.*, Vol. 27, No. 22, pp. 3615-3618.
- BLEWITT, G., D. LAVALLEE, P. CLARKE, AND K. NURUTDINOV, (2001). A New Global Mode of Earth Deformation: Seasonal Cycle Detected, *Science*, Vol. 294, No. 5550, pp. 2342-2345.
- BLEWITT, G., AND D. LAVALLEE, (2002). Effect of Annual Signals on Geodetic Velocity, *Journ. Geophys. Res.*, Vol. 107(B7), DOI: 10.1029/2001JB000570.
- BLEWITT, G., (2003). Self-consistency in Reference Frames, Geocenter Definition, and Surface Loading of the Solid Earth, *Journ. Geophys. Res.*, Vol. 108 (B2) 210, DOI: 10.1029/2002JB002082.
- BLEWITT, G., AND P. CLARKE, (2003). Inversion of Earth's Changing Shape to Weigh Sea Level in Static Equilibrium with Surface Mass Redistribution, *Journ. Geophys. Res.*, 108 (B6), 2311, DOI: 10.1029/2002JB002290.
- BLEWITT, G., (2004). Fundamental Ambiguity in the Definition of Vertical Motion, *Cahier du Centre Européen de Géodynamique et de Séismologie*, Ed. T. van Dam & O. Francis, Vol. 23, pp. 1-4.
- BOEHM, J., AND H. SCHUH, (2004). Vienna Mapping Functions in VLBI Analyses, *Geophys. Res. Lett.*, 31, L01603, DOI: 10.1029/2003GL018984.
- BOEHM J., B. WERL, AND H. SCHUH, (2006a). Troposphere Mapping Functions for GPS and Very Long Baseline Interferometry from European Centre for Medium-Range Weather Forecasts Operational Analysis Data, *J. Geophys. Res.*, 111, B02406, DOI: 10.1029/2005JB003629.
- BOEHM, J., P.J. MENDES CERVEIRA, H. SCHUH, AND P. TREGONING, (2006b). The Impact of Mapping Functions for the Neutral Atmosphere based on Numerical Weather Models in GPS Data Analysis, *IAG Scientific Assembly 2005*, Springer Verlag, in print.
- BOS, M.S., AND T.F. BAKER, (2000). Ocean Tides and Loading in the Nordic Seas, *Memoirs of*

- BOS, M.S., AND T.F. BAKER, (2005). An Estimate of the Errors in Gravity Ocean Tide Loading Computations. *Journ. of Geodesy*, Vol. 79, pp. 50-63, DOI: 10.1007/s00190-005-0442-5.
- BOY, J.-P., AND B.F. CHAO, (2005). Precise Evaluation of Atmospheric Loading Effects on Earth's Time-Variable Gravity Field, in print, *Journ. Geophys. Res.*
- BRASWELL, W.D., AND R.S. LINDZEN, (1998). Anomalous Short Wave Absorption and Atmospheric Tides, *Geophys. Res. Lett.*, Vol. 25(9), pp. 1293-1296, DOI: 10.1029/98GL01031.
- BUELLESFELD, H., AND H. SCHUH, (1986). New Harmonic Development of the Tide-Generating Potential, ETMB85, with Application on VLBI Data Analysis, in *Proceedings of the 10th Symposium on Earth Tides*, Madrid, edited by R. Vieira, pp. 933-942, Cons. Super. de Invest. Cient., Madrid.
- BUFFETT, B.A., P.M. MATHEWS, AND T.A. HERRING, (2002). Modelling of Nutation and Precession: Effect of Electromagnetic Coupling, *Journ. Geophys. Res.*, Vol. 107 (B4), DOI: 10.1029/2000JB000056.
- CAMPBELL, J., (1979): Die Radiointerferometrie auf Langen Basen als Geodaetisches Messprinzip Hoher Genauigkeit. DGK Reihe C, Nr. 254, Muenchen.
- CAPITAINE, N., (2002). Comparison of 'old' and 'new' Concepts: The Celestial Intermediate Pole and Earth Orientation Parameters, In: Capitaine, N., D. Gambis, D.D. McCarthy, G. Petit, J. Ray, B. Richter, M. Rothacher, E.M. Standish and J. Vondrak (Editors), *Proceedings of the IERS workshop on the implementation of the new IAU resolutions*, pp. 35-44, *IERS Technical Note 29*, Verlag des Bundesamtes fur Kartographie und Geodäsie, Frankfurt am Main.
- CARTWRIGHT, D.E., AND R.J. TAYLER, (1971). New Computations of the Tide-Generating Potential, *Geophys. J. R. Astr. Soc.*, Vol. 23, pp. 45-74.
- CARTWRIGHT, D.E., AND A.C. EDDEN, (1973). Corrected Tables of Tidal Harmonics, *Geophys. J. R. Astr. Soc.*, Vol. 33, pp. 253-364.
- CARTWRIGHT, D.E. (1993). Theory of Ocean Tides with Application to Altimetry, in *Satellite Altimetry in Geodesy and Oceanography*, pp. 99-141, Springer-Verlag, Berlin/New York.
- CARTWRIGHT, D.E. (1999). Tides: A Scientific History, Cambridge: Cambridge University Press.
- CHAO, B.F., (1985). As the World Turns, *EOS, Trans. Amer. Geophys. Union*, Vol. 46, pp. 766-770.
- CHAO, B.F., (1991). As the World Turns, II, *EOS, Trans. Amer. Geophys. Union*, Vol. 72, pp. 550-551.
- CHAO, B.F., (2005). On Inversion for Mass Distribution from Global (Time-Variable) Gravity Field, *J. Geodynamics*, Vol. 39, pp. 223-230, DOI: 10.1016/j.jog.2004.11.001.
- CHAPMAN, S., AND R.S. LINDZEN, (1970). Atmospheric Tides, Dordrecht: D. Reidel.
- DAHLEN, F.A., (1976). The Passive Influence of the Oceans upon the Rotation of the Earth, *Geophys. J. R. Astron. Soc.*, Vol. 46, pp. 363-406.
- DARWIN, G.H., (1882). On Variations in the Vertical due to Elasticity of the Earth's Surface, *Phil. Mag., Ser. 5*, col. 14, N. 90, pp. 409-427.
- DARWIN, G.H., (1886). On the Dynamical Theory of the Tides of Long Period, *Proc. R. Soc. London A*, Vol. 41, pp. 337-342.
- DAVIES, P., AND G. BLEWITT, (2000). Methodology for Global Geodetic Time Series Estimation: A New Tool for Geodynamics, *Journ. Geophys. Res.*, Vol. 105, No. B5, pp. 11083-11100.
- DE CORIOLIS, G.G., (1835). Sur les Equations du Mouvement Relatif des Systèmes de Corps, *J. de l'Ecole royale polytechnique*, Vol. 15, pp. 144-154.
- DEHANT, V., (1987). Tidal Parameters for an Inelastic Earth, *Phys. Earth Planet. Inter.*, 49, 242.
- DESAI, S.D., (1996). Ocean Tides from TOPEX/POSEIDON Altimetry with Some Geophysical Applications, Ph.D. dissertation submitted to the Department of Aerospace Engineering Sciences, University of Colorado, Boulder, CO.
- DE VRIES, D., AND WAHR, J., (1991). The Effects of the Solid Inner Core and Non-Hydrostatic Structure on the Earth's Forced Nutations and Earth Tides, *Journ. Geophys. Res.*, Vol. 96, B5, pp. 8275-8293.
- DONG, D., J. Q. DICKEY, Y. CHAO, AND M. K. CHENG, (1997). Geocenter Variations Caused by Atmosphere, Ocean and Surface Ground Water, *Geophys. Res. Lett.*, Vol. 24(15), pp. 1867-1870, DOI: 10.1029/97GL01849.
- DONG, D., P. FANG, Y. BOCK, M.K. CHENG, AND S. MIYAZAKI, (2002). Anatomy of Apparent Seasonal Variations from GPS Derived Site Position Time Series, *Journ. Geophys. Res.*, Vol.107, DOI: 10.1029/2001JB000573.
- DONG D., T. YUNCK, AND M. HEFLIN, (2003). Origin of the International Terrestrial Reference Frame, *J. Geophys. Res.*, Vol. 108 (B4), 2200, DOI: 10.1029/2002JB002035.

- DOODSON, A.T., (1921). The Harmonic Development of the Tide-Generating Potential, *Proc. R. Soc. London A*, Vol. 100, pp. 305-329.
- DOUVILLE, H., E. BAZILE, P. CAILLE, D. GIARD, J. NOILHAN, L. PEIRONE, AND F. TAILLEFER, (1999). Global Soil Wetness Project: Forecast and Assimilation Experiments Performed at Météo-France. *J. Meteorological Soc. Japan*, Vol. 77, pp. 305-316.
- DZIEWONSKI, A.M., AND D.L. ANDERSON (1981). Preliminary Reference Earth model (PREM), *Phys. Earth Planet. Int.*, Vol. 25, pp. 297-356.
- EANES R.J., AND S.V. BETTADPUR, (1996). The CSR 3.0 Global Ocean Tide Model. Center for Space Research, *Techn. Memorandum*, CSR-TM-96-05.
- EANES R.J., AND S.V. BETTADPUR, (1999). The CSR 4.0 Global Ocean Tide Model. <ftp://ftp.csr.utexas.edu/pub/tide/>
- EGBERT, G.D., AND S.Y. EROFEEVA, (2002). Efficient Inverse Modelling of Barotropic Ocean Tides, *J. Atmos. Oceanic Technol.*, Vol. 19(2), pp. 183-204.
- ENGELS, J., (2006). Zur Modellierung von Auflastdeformationen und Induzierter Polwanderung. Habilitation, in print.
- FARRELL, W.E., (1972). Deformation of the Earth by Surface Loads. *Rev. Geophys. Space Phys.*, No.10, pp. 761-797.
- FRANCIS, D., AND P. MAZZEGA, (1990). Global Charts of Ocean Tide Loading Effects, *Journ. Geophys. Res.*, Vol. 95(C7), pp. 11411-11424, DOI: 10.1029/89JC02994.
- FRITSCHÉ M., R. DIETRICH, C. KNOEFEL, A. RUELKE, S. VEY, M. ROTHACHER, AND P. STEIGENBERGER (2005). Impact of Higher-Order Ionospheric Terms on GPS Estimates, *Geophys. Res. Lett.*, Vol. 32, L23311, DOI: 10.1029/2005GL024342.
- GILBERT, F., AND A.M. DZIEWONSKI, (1975). An Application of Normal Mode Theory to the Retrieval of Structural Parameters and Source Mechanisms from Seismic Spectra, *Phil. Trans. R. Soc. London, A*, Vol. 278, pp. 187-269.
- GONDHALEKAR, P., (2001). The Grip of Gravity: The Quest to Understand the Laws of Motion and Gravitation, Cambridge: *Cambridge University Press*.
- GROSS, R.S., G. BLEWITT, P.J. CLARKE, AND D. LAVALLÉE, (2004). Degree-2 Harmonics of the Earth's Mass Load Estimated from GPS and Earth Rotation Data, *Geophys. Res. Lett.*, Vol. 31, L07601, DOI: 10.1029/2004GL019589.
- GUTENBERG, B., (1951). Internal Constitution of the Earth, 2nd Ed., *Dover Publications*, NY.
- HAAS, R., AND H. SCHUH, (1996). Determination of Frequency Dependent Love and Shida Numbers from VLBI Data, *Geophys. Res. Lett.*, Vol. 23, pp. 1509-1512.
- HAAS, R., H.-G. SCHERNECK, AND H. SCHUH (1997). Atmospheric Loading Corrections in Geodetic VLBI and Determination of Atmospheric Loading Coefficients. In: *Proceedings of the 12th Working Meeting on European VLBI for Geodesy and Astronomy*, Hønefoss, Norway, 12-13 September 1997, edited by B. R. Pettersen, pp. 111-121.
- HARTMANN, T., AND H.-G. WENZEL, (1995). The HW95 Tidal Potential Catalogue, *Geophys. Res. Lett.*, Vol. 22(24), pp. 3553-3556, DOI: 10.1029/95GL03324.
- HATANAKA, Y., A. SENGOKU, T. SATO, J. M. JOHNSON, C. ROCKEN, AND C. MEERTENS, (2001). Detection of Tidal Loading Signals from GPS Permanent Array of GSI Japan, *J. Geod. Soc. Jpn.*, Vol. 47(1), pp. 187-192.
- HAWAREY, M., T. HOBIGER, AND H. SCHUH (2005). Effects of the 2nd Order Ionospheric Terms on VLBI Measurements, *Geophys. Res. Lett.*, Vol. 32, L11304, DOI: 10.1029/2005GL022729.
- HEFLIN, M.B., W.I. BERTIGER, G. BLEWITT, A.P. FREEDMAN, K.J. HURST, S.M. LICHTEN, U.J. LINDQWISTER, Y. VIGUE, F.H. WEBB, T.P. YUNCK, AND J.F. ZUMBERGE, (1992). Global Geodesy Using GPS Without Fiducial Sites, *Geophys. Res. Lett.*, Vol. 19, pp. 131-134.
- HERRING T.A., P.M. MATHEWS, AND B.A. BUFFETT, (2002). Modelling of Nutation and Precession: Very Long Baseline Interferometry Results *Journ. Geophys. Res.*, Vol. 107 (B4), DOI: 10.1029/2001JB000165.
- HOBSON, E.W., (1955). The Theory of Spherical and Ellipsoidal Harmonics, New York: *Chelsea Publishing Company*.
- HOFMANN-WELLENHOF, B., H. LICHTENEGGER, AND J. COLLINS, (1997). GPS Theory and Practice, *Springer*, Berlin, 4. Ausgabe.
- HOLLAND, P.W., AND R.E. WELSCH (1977). Robust Regression Using Iteratively Reweighted Least-Squares, *Communications in Statistics: Theory and Methods*, A6, pp. 813-827.
- HUANG, J., H. VAN DEN DOOL, AND K.P. GEORGAKAKOS, (1996). Analysis of Model-Calculated Soil Moisture over the United States (1931-1993) and Application to Long-Range Temperature Forecasts, *Journal of Climate*, Vol.9, No.6, pp. 1350-1362.
- HUGENTOBLE, U., R. DACH, P. FRIDEZ, AND M. MEINDL, (2006). Bernese GPS Software. Version 5.0 DRAFT. Printing Office of the University of Bern, 499 pages.

- JEFFREYS, H., (1962). The Earth, Cambridge: Cambridge University Press.
- JEFFREYS, H., AND R.O. VICENTE (1966). Comparison of Forms of the Elastic Equations for the Earth, Obs. Roy. Belg. Comm. Ser. B, N°3, S.Geoph. N°72, BIM, N°43, pp. 1611.
- JOHNSON, T.J., C.R. WILSON, AND B.F. CHAO, (1999). Oceanic Angular Momentum Variability Estimated from the Parallel Ocean Climate Model, 1988-1998. *Journ. Geophys. Res.*, Vol.104, pp. 25183-25196.
- KANIUTH, K., AND S. VETTER, (2005). Estimating Atmospheric Loading Regression Coefficients from GPS Observations, *GPS Solutions*, DOI: 10.1007/s10291-005-0014-4.
- KANTHA, L.H., AND C.A. CLAYSON, (2000). Numerical Models of Oceans and Oceanic Processes, Volume 66 of International Geophysics Series, San Diego: Academic Press.
- KAPLAN, E., (2005). Understanding GPS: Principles and Applications, 2nd ed., Artech House Mobile Communications.
- KELLOGG, O.D., (1954). Foundations of Potential Theory, New York: Dover Publications, (unabridged and unaltered republication of the work originally published in 1929 by J. Springer).
- KING, R.W., AND Y. BOCK, (2005). Documentation for the GAMIT GPS Processing Software, Release 10.2, Mass. Inst. of Technol., Cambridge, MA.
- KING, M.A., AND L. PADMAN (2005). Accuracy Assessment of Ocean Tide Models Around Antarctica, *Geophys. Res. Lett.*, Vol. 32, L23608, DOI: 10.1029/2005GL023901.
- KUDRYAVTSEV, S.M. (2004). Improved Harmonic Development of the Earth Tide-Generating Potential, *Journ. of Geodesy*, Vol. 77, pp. 829-838.
- KUSCHE, J., AND E.J.O. SCHRAMA, (2005). Surface Mass Redistribution Inversion from Global GPS deformation and GRACE Gravity Data, *Journ. Geophys. Res.*, Vol. 110, B09409, DOI: 10.1029/2004JB003556.
- LAMBECK, K., (1980). The Earth's Variable Rotation: Geophysical Causes and Consequences, Cambridge: Cambridge University Press.
- LAMBECK, K., (1988). Geophysical Geodesy: The Slow Deformations of the Earth, Oxford University Press.
- LAMBERT, A., S.D. PAGIATAKIS, A.P. BILLYARD, AND H. DRAGERT, (1998). Improved Ocean Tide Loading Corrections for Gravity and Displacements: Canada and Northern United States, *Journ. Geophys. Res.*, Vol. 103, pp. 30231-30244.
- LANDAU, L.D., AND E.M. LIFSCHITZ, (1991). Lehrbuch der Theoretischen Physik, Band 7, Elastizitätstheorie, Verlag Harri Deutsch.
- LAVALLEE, D., AND G. BLEWITT, (2002). Degree-one Earth Deformation from Very Long Baseline Interferometry, *Geophys. Res. Lett.*, Vol. 29(20), DOI: 10.1029/2002GL015883.
- LEICK, A., (2005). GPS Satellite Surveying, 3rd edition, Wiley and Sons.
- LEFEVRE, F., F.H. LYARD, C. LE PROVOST AND E.J.O. SCHRAMA, (2002). FES99: a Global Tide Finite Element Solution Assimilating Tide Gauge and Altimetric Information, *J. Atmos. Oceanic Technol.*, Vol. 19, pp. 1345-1356.
- LETELLIER, T., (2004). Etude des Ondes de Marée sur les Plateaux Continentaux, Thèse doctorale, Université de Toulouse III, Ecole Doctorale des Sciences de l'Univers, de l'Environnement et de l'Espace.
- LE PROVOST C., M. GENCO, F. LYARD, P. INCENT, AND P. CANCEIL, (1994). Spectroscopy of the World Ocean Tides from a Finite Element Hydrological Model. *Journ. Geophys. Res.*, Vol. 99, pp. 24777-24798.
- LOVE, A.E.H., (1967). Some Problems of Geodynamics, (unabridged and unaltered republication of the originally published in 1911 by Cambridge University Press), New York: Dover Publications, INC.
- LOVELOCK, D., AND H. RUND (1989). Tensors, Differential Forms, and Variational Principles, New York: Dover Publications, INC.
- LUTHCKE, S.B., D.D. ROWLANDS, F.G. LEMOINE, S.M. KLOSKO, D. CHINN, AND J.J. MCCARTHY, (2006). Monthly Spherical Harmonic Gravity Field Solutions Determined from GRACE Inter-Satellite Range-Rate Data Alone, *Geophys. Res. Lett.*, Vol. 33, L02402, DOI: 10.1029/2005GL024846.
- MA, C., AND L. PETROV, (2003). SINEX File Implementation in the VLBI Calc/Solve Analysis System, IERS Technical Note No. 30.
- MACMILLAN, D.S., AND J.M. GIPSON, (1994). Atmospheric Pressure Loading Parameters from Very Long Baseline Interferometry Observations, *Journ. Geophys. Res.*, Vol. 99, pp. 18081-18087.
- MATHERS, E. L., AND P. L. WOODWORTH, (2001). Departures from the Local Inverse Barometer Model Observed in Altimeter and Tide Gauge Data and in a Global Barotropic Numerical Model, *Journ. Geophys. Res.*, Vol. 106(C4), pp. 6957-6972, DOI: 10.1029/2000JC000241.
- MATHEWS, P.M., B.A. BUFFETT, AND I.I. SHAPIRO, (1995). Love Numbers for a Rotating Spheroidal Earth: New Definitions and Numerical Values, *Geophys. Res. Lett.*, Vol. 22, pp. 579-582.

- MATHEWS, P.M., V. DEHANT, AND J.M. GIPSON, (1997). Tidal Station Displacements, *Journ. Geophys. Res.*, Vol. 102, pp. 20469-20477.
- MATHEWS, P.M., (2001). Love Numbers and Gravimetric Factor for Diurnal Tides, *J. Geod. Soc. Jpn.*, Vol. 47(1), pp. 231-236.
- MATHEWS, P.M., T.A. HERRING, AND B.A. BUFFETT, (2002). Modelling of Nutation and Precession: New Nutation Series for Non-Rigid Earth and Insights into the Earth's Interior, *J. Geophys. Res.*, Vol. 107 (B4), DOI: 10.1029/2001JB000390.
- MATSUMOTO, K., T. TAKANEZAWA, AND M. OOE, (2000). Ocean Tide Models Developed by Assimilating TOPEX/POSEIDON Altimeter Data into Hydrodynamical Model: A Global Model and a Regional Model Around Japan, *Journal of Oceanography*, Vol. 56, pp. 567-581.
- MAUTZ, R., (2001). Zur Lösung Nichtlinearer Ausgleichungsprobleme bei der Bestimmung von Frequenzen in Zeitreihen, *Deutsche Geodätische Kommission, Reihe C, Nr. 532*, München.
- MCCARTHY, D.D., AND G. PETIT, (2003). IERS Conventions 2003. <http://maia.usno.navy.mil/conv2000.html>
- MEESON, B.W., F.E. CORPREW, J.M.P. MCMANUS, D.M. MYERS, J.W. CLOSS, K.J. SUN, D.J. SUNDAY, AND P.J. SELLERS, (1995). ISLSCP Initiative I - Global Data Sets for Land-Atmosphere Models, 1987-1988, Vol. 1-5, *Published on CD-ROM by NASA*.
- MELCHIOR, P.J., (1978). The Tides of the Planet Earth, Paris: *Pergamon*.
- MELLOR, G.L., (1996). Introduction to Physical Oceanography, *Springer-Verlag*.
- MENDES CERVEIRA, P.J., R. HEINKELMANN, J. BOEHM, R. WEBER AND H. SCHUH, (2006a). Contributions of GPS and VLBI in Understanding Station Motions, *Journal of Geodynamics*, pp. 87-93, DOI: 10.1016/j.jog.2005.08.024.
- MENDES CERVEIRA, P.J., T. HOBIGER, R. WEBER AND H. SCHUH, (2006b). Spatial Spectral Inversion of SOPAC GPS Data, *IAG Scientific Assembly 2005*, Springer Verlag, in print.
- MENTES, G., (2004). Atmospheric Tide Obtained by the Microbarograph Developed at the Geodetic and Geophysical Research Institute of the Hungarian Academy of Sciences, *Acta Geod. Geoph. Hung.*, Vol. 39(1), pp. 39-48.
- MEURERS, B., (2002). Erdgezeiten und Eigenschwingungen, lecture notes, University of Vienna.
- MILLY, P.C.D., A.B. SHMAKIN, AND K.A. DUNNE, (2002). Global Modelling of Land Water Balances: The Land Dynamics Model (LaD). *Journal of Hydrometeorology*, Vol. 3, pp. 283-299.
- MOLODENSKY, M.S., (1961). The Theory of Nutation and Diurnal Earth Tides, *Comm. Obs. R. Belgique*, Vol. 142, pp. 25-56.
- MORITZ, H., AND I.I. MUELLER, (1987). Earth Rotation. Theory and Observation, New York: *Ungar*.
- MUNK, W.H., AND G.J.F. MACDONALD, (1960). The Rotation of the Earth. A Geophysical Discussion, Cambridge: *Cambridge University Press*.
- MUNK, W.H., AND D.E. CARTWRIGHT, (1966). Tidal Spectroscopy and Prediction, *Proc. R. Soc. London, A*, Vol. 259, pp. 533-581.
- NEWTON, I., (1999). The Principia: Mathematical Principles of Natural Philosophy, translated by Cohen, B., and A. Whitman, preceeded by 'A Guide to Newton's Principia', *University of California Press*.
- NIKOLAIDIS, R., (2002). Observation of Geodetic and Seismic Deformation with the Global Positioning System, *Ph.D. Thesis, University of California*, San Diego.
- OGDEN, R.W., (1997). Non-Linear Elastic Deformations, Mineola, New York: *Dover Publications*, 2nd Ed..
- PAGIATAKIS, S.D., (1990). The Response of a Realistic Earth to Ocean Tide Loading, *Geophys. J. Int.*, Vol. 103, pp. 1541-1560.
- PENNA, N.T., AND M.P. STEWART, (2003). Aliased Tidal Signatures in Continuous GPS Height Time Series, *Geophys. Res. Lett.*, Vol. 30(23), 2184, DOI: 10.1029/2003GL018828.
- PETROV, L.Y., (1998). VLBI Measurements of the Crustal Deformations Induced by Polar Motion, *Izvestiya, Physics of the Solid Earth*, Vol.34, N3, pp. 228-230.
- PETROV, L.Y, AND G. MA, (2003). Study of Harmonic Site Position Variations Determined by Very Long Baseline Interferometry. *Journ. Geophys. Res.*, Vol. 108(B4), 2190, DOI: 10.1029/2002JB001801.
- PETROV, L.Y, AND J.-P. BOY, (2004). Study of the Atmospheric Pressure Loading Signal in VLBI Observations, *Journ. Geophys. Res.*, Vol. 109, No. B03405, DOI: 10.1029/2003JB002500.
- PONTE, R.M., AND R.D. RAY, (2002). Atmospheric Pressure Corrections in Geodesy and Oceanography: A Strategy for Handling Air Tides, *Geophys. Res. Lett.*, Vol. 29 (24), 2153, DOI: 10.1029/2002GL016340.
- PRATT, W.K., (1978). Digital Image Processing, John Wiley & Sons, pp. 330-333.

- PUGH, D., (2004). Changing Sea Levels. Effects of Tides, Weather and Climate. Cambridge: Cambridge University Press.
- RABEL, W., AND J. ZSCHAU, (1985). Static Deformations and Gravity Changes at the Earth's Surface due to Atmospheric Loading, *Journal of Geophysics*, Vol. 56, pp. 81-99.
- RABEL, W. AND H. SCHUH, (1986). The Influence of Atmospheric Loading on VLBI Experiments, *Journal of Geophysics*, Vol. 59, pp. 164-170.
- RAY, R.D., (1998). Diurnal Oscillations in Atmospheric Pressure at Twenty-Five Small Oceanic Islands, *Geophys. Res. Lett.*, Vol. 25(20), pp. 3851-3854, DOI: 10.1029/1998GL900039.
- RAY, R.D., (1999). A Global Ocean Tide Model from TOPEX/POSEIDON Altimetry: GOT99.2. NASA/TM-1999-209478. *National Aeronautics and Space Administration*. Goddard Space Flight Center, Greenbelt, MD.
- RAY, J., D. DONG, AND Z. ALTAMIMI, (2005). IGS Reference Frames: Status and Future Improvements, Proceedings of the Workshop and Symposium "Celebrating a Decade of the International GPS Service", Astronomical Institute, University of Bern, Switzerland, pp. 37-63.
- ROTHACHER, M., G. BEUTLER, T. A. HERRING, AND R. WEBER, (1999). Estimation of Nutation using the Global Positioning System, *J. Geophys. Res.*, Vol. 104 (B3), pp. 4835-4860, DOI: 10.1029/1998JB900078.
- ROTHACHER, M., G. BEUTLER, R. WEBER, AND J. HEFTY, (2001). High-frequency Variations in Earth Rotation from Global Positioning System Data, *J. Geophys. Res.*, Vol. 106 (B7), pp. 13711-13738, DOI: 10.1029/2000JB900393.
- SCHERNECK, H.G., (1991). A Parameterized Solid Earth Tide Model and Ocean Tide Loading Effects for Global Geodetic Baseline Measurements. *Geophys. J. Int.*, Vol. 106, pp. 677-694.
- SCHERNECK, H.G., (1996). Site Displacement due to Ocean Loading, McCarthy D.D. (editor): *IERS Technical Note 21*, pp. 52-56.
- SCHERNECK, H.G., AND R. HAAS, (1999). Effect of Horizontal Displacements due to Ocean Tide Loading on the Determination of Polar Motion and UT1, *Geophys. Res. Lett.*, 26(4), pp. 501-504, DOI: 10.1029/1999GL900020.
- SCHERNECK, H.-G., (2000). HGS Air Pressure Loading.
<http://www.oso.chalmers.se/%7Eloading/index.html>
- SCHLUETER, W., E. HIMWICH, A. NOTHNAGEL, N. VANDENBERG, AND A. WHITNEY, (2002). IVS and Its Important Role in the Maintenance of the Global Reference Systems, *Advances in Space Research*, Vol. 30, No. 2, pp. 145-150.
- SCHMID, R., AND M. ROTHACHER, (2003). Estimation of Elevation-Dependent Satellite Antenna Phase Center Variations of GPS Satellites, *Journ. of Geodesy*, Vol. 77, pp. 440-446, DOI: 10.1007/s00190-003-0339-0.
- SCHMID, R., M. ROTHACHER, D. THALLER, AND P. STEIGENBERGER, (2005). Absolute Phase Center Corrections of Satellite and Receiver Antennas: Impact on Global GPS Solutions and Estimation of Azimuthal Phase Center Variations of the Satellite Antenna; *GPS Solutions*, Vol. 9, No. 4, pp. 283-293, DOI: 10.1007/s10291-005-0134-x.
- SCHRAMA, E.J.O., (1984). Orbit Integration Based upon Interpolated Gravitational Gradients, PhD Thesis, Delft University of Technology.
- SCHUH, H., AND L. MOEHLMANN, (1989). Ocean Loading Station Displacements Observed by VLBI, *Geophys. Res. Lett.*, Vol. 16, pp. 1105-1108.
- SCHUH, H., AND R. HAAS, (1997). Earth Tides in VLBI Observations, *Proceedings of the Thirteenth International Symposium on Earth Tides*. Brussels 1998.
- SCHUH, H., S. NAGEL, AND T. SEITZ, (2001). Linear Drift and Periodic Variations Observed in Long Time Series of Polar Motion, *Journal of Geodesy*, 74, pp. 701-710.
- SCHUH, H., M. SOFFEL AND H. HORNIK, (2002). Vorträge beim 4. DFG-Rundgespräch im Rahmen des Forschungsvorhabens 'Rotation der Erde' zum Thema 'Wechselwirkungen im System Erde', Hollenstein/Wetzell, 08./09. März 2001, Reihe A 118, *Deutsche Geodätische Kommission*, München.
- SCHUH, H., G. ESTERMANN, J.F. CRETAUX, M. BERGE-NGUYEN, AND T. VAN DAM, (2003). Investigation of Hydrological and Atmospheric Loading by Space Geodetic Techniques, International workshop on satellite altimetry for geodesy, geophysics and oceanography. Wuhan, September 2002, *IAG Symposia Series*, Springer.
- SCHUH, H., R. DILL, H. GREINER-MAI, H. KUTTERER, J. MUELLER, A. NOTHNAGEL, B. RICHTER, M. ROTHACHER, U. SCHREIBER, AND M. SOFFEL, (2003). Erdrotation und Globale Dynamische Prozesse, Mitteilungen des Bundesamtes für Kartographie und Geodäsie; 32, *Verlag des Bundesamtes für Kartographie und Geodäsie*.
- SCHWEYDAR, W.V., (1916). Die Bewegung der Drehachse der Elastischen Erde im Erdkörper und im Raum, *Astron. Nachr.*, Vol 203, pp. 103-114.

- SCHWIDERSKI, E., (1983). Atlas of Ocean Tidal Charts and Maps Marine Geodesy, Vol. 6, pp. 219-256.
- SEITZ, F., (2004). Atmosphärische und Ozeanische Einflüsse auf die Rotation der Erde - Numerische Untersuchungen mit einem Dynamischen Erdsystemmodell, *Deutsche Geodätische Kommission*, Reihe C, Nr. 578, München.
- SEITZ, F., J. STUCK, AND M. THOMAS, (2004). Consistent Atmospheric and Oceanic Excitation of the Earth's Free Polar Motion, *Geophys. J. Int.*, Vol. 157, pp. 25-35.
- SLICHTER, L.B., (1961). The Fundamental Free Mode of the Earth's Inner Core, *Proc. Nat. Acad. Sci.*, USA, Vol. 47, pp. 186-190.
- SOVERS, D.J., AND J.S. BORDER, (1990). Observation Model and Parameter Partial for the JPL Geodetic Modelling Software 'GPSOMC', *JPL Publication 87-21*, Rev. 2, JPL, Pasadena, CA, USA.
- SOVERS, D.J., J.L. FANSELOW, AND C.S. JACOBS, (1998). Astrometry & Geodesy with Radio Interferometry: Experiments, Models, Results, *Rev. Mod. Phys.*, Vol. 70, 4, pp. 1393-1454.
- STANDISH, E.M. (1998). JPL Planetary and Lunar Ephemerides DE405/LE405, JPL IOM 312.F-98-048, Pasadena.
- STACEY, F.D., (1977). Physics of the Earth, 2nd ed, New York: Wiley.
- STEWART, M.P., N.T. PENNA AND D.D. LICHTI, (2005). Investigating the Propagation Mechanism of Unmodelled Systematic Errors on Coordinate Time Series Estimated using Least Squares, *Journal of Geodesy*, Springer-Verlag, Vol. 79, 8, pp. 479 – 489, DOI: 10.1007/s00190-005-0478-6.
- SUN, H.P., B. DUCARME, AND V. DEHANT, (1995). Effect of the Atmospheric Pressure on Surface Displacements. *Journal of Geodesy*, Vol. 70, pp. 131-139.
- TAMURA, Y., (1987). A Harmonic Development of the Tide-Generating Potential, *Marées Terrestres Bull. d'Informations*, Vol. 99, pp. 6813-6855.
- TAPLEY, B., J. RIES, S. BETTADPUR, D. CHAMBERS, M. CHENG, F. CONDI, B. GUNTER, Z. KANG, P. NAGEL, R. PASTOR, T. PEKKER, S. POOLE, AND F. WANG, (2005). GGM02 - An Improved Earth Gravity Field Model from GRACE, *Journal of Geodesy*, DOI: 10.1007/s00190-005-0480-z.
- THOMSON, W., AND P.G. TAIT, (1879). Treatise on Natural Philosophy, Cambridge: Cambridge University Press.
- TITOV, D.A., V. TESMER, AND J. BOEHM, (2001). Version 5.0 of the OCCAM VLBI Software. User Guide. *AUSLIG Technical Reports 7*, AUSLIG, Canberra.
- TREGONING, P., AND T. VAN DAM, (2005a). Effects of Atmospheric Pressure Loading and Seven-Parameter Transformations on Estimates of Geocenter Motion and Station Heights from Space Geodetic Observations, *Journ. Geophys. Res.*, Vol. 110, B03408, DOI: 10.1029/2004JB003334.
- TREGONING, P., AND T. VAN DAM, (2005b). Atmospheric Pressure Loading Corrections Applied to GPS Data at the Observation Level, *Geophys. Res. Lett.*, Vol. 32, L22310, DOI: 10.1029/2005GL024104.
- TURCOTTE, D.L., AND G. SCHUBERT, (2002). Geodynamics, 2nd edition, Cambridge: Cambridge University Press.
- URSCHL, C., R. DACH, U. HUGENTOBLE, S. SCHAER, AND G. BEUTLER, (2005). Validating Ocean Tide Loading Models using GPS, *Journ. of Geodesy*, Berlin, Vol. 78, pp. 616-625.
- VAN DAM, T.M., AND J.M. WAHR, (1987). Displacements of the Earth's Surface Due to Atmospheric Loading: Effects on Gravity and Baseline Measurements, *Journ. Geophys. Res.*, Vol. 92, pp. 1281-1286.
- VAN DAM, T.M., G. BLEWITT, AND M.B. HEFLIN, (1994a). Atmospheric Pressure Loading Effects on GPS Coordinate Determinations, *Journ. Geophys. Res.*, Vol. 99, pp. 23939-23950.
- VAN DAM, T.M. AND T.A. HERRING, (1994b). Detection of Atmospheric Pressure Loading using Very Long Baseline Interferometry Measurements, *Journ. Geophys. Res.*, Vol. 99, pp. 4505-4517.
- VAN DAM, T.M., WAHR, J., CHAO, Y., AND LEULIETTE, E., (1997). Predictions of Crustal Deformation and Geoid and Sea Level Variability Caused by Oceanic and Atmospheric Loading, *Geophysical Journal International*, Vol. 99, pp. 507-517.
- VAN DAM, T.M., H.-P. FLAG, O. FRANCIS, AND P. GEGOUT, (2003). GGFC Special Bureau for Loading: Current Status and Plans, IERS Technical Note No. 30: Proceedings of the *IERS Workshop on Combination Research and Global Geophysical Fluids*, Bavarian Academy of Sciences, Munich, Germany, 18-21 November 2002, Edited by Bernd Richter, Wolfgang Schwegmann, and Wolfgang R. Dick, pp. 180-198.
- VARGA, P., (1983). Potential Free Love Numbers, *Manuscripta Geodetica*, Vol. 8, pp. 85-92.
- VARGA, P., J. ENGELS, AND E. GRAFAREND, (2004). Temporal variations of the polar moment of inertia and the second-degree geopotential, *Journal of Geodesy*, Vol. 78, pp. 187-191.

- VEY, S., R. DIETRICH, M. FRITSCH, A. RÜLKE, M. ROTHACHER, AND P. STEIGENBERGER, (2006). Influence of Mapping Function Parameters on Global GPS Network Analyses: Comparisons Between NMF and IMF, *Geophys. Res. Lett.*, Vol. 33, L01814, DOI:10.1029/2005GL024361.
- VICENTE, R.O. AND C.R. WILSON, (2005). The Need for a New Definition of a Conventional International Origin, *Journ. of Geodesy*, DOI: 10.1007/s00190-005-0469-7.
- VIGUE, Y., S.M. LICHTEN, G. BLEWITT, M.B. HEFLIN, AND R.P. MALLA, (1992). Precise Determination of the Earth's Centre of Mass using Measurements from the Global Positioning System, *Geophys. Res. Lett.*, Vol. 19, pp. 1487-1490.
- VOLLAND, H., (1988). Atmospheric Tidal and Planetary Waves, Dordrecht, Netherlands: *Kluwer Academic Publishers*.
- VOLLAND, H., (1997). Atmospheric Tides, in: Tidal Phenomena, eds. H. Wilhelm, W. Zürn and H.G. Wenzel, *Springer*.
- WAHR, J.M., (1981). Body Tides on an Elliptical, Rotating, Elastic and Oceanless Earth, *Geophys. J. R. Astr. Soc.*, Vol. 64, pp. 677-703.
- WAHR, J.M., (1985). Deformation Induced by Polar Motion, *Journ. Geophys. Res.*, Vol. 90, pp. 9363-9368.
- WAHR, J., S. SWENSON, V. ZLOTNICKI, AND I. VELICOGNA, (2004). Time-Variable Gravity from GRACE: First Results, *Geophys. Res. Lett.*, Vol. 31(11), L1150110, DOI: 10.1029/2004GL019779.
- WANG, R., (1994). Effect of Rotation and Ellipticity on Earth Tides, *Geophys. J. Int.*, Vol. 117, pp. 562-565.
- WEBER, R., (1999). The Ability of the GPS to Monitor Earth Rotation Variation, in *Acta Geodaetica et Geophysica Hungarica*, Vol. 34, Number 4, pp. 457-473, Akademiai Kiado, Budapest. *Res. Lett.*, Vol. 30(14),1742, DOI: 10.1029/2003GL017546.
- WEBER, R., J.A. SLATER, E. FRAGNER, V. GLOTOV, H. HABRICH, I. ROMERO, S. SCHAEER, (2005). Precise GLONASS Orbit Determination within the IGS/IGLOS Pilot Project, *Advances in Space Research*, Vol. 36, Issue 3, Satellite Dynamics in the Era of Interdisciplinary Space Geodesy, (edited by Phillip Moore), pp. 369-375.
- WEGENER, A., (1966). The Origin of Continents and Oceans, translated by John Biram of the fourth revised edition of 'Die Entstehung der Kontinente und Ozeane' published in 1929 by Fried. Vieweg & Sohn, Mineola, New York: *Dover Publications*.
- WENZEL, H.-G., AND W. ZUERN, (1990). Errors of the Cartwright-Taylor-Edden 1973 Tidal Potential Displayed by Gravimetric Earth Tide Observations at BFO Schiltach, *Marées Terrestres Bull. d'Informations*, Vol. 107, pp. 7559-7574.
- WU, X., D.F. ARGUS, M.B. HEFLIN, E.R. IVINS AND F.H. WEBB, (2002). Site Distribution and Aliasing Effects in the Inversion for Load Coefficients and Geocentre Motion from GPS Data, *Geophys. Res. Lett.*, Vol. 29 (24), 2210, DOI: 10.1029/2002GL016324.
- WU, X., M.B. HEFLIN, E.R. IVINS, D.F. ARGUS AND F.H. WEBB, (2003). Large-Scale Global Surface Mass Variations Inferred from GPS Measurements of Load-Induced Deformation, *Geophys. Res. Lett.*, Vol. 30(14), 1742, DOI: 10.1029/2003GL017546.
- WUNSCH, C., AND D. STAMMER, (1997). Atmospheric Loading and the Inverted Barometer Effect, *Rev. Geophys.*, Vol. 35, pp. 79-107.
- XI, Q., (1989). The Precision of the Development of the Tidal Generating Potential and Some Explanatory Notes, *Bull. Inf. Mar. Terr.*, 105, pp. 7396-7404.
- ZHARKOV, V.N., S.M. MOLODENSKY, A. BREZINSKI, E. GROTEN, AND P. VARGA, (1996). The Earth and its Rotation: Low Frequency Geodynamics, *Herbert Wichman Verlag*.

List of Figures

Figure 1: Cross-section illustrating the main types of plate boundaries (source from USGS)	14
Figure 2: Schematic diagram showing how GPS pseudorange observations are related to the satellite and receiver clocks (here T stands for T_k ; source obtained from BLEWITT).	20
Figure 3: Basic principle of VLBI time delay.....	23
Figure 4: Contribution of techniques to combination in polar motion (top) and UT1 (bottom) (source from GAMBIS), over the last decades.....	25
Figure 5: IGS 332 active stations as of January 4 th , 2006 (source from IGS).....	26
Figure 6: (a) Horizontal velocities of all 31 SIRGAS stations available in the ITRF2000 reference frame and (b) vertical velocities of 12 SIRGAS stations that have a standard deviation larger than 5 [mm/year].	26
Figure 7: Vectors involved in tidal acceleration.....	31
Figure 8: Two bodies revolving about a common axis placed at their barycentre.	31
Figure 9: Centrifugal acceleration is a homogeneous vector field.	32
Figure 10: Graphic illustrating equation (3.2.12).	33
Figure 11: Graphic illustrating the theory of LOVE, where c is a constant.	36
Figure 12: Permanent deformation correction from “conventional tide free” to “mean tide” coordinates.	40
Figure 13: Load Love Numbers (from Gegout) up to degree 1024, expressed in the reference frame of the total Earth system’s centre of mass CM (solid Earth + atmosphere).	41
Figure 14: Graphic illustrating the deformation due to indirect effects (e.g. due to ocean tides).	41
Figure 15: Sketch illustrating the gravitational attraction of a mass element at a point P.	42
Figure 16: Green’s functions (for radial and horizontal displacements) in the centre of solid Earth frame (CE) (a) and their difference compared to the centre of mass frame of solid Earth and the mass which causes the loading (CM) (b).....	43
Figure 17: Mean pole coordinates (a) for the 20 th century available at BIPM, and C04 long-term pole coordinates (b) for the period 1996-2006.....	45
Figure 18: Primary and secondary waves’ velocity (a) and density/gravity (b) for PREM.	48
Figure 19: Radial displacement: (a) RMS distribution of difference NCEPR vs. ECMWF in the CM frame (source: VAN DAM), and (b) NCEPR vs. ECMWF for station Wuhan (WUHN), China.	51
Figure 20: Surface versus sea level pressure: RMS of radial surface displacement between ECMWF (TVD) – ECMWF (SBL) (a), and NMC/NCEP (TVD) – ECMWF (SBL) (b). Source: VAN DAM.	51
Figure 21: Surface pressure field (a) for January 1, 2000, at 00 hours UTC, computed from sea level pressure and temperature at the 1000 hPa level. The scale is in units of hPa. Difference between correct and erroneous surface	52
Figure 22: Offset (APLO-TVD) introduced into the predicted radial displacements by using either APLO or the TVD reference pressure. Source: VAN DAM.	53
Figure 23: RMS (a) and maximum (b) of the difference between the ‘exact’ time series (see text) and time series estimated by extracting data using the bicubic interpolation method for the radial component. Source: VAN DAM.....	53
Figure 24: Radial displacements caused by the loading of the diurnal S_1 (a) and semi-diurnal S_2 (b) variations in the atmospheric pressure (non-inverted barometer NIB assumption over the oceans). N.B.: Even if (a) looks like an IB assumption, it is not. Applying IB to the oceans at these frequencies is physically wrong. Source: VAN DAM.....	54

Figure 25: Differences between the land-ocean mask used by TVD and APLO. Red patches are locations where the TVD mask indicates that there is land and the APLO mask indicates there is water. Blue patches indicate the opposite. Source: VAN DAM.	55
Figure 26: Differences (APLO-TVD) in radial (left), latitudinal (middle) and longitudinal displacement (right) at station VIS0 situated in the Baltic Sea.	55
Figure 27: Observed regional variability of RMS (APLO-TVD) for the radial component (year 2004, source: VAN DAM) (a), and difference of APLO-TVD over the years 1992-2004 for the station LPGS, La Plata, Argentina (b).	55
Figure 28: Influence (RMS) of the Earth model (GB-A or PREM) on the Green's functions and on the induced displacements. Source: VAN DAM.	56
Figure 29: Difference of radial displacement between the erroneous and corrected CM Green's functions (after June 22 nd 2005) at the APLO service on day of year (doy) 9.00 of the year 2004. N.B.: previous APLO versions did not include displacements for the polar regions!	58
Figure 30: RMS of the differences of radial displacement due to pressure effects when using the convolution sum versus the spherical harmonic approach. Source: VAN DAM.	58
Figure 31: North (a) and east (b) deformation due to atmospheric pressure loading for January 1 st , 6 UT of the year 2004 (APLO in CE frame, atmospheric tides removed).	59
Figure 32: (a-c) Sketch illustrating the different reference frames used in geodesy. The red solid circle represents the centre of mass of the rigid Earth (CE), while the red cross represents the centre of mass of the total Earth (CM), which consists of the solid Earth plus the total mass within the fluid and gaseous envelope (FE). (b) In the case of very few stations (black filled triangles), the centre of network (CN) differs from both CE and CM frames. (c) For a non-degenerate network, the centre of figure (CF) frame, which is an idealization, however, roughly approximates the CE frame, and the CN frame too.	61
Figure 33: Horizontal station velocities of (a) the IGS specific reference frame IGb00 and (b) ITRF2000 for GPS only. N.B.: Note that colours represent the scale of the arrows in both figures!	62
Figure 34: Distribution of 50 chosen VLBI stations.	64
Figure 35: Histogram showing the number of baselines in function of the (a) length and (b) number of datapoints (observations).	65
Figure 36: Baseline length repeatability in function of the (a) VLBI baseline length (OA means without and WA means with applying the Goddard Space Flight Centre (GSFC) atmospheric loading model), and of the (b) GPS SOPAC baseline length. The repeatability "r" is given in mm, whereas "b" is the baseline length in km. (c) Histogram showing the improvement, given in percentage, of 216 VLBI baseline length repeatabilities, after applying the GSFC atmospheric model. We acknowledge that we used "atmospheric pressure loading time series", which are available on the web at http://gemini.gsfc.nasa.gov/aplo by PETROV AND BOY (2004).	66
Figure 37: Topocentric coordinate time series for site Wettzell (code 7224/WTZR) (a) VLBI IGG solution, (b) VLBI GSFC solution and (c) GPS SOPAC solution.	67
Figure 38: The lowercase solution "mit" has been discarded in the analysis, due to its recent upcoming. The COD solution is questionable due to the error detected in the corrections of the solid Earth tides, in mid-2004. The IGS final solution is a combination of the eight ACs. Presently, the IGS final solution is therefore slightly corrupted by the COD solution, since no reprocessing has been undertaken, yet. NCL and MIT figure as a control for the final IGS solution. Three ACs use a Kalman filtering approach (NRC=EMR,	

<i>JPL, MIT) to generate the daily coordinate solutions. However, the IGS coordinator does not use a Kalman filter to connect the weekly solutions.</i>	<i>69</i>
<i>Figure 39: Distribution of (a) 359 IGS stations and (b) 675 SOPAC stations used in this investigation.</i>	<i>70</i>
<i>Figure 40: Matrix of correlation coefficients (a) between the 537 parameters (3D geocentric coordinates of 161 stations (block 1-483), daily polar motion offsets and rates, daily UT offsets and daily LOD parameters). Zoom (b) on the Earth orientation parameters (block 484-537) for the COD weekly solution of the GPS week 1321.</i>	<i>71</i>
<i>Figure 41: Histogram of the 483 coordinate corrections applied to deconstrain the coordinates of the COD weekly solution of the GPS week 1321. The geocentric coordinate corrections do not exceed 6 mm for the week 1321. The AC at COD applies loose coordinate constraints at the 4 m level.</i>	<i>72</i>
<i>Figure 42: Matrix of correlation coefficients (a) between the 618 parameters, representing 3D geocentric coordinates of 188 stations (block 1-564), daily polar motion offsets and rates, daily UT offsets and daily LOD parameters. Zoom (b) on the Earth orientation parameters (block 565-618) for the GFZ weekly solution of the GPS week 1321.</i>	<i>72</i>
<i>Figure 43: Histogram of the 564 coordinate corrections applied to deconstrain the coordinates of the GFZ weekly solution of the GPS week 1321. The geocentric coordinate corrections do not exceed 6 mm for the week 1321, although the AC at GFZ applies tight coordinate constraints at the sub-cm level.</i>	<i>72</i>
<i>Figure 44: Histogram of the 537 coordinate corrections applied to deconstrain the coordinates of the SIO weekly solution of the GPS week 1321. The geocentric coordinate corrections do not exceed 1 mm for the week 1321. SIO applies very loose coordinate constraints at the 10 m level.</i>	<i>73</i>
<i>Figure 45: Seven Helmert parameters for AC COD, where the 3 translations, 3 rotations and the scale are given in the upper panel. The lower panel shows the standard deviation of unity weight, and the number of stations (A=all in SINEX, I=intersection with IGB00, and R=removed before parameter estimation).</i>	<i>73</i>
<i>Figure 46: Helmert parameters for AC EMR, where the 3 translations, 3 rotations and the scale are given in the upper panel. The lower panel shows the standard deviation of unity weight, and the number of (A=all in SINEX, I=intersection with IGB00, and R=removed before parameter estimation).</i>	<i>74</i>
<i>Figure 47: Helmert parameters for AC ESA, where the 3 translations, 3 rotations and the scale are given in the upper panel. The lower shows the standard deviation of unity weight, and the number of stations (A=all in SINEX, I=intersection with IGB00, and R=removed before parameter estimation).</i>	<i>74</i>
<i>Figure 48: Helmert parameters for the IGS final combined solution, where the 3 translations, 3 rotations and the scale are given in the upper panel. The lower panel shows the standard deviation of unity weight, and the number of stations (A=all in SINEX, I=intersection with IGB00, and R=removed before parameter estimation).</i>	<i>75</i>
<i>Figure 49: Helmert parameters for the MIT final combined solution, where the 3 translations, 3 rotations and the scale are given in the upper panel. The lower panel shows the standard deviation of unity weight, and the number of stations (A=all in SINEX, I=intersection with IGB00, and R=removed before parameter estimation).</i>	<i>75</i>
<i>Figure 50: In total, on GPS week 1321, (a) 179 stations were processed at SIO; 87 transforming stations intersected with the IGB00 frame, but (b) 14 stations were removed from the 7-Helmert-parameter estimation process.</i>	<i>76</i>

Figure 51: Variation of the 7 Helmert parameters in function of the number of transforming stations, at SIO for GPS week 1321. Rotation parameters are shown in (a), translation in (b) and scale in (c). The errorbars are formal errors at the 1-sigma level.	76
Figure 52: Break detection algorithm tested for the north component of the station NTUS (IGS final solution). The first largest break occurred during the Sumatra earthquake in December 2004 (doy 361), followed by a second one, a few months later, which displaced this station by a few cm in the east component.	77
Figure 53: A great earthquake occurred at 16:09:36 (UTC) on Monday, March 28, 2005. The magnitude 8.7 event has been located in northern Sumatra, Indonesia. (source USGS).	77
Figure 54: Break detection algorithm applied to the east component of the station (a) FAIR after the Delani earthquake in 2002 (doy 307) and (b) to the north component of the station MAC1 after the Macquarie Island earthquake (M 8.1) in 2004 (doy 358).	78
Figure 55: Break detection algorithm applied to the vertical component of the station (a) HOLP showing the Hector Mine earthquake on 1998 (doy 24), and an unknown jump in 2002 (doy 76), and (b) of the station LONG, where an antenna and receiver change occurred in 1995 (doy 139), as well as the Hector Mine earthquake in 1999 (doy 289).	79
Figure 56: Break detection algorithm applied to the vertical component of the station (a) WUHN with a receiver change in 1999 (doy 265), an antenna offset in 2002 (doy 26) and in 2002 (doy 304) and (b) HOFN with an antenna and receiver change in 2001 (doy 264).	79
Figure 57: Break detection algorithm applied to the vertical component of the station (a) KELY showing a receiver change in 2001 (doy 257) and (b) HOLB with an antenna and receiver change in 2002 (doy 23).	79
Figure 58: Break detection algorithm applied to the vertical component of the stations (a) RIOG and (b) BRAZ. Small probable breaks of unknown (and unreported) origin were detected.	80
Figure 59: Topocentric coordinate differences between two TRFs and SIO for the station ZIMM located in Zimmerwald, Switzerland. The height component drifts at a velocity of (a) 4.1 mm/year w.r.t. the Igb00 reference frame, while it reaches only (b) 1.9 mm/year w.r.t. ITRF2000.	81
Figure 60: Statistics about the difference IGS minus SIO. The difference in the vertical component for the 359 IGS stations (a). Histogram of the topocentric differences for the 359 stations over the integral time period (b). A cut-off of 50 mm has been enforced.	82
Figure 61: Histogram of the 3D deviation of differences (IGS-SIO) for the 359 stations over the integral time period.	82
Figure 62: Standard deviation of the difference between the ACs and the IGS final solution, in the three components. A cut-off of 50 mm has been enforced.	82
Figure 63: Impact of the COD bug into the IGS final solution for the station MONP in Laguna Mountains, USA for (a) IGS solution and (b) COD solution.	83
Figure 64: Seasonal amplitudes distribution of the height component at COD for 55 stations that passed the selection criteria (see text): (a) annual amplitudes, (b) semi-annual amplitudes.	84
Figure 65: Seasonal amplitudes distribution of the height component at COD for 55 stations that passed the selection criteria (see text): (a) RMS of annual amplitudes, and (b) standard deviation of unity weight.	84
Figure 66: Phase of annual amplitudes distribution of the height component at COD for 55 stations that passed the selection criteria (see text): (a) phase, and (b) RMS of phase.	85
Figure 67: Seasonal amplitudes distribution of the height component at SIO for 45 stations that passed the selection criteria (see text): (a) annual amplitudes, (b) semi-annual amplitudes.	85

Figure 68: Seasonal amplitudes distribution of the height component at SIO for 45 stations that passed the selection criteria (see text): (a) RMS of annual amplitudes, and (b) standard deviation of unity weight.....	85
Figure 69: Phase of annual amplitudes distribution of the height component at SIO for 45 stations that passed the selection criteria (see text): (a) phase, and (b) RMS of phase.....	86
Figure 70: A model change in resolving ambiguities (fixing to integers) for the carrier phase pseudoranges at the European Space Agency (ESA) introduced a jump in the north component of the stations POTS (Potsdam) and WTZR (Wetzell).	86
Figure 71: Vertical displacement of station QAQ1, located in the south of Greenland, as estimated from the available (a) ACs and (b) the daily SOPAC solution.....	87
Figure 72: Baseline length variation between NYA1 and NYAL for IGS. The stations are only separated by ca. 8 m...	87
Figure 73: Baseline length variation between TROM and TRO1 for IGS. The stations are only separated by ca. 51 m.	88
Figure 74: Daily versus weekly topocentric coordinate time series from SOPAC and SIO respectively. Station (a) ZIMM, Zimmerwald, Switzerland and (b) ALIC, Alice Springs, Australia. The black curves show the weekly SIO solution, while red (vertical), blue (north) and green (east) show the topocentric daily SOPAC coordinate time series.....	88
Figure 75: Periodic vertical deformation of the stations (a) BAHN (Bahrain) and (b) HOFN (Iceland), derived from SOPAC and from the modelled deformation calculated by APLO, due to atmospheric pressure loading. 70% of the deformation can be explained by atmospheric loading for the station BAHN, however only 30% of the amplitude is recovered for the station HOFN.....	89
Figure 76: Spectral and aperiodic decomposition of the vertical component of the station WTZR (Wetzell) from SOPAC. (nout=16, so=5.6 mm, s0=5.0 mm, s02=4.2 mm). The black circle points to a common aperiodic deformation observed at the beginning of the year 2003 at many central-European stations (e.g. POTS, GRAZ and BOR1). Offsets are applied for better visibility. See Table 13 for the acronyms on the legend.....	89
Figure 77: Spectral and aperiodic decomposition of the vertical component of the station WTZR (Wetzell) from APLO. (nout=115, so=3.7 mm, s0=3.6 mm, s02=3.6 mm).....	89
Figure 78: Spectral and aperiodic decomposition of the vertical component of the station IRKT (Irkutsk) from SOPAC. (nout=12, so=10.0 mm, s0=7.9 mm, s02=6.3 mm).....	90
Figure 79: Spectral and aperiodic decomposition of the vertical component of the station IRKT (Irkutsk) from APLO. (nout=126, so=4.3 mm, s0=3.4 mm, s02=3.3 mm).....	90
Figure 80: Spectral and aperiodic decomposition of the vertical component of the station MKEA (Hawaii) from SOPAC. (nout=30, so=10.0 mm, s0=9.5 mm, s02=8.0 mm).....	90
Figure 81: Spectral and aperiodic decomposition of the vertical component of the station MKEA (Hawaii) from APLO. (nout=102, so=0.5 mm, s0=0.4 mm, s02=0.4 mm).....	91
Figure 82: Spectral and aperiodic decomposition of the vertical component of the station HOFN (Iceland) from SOPAC. (nout=30, so=10.0 mm, s0=9.5 mm, s02=8.0 mm).....	91
Figure 83: Spectral and aperiodic decomposition of the vertical component of the station HOFN (Iceland) from APLO. (nout=112, so=2.7 mm, s0=2.2 mm, s02=2.1 mm).....	91
Figure 84: Spectral and aperiodic decomposition of the vertical component of the station MAS1 (Las Palmas, Spain) from SOPAC: (a) before 2001 and (b) after November 2000.....	92

Figure 85: Tidal signal of the vertical component of the station MAS1 (Las Palmas, Spain) from SOPAC (red) and ocean tide loading model GOTIC2 from MATSUMOTO et al. 2000.....	92
Figure 86: Simplified integrated loading model. On the one hand, space geodetic techniques allow one to derive polar motion and length of day (LOD) variations as well as geometric deformations. These changes can be related to the so-called equivalent load height column (ELHC) through the LLNs h' and l' . On the other hand, satellite gravity missions produce height anomaly variations. These variations are, once again, related to the same ELHC through the LLNs k' . These LLNs are usually only zonal.....	94
Figure 87: Determination of the height of the load (red arrow), given a measured deformation (black arrow).....	96
Figure 88: Monthly height anomaly variations derived from the Jet Propulsion Laboratory JPL constrained geopotential coefficients for February and March 2005.	96
Figure 89: Generally, for a truncation degree n , there are $n(n+2)$ radial poloidal coefficients H_{nm}^Φ sensitive to the radial deformation (in blue), $n(n+1)$ lateral poloidal coefficients Ψ_{nm}^Φ sensitive to the deformation of the east component (in green), and $n(n+2)$ lateral poloidal coefficients Ψ_{nm}^Φ sensitive to the deformation of the north component (in red). So, in total, there are 6 degree-1 poloidal coefficients. However, in a centre of figure frame, where a no-net-translation condition $2\Psi_{1m}^\Phi + H_{1m}^\Phi = 0$ is imposed on station coordinates, the six degree-1 poloidal coefficients melt into one set of three coefficients.	100
Figure 90: Selected station distribution (609 SOPAC stations) fulfilling specific requirements (see text) (a), and RMS of lateral annual amplitudes (b).	103
Figure 91: Fourier analysis of the vertical deformation for the stations (a) BAHF and (b) WTZR. The period window is limited from two to thirty days.	104
Figure 92: Tidal waves (28806) of the tidal potential catalogue (KSM) of KUDRYAVTSEV (2004) (a), and (b) aliased periods derived from the KSM tidal catalogue with the 24-hours-processing period (blue) and GPS repeat orbit period (red).	105
Figure 93: Temporal variation of the radial degree-0 poloidal coefficient in blue (a), and of the (b) difference of the radial zonal degree-2 coefficient in red (by fixing degree-0 to zero or not fixing it). The coefficient H_{20}^C absorbs approximately one half of the amplitude of coefficient H_{00}^C , if the latter is not estimated.	105
Figure 94: Temporal variation of the radial degree-1 poloidal coefficients.	106
Figure 95: Temporal variation over one year of the radial degree-1 poloidal coefficients (a) H_{11}^C , (b) H_{11}^S and (c) H_{10}^C . These three coefficients (representing the X-, Y- and Z- components of geocentre motion) are determined from the east deformation (E=blue), north deformation (N=green), radial deformation (U=red), separately as well as from the 3D-combined deformation (ENU=cyan=NU). Each dot represents the deformation as estimated by one single station for that specific component. The different results are shifted by 10 mm for better visibility.	107
Figure 96: Temporal variation of (a) the radial and (b) the lateral degree-2 poloidal coefficients.....	108
Figure 97: Angular variation of the principal axes of the vertical deformation w.r.t. the Greenwich meridian.	109
Figure 98: Ratios of degree-2 poloidal coefficients H_{20}^C / Ψ_{20}^C , H_{21}^C / Ψ_{21}^C , H_{22}^C / Ψ_{22}^C , H_{21}^S / Ψ_{21}^S and H_{22}^S / Ψ_{22}^S (from left to right, from top to bottom). The y-axis is unitless. The red line is the ratio of the height and lateral degree-2 LLNs, for a GB-A Earth model, in a CF frame.....	110

List of Tables

Table 1: Acronyms of ACs used in Table 2.....	27
Table 2: Tides-related part of the Analysis Strategy Summaries of the IGS ACs (status of December 2001, source taken from GPS WG6 report).	28
Table 3: Tides-related part of the Analysis Strategy Summaries of the IGS ACs (status as of April 2006, source from IGS) for the displacement.	28
Table 4: Six astronomical arguments. The meaning of msd is mean solar days.	35
Table 5: Harmonic development of the luni-solar tidal potential.....	35
Table 6: Effects influencing the effective values of Love and Shida Numbers.	37
Table 7: Characteristics of publicly available atmospheric loading products (source taken from a presentation given by VAN DAM at the IERS Workshop Combination 2005).	50
Table 8: Trend of topocentric coordinate time series over the years 1996-2004, for the site Wettzell (code 7224/WTZR).	67
Table 9: Trend of topocentric coordinate time series over the years 1996-2004, for the site Westford (code 7209/WES2).	68
Table 10: Trend of topocentric coordinate time series over the years 1996-2004, for the site Onsala (code 7213/ONSA).	68
Table 11: Acronyms used for Analysis Centres (ACs) and Global Network Associate Analysis Centres (GNAACs).....	69
Table 12: Station codes.	78
Table 13: Periods corresponding to the frequencies q_j in the model of parameters.	81
Table 14: Mean and standard deviation of the differences w.r.t. the IGS final solution. (N=north, E=east, and U=vertical component).	83
Table 15: Azimuth-independent ($m=0$) theoretical conversion factors a_{n0} , b_{n0} and c_{n0} up to degree-11, in the centre of figure frame (CF) for the Gutenberg-Bullen GB-A Earth model.....	98
Table 16: Minimum number s of well distributed stations in function of the truncation degree n	100
Table 17: Partial derivatives of the geometric deformation w.r.t. the radial degree-2 poloidal coefficients (PC), which are only sensitive to the radial deformation U	101
Table 18: Partial derivatives of the geometric deformation w.r.t. the lateral degree-2 poloidal coefficients (PC), which are only sensitive to the east (E) and north (N) deformation.	101
Table 19: Comparison of degree-1 coefficients H_{1m}^{Φ} from GPS inversion between BLEWITT AND CLARKE (2003) (denoted by BaC) and our study (OS). AA=Annual Amplitude [mm], SA=Semi-annual Amplitude [mm], AP=Annual Phase [deg], SP=Semi-annual Phase [deg], using the same conventions as BLEWITT AND CLARKE (2003). Here, only the radial deformation has been used.	107

Curriculum vitae

Mendes Cerveira Paulo Jorge

mendes@mars.hg.tuwien.ac.at

<http://mars.hg.tuwien.ac.at/~mendes/>

Profile

Country of Nationality: Luxembourg

Date of Birth: February 4, 1976

Place of Birth: Pombal (Portugal)

Education

April 2002 – present

Ph.D. Thesis entitled: “Tidal and non-tidal contributions of surface loading processes on station coordinates” at the Vienna University of Technology. Department of Advanced Geodesy.

March 2002:

Diploma (M.Sc.) in Surveying Science at the Vienna University of Technology. Department of Advanced Geodesy. Diploma Thesis entitled “The quality of real-time GPS-orbits”.

Feb.-Aug. 2001:

ERASMUS Exchange at the “Universidad Politécnica de Valencia” (Spain).

May 1999:

Vienna University of Technology. First Diploma Degree. Inscription in Geodesy and Geophysics.

September 1995:

Vienna University of Technology. Inscription in Surveying Science.

1988 – 1995:

Graduated at Lycée Classique de Diekirch LCD, Luxembourg.

